THÈSE DE DOCTORAT

de

L'UNIVERSITÉ DE LILLE

École doctorale Sciences de la Matiére, du Rayonnement et de l'Environnement
(SMRE, ED 104)

Discipline : Physique, Milieux dilués et optique fondamentale

Présentée par

Anastasia PIENKINA

Récepteur Hétérodyne pour la Spectroscopie de Molécules Interstellaires en Laboratoire

---

Date de soutenance : 12 Mars 2018

Jury de soutenance :

M.	Laurent MARGULES	Professeur, Université de Lille	Directeur de thèse
Mme	Martina WIEDNER	LERMA, Observatoire de Paris	Co-Directrice de thèse
M.	Roman MOTIYENKO	Université de Lille	Co-Encadrant de thèse
Mme	Agnès PERRIN	Ecole Polytechnique	Rapporteur
M.	François PAJOT	Université de Toulouse	Rapporteur
Mme	Maud ROTGER	Université de Reims Champagne-Ardenne	Examinateur
M.	Michel PIAT	Université Paris Diderot	Examinateur

"Humanity's deepest desire for knowledge is justification enough for our continuing quest. And our goal is nothing less than a complete description of the universe we live in."

Stephen Hawking, A Brief History of Time

"Notre soif de découverte stimule notre créativité dans tous les domaines. Si notre quête prenait fin, l'esprit humain dépérirait et mourrait. "

Stephen Hawking

Contents

Resumé

L'objectif de cette thèse est de développer un instrument - récepteur hétérodyne à 600 GHz basé sur un mélangeur Schottky pour améliorer la sensibilité de la spectroscopie moléculaire en laboratoire, combiné avec l'analyse des molécules d'intérêt astrophysique.

Le sujet principal a été d'étudier des molécules en phase gazeuse qui peuvent être présentes dans le milieu interstellaire. Des études en laboratoire et pour l'observation nous ont permis de nous intéresser aux dérivés substitués en méthoxy- (CH_3O), aux isotopologues et aux états vibrationnels excités.

Le méthoxy isocyanate CH_3ONCO et ses états vibrationnels excités, est une molécule qu'il est possible de chercher et d'identifier dans les nuages interstellaires en raison de la détection de méthyle isocyanate (CH_3NCO) dans Orion KL, vers Sgr B2 (N), proto-étoile de faible masse IRAS 16293-2422 et sur la surface de la comète 67P/CG.

Le cyanure d'éthyle est une molécule abondante observée dans les nuages moléculaires. Dériver le fractionnement isotopique de ^{13}C des molécules grâce à des observations est l'une des méthodes pour comprendre leur mécanisme principal de formation. L'abondance des mono-, doubles et triples isotopologues $^{13}CH_3^{13}CH_2^{13}CN$ obtenue par les observations, peut donner des suggestions sur les mécanismes de fractionnement et l'origine du carbone fractionné.

Le spectre de rotation de deux molécules organiques complexes d'intérêt astrophysique, ^{13}C isotopologues du cyanure d'éthyle, $^{13}CH_3^{13}CH_2^{13}CN$ et du méthoxyisocyanate, CH_3ONCO, ont été étudiées dans les gammes de fréquences millimétrique et sub- millimétrique avec le spectromètre à balayage rapide du laboratoire PhLAM. Ces deux molécules ont et seront recherchées à l'aide de radio télescopes tels que celui de l'IRAM 30m, ALMA et NOEMA afin de détecter leur présence dans le milieu interstellaire. Les paramètres spectroscopiques précis et fiables de $^{13}CH_3^{13}CH_2^{13}CN$ et CH_3ONCO ont été obtenus pour fournir des prédictions pour observer ces molécules pour la première fois dans l'espace.

D'autre part, la spectroscopie moléculaire de laboratoire dans la gamme THz nécessite le développement instrumental pour améliorer les performances du spectromètre à balayage rapide au laboratoire PhLAM: sensibilité, résolution, précision, etc.

Le récepteur non cryogénique à l'état solide hétérodyne Schottky à 600 GHz a été conçu au LERMA, Observatoire de Paris en partenariat avec le Laboratoire de Photonique et de Nanostructures (LPN-CNRS). Le récepteur est basé sur un synthétiseur de fréquence micro-ondes et un mélangeur Schottky sub-harmonique, pompé par une chaîne de multiplicateurs et d'amplificateurs de fréquence. Le récepteur hétérodyne Schottky est le plus sensible à 600 GHz, avec la température de bruit de 1000-1500 K à la température ambiante. Il fournit un niveau de sensibilité comparable à celui des bolomètres refroidis à l'hélium et on considère qu'il permet d'offrir la plus haute sensibilité pour la spectroscopie moléculaire en laboratoire dans une gamme de fréquences de 600 GHz, notamment pour le spectromètre de Lille.

Mots clés: spectroscopie moléculaire; terahertz techniques; hétérodyne; molécules organiques complexes (MOC); milieu interstellaire (MIS)

Abstract

The objective of this PhD thesis is to develop an instrument - a 600 GHz Schottky heterodyne receiver for more sensitive molecular spectroscopy in the laboratory, combined with the analysis of the molecules of astrophysical interest.

The principal subject of a thesis was the gas-phase spectroscopic studies of molecules that are expected to be present in the interstellar media. The rotational spectrum of two complex organic molecules of astrophysical interest, triple- ^{13}C isotopologues ^{13}CH$_3$^{13}CH$_2$^{13}CN of ethyl cyanide and methoxyisocyanate, CH$_3$ONCO, have been was recorded and analyzed in millimeter and sub-millimeter frequency ranges with Lille fast scan DDS spectrometer in PhLAM. These molecules will be searched by radio telescopes as IRAM 30m and ALMA in order to detect their presence in the interstellar medium.

Methoxy isocyanate with its low lying vibrational states, is a possible candidate molecule for searches in the interstellar clouds by reason of the detection of methyl isocyanate (CH$_3$NCO) in Orion KL, towards Sgr B2(N), the low-mass protostar and on the surface of the comet 67P/C-G. Such wise, investigation of the vibrationally excited states, perturbed by interactions of Coriolis type, as in the case of methoxy isocyanate, CH$_3$NCO is of great interest.

Ethyl cyanide is an abundant molecule observed in hot molecular clouds. Deriving ^{13}C isotopic fractionation of the molecules by observations is one of the promising methods to constrain their main formation mechanism. The derived abundance ratios of mono-, double and triple- ^{13}C isotopologues ^{13}CH$_3$^{13}CH$_2$^{13}CN, which is one of the subjects of the current study, can give suggestions about fractionation mechanisms and the origin of the fractionated carbon.

A set of accurate and reliable spectroscopic parameters has been obtained to provide predictions to support observation of these molecules for the first time in space.

On the other hand, THz laboratory molecular spectroscopy requires the development in instrumentation that can improve the total performance of a spectrometer, its sensitivity, resolution, accuracy measurement etc. The part of the PhD thesis was dedicated to the development and testing a prototype of a non-cryogenic solid-state Schottky het-

erodyne receiver, operating in 600 GHz frequency range, that provides level of sensitivity, comparable to those of Helium-cooled bolometers and its further integration with Lille spectrometer. A 600 GHz Schottky heterodyne receiver was designed at LERMA, Observatoire de Paris in partnership with LPN-CNRS (Laboratoire de Photonique et de Nanostructures) for European Space Agency (ESA) Jupiter Icy Moons Explorer (JUICE) (O. Grasset et al. 2013) that will investigate the composition of Jupiter's and its icy moon atmospheres. Receiver is based on microwave frequency synthesizer, and sub-harmonic Schottky mixer, pumped by frequency amplifier multiplier chains (AMCs). It has a DSB (double side band) noise temperature of 1000-1500 K at room temperature, which makes it the most sensitive up to date non-cryogenic solid-state heterodyne receiver at 600 GHz frequency range. It is considered to provide reasonably high level of sensitivity for laboratory molecular spectroscopy in a 600 GHz frequency range with Lille fast scan DDS spectrometer.

Keywords: molecular spectroscopy; terahertz technics; heterodyne; complex organic molecules (COMs); interstellar medium (ISM)

Acknowledgements

Remerciements

Lille/Paris 2015-2018

Acronyms

ADC analog-to-digital converter

FM frequency modulated signal

FT Fourier transform

IF intermediate frequency

PLL phase-locked loop

SNR signal-to-noise ratio

THz terahertz

MM millimeter

SHR Schottky heterodyne receiver

FSS fast scan spectrometer

HEB hot electron bolometer

DDS Direct digital synthesizer

AMC amplifier multiplier chain

Introduction

THz Astronomy

The THz spectral range has become of great importance in a wide range of disciplines, including space research, astronomy, atmospheric studies, non-destructive testing, etc. THz techniques also have been applied in the pharmaceutical and security applications. THz spectral range is considered as the band from 0.3 to 10 THz (1 mm - 30μm), it is partly overlapping with the sub-millimeter (sub-mm) region 0.1–3 THz (3 mm - 100 μm), term mainly utilized by some astronomers and spectroscopists, far-infrared (FIR) ($\sim$300 - 50 μm), and mid-infrared (MIR) ($\sim$50 - 3 μm) .

One of a major reason for the research at THz frequencies comes from astronomy. The region between 0.1 and 10 THz corresponds to the peak of thermal emission from dust and molecules throughout the Universe. THz range, up to about 1 THz is rich in the rotational lines of molecules present in the interstellar medium (ISM). In particular, the submillimeter-wave range is rich in spectral lines of important molecular species, whose detection is important to understand the formation of stars and galaxies.

Historically, the region of the THz spectrum above 600 GHz has been relatively unexplored due to atmospheric absorption and technical difficulties in generating and detecting THz radiation. The observatories such as Herschel, SOFIA[1] and ALMA[2] have driven the development of THz heterodyne receivers, solid-state radiation sources and spectrometers.

Ground-based telescopes around the world such as the IRAM 30m[3] in the Sierra Nevada, NOEMA[4], Interferometer at Plateau de Bure located in the French Alps, ALMA in the Atacama desert in Chile, have contributed significantly to the exploration of the THz spectral region, with IRAM 30 m and NOEMA covering the range from about 80 to 300 GHz, and ALMA bands up to 950 GHz. Because of the high absorption of the Earth's atmosphere in the presence of water vapour over most of the THz frequency range, these

---

[1]Stratospheric Observatory for Infrared Astronomy

[2]The Atacama Large Millimeter/submillimeter Array

[3]The 30m millimeter radio telescope operated by the Institute for Radio Astronomy in the Millimeter Range (IRAM).

[4]The NOrthern Extended Millimeter Array

telescopes and observatories are located at high altitude sites such as the high altitude Chajnantor plateau in the Atacama desert about 5,058 m above sea level in Chile.

Detailed astronomical observations with such instruments provide information on the chemical evolution and composition of the ISM. Several extensive molecular line surveys of astronomical sources over a broad frequency range have been already performed with ALMA and IRAM 30 m for the search of new molecules in the ISM [1–3]. Observation of rotational transitions could not only identify the molecules present in the ISM, but can also be used to derive the abundance of that molecule and the physical conditions of the source where it has been observed – the gas density and the temperature.

Interstellar Media and Molecules of Astrophysical Interest

The ISM consists mainly of molecular species and interstellar dust, with a % ratio of gas to dust of about 99:1. The species present in ISM are predominantly in the gas phase in neutral form and may consist of molecules, atoms, free radicals.

By 2017 approximately 200 molecules have been detected in the ISM according to CDMS [5] [4, 5]. The existence of such a diverse chemistry indicates a chemical evolution occurring in space. There are fairly simple molecules, such as CO and NH_3, but molecules consisting of ten or more atoms have also been detected. A very large fraction of these are complex organic molecules (COMs). COMs are traditionally defined as carbon-based molecular species with more than six atoms in their structure. With this definition, about one third of the molecules detected in the ISM are complex organic molecules. A comprehensive review of complex organic interstellar molecules is given by [6].

The majority of identified COMs in the ISM has been detected towards hot cores of dense molecular clouds, such as Orion KL and Sgr B2. The molecular clouds in the ISM contain the material for the formation of stars and the subsequent development of life. The understanding of the formation routes of COMs, how they form, when they form and where they come from, are the fundamental questions in astrochemistry and the origins of life.

In hot molecular cores, significant amount of the observable lines are still unidentified. There is a common view that many of these unidentified lines may belong to low lying excited vibrational states, that can be significantly populated in hot core sources, or/and isotopologues of abundant molecules, referred to as the astrophysical weeds. The spectroscopic problem is not only that there might be a large number of vibrational states and lines, but more importantly it is also often difficult to assign and analyze them because of strong perturbations and interactions (Fermi, Coriolis types for example) among states.

---

[5]Cologne Database for Molecular Spectroscopy

With the increase in sensitivity of instruments such as ALMA, more and more of these lines will be detected and it becomes necessary to identify them and assign the detected lines belonging to the vibrational states and isotopologues of abundant molecules.

Thus a detailed laboratory study of the isotopologues of the most abundant species and vibrationally excited states is required. Without this spectroscopic information, the analysis of the data from instruments such as ALMA will be limited.

Laboratory Spectroscopy

The large number of COMs leads to a rich spectrum with a large number of lines that astronomers must observe to "identify" molecule in space. In order to prove whether observational astronomical spectra contain features that can be attributed to different molecules, these features have to be compared with laboratory spectra. A knowledge of the molecular spectra can only be accomplished by a detailed measurements in a laboratory. For that, we, spectroscopists, need to perform high-resolution laboratory studies and provide accurate spectroscopic data for astronomers. Laboratory data can be also used to suggest what other molecules may be present and which processes take place in the ISM for their formation.

Spectroscopic data obtained from laboratory studies are currently available in molecular data bases, such as the Jet Propulsion Laboratories (JPL) data base and the CDMS.

One of the objectives of the thesis is to measure and analyze rotational spectra of potential ISM molecules in the sub-mm range, to obtain accurate spectroscopic parameters and to provide reliable frequency predictions to search for astronomically interesting molecules in the ISM and to facilitate astronomers with their detection in space.

In this thesis a new experimental study of the rotational spectrum of CH_3ONCO, methoxy isocyanate, and $^{13}CH_3^{13}CH_2^{13}CN$, triple- ^{13}C isotopologue of ethyl cyanide, which are thought to be present in detectable abundances in hot molecular clouds such as Sgr B2, was performed in a laboratory.

Space Instrumentation Development for Laboratory Spectrometers

Assigning the observed lines in astronomical spectra to particular molecules involves a comparison with rotational spectra from laboratory experiments. For the identification in space, precise frequency measurements of molecular pure rotational transitions in laboratory are important. Accurate measurements of the frequencies of spectral lines depend on the spectral resolution and on the sensitivity (or the achievable signal-to-noise ratio) of the spectrometer. To improve sensitivity and/or resolution of laboratory spectrometers, instrumental development is needed. High sensitivity, most often, is related to high sen-

sitive detection, that can detect weak molecular lines. High sensitivity of a spectrometer, for example, will allow to detect and identify isotopologues or vibrational excited states, whose intensities are weak. More sensitive laboratory spectroscopy will be also advantageous in recording weak molecular lines. High resolution is relevant to the ability of spectrometer to resolve single spectral lines of molecules in a spectrum. The high resolution will clearly distinguish the molecular lines from different species and resolve blended lines.

To study spectra of gas phase molecules in the laboratory at very high spectral resolution, absorption spectroscopy is widely used. Since THz absorption spectroscopy usually uses highly monochromatic radiation sources and sensitive detectors, absorption spectroscopy is a high resolution and high sensitive technique. The design of a THz laboratory spectrometer, operating in absorption, needs reliable radiation sources with sufficient output power, and sensitive detectors.

Until recently sub-millimeter and THz molecular spectroscopy has been a technical challenge due to the lack of appropriate radiation sources. The Herschel mission contributed significantly to the development and industrial production of compact solid-state THz sources and detectors which now find scientific use in space research, astronomy, laboratory spectroscopy and remote sensing. Nowadays solid state radiation sources, based on Schottky diode frequency multipliers are the most widely used solid-state devices for high-resolution spectroscopy up to 3 THz. Up to date the most sensitive detectors, used for laboratory THz spectroscopy are bolometers cryogenically cooled with liquid Helium (4.2K).

The Lille solid state fast-scan spectrometer (FSS) was used to measure the spectra of molecules of astrophysical interest, investigated in this work. FSS is an absorption frequency-modulated spectrometer with lock-in detection that offers both highly sensitive detection and rapid spectral acquisition. It covers the 88% of 75-1550 GHz range. The spectrometer is equipped with a 4.2 K Helium cooled (InSb) hot-electron bolometer from QMC Instruments Ltd, can be employed as detector up to 1.5 THz. The room temperature, zero biased, Schottky diode detectors from VDI Inc. can used as well below 400 GHz. FSS is of state of the art instrument to perform THz molecular spectroscopy in a laboratory.

However, 4K QMC InSb hot electron bolometer (HEB), employed as a broad-band detector with FSS, requires cryogenic cooling by liquid Helium in cryostat which complicates practical use of HEB and increases the cost of operation. The part of the thesis will be devoted to the development of a new compact non-cryogenic solid-state Schottky heterodyne receiver, operating in 600 GHz frequency range that provides high level of sensitivity at room temperature and its further integration with FSS.

Thesis Outline

The thesis consists of two parts, it is organized as follows:

The Part I is dedicated to the instrumentation for molecular laboratory spectroscopy at the Millimeter-Wave and Terahertz ranges. Chapter 1 gives an introduction to high resolution laboratory molecular spectroscopy at MM-wave and THz ranges, noticeably to radiation sources and detectors, used in the experimental spectroscopy in the laboratory. Chapter 2 describes the Lille fast scan DDS spectrometer that was used to measure the spectra of molecules of astrophysical interest, investigated in this work. Chapter 3 presents experimental investigation of transmission properties of a number of important materials: High-density Polyethylene (HDPE), high resistivity Silicon, Zitex and Mylar at 600 GHz and 1.4 THz, that can be used to design components in instrumentation for astronomy and spectroscopy in THz frequency range. Chapter 4 is dedicated to the development and testing a prototype of a 600 GHz Schottky heterodyne receiver, that was built for this thesis using components initially designed for the ESA space mission JUICE and its integration with the Lille fast scan DDS spectrometer. The configuration and the main components of the Schottky heterodyne receiver will be described and the first measured spectra of CH $_3$CH$_2$CN will be presented.

The Part II of the thesis is dedicated to the laboratory molecular spectroscopy. The theoretical background, needed for the analysis of the molecular spectra is given in Chapter 5. Watson's A- and S-reduced Hamiltonian for analysis of asymmetric rotor molecules and Hamiltonian to treat Coriolis interactions are introduced. The analysis of the rotational spectrum of two molecules of astrophysical interest, triple- ^{13}C isotopologues ^{13}CH$_3$^{13}CH$_2$^{13}CN of ethyl cyanide and methoxyisocyanate, CH$_3$ONCO in the ground and excited states of four lowest lying vibrational modes (ν_{18}=1, ν_{18}=2, ν_{18}=3 and ν_{11}=1) are presented in Chapter 6. Conclusions are given in Chapter 7.

Part I

Instrumentation for Millimeter-Wave and Terahertz Laboratory Spectroscopy

Chapter 1

Introduction to High Resolution Laboratory Molecular Spectroscopy at MM-Wave and THz Ranges

1.1 Overview

The rotational spectra of the majority of astrophysical molecules cover the frequency range up to about 1 THz. For the studies of molecules in a laboratory, an instrument, a spectrometer, with high sensitivity and spectral resolution, should be built. To study spectra of gas phase molecules in a laboratory at the highest spectral resolution, it is preferably to use absorption spectroscopy.

A typical spectrometer, operating in absorption, consists of 3 essential components: radiation source, an absorption gas cell, and a detector. The rational choice of the components and/or of the applied technique, used for the experimental spectroscopy in laboratory, is important since it determines the performance of the spectrometer, e.g. its sensitivity, spectral resolution, achievable frequency measurement accuracy etc. However it is important to make proper selection of the components, currently present on the market, with regard to their characteristics and application purposes, these criteria will be discussed here.

1.2 Design of Absorption Spectrometer

The selection of the type of spectrometer for an experiment is determined by its relevance to the particular application. There are 3 categories of spectrometers: those operating in 1) absorption, 2) emission and 3) non-radiative relaxation. Onwards, among these 3 categories, there are the different types of spectrometers: they include conventional absorption spectrometers, chirped-pulse Fourier Transform Microwave (CP-FTMW) spectrometers, cryogenic ion trapping techniques, gas discharge, supersonic jet CP-FTMW, cavity en-

hanced molecular beam (MB-) FTMW spectroscopy and other techniques. The current discussion will be limited to the spectrometers, operating in absorption, and the focus will be on its measurement methods and techniques.
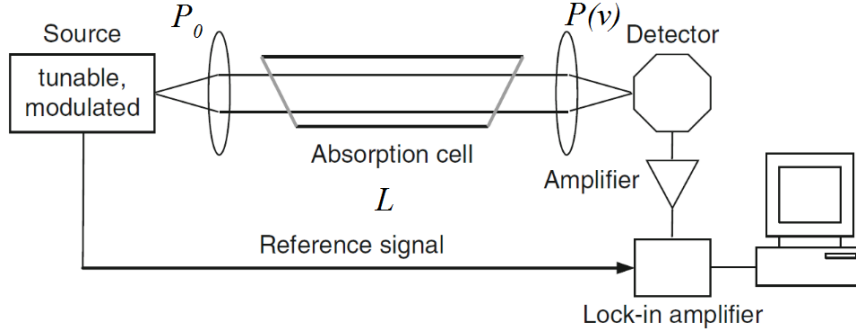
Figure 1.1 – Simplified scheme of an absorption spectrometer for molecular spectroscopy [7]. The frequency of the source is tunable and its power or frequency can be modulated by some method.

The scheme of an absorption spectrometer to perform molecular spectroscopy in a laboratory is shown at Fig. 1.1. Generally, an absorption spectrometer consists of: an tunable, monochromatic radiation source, modulated by some method; an absorption cell containing the gas sample; and a sensitive broad-band detector. The radiation source emits radiation with a given power at a particular frequency. Then, it is transmitted through an absorption cell, which is filled with a gas at a particular pressure, and the signal is detected by an appropriate detector and is usually then also amplified. Computer is normally used to control the spectrometer's hardware. The frequency of radiation source is swept across the given frequency range where absorption features should be present, and the amount of transmitted source power is measured; and spectra are recorded in a such way. Often, some modulation technique is applied in order to increase sensitivity and to minimize baseline fluctuations in the recorded spectrum.

The general method for measuring spectra with absorption spectrometers is based on the determination the absorption coefficient $\alpha(\nu)$ (Beer–Lambert law):

$$P(\nu) = P_0 \exp(-\alpha L) \tag{1.1}$$

where $P(\nu)/P_0$ is the power transmitted through an absorption gas cell with a path length L. The change in the power due to the absorption by a gas is $\Delta P \approx \alpha \, LP_0$ (for the small absorptions $\alpha \, L \ll 1$).

1.3   Limitations of the Absorption Spectrometers

Many molecular lines in spectra may give very weak absorption, but that might be important for providing additional information and contribute to the spectroscopic analysis. To detect *them*, spectrometer must be *sensitive*. The sensitivity of the absorption spectrometer is determined by the lowest measurable absorption in the gas cell, which is usually limited by phase noise of the radiation source and by detector noise. Phase noise of the radiation source represents random fluctuations in the phase of a signal (and hence frequency). Standing waves are one of the most troublesome issues, that cause a spurious signal, "baseline", that [periodically] varies with a frequency. Variations in a power might be also produced by variation in transmission due to the reflections in waveguides and/or absorption cell. (Transmission of windows of the absorption cell can vary with frequency; etc). These factors generally limit a performance of absorption spectrometer. However, to improve its sensitivity (but not always overcome), we may try to use the following techniques:

- Rationally choose the main components to build a spectrometer or to employ those with superior characteristics. Radiation source with lower phase noises and/or detector with lower NEP will improve the performance of a spectrometer. Requirements for the radiation sources and detectors for high resolution spectroscopy will be discussed below in Sec. 1.4.

- Source modulation and lock-in detection. Considerable improvements in increasing signal-to-noise ratio of absorption molecular line can be achieved by a frequency modulation (FM) of the radiation source. If/When absorption line occurs in a spectra, the frequency modulation is converted into amplitude variations, whose output signal is amplified and measured with reference to the modulation frequency by a lock-in amplifier (that also converts an AC signal into a DC signal). Stark modulation, i.e. applying and interrupting an electric field to a molecule under investigation, or Zeeman modulation, magnetic modulation, to study paramagnetic molecules or free radicals, can be applied as well. By using frequency modulation combined with lock-in (synchronous) detection at the n harmonic of the modulation frequency, we normally can suppress the baseline. A signal thus will be proportional to the n th derivative with respect to frequency of the baseline. Lock-in technique with frequency modulation provides high sensitive detection and accurate measurements by also removing low frequency noise signals (that could arise from vibrations in a laboratory, for example).

- Pressure optimization in a gas cell. Pressure broadening of a molecular line can be

reduced by adjusting (low) pressures, that will help to improve spectral resolution and keep the high sensitivity level.

- Standing waves can be reduced by putting an attenuator between two sources of reflection. The attenuator, however, may introduce new reflections.

- To "filter", or suppress unwanted (usually low frequency noise signals that could arise from vibrations in a laboratory, for example) frequencies except those from the radiation source, in a laboratory from affecting the instrument.

- Heterodyne detection. The frequency of radiation source can be shifted to a significantly lower frequency (a few MHz or GHz), where the signal can be easily amplified, which is not possible for frequencies above 150 GHz, because there are no commercially available amplifiers at MM-wave and THz frequency ranges. Thus a gain in sensitivity can be achieved. (This will be presented in Chapter 4.)

- A careful optical design of spectrometer: appropriate use of materials for windows for absorption gas cell to minimize losses and maximize signal-to-noise ratio. Choice of a particular material depends on a frequency range. Besides, focussing elements such as off-axis mirrors or/and lenses, may be used to guide radiation and match the apertures of each component in a spectrometer to avoid power dissipation. (This investigation will be carried out in Chapter 3)

1.4   MM-wave and THz radiation sources

There are many methods of generating and detecting THz and MM-wave radiation. A good review of sources, developed in the last years is given in [8–10]. Although, in selecting a radiation source (or detector) for spectroscopy, it is not only important to consider the desirable operation characteristics, but also practicalities.

A radiation source for high-resolution molecular spectroscopy in THz and MM-wave range needs to meet the following requirements:

1. Sufficient output power. For frequencies in the THz range, even producing a few microwatts of output power is a significant technical challenge.

2. Spectral purity and low phase noise. A source should be spectrally clean, that is, as possible, without spurious spectral components. This is particular critical in systems with frequency multiplication, since all spectral components will be multiplied and present in the spectra, besides those arising from molecular lines. Phase noise of the radiation source represents random fluctuations in the phase of a signal (and

hence frequency). It is an important parameter of a MW frequency synthesizer that is mainly determined by the performance of the oscillator used to build the synthesizer.

3. Stability of frequency and output power.

4. Tunability over a wide frequency range.

5. Source should be monochromatic, i.e. emitting only a single frequency, and thus have a narrow spectral linewidth.

6. Continuous wave operation (constant amplitude and frequency).

7. Preferably to be in a compact package and easy to handle (without cryogenic or water cooling etc.)
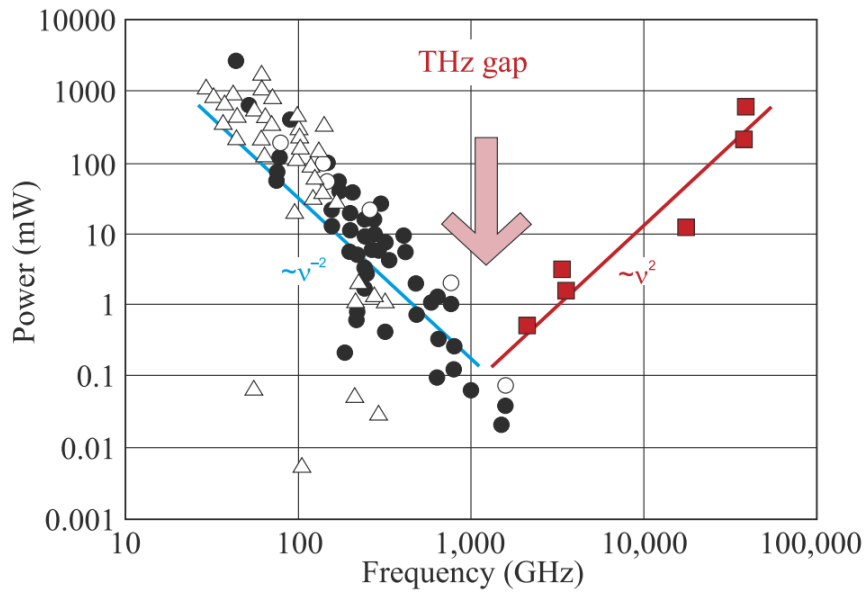
Figure 1.2 – THz gap with respect to source technology: (□∗) quantum cascade lasers (QCL) are progressing downward from high frequencies; (●) frequency multipliers dominate other electronic devices (△) above about 150 GHz; crycryogenic sources are shown as hollow symbols (○). Reproduced from Ref. [11].

Until the recent developments, following HIFI Herschel launch, the lack of compact monochromatic tunable and reliable power radiation sources in the submillimeter-wave frequency range has been a limiting factor for high resolution spectroscopy in this spectral range [12]. The 1–3 THz frequency range lies in the so-called "terahertz gap", namely because there are not so many commercial available radiation sources with sufficient output power. Figure 1.2 shows a summary of THz and MM-wave sources, ranging

from frequency multipliers to quantum cascade lasers (QCL) and other electronic devices (Gunn diodes, Klystrons, resonant tunneling diodes, backward-wave oscillators), available to generate radiation from 100 GHz to 10 THz. Electronic devices such as Klystrons or Gunn diodes [13–15] generate radiation up to about 100 GHz and then subsequent frequency multiplication (by Schottky or lattice multipliers) can be used to achieve the frequencies, up to a few THz, although with a significant drop in output power. As is seen, above 800 GHz the efficiency of electronic devices, and below 2 THz the semiconductor lasers decreases significantly.

Table 1.1 summarizes key characteristics of the most important radiation sources, that could be employed to perform molecular laboratory spectroscopy in THz and MM-wave range: Multiplier chains (sources based on microwave frequency synthesizers and Schottky frequency multipliers), molecular gas lasers, backward-wave oscillators (BWO), quantum cascade lasers (QCL). The disadvantages or simply inaccessibility of radiation sources at THz frequencies made the implementation of compact and reliable radiation sources for laboratory spectroscopy, that operate at a room temperature with sufficient output power, of a great concern in this frequency range.

Table 1.1 – Key characteristics of frequency radiation sources, that could be employed for THz and MM-wave spectroscopy

	Frequency range	Output power	Relative bandwith	Power need to drive	Mass	Operation temperature
Multiplier chain (Schottky)	40 GHz to 3.2 THz	microwatt to milliwatt	≈10% to 15%	medium	small compact	293 K
Gas laser	>10 THz	high	very narrow	high	large bulky	Room T
QCL	1.2 to 4.7 THz	milliwatt	few percent	medium to high	small compact	Cryogenic
BWO	33 GHz to 1.2 THz	high (3-50 mW)	≈20% to 30%	high	compact, but bulky power supply	water cooling, high voltage

The backward-wave oscillators (BWO), also known as "O-Carcinotrons" in France, were one of the most powerful monochromatic sources used for molecular spectroscopy in the millimeter and sub-millimetre wave ranges. The first BWOs were invented independently in France [16] and in the USA [17] in the 1950s. Despite the fact that BWOs are currently practically not used due to their manufacturing difficulties and limited commercial availability, these sources deserve special attention since for the decades they have been implemented in high resolution spectrometers in many laboratories (groups in Köln, Lille, Kharkiv, Warsaw, JPL, ...) to measure the spectra of molecules and to obtain valuable spectroscopic data. BWO tubes have been designed and fabricated by the Russian company ISTOK and are still commercially available but in a limited edition. BWO produces radiation from a guided electron beam traveling along a high voltage periodic structure, placed in a magnetic field (Figs. 1.3,1.4). These tunable sources can cover the range from 36 GHz to 1.2 THz with output power of some tens of mW at 300–600 GHz and one to a few mW up to 1.2 THz. The disadvantages of BWO are the need to use high-voltage

power supplies of about 1–6 kV, magnets necessary to collimate the electron beam and external water cooling. Besides, operational lifetime of a BWO could be quite short if source operates at full power.
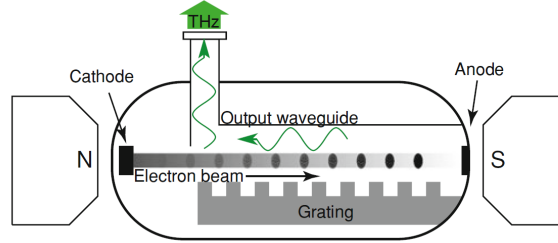
Figure 1.3 – Schematic diagram of a back wave oscillator. Reproduced from Ref. [18]
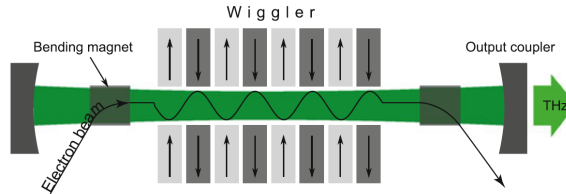
Figure 1.4 – BWO consists of a periodic metallic structure placed inside a tube. The electron beam performs a sinusoidal motion, producing THz radiation.

The molecular gas lasers [19–21] are another method for generation THz radiation that have been used in the past for molecular spectroscopy. Operation of molecular lasers is based on the transitions between different rotational states of molecules (HCN, NH_3, CH_3OH for example). They can cover wide frequency range from hundreds GHz to 10 THz and reach the output power to several milliwatts. But, being bulky and difficult to operate, these sources are nearly currently not used in spectroscopy. Besides, the lack of significant frequency tunability and power stabilization (which is mainly due to the nature of the active medium), ultimately limits their use for high-resolution spectroscopy.

Quantum cascade lasers (QCL) [22–24] are another promising technology to realize compact THz sources especially in the range of 1–5 THz and apply this technique for laboratory spectroscopy. QCL have recently started to become commercially available. The operating principle of a QCL relies on the photon emission created by a series of quantum wells, mostly based on GaAs superlattices, when they're exposed to an electric field. The output power from QCL can be very high, exceeding 100 mW in CW mode. But these sources are usually expensive, they require special design and fabrication technology, besides, cryogenic cooling is needed, thus QCL are not very accessible for laboratory spectroscopy at the moment.

9

Also today the French SOLEIL (Source Optimisée de Lumière d'Energie Intermédiaire) and the Canadian Light Source, particle accelerators of electrons, that produce collimated *synchrotron radiation*, an extremely bright light, are used as sources for molecular spectroscopy, but in the far infrared. The beam of synchrotron light is then combined with high resolution Fourier-Transform spectrometers. For example, the AILES beamline at SOLEIL, conceived for absorption spectroscopy, cover the range 0.15-45 THz with the resolution of about 30 MHz (it is mainly limited due to the use of the FT Bruker interferometer).

1.5 Frequency Amplifier Multiplier Chains (AMC)

Nowadays Schottky frequency multipliers in combination with microwave frequency synthesizers (and medium power amplifiers, MPA) are the most widely used solid state radiation sources in majority spectroscopy groups, working in THz and/or MM-wave. These radiation sources are also known as frequency Amplifier Multiplier Chains (AMCs) and were developed for primary use as the local oscillators (LO) of heterodyne receivers for astrophysics instruments (HIFI on Herschel Space Observatory, ALMA) [25, 26].

Modern *amplifier multiplier sources, based on MW frequency synthesizers*, have greatly simplified high sensitivity molecular spectroscopic measurements in a MM-wave and THz range. *These radiation sources* are very frequency stable and accurate which is extremely valuable for precise measurements of molecular spectra. In comparison to other MM-wave and THz sources, briefly reviewed in the previous section, frequency amplifier multiplier chains, in combination with MW frequency synthesizers have many advantages, especially for high-resolution spectroscopy. They are commercially available, completely solid state electronic sources, operating at a room temperature. They provide stable power output and precise frequency control in a compact package without any mechanical tuners, high voltage, phase lock schemes, magnets (as in the case of backwards wave oscillators or lasers) and other complications in use. All components of frequency multipliers have input and output waveguides, with horn antenna mounted for radiation coupling.

The principle of frequency multiplier is illustrated in Fig. 1.5. In a frequency multiplier, Schottky diodes function as nonlinear media, converting incoming microwaves (MW) into their harmonic waves. A frequency multiplier of order N converts an input sinusoidal signal of frequency F_1 and power P_1 to an output sinusoidal signal of frequency $F_N = NF_1$ and power P_N. Typically the order N of multiplication is limited to $N = 3$ and more rarely to $N = 4$ or to $N = 5$. A frequency multiplier of order 2,3,4, N is called respectively a doubler, a tripler, a quadrupler, a N-upler.

Whisker-contacted diodes have been the most common multipliers in the sub-mm frequency range. Yet, considerable improvements have been made during the last years in
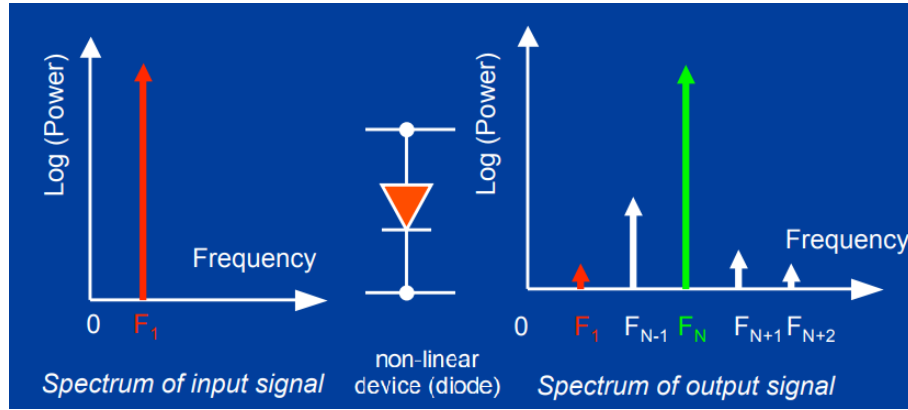
Figure 1.5 – Principle of a frequency multiplier. Modified from Ref.[27]

fabrication technology of planar Schottky diodes. Planar diodes in general are less fragile, can be handled more easily, and are therefore replacing whisker-contacted Schottky diodes. Besides, they operate over a full waveguide band without mechanical tuning. Schottky diodes are very fast devices and are still the best devices for high efficiency THz frequency multipliers.

Nowadays Schottky multipliers up to 2.7 THz (frequency doublers, triplers, quadruplers and so on) are based on planar GaAs Schottky diode technology and commercially available from various suppliers, Virginia Diodes, Inc. (VDI), and RPG-Radiometer Physics GmbH are among the most famous ones. At THz frequencies the multipliers are demonstrated with reported powers of 75 µW at 1.2 THz, 15–20 µW at 1.5–1.6 THz and 3 µW at 1.9 THz at room temperature [28]. The use of multiplier chains up to frequencies above 2 THz in molecular spectroscopy has recently been described thoroughly by [29]. But, regardless recent improvements in the performance of multipliers, their output powers are still of concern.

Modern frequency multipliers are based on GaAs planar Schottky diodes, fabricated with lithography techniques that are mounted in waveguide. The following sections will provide short explanation of the Schottky diode theory and give basic introduction to waveguides techniques, since all THz and MM-wave solid-state components (frequency multipliers, mixers, power detectors), used in spectroscopy instrumentation in PhLAM, Lille, are built on these elements.

1.5.1 Schottky diode devices theory

Schottky diode is a non-linear device, which employs a metal-semiconductor junction known as a Schottky barrier, first proposed by W. Schottky. When a metal and a semiconductor are brought into close contact, a potential barrier is formed which height is determined by the position of the Fermi level inside the band gap of the semiconductor.
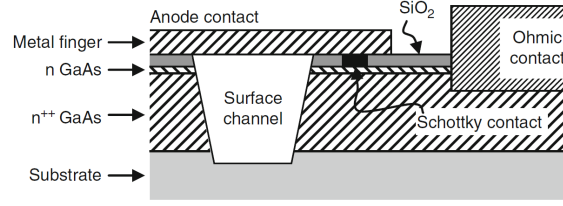
Figure 1.6 – Schematic of a planar GaAs Schottky diode.
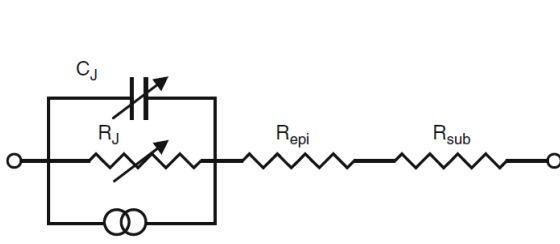
(a) Equivalent circuit of a Schottky diode.
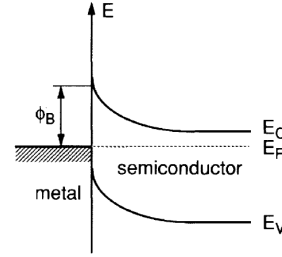
(b) Schottky barrier at the contact layer between metal and n-type semiconductor
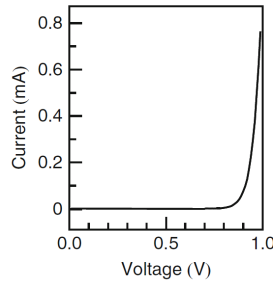
(c) Typical I-V-curve of a Schottky diode

Figure 1.7 – Schottky barrier

Figure 1.6 shows the cross-section of a typical Schottky diode. In the THz range Schottky diodes are made from GaAs, due to the high electron mobility of this semiconductor. To improve its performance and reliability, it is passivated with silicon dioxide (SiO_2). The ohmic contact is made on the surface of the GaAs crystal to reduce the ohmic resistance.

Schottky diode can be described by the equivalent circuit model which is shown in Fig 1.7a. It may be regarded as a nonlinear resistance R_J shunted by a capacitance C_J in series with a series resistance R. The current is carried by electrons only, making Schottky diodes very fast devices. The current in a Schottky barrier diode flows because of charge transport from the semiconductor to the metal or in the reverse direction (Fig. 1.8).

In principle, the current consists of different components: thermionic emission over the barrier, tunneling through the barrier, and generation-recombination inside or outside the depletion region. The ohmic behavior of metal-semiconductor contact is based on carriers
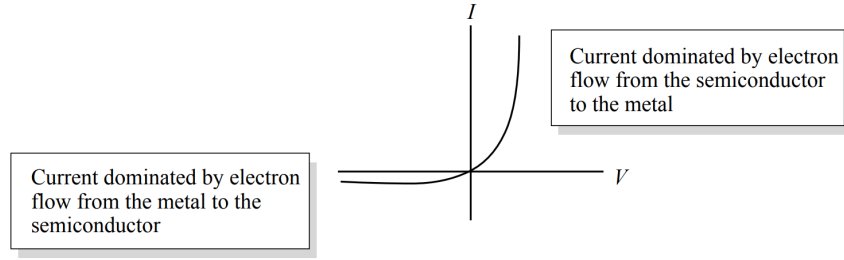
Figure 1.8 – The exponential current through the diode. In a Schottky barrier junction tunneling can occur in (*a*) forward bias and (*b*) for reverse bias.

tunneling through thin barriers. In the case of pure thermionic emission, the current flow can be described by the following equation

$$I = I_S \exp(\frac{e(V_B - IR_S)}{\eta k_B T})(1 - \exp(\frac{eV_B}{k_B T}))$$
(1.2)

Here, T is the temperature, V_B is the applied forward voltage, R_S is the series resistance, η is the so-called ideality coefficient, and I_S is the saturation current.

In the case of thermionic emission, it is given by

$$I_S = A^{**}AT^2 \exp(-\frac{e\Phi_B}{k_B T})$$
(1.3)

A^{**} is the effective Richardson constant, A is the anode area, and Φ_B is the barrier height when no bias voltage is applied.

In the case of tunneling, I_S is a complicated function of the barrier height, temperature, and doping density. However, for THz diodes the tunneling component is small and the current flow can be well described by Eq. (1.2) and (1.3).

1 Example of a Schottky diode, employed as a frequency multiplier

Frequency tripler is a circuit that generates a sinusoidal signal with a frequency 3-times higher than frequency of the input signal. Figure 1.9 shows example of a frequency tripler [30]. The tripler is an array of four Schottky planar diodes put in a waveguide. It is monolithically fabricated on a GaAs-based substrate.

Fig. 1.10 illustrates the principle of frequency tripler, which uses the cubic dependence of current-voltage characteristic to generate output sinusoidal signal at a frequency 3-times higher than frequency of an input signal. Frequency tripler is designed by exploiting the cubic-law current–voltage characteristic of Schottky diode $I \sim V^3$ by using antiparallel
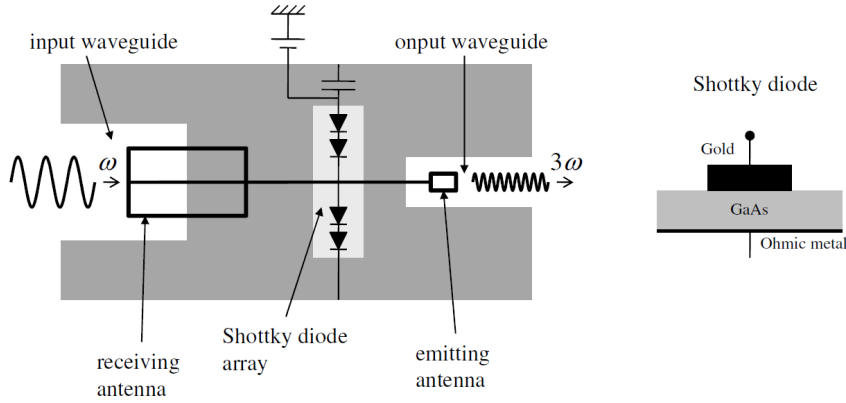
Figure 1.9 – Schematic diagram of a frequency tripler, integrated into waveguide. Reproduced from Ref.[30]
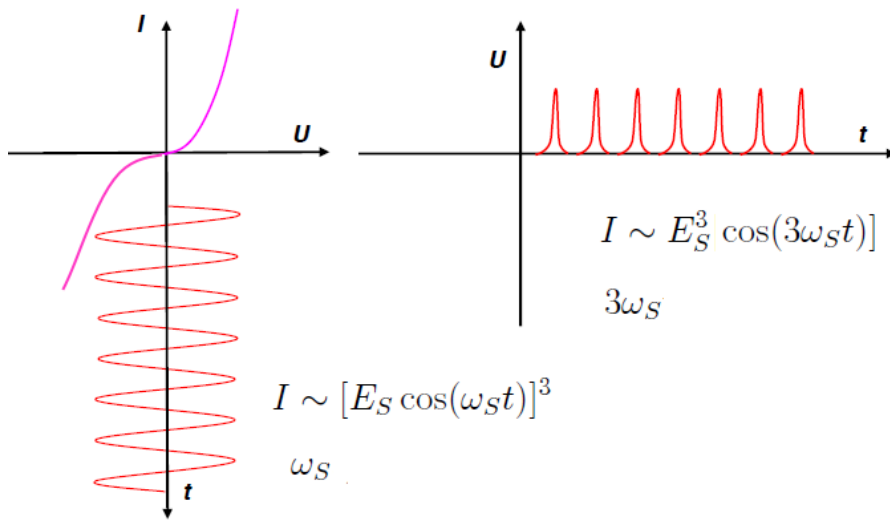
Figure 1.10 – Principle of a frequency tripler.

diodes. Third harmonic generation relies on the optimal design of the shape and dimension of the circuit elements. By proper design of the multiplier all other harmonics except the 3rd one are suppressed. Frequency tripler will generate an output sinusoidal signal I with a frequency 3-times higher than frequency ν_s of the input signal $E_S \cos(\omega_S t)$, where $\omega_S = 2\pi\nu_s$.

$$I \sim [E_S \cos(\omega_S t)]^3$$

Since

$$\cos^3 x = \frac{3}{4}\cos(x) + \frac{1}{4}\cos(3x)$$

So that

$$I \sim E_S^3[\cos(\omega_S t) + \cos(3\omega_S t)]$$

The current dependence for the multiplier when the voltage is applied, Eq. 1.2 in a simple form can be written by Taylor series as:

$$I = a_1 V + a_2 V^2 + a_3 V^3 + ...$$

In order to isolate desired harmonics from the output and to transfer the third harmonic, matched filters are used.

2 Schottky diodes fabrication

For millimeter- and sub-mm wave frequencies Schottky diodes are generally fabricated from n-type GaAs epitaxial material because of its higher mobility, wide bandwidth, and room temperature operation. Diodes are developed on membranes with a thickness of a few micrometers (Fig. 1.11), which is quite difficult to machine. There are only a few research laboratories worldwide fabricating planar GaAs Schottky diodes, first at the University of Virginia (which spun-off Virginia Diodes Inc. that is now commercializing diodes), and later at the Jet Propulsion Laboratory (JPL) [31, 32]. In Europe, several groups or companies like RPG-Radiometer Physics GmbH, the University of Chalmers, the Advanced Compound Semiconductor Technologies (ACST) GmbH in Darmstadt, the Rutherford Appleton laboratory in UK are now fabricating high quality Schottky diode-based devices for submillimeter wave applications. The Observatoire de Paris–LERMA and CNRS, Laboratoire de Photonique et de Nanostructure, with the support of CNES, developped Schottky diode process [33, 34] entirely based on e-beam lithography to fabricate devices for THz mixers and frequency multipliers.

The maximum frequency that commercially available Schottky diodes can achieve is around 0.8 THz using direct detection, but the frequency can go higher if the heterodyne technique is used and then the Schottky diode works as a mixer. A planar Schottky diode mixer has been operated successfully at 2.5 THz for space application.
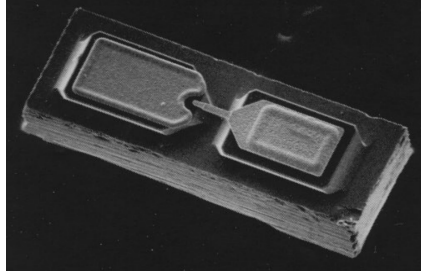
Figure 1.11 – Scanning electron micrograph of a planar Schottky barrier diode. Chip dimensions approximately 180x80x40 μm. Picture is taken from [35]

3   Waveguides techniques

After the fabrication, Schottky diode can be used for a specific design of THz or MM-wave component: frequency multiplier, mixer, detector. Schottky diodes are usually mounted on a substrate and then integrated into waveguides and a horn antenna is used for the radiation coupling to free space. The feed-horns are mouted on the multiplier chain output or mixer input, to focus the radiation beam. All modern solid state radiation sources, based on frequency multipliers, in particular those employed with the Lille spectrometer, fully built on rectangular waveguides components.

Thus rectangular waveguides (usually single-mode) and horn antennas are the most important components in the MM-wave and THz range. Rectangular waveguides and horn antennas can be described by classical transmission line theory [36, 37] and radiation propagation at THz frequencies is best described by Gaussian beams [38].

Hereafter, basic concepts of rectangular waveguides theory, necessary for understanding how to assemble multipliers-based radiation source, will be introduced. This section doesn't aim to give a complete comprehension of waveguide techniques, but rather practical aspects related to spectroscopic instrumentation.
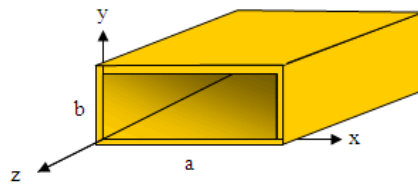
Figure 1.12 – Rectangular waveguide

Waveguides are used to guide electromagnetic waves. The geometry of a rectangular waveguide with $0 < x < a$, $0 < y < b$ and $a > b$ is shown in Fig. 1.12. The fundamental waveguide mode in rectangular waveguide is TE_{10}, called also H_{10}. The TE means transverse electric and indicates that the electric field is transverse to the direction of propagation. The mode TE_{10} has the lowest cutoff frequency $f_{cut-off} = \frac{c}{2a}$ and the high-

est cutoff wavelength $\lambda_{cut-off} = 2a$. At a given operating frequency f, only those modes having $f_{cut-off} < f$ will propagate. Waveguide cutoff frequency is an essential parameter for any waveguide. It is the frequency below which the waveguide will not operate. It is essential that the frequency of a signal, required to pass through the waveguide, higher than the cutoff frequency. The cut-off frequency of the waveguide depends upon its dimensions. It is almost always the fundamental mode TE_{10} that is used in the waveguide. It is then crucial to make sure that the frequency is low enough such that only the fundamental mode can propagate.

The rectangular waveguides are specified according to EIA, Electronic Industries Alliance, band designation. Waveguide sizes are standardised to enable waveguides from different manufacturers to be used together.

Table 1.2 – Waveguide Band Designations

Designation	Internal dimensions a (μm) x b (μm)	Cut-off frequency, GHz	Operating min. frequency, GHz	Operating max. frequency, GHz
WR-10	2540 x 1270	59.01	75	110
WR-5.1	1295 x 647.5	115.75	140	220
WR-3.4	864 x 432	173.49	220	330
WR-1.9	470 x 235	318.93	400	600
WR-1.5	380 x 190	394.46	500	750
WR-1.0	250 x 125	599.58	750	1100
WR-0.65	164 x 82	914	1100	1700

Different rectangular waveguide elements like frequency multipliers, mixers, transitions, isolators, attenuators are used as components of mm-wave and THz solid-state radiation sources for Lille spectrometer. Tapered transitions, for example, are used for connection of elements with different waveguide dimensions and flange types. Attenuators are used to reduce power input, e.g. to prevent power saturation in an absorption spectrometer. Attenuation also helps to reduce standing waves. i.e. variations in power at the detector as the frequency is varied since reflected waves must pass an attenuator twice in each back-and-forth direction through the waveguide. Isolators are one-way transmitters that can be used, for example, to isolate a waveguide section from reflections. Table 1.2 gives their waveguide band designations for the correct mounting. Flanged joints must be carefully assembled to ensure accurate alignment of the waveguide sections. The assembly (mounting) of radiation sources for Lille spectrometer involves a human factor. Every waveguide component has input and output ports, which should correspond in dimensions to the successive one and be well matched while connecting different elements. Rectangular waveguide sections have standard waveguide flanges at ends. Mounting of

the components starts with preliminary choice of the required elements to achieve a given frequency with the current configuration of radiation source, i.e. a set of multipliers, transitions and horn antennas. Then all elements are fixed with each other with screws, and the radiation source is installed with the aid of mounting plates allowing to adjust its height and position on an optical table. Any misalignment between the waveguide components for radiation source such as incorrect waveguide orientation or wrong connexion element can cause a serious perturbation on spectrometer's performance, that's why a care should be taken while preparing an amplifier multiplier chains for the set-up in a spectrometer. Figure 1.13 shows an example, the 265-400 GHz frequency multiplier [with the mounted horn antenna] to practically illustrate the technique to assemble a multiplier chain.

Figure 1.13 – Frequency multiplier. Credits: VDI

Waveguide components fabrication at THz and MM-wave frequencies faces the difficulties, because of the small dimensions. Typical dimensions are 0.254 x 0.127 mm^2 for a band from 0.75 to 1.1 THz and 0.164 to 0.082 mm^2 for a band from 1.14 to 1.7 THz. In addition, losses are increasing because of surface inaccuracies and surface roughness. Several fabrication technologies as ultra high precision machining [39] for THz waveguide components have been developed that currently enables the fabrication of commercially available THz components up to 2.5 THz.

1.5.2 Design and Principle of Operation

Amplifier multiplier chains (AMCs) are the solid-state MM-wave/THz sources, based on microwave frequency synthesizers, Schottky frequency multipliers and medium power amplifiers. The operation principle of the AMC will be given on an example of AMC that is employed as radiation source with Lille spectrometer. The radiation source, presented here, is based on multiplication chain and MW frequency synthesizer. It allows to achieve

frequency up to 1 THz and is tunable over 700-990 GHz range. The schematic is shown at Fig. 1.14, and its picture at Fig. 1.15.
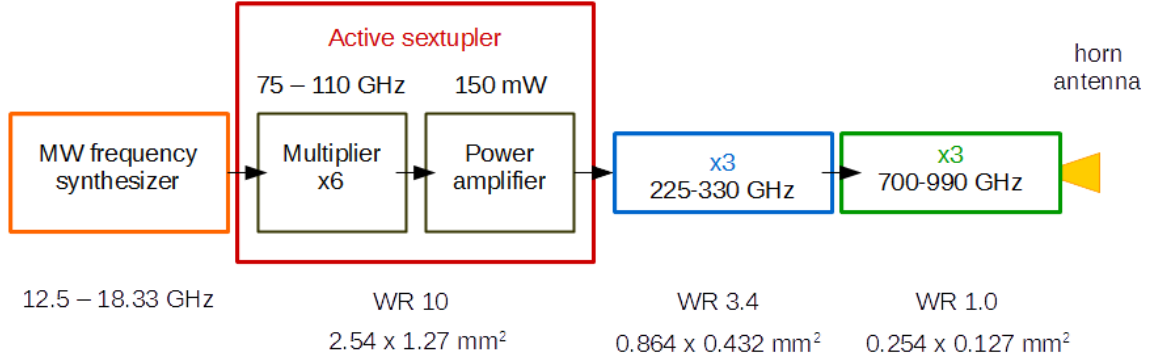
Figure 1.14 – Schematic block diagram of the solid-state radiation source used with Lille spectrometer, based on frequency amplifier multiplier chain (AMC) and MW frequency synthesizer. Radiation source operates at a room-temperature and generates a few μW of power, using a cascade of two frequency triplers. A total multiplication factor is 54.

Figure 1.15 – Photograph of a compact AMC from VDI [40].

The key components of amplifier multiplier chain, described here, are namely: microwave frequency synthesizer, an active multiplier (sextupler with power amplifier), and a cascade of two frequency multipliers (triplers). All components are commercially available.

A MW frequency synthesizer, usually locked to a high accuracy frequency standard, is typically tunable in a frequency range from 10 MHz to 40 GHz. Noise output from MW synthesizer is important for the low noise operation of the AMC, as any noise from the synthesizer will propagate through the AMC. The output power of AMCs falls off

as $\sim 1/\nu^3$ (Fig. 1.16) as the frequency increases and the overall efficiency of amplifier multiplier chains can be as low as a few percents.

Figure 1.16 – Output power of a variety of Schottky diode frequency multiplier chains measured at room temperature. Modified from Ref. [41]

Modern commercial available microwave synthesizer from Agilent Technologies is chosen as fundamental MW frequency source in Lille spectrometer because it provides low phase noise, high spectral purity, fast switching, and synthesizer accuracy needed for high-resolution spectroscopy.
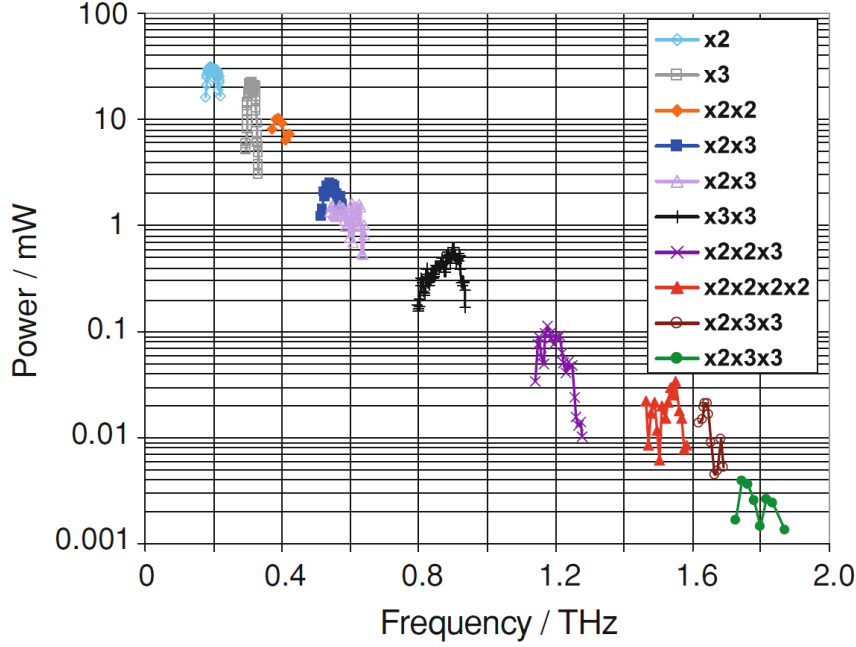
Then, in more detail, the signal from MW frequency synthesizer, operating in the 12.5-18.33 GHz frequency range, is fed into the sextupler (x6), followed by a W-band medium power amplifier (MPA). The commercial MPA delivers up to 150 mW at the first multiplier stage (75-110 GHz). The system which consists of passive multiplier and power amplifier is called active multiplier. A variable attenuator, placed between the amplifier and the following multiplier stage can be used to smoothly adjust the output power. The amplified 75-110 GHz signal is successively multiplied by a cascade of two (passive) frequency triplers (x3x3), similar in design to those presented previously (Fig. 1.9) and thus the AMC reaches consistently 225-330 and 700-990 GHz. The chain performs a frequency multiplication in total by 54 (x6x3x3). Frequency multipliers and amplifiers for Lille spectrometer were purchased from VDI.

One of the important features of AMC principle is that the frequency stability at the output of the last multiplication stage (around 1 THz) is the same as that of the input source (MW synthesizer), i.e. it is determined by frequency standard.

In a such *"a lego poupées"* manner, the multiplier chains can be assembled from the appropriate choice of elements and thus achieve a desired frequency operation range.

1.6 Detectors for spectrometers, operating at THz and MM-wave frequencies

On the other hand, to build a spectrometer, operating at THz and MM-wave frequencies, we need suitable detectors or detection system. In the following, some detection techniques will be reviewed and their applicability for instrumentation in high resolution spectroscopy will be discussed.

To select the optimal detector for a high resolution spectroscopy, a different characteristics need to be considered. Sensitivity, responsivity, the frequency range, the detector bandwidth, etc. Detectors for high-resolution spectroscopy should match the following requirements:

1. Be sensitive enough. Because photon energies at THz frequencies is low, ambient background thermal noise dominates. Commonly, the most sensitive detectors, are helium-cooled bolometers. In general; the sensitivity of a [direct] detector can be characterized by Noise Equivalent Power (NEP). NEP is usually defined as the power of an input signal that results in a signal-to-noise ratio (SNR) of 1 in a 1 Hz output bandwidth. The NEP is given in Watts per square root of Hertz (W/$\sqrt{Hz}$). In other words, NEP is the lowest detectable power by a given detector; it's a measure of the weakest signal that can be observed. The lower NEP, the more sensitive detector. The minimum detectable power of a [direct] detector, P_{min} can be calculated as: $P_{min}=$ NEP(ν) $\cdot$ $\sqrt{BW}$, where NEP(ν) is NEP, that can be frequency-dependent and BW is the measurement bandwidth. When comparing NEP values between different detectors and manufacturers, it is important to pay attention to the NEP's specified bandwidth and specified frequency range.

2. Provide high responsivity (fast time response, or high response rate). This characteristic of a detector is of crucial importance to perform high resolution spectroscopy. Response time of the detector determines how fast the detector responds to a change in radiation intensity. The time response is inversely proportional to the frequency response. Frequency modulation (FM) and subsequent lock-in detection is widely used in [absorption] spectroscopy for the sensitive detection (to suppress a variation of "baseline"). Radiation source in [absorption] spectrometer is frequency modulated, typically from a few kHz to a few MHz, that means the response time of detector should be of the order of a micro/nanoseconds or less. In general, the sensitivity of spectrometer is limited by low frequency noise in the signal, which

originates mainly from radiation source phase noise, mechanical instabilities, spectral response of detector and other fluctuations in a laboratory. This noise is often referred to as the $1/f$-noise, because its power spectrum scales roughly with inverse frequency (Fig. 1.17). The influence of the $1/f$-noise can be greatly reduced by shifting the detection to higher frequencies with the use of modulation technique, and the following lock-in detection. Even 5 kHz frequency modulation is enough to make the $1/f$ noise of the detection negligible, which corresponds to 0.2 ms of a response rate.
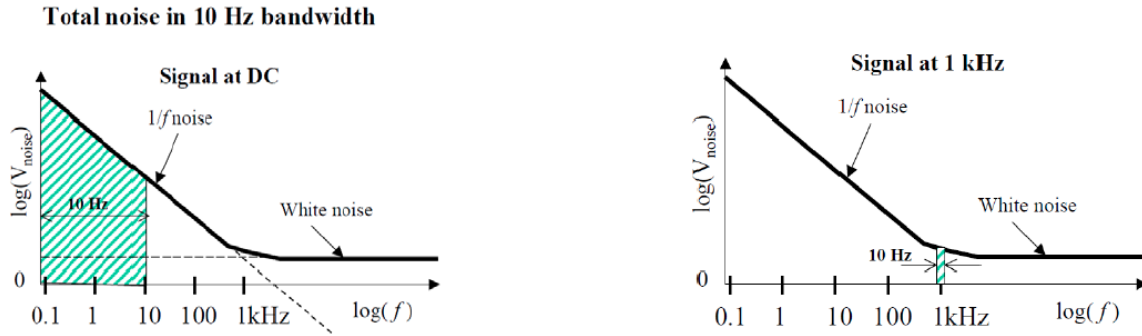
Figure 1.17 – Illustration of a $1/f$ noise reduction when applying frequency modulation: signal shifts to higher frequency and noise floor transfers to "white noise"

3. Detection bandwidth (frequency response) - inverse to a response rate. By frequency response usually means the detector response to modulated radiation input as a function of modulation frequency. [42]

4. Linear response over the frequency range. The spectral response indicates the radiation output intensity at different frequencies, i.e. the relative responsivity versus frequency.

5. Stable. With time, the detector baseline can change (drift). Stability of a detector can be characterized by measuring Allan variance (deviation) and to avoid baseline drift errors in measurements.

6. Operate over a wide frequency range.

7. Preferably to be compact and easy to handle (if possible, without cryogenic cooling and bulky cryostats)

The most important [direct] detectors of THz and MM-wave radiation are: Schottky diodes, bolometers, Golay cells, and pyroelectric detectors. During my PhD, I used all

of types of these detectors to perform different kinds of measurements, below their short review will be given and operation principles will be briefly discussed. Other, "special" type of detectors, heterodyne receivers and their characteristics, will be given in Chapter 4.

Bolometers [43] are commonly used detectors in a majority of spectroscopy laboratories. They can operate over a wide frequency range from 60 GHz to 20 THz and provide excellent sensitivity. Their operation principle relies on detecting the change in a temperature, induced by the absorption of the radiation. A typical bolometer device, a thermal detector, is shown in Fig. 1.18. It employs a material whose electric resistance is highly sensitive to temperature change. Typically the active element is a highly doped III-V semiconductor, such as Si, Ge or InSb. A radiation absorber is deposited on a substrate that has a low heat capacity and large thermal conductivity. When absorption of radiation occurs, the electrons are heated, leading to the change in their mobility and, because the conductivity of a semiconductors is proportional to the mobility, the resistance of semiconductor also changes. The change in temperature depends on the intensity of incident radiation and on the thermal capacity of the detector.
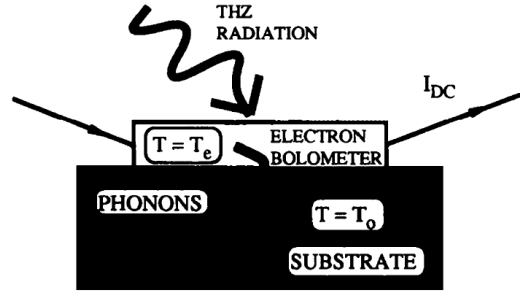
Figure 1.18 – Schematic of a bolometer device [44].

The most widely types of bolometers for spectroscopy are either Ge or Si semiconducting [45, 46], and Hot Electron Bolometers (HEB) [47]. Cryogenic cooling by liquid Helium at 4.2 K is inevitable to obtain high sensitivity in bolometers due to their operational principal. Semiconductor detectors are very sensitive and very fast. Their fast response time permits frequency-modulated spectroscopy with lock-in detection.

QMC Instruments Ltd. offers a high sensitivity (NEP $\sim 10^{-12}$ W/$\sqrt{Hz}$) Indium antimonide (InSb) hot-electron and niobium (Nb) superconducting bolometers that are operated at or below 4.2 K. InSb HEB offers much high frequency response than Nb bolometers: 1 MHz and 1 kHz respectively, that makes InSb HEB nowadays the 1st choice detector for high-resolution laboratory molecular spectroscopy up to 2.5 THz. In particular, Lille spectrometer is equipped with inhomogeneously tuned QMC InSb bolometer

(model QFI/2BI). The detector (Fig. 1.19b) mounts in an optical integrating cavity behind Winston Cone (for coupling radiation) with low-pass filters (to reduce heating) that efficiently reject the high frequencies. Cooling is provided by cryostat, (designed by Thomas Keating Ltd.) with liquid helium (Fig. 1.19a), that allows significant long-term hold times (up to 7 days). A low noise pre-amplifier is mounted directly onto the side of the InSb HEB cryostat, which runs from an external supply.

(a) Liquid helium cryostat with a mounted preamplifier

(b) The inside view : Winston cone is mounted to maximise the collection of radiation. Magnetic fields are applied to detector elements using permanent magnets.

Figure 1.19 – Magnetically tuned QMC InSb hot electron bolometer (Courtesy of Thomas Keating Ltd) [48].

Zero bias Schottky diode (ZBD) detectors are well suited as direct power detectors for high resolution spectroscopy up to the MM-wave, and possible at THz ranges. ZBD are compact, sensitive, fast and easy in use detectors that operate at room temperature. The principle of ZBD relies on the rectification of a signal to DC component that is proportional to the radiation intensity. A typical detector includes an asymmetric Schottky diode array that down-converts the signal frequency by non-linear mixing. For incoming radiation given as $E_S \cos(\omega_S t)$, the output signal of the diode array is expressed as

$$V_0 = \chi[E_S \cos(\omega_S t)]^2 = \frac{1}{2}\chi E_S^2 + \frac{1}{2}\chi E_S^2 \cos(2\omega_S t)$$

where χ is the quadratic non-linear coefficient of the device. Schottky diode direct

detectors have a high sensitivity and fast response time.

ZBD are commercially available from Virginia Diodes (Fig. 1.20). VDI ZBD cover the frequency range up to 1.7 THz and provide good sensitivity and fast response time (sub-nano seconds). Detectors are planar GaAs Schottky barrier diodes fabricated using the process described in [49]. The diodes are optimized to have a low forward turn-on voltage, even with zero-bias, i.e. when no bias voltage required. ZBD are optimized for operation over the full waveguide band and without any mechanical tuners. ZBD achieve NEP of $\sim 10^{-11}$ - 10^{-10} W/$\sqrt{Hz}$, depending on a frequency range. The responsivity of ZBD typically ranges from about 2000 V/W at 100 GHz to 250 V/W at 900 GHz [50]. Schottky diode detectors have the benefit of fast response time and high sensitivity compared with other room temperature detectors, such as Golay cells, pyroelectric detectors, or even bolometers. However for high resolution measurements with Lille spectrometer, only VDI ZBD, operating up to 330 GHz are used since their sensitivity drops significantly while approaching THz frequencies.

(a) ZBD with mounted horn

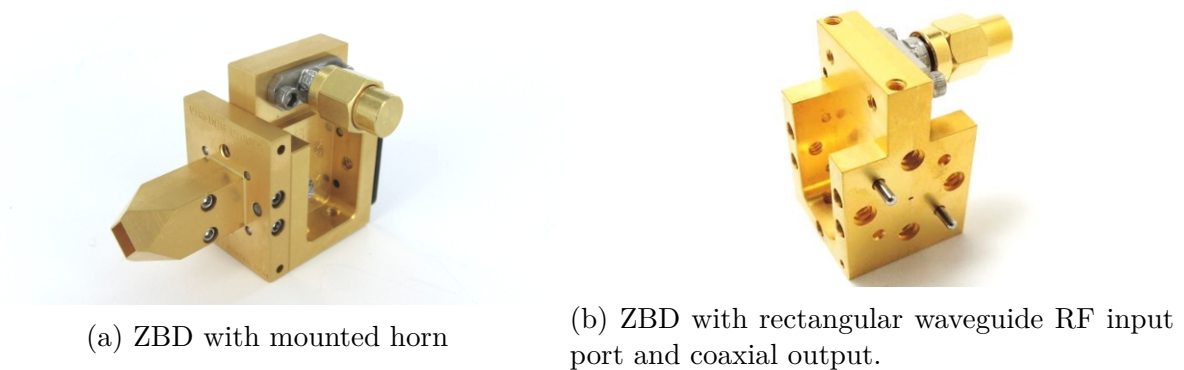(b) ZBD with rectangular waveguide RF input port and coaxial output.

Figure 1.20 – Typical compact Zero Bias Detectors, manufactured by VDI. Credits: VDI [50]

VDI also produces a series of broad band *Quasi-optical Schottky-diode detectors (QOD)* [51, 52]. QOD consists of a Schottky diode and a coupling structure - broadband antennas mounted on Silicon substrate lens. QOD allow to achieve wide operating bandwidth, from 0.1 to 1 THz. However, as ZBD, they provide a good performance for high resolution spectroscopy, only up to 600 GHz.

For the spectroscopy applications that do not require high sensitivity, room-temperature detectors such as *Golay cells* [53], or *pyroelectric detectors* [54] may be a convenient choice. They have NEP of $\sim 10^{-10}$ - 10^{-9} W/$\sqrt{Hz}$. Both the Golay and the pyroelectric detector have been widely used in laboratory infrared spectrometers since the 1960s.

The operation principle of *a Golay cell detector* relies on the thermal expansion of an inert gas with temperature. Incident radiation is absorbed and heats the gas which increases the pressure thereby leads to the membrane deformation which can be detected.

Golay cell detector can operate through in a wide spectral range of 20 GHz–20 THz. An important advantage of Golay detector is that its frequency range is very wide, but the detector is somewhat fragile and has slow response rate (∼100 ms). Golay cell detectors can be purchased from TYDEX.

A pyroelectric detector [55, 56] consists of a pyroelectric (dielectric) material placed in electrostatic field between two electrods which acts as a temperature-dependent capacitor. Dielectric constant of a pyroelectric material is sensitive to the temperature change. When absorbing a radiation, pyroelectric exibit a spontaneous electric polarization which magnitude depends on the dielectric constant. The most common pyroelectric materials are ferroelectric materials such as trigylcine sulfate or Lithium Tantalate. Pyroelectric detectors are commercially available from Thorlabs, InfraTec and Laser components. QMC Instruments Ltd. has a commercial line of room temperature pyroelectric detectors, covering the range from 300 GHz to 20 THz. Their characteristics are similar to those of Golay detectors.

Table 1.3 summarizes key characteristics - covered frequency range, noise equivalent power (NEP) and response time of commonly used detectors, employed at MM-wave and THz frequencies: QOD, ZBD, pyroelectric, Golay detectors, hot electron and superconducting bolometers - for a representative choice of a detector suitable for use spectrometer, operating in MM-wave and THz ranges. The two most useful characteristics for comparing detectors are NEP, noise equivalent power, relevant to the detector noise, which limits sensitivity, and the response time, which determines if frequency modulation (FM) technique may be used. The most sensitive are Nb semiconducting and InSb hot electron bolometers, which perform at or below liquid He temperature. Schottky diode detectors are less sensitive, but they provide very fast response times, and offer the advantage that they do not require cryogenic cooling. Golay and pyroelectric detectors are quite sensitive, but have a minimum response time of about 50 ms, which limits modulation frequency, making these detectors very sensitive to $1/f$ noise and thus inapplicable for high-sensitive spectroscopy.

Given this, for the Lille spectrometer, zero bias Schottky diode detectors provide the optimum sensitivity up to 400 GHz, and InSb hot electron bolometer offers the excellent sensitivity up to 1.5 THz. Both detectors allow modulation frequencies up to 1 MHz.

1.7   Gas cells for absorption spectroscopy

Finally, gas cells for absorption spectroscopy are needed as well to record spectra of molecules in a gas phase. The set-up of a gas cell for spectroscopy is shown at Fig. 1.21. The cell is evacuated to a vacuum and filled with the gas sample to the desired pressure by a vacuum pump. The gas cells are usually mounted on baseplate and properly aligned

Table 1.3 – Key characteristics of detectors, that could be employed for THz and MM-wave spectroscopy

|	Operating range	Noise-equivalent power (typical), $W/Hz^{1/2}$	Modulation frequency (frequency response)	Optical responsivity (typical), V/W	Response rate (typical)
Golay Detector (TYDEX)	15 - 8000 μm (0.03-20 THz)	1.4×10^{-10} at 20 Hz	15 ± 5 Hz	1×10^{5} at 20 Hz	50-100 ms
QOD (VDI)	110-1000 GHz	$50\text{-}115 \times 10^{-12}$	up to 40 GHz	100-250	25 ps
ZBD (VDI)	50 GHz-1.7 THz	$13.2\text{-}113.7 \times 10^{-12}$	up to 40 GHz	100-2000	25 ps
Superconducting (Nb) bolometer (QMC)	100 GHz (3 mm) to 20 THz (15 μm)	1×10^{-12} at 275 GHz (80 Hz)	2 Hz to 1 kHz	N/A	1 ms
Hot electron (InSb) bolometer (QMC)	60 GHz to 1.5 THz (peak at 2.5 THz)	1×10^{-12} at 275 GHz ($\sim$ kHz)	up to 1 MHz	5000	1 μs
Pyroelectric detector (QMC)	0.3-20 THz	1×10^{-9}	10-320 Hz	N/A	3-100 ms
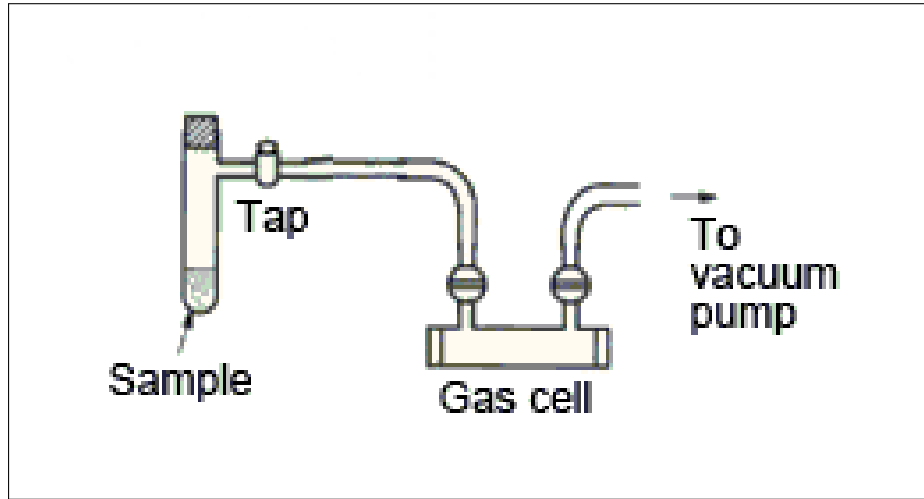
Figure 1.21 – Typical gas cell installation for absorption spectroscopy.

between frequency radiation source and detector, augmented with horns, waveguides or other structures, in a spectrometer set-up. The gas cells could be in single pass or multi-pass path length configuration. The cells are usually made of Pyrex glass or stainless steel and equipped with quality windows with appropriate material (Teflon, for example) and thickness at a given frequency range. They should be leak tight, capable of high vacuum performance and suitable for use over a wide temperature range (normally from 4K to about 600 K) and pressures up to mbar to perform pyrolysis or other chemical reactions in static or flow conditions. In many spectroscopic applications it is necessary to use an absorption cell which allows a long optical path to be attained through a sample, while allowing the absorption cell to be compact. There are two basic types of multiple-pass (or multi-pass) absorption cell: non-resonant, used for linear absorption spectroscopy; and resonant, where the measurement of absorption depends on treating the cell as a resonant optical cavity.

Chapter 2

The Lille Fast Scan Solid-State DDS Spectrometer

2.1 Overview

As has been pointed out in Chapter 1, appropriate tunable radiation sources and sensitive detectors are essential to achieve high spectral resolution in spectrometer. Modern multiplier-based spectrometers are the most powerful in the sense of frequency coverage and ease of handling, than for example, those based on BWO or laser sources. And the most suitable detectors for laboratory spectroscopy investigations are room temperature Schottky diodes and liquid helium cooled hot electron bolometers.

During my PhD, I had the opportunity to use Lille fast-scan solid-state DDS spectrometer (FSS) to measure the spectra of molecules of astrophysical interest.

A number of stable molecules (in gas phase), such as formamide [57], methylamine [58], carbonyl cyanide [59] and many others, including isotopologues, have been recorded with the Lille spectrometer. Beside stable molecular species a large number of unstable molecules, produced by pyrolysis process have been studied as well.

This chapter will introduce the Lille spectrometer, which the author of this thesis got acquainted with and used to perform measurements during PhD. Different configurations of the spectrometer experimental set-up will be described; a short overview of applied techniques and methods will be given; concept of operation principle will be discussed; and performance characteristics will be presented. Studies of gas-phase molecules, performed with Lille fast-scan solid-state DDS spectrometer during the author's PhD, will be presented in Chapter 6.

2.2 Spectrometer in Lille

FSS is state of the art instrument to perform THz molecular spectroscopy in a laboratory. Yet, it is user's friendly and could be attractive for a number of applications not only in

the laboratory for the studies of molecules of astrophysical interest, but also in the field.

Lille spectrometer is built on solid-state radiation sources and broad band detectors. Instrument is based on a commercial microwave frequency synthesizer and relies on direct frequency multiplication (and amplification) by AMCs up to the MM-wave and THz frequencies. To achieve a fast scan mode, direct digital synthesizers (DDS) are employed. Room temperature Schottky diodes detectors and liquid helium cooled hot electron bolometer are employed as detectors. Spectrometer covers the frequency range from 75 GHz to 1.52 THz. It should be clarified that the author of the current thesis didn't contributed to the development of Lille spectrometer, but will give description and operation principle of a spectrometer in some extent, as necessary to perform measurements of high resolution molecular spectra recordings. Emphasis will be placed on those parts of the spectrometer which are specific for the laboratory spectroscopy at MM-wave and THz ranges, rather than on particular features such as absorption cell or passive components (focussing elements etc).

2.2.1 Design and main components

The Lille spectrometer is a typical absorption spectrometer with a tunable frequency radiation source, an absorption cell, and a broadband detector. A schematical drawing of the spectrometer typical configuration is presented in Figure 2.1. More details on Lille spectrometer can be found in [60, 61].

The major components of Lille spectrometer are *a microwave frequency synthesizer* (Agilent E8257D analog signal generator [62]), *a direct digital synthesizer (DDS)* unit (AD9915 from Analog Devices, [63]), a system of *frequency amplifier multiplier chains (AMCs)* from Virginia Diodes, Inc. (VDI) [50] and a *detection system* (DSP lock-in amplifier SR 7270 [64] and appropriate detector). Absorption gas cells are made on the base of Pyrex glass and stainless tubes, typically between 1 and 2 m in length.

Agilent E8257D *frequency synthesizer* is used as a frequency reference source, it may be continuously tuned between 100 kHz and 20 GHz with an accuracy better than 1 Hz. E8257D is a analog synthesized signal generator with high output power, low phase noise, and modulation capability that suits perfectly as fundamental frequency source for the laboratory spectroscopy. It is locked onto Rubidium frequency standard (10 MHz), that provides very stable and reliable high frequency precision standard ($\Delta\nu/\nu < 10^{-10}$).

DDS AD9915, *a direct digital synthesizer* is employed to provide the fast frequency scan in Lille spectrometer's set-up. AD9915 is a digitally programmable frequency synthesizer, that can generate a stable frequency and phase-programmable digitized analog output sine wave up to 1.0 GHz. This sine wave can be used directly as a frequency source or for a frequency multiplication. DDS enables very high resolution of output frequency.
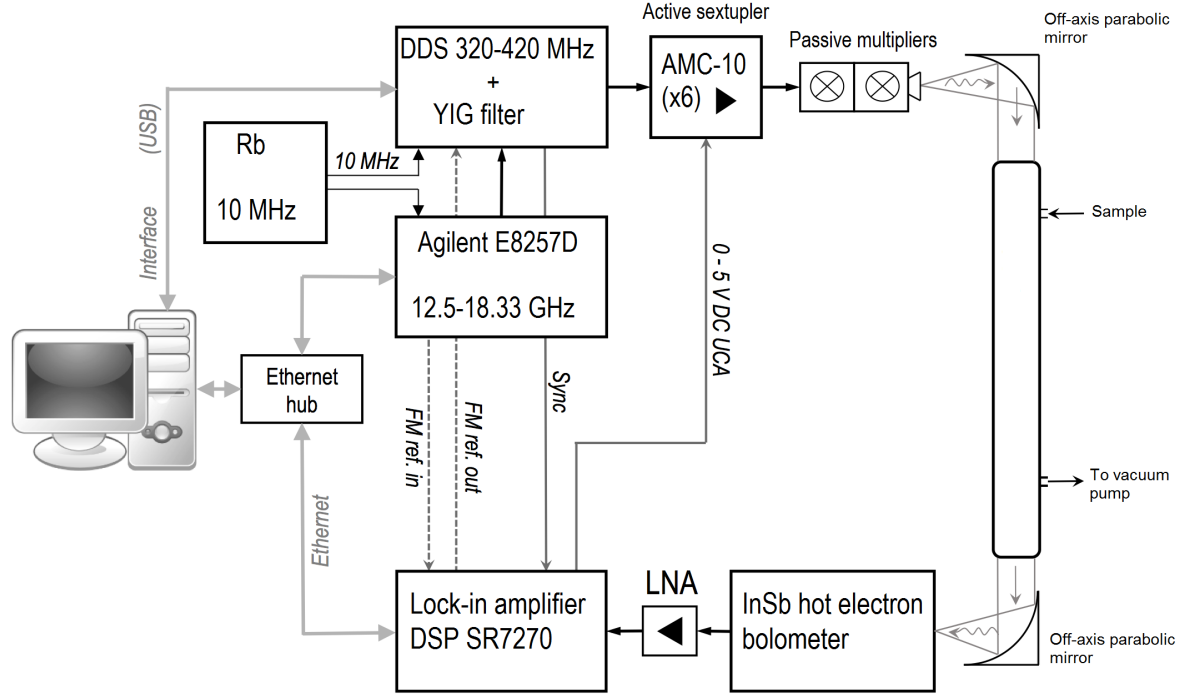
Figure 2.1 – The scheme of one of the possible configurations of the Lille fast scan DDS spectrometer.

The advantages of DDS is the high frequency precision and extremely fast frequency switching between values with continuous phase (without overshots) that prevents signal from distortions. DDS digitally sets up and switches the value of output frequency (down to 10 ns, but for spectroscopic applications 25 μ s is a minimum optimum), compared to real "synthesizing" by Agilent (which typically takes 25 m s). Application of DDS to Lille spectrometer will be given below in Sec. 2.2.2.

Commercially available components (frequency multipliers and amplifiers) from Virginia Diodes, Inc. (VDI) are used to build *amplifier multiplier chains (AMCs)* as the radiation sources for Lille spectrometer. The principle of frequency amplifier multiplier chains was presented in details in Sec. 1.5.2. AMCs of Lille spectrometer consist of an active frequency sextupler (x6), generating frequencies in the 75–110 GHz frequency range, AMC-10 from Virginia Diodes, Inc. (VDI), which is driven by Agilent E8257D frequency synthesizer, and a series of exchangeable successive passive multipliers, also from VDI, doublers and triplers, that allow to reach ~ 1 THz. The possible combinations of frequency multipliers to assemble AMC for Lille spectrometer are given together with the corresponding frequency ranges at Fig. 2.2. Practical schema of AMCs configurations of radiation sources of Lille spectrometer, is shown in Fig. 2.3. There is as well the second amplifier multiplier chain from VDI (that, however, I didn't have a chance to use, but is

available with spectrometer configuration) that covers the frequency range from 1.1 THz to 1.52 THz. It consists of four active multipliers (x12): AMC-350 (122-134 GHz), AMC-351 (134-145 GHz), AMC-352 (145-156 GHz), AMC-353 (156-169 GHz), followed by a cascade of two passive triplers (WR2.2x3: and WR0.65x3) that reach 366 – 507 GHz and 1090 – 1520 GHz, respectively. Table 2.1 summarizes the elements (passive and active multipliers) with typical output power in mW (provided by VDI), that may be used to assemble different configurations of AMCs for radiation sources and thus achieve desired operation frequency range of spectrometer.
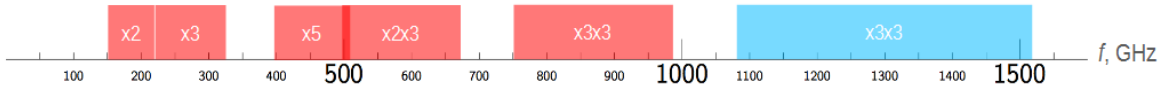

Figure 2.2 – Possible combinations of frequency multipliers, that could be employed to build AMCs for Lille spectrometer.
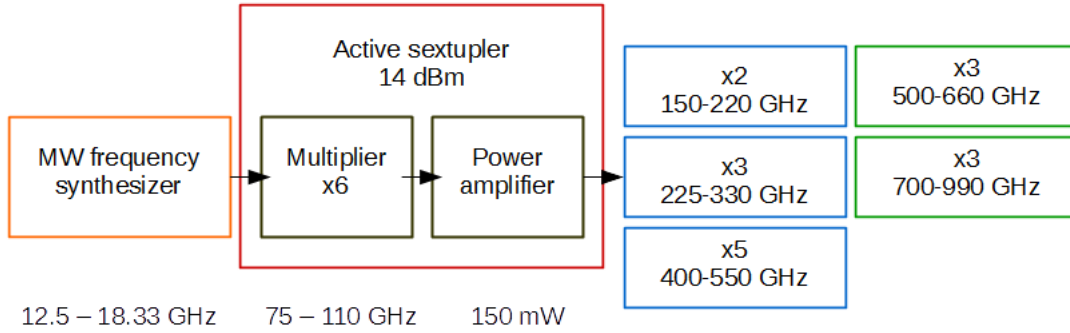

Figure 2.3 – Configuration schemas of radiation sources of Lille spectrometer.

Detection system of Lille spectrometer consists of an appropriate detector (either InSb hot-electron bolometer from QMC or zero bias Schottky diodes from VDI), followed by a low-noise amplifier (LNA), particular for each detector's type, and a lock-in amplifier (Signal recovery Model 7270, frequency range from 0.001 Hz to 250 kHz).

A 4 K helium-cooled InSb hot-electron bolometer (model QFI/2BI, QMC Instruments, Ltd.) is used as a broadband detector up to 1.5 THz. Table 2.2 lists its main characteristics.

In the 75–330 GHz frequency range VDI zero bias Schottky diode detectors (models WR10ZBD, WR5.1ZBD, and WR3.4ZBD), operating at room temperature, may also be used as well. The use of Schottky solid state detectors leads to (a slightly) loss of sensitivity

Table 2.1 – VDI components, used in AMCs sources with Lille spectrometer.

Element	Band (GHz)	RF Frequency Multiplication Factor	Typical Output Power (mW)
AMC-10 (x6)	75-100	6	30
AMC-350 (x12)	122-134	12	150
AMC-351 (x12)	134-145	12	150
AMC-352 (x12)	145-156	12	150
AMC-353 (x12)	156-167	12	150
WR5.1 (x2)	150 - 220	12	3
WR3.4 (x3)	225 - 330	18	1
WR1.9 (x5)	400 - 520	30	0.05
WR1.5 (x2x3)	500 - 660	54	0.03
WR1.0 (x3x3)	750 - 990	81	0.01
WR0.65 (x3x3)	1100 - 1520	108	0.02

compared to 4 K InSb hot electron bolometer but has the advantage of operating at room temperature. A list of VDI ZBD, that could be employed as detectors with Lille spectrometer is given in in Table. 2.3.

The interaction of the radiation with molecules occurs in an *absorption cell*. Either cell from the Pyrex glass or stainless one (2.2 m long with the internal diameter equal to 56 mm) can be used. In both cases the radiation passes through Teflon windows which have low absorption coefficients up to the THz region. Two off-axis parabolic mirrors (with a focal length f=17 cm, diameter $\sim$ 6cm) are used to guide the radiation. Although off-axis parabolic mirrors may introduce some distortion and cross-polarisation effects, they are preferred for use at MM-wave and THz frequencies due to their high reflectance and very low losses. The pumping system consists of a rotary pump followed by a turbo diffusion pump and pressures of 2.5$\cdot$ 10^{-4} mbar can be reached.

2.2.2   Operation principle

Agilent E8257D and DDS AD9851 are used in Lille spectrometer as frequency synthesizers. Both synthesizers are locked to 10 MHz Rb frequency reference standard. The AD9915 generates a stable frequency and phase-programmable digitized analog output

Table 2.2 – Technical specifications of helium-cooled (4K) QMC hot-electron bolometer (model QFI/2BI), used with Lille spectrometer

Frequency range	60 GHz to 1.5 THz
Typical NEP (pW/Hz)	1.5
Typical Responsivity (V/W)	5000
Operating resistance	from 5 to 20 kOhm

Table 2.3 – Specifications for room temperature Zero-Bias Schottky Detectors (ZBD), used with Lille spectrometer

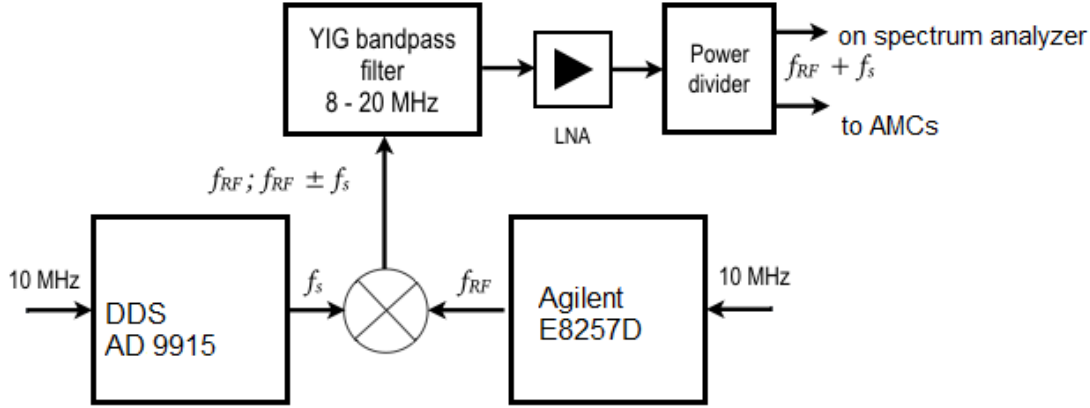| Model	RF (GHz)	Typical NEP (pW/Hz)	Typical Responsivity (V/W)
WR10ZBD	75 - 110	13.2	2000
WR5.1ZBD	140 - 220	13.2	2000
WR3.4ZBD	220 - 330	17.6	1500

Figure 2.4 – Up convertor.

sine wave at f_S, (up to 1 GHz). E8257D generates very accurate sine wave as well, but in microwave frequency range (f_{RF}, up to 20 GHz). The signal is frequency modulated (FM) by the internal low frequency generator of the Agilent E8257D. The modulation frequency and the modulation deviation is chosen according to the molecular linewidth (see Sec. 2.2.4 for details). Modulations frequencies are typically tenth of kHz, fast detectors should be employed. This aspect was discussed in Chapter 1. Frequency stabilization of synthesized signal is provided by Agilent E8257D. The frequency of DDS AD9915, f_S =365 MHz is mixed with a radiation, generated by Agilent E8257D at f_{RF}, operating in the 12.5–18.5 GHz range (Fig. 2.4). It is a simple frequency up-converting, or mixing, i.e. multiplying two signals (two sine waves) together. After mixing the lower frequency component ("difference frequency"), f_{RF}- f_S is removed by a YIG narrowband pass filter. Care should be taken to get rid of the spurious spectral components in the output signal since they will appear critically in the systems with frequency multiplication. Then the stabilized FM output signal with a frequency f_{RF}+ f_S is amplified and used directly for multiplication by a cascade of VDI multipliers and displayed at spectrum analyzer (the power divider is mounted to split power in two). Primarily, amplitude modulated (AM) signal is used for the alignment of a spectrometer, it is displayed at oscilloscope.

The absorption cell is filled with the molecules under the investigation. After the signal has passed through the absorption cell, it is detected either by 4 K QMC InSb bolometer or room temperature VDI Schottky diodes. Then the signal is fed to a lock-in amplifier (Signal Recovery 7270 DSP) and it is converted from analog to a digital form by ADC (an analog-to-digital converter). The demodulation of the signal is done at 2nd harmonic of the modulation frequency. To avoid distortion of molecular line, the frequency of the modulation and frequency deviation (range of variation) must be small compared to the line width. Even if the first derivative is more sensitive form for detection, the second derivative is more convenient for measurements of the line center frequency.

The radiation source (MW frequency synthesizer + specific AMC) is swept across the given frequency range (usually from the lower to higher frequencies). Records of molecular spectra are obtained by scanning the frequency step-by-step in a given range and measuring the variations in power, transmitted through the absorption cell. The fast frequency scan is provided by sweeping the frequency of DDS AD9851 with a smaller frequency step (depending on molecular line width) and Agilent E8257D frequency synthesizer - within a larger range (typically 100 MHz).

The control of spectrometer: frequency synthesizers Agilent E8257D and DDS AD9851, data acquisition from DSP 7270 lock-in amplifier is carried out by a computer. The spectrometer hardware communicates with the PC through a standard Ethernet protocol. The IP address of every device is unique. A home-made software for a spectrometer, specially developed in Lille, allows the data measurement (averaging) in several scans, that improves the signal to noise ratio. Control of the hardware consists of the computer sending commands to the instrument, with it responding either by sending back some data after the measurements have been made (the signal from the lock-in amplifier, i.e. voltage, to stock in a memory) or by changing the setting of one of its controls (e.g. set up the frequency value or frequency sweeping range). The commands and responses are ASCII text strings. The data acquisition process is fully automatized. The data is transferred to a file *.dat and is stored in a computer.

2.2.3   Key parameters and performance

- Frequency coverage: 88% of the 75-1550 GHz frequency range. The frequency coverage should be optimized so that all important spectral lines from molecules under investigation can be covered. It is preferable that spectrometer operates over a wide frequency range.

- Sensitivity: typically 10^{-6} cm^{-1}, depending on acquisition time and frequency range. The main measure in [absorption] spectroscopy is how smaller a change in power with a gas presence can be detected. The fundamental sensitivity (detection limit) of

an [absorption] spectrometer is given by the phase noise limit of the radiation source. With Lille spectrometer it is determined by the spectral purity of the fundamental frequency source (Agilent E8257D MW frequency synthesizer), multiplied by 20 $\log(N)$, where N is the total harmonic number of the output frequency. Power fluctuations of the source and standing waves in the spectrometer also limit its performance and leads to a loss in a sensitivity.

- Spectral resolution: is limited by the width of absorption lines and is given by their Doppler width. Doppler width for each molecule mainly depends on a frequency range, it will be discussed further in Sec. 2.2.4. The resolution should be good enough to measure accurately a single isolated spectral line. This means that the investigated spectral line should be separated from other lines in spectrum so that its intensity and central frequency are determined with sufficient precision. Usually, 10-20 points are measured across each line shape to quantitatively determine the line width and intensity. In this manner, for Lille spectrometer, operating in MM-wave and THz ranges, to record a molecular line, frequency step is chosen to keep at least 10 points at full width at half maximum (FWHM) for accurate line profile fitting. For example, if the line width at FWHM is 0.5 MHz, to acquire 10 points, we should choose a maximum frequency step of 50 kHz.

- The frequency stability of spectrometer: is defined by the lock of the frequency synthesizers to a reference (1 part in 10^8 is reasonable). The absolute frequency accuracy of the Lille spectrometer is determined by Rb frequency standard ($5 \cdot 10^{-9}$ to $5 \cdot 10^{-12}$).

- Measurement accuracy: better than 30 kHz for a single isolated line below 600 GHz and 50 kHz up to 1.5 THz. Frequency measurement accuracy depends on the linewidth, line shape and signal-to-noise ratio of the recorded lines.

- Data acquisition rate (or sample rate): (typical) with 1 ms/point. The rate of molecular spectrum recording with Lille fast scan DDS spectrometer can reach 100 GHz/hour with a high accuracy measurements of transition frequencies of molecular lines. To scan the whole frequency range of 75-1550 GHz covered by Lille spectrometer, we need typically 24 hours. Sample rate is the speed at which data is collected by acquisition system. It is expressed in samples (data points) per second. The fast frequency scan mode has a few limitations. The most important, is to keep a 5τ relation between the frequency switching time Δt and the time constant τ of the lock-in amplifier. "5τ rule" will prevent the shift in a frequency of the observed molecular line. The minimum time interval between switching of two frequency

values with Lille spectrometer is about 1 ms, means the minimum possible value of the time constant of the lock-in amplifier should be 200 µs.

2.2.4 Line Broadening Mechanisms and Doppler-limited Spectroscopy

In absorption molecular spectroscopy the knowledge of 3 spectral parameters: line positions (frequencies), widths and intensities is essential for the correct interpretation of spectra. Observed line shape must be taken into account in order to "fit" line and to obtain accurate central frequencies. Whereas the frequency stability of the radiation sources of Lille spectrometer (Agilent E8257D and DDS AD9915 frequency synthesizers and frequency multiplication chains) is with a few Hz and extremely accurate, the limiting factor for the accuracy with which the transition frequencies can be measured is the broadening of the molecular [absorption] lines due to the different phenomena. The spectral resolution of Lille spectrometer is limited by the Doppler linewidth, here we will briefly describe Doppler and some other important line broadening mechanisms since they can affect frequency measuring accuracy.

The main mechanisms that cause the broadening of molecular lines are *Doppler (thermal)*, *collisional (pressure)* and *natural* line broadening. In general, all broadening mechanisms are present simultaneously while recording a spectral line, but with a domination of one or two broadening mechanisms. That depends on a frequency range and other factors, that are to be discussed below.
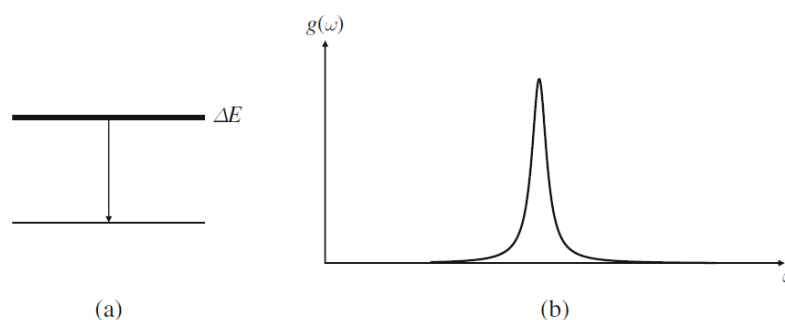
Figure 2.5 – (a) Because of the finite lifetime of a state, each state has a certain width, so that the molecule can absorb or emit radiation over a range of frequencies. The corresponding lineshape is shown in (b)

Natural broadening is caused by the spontaneous energy emission. As follows from the uncertainty principle, any given energy level i does not have a perfectly defined energy E_i, but rather a superposition of possible states ranging around E_i (Fig. 2.5a). As a result, transitions between any two energy levels do not correspond to any exact, specific energy difference; equivalently, absorption of photons does not take place at one exact, unique

37

frequency, but over a [small] range. Thus the absorption will be distributed over a range of frequencies, and the absorption coefficient will be a function of the frequencies within the absorption range. This function is called the line-shape function (Fig. 2.5b). The natural linewidth $\Delta\nu_N$ is determined by a spontaneous emission probability, or Einstein coefficient A_i and can be calculated as:

$$\Delta\nu_N[Hz] = \frac{A_i}{2\pi} = 1.86 \times 10^{-11}(\nu_0[GHz])^3|\mu_{12}[D]|$$

where ν_0 is the center transition frequency and μ_{12} is the transition matrix element. The natural width of a line is generally very small, it can be entirely neglected in comparison with line width arising from other mechanisms, described later here. An example from an experiment, carried out in the present work: a molecule of a triple ^{13}C-substituted ethyl cyanide, $^{13}CH_3{}^{13}CH_2{}^{13}CN$ ($\mu_a = 3.82\ D$), studied in the current thesis, has natural width of $\Delta\nu_N = 12 \cdot 10^{-4}$ Hz at 300 GHz.

In *collision, or pressure broadening*, random collisions occur between molecules in a gas cell. The energy levels of the molecules change when the interaction molecules are close. As the molecules come close together their energy levels are perturbed and thus the transition frequency changes during the collision time. Molecular collisions are the dominant cause of line broadening if the pressures are sufficiently high. The higher the pressure, the more molecules in a gas cell and thus the higher the absorption. However, at pressures, low enough, collisional broadening of spectral lines is small. And at pressures, sufficiently low, the line width is directly proportional to pressure. Collision-broadened lines have the Lorentzian shape function:

$$\phi_L(\nu) = \frac{1}{\pi}\frac{\Delta\nu_L}{(\nu - \nu_0)^2 + (\Delta\nu_L)^2}$$

where $\Delta\nu_L = 1/(2\pi\tau)$ is the Lorentz line width, and τ is the time between collisions. The mean collision time τ changes inversely to the pressure, and therefore $\Delta\nu_L$ increases linearly with the pressure.

Doppler broadening is caused by a thermal motion of the molecules which shifts the frequencies at which the molecule absorbs or emits radiation. Molecules, affecting by a Doppler broadening effect, have different velocity components which results in a width that is proportional to the frequency of the transition ν_0 and depends on temperature T (in Kelvin, K) and on the molecular weight M (in atomic mass units, amu). The Doppler width $\Delta\nu_D$ is given by a formula

$$\Delta\nu_D[MHz] = 7.15 \cdot 10^{-4}\nu_0[GHz] \sqrt{\frac{T[K]}{M[amu]}}$$

Experimental example: for the $^{13}CH_3{}^{13}CH_2{}^{13}CN$ molecule at 300 K and 300 GHz the Doppler width (theoretical) is 0.5 MHz; and at 900 GHz it is 1.5 MHz. The Doppler-broadened line width increases directly with the transition frequency, it becomes an important factor in limiting the accuracy of transitions measured with [absorption] spectrometers at high frequencies. Illustration from experiment, calculations of a Doppler width for a triple ^{13}C ethyl cyanide, will be given in Sec. 2.2.5.

Lines, affected by Doppler broadening, have the Gaussian profile which results from an ensemble of molecules with Maxwell – Boltzmann velocity distribution when they absorb radiation at Doppler shifted frequencies $\nu = \nu_0 + \Delta\nu_D$:

$$\phi_G(\nu) = \frac{1}{\nu_D \sqrt{\pi}} \exp\left(-\frac{(\nu - \nu_0)^2}{\Delta\nu_D^2}\right)$$

In general, at MM-wave and THz frequencies, the overall line broadening is a mixture of thermal (Doppler) and the pressure (collisional) mechanisms. In a case of a presence two or more broadening mechanisms, the line shape function, [that describes the relative absorption around the center frequency of the transition], will be the combination of each individual function for every broadening type. This is known as the Voigt profile, that is the convolution of Lorentz and Gauss line profile. Voigt line function can be written as

$$\phi_V(\nu) = \phi_G(\nu) * \phi_L(\nu)$$

$$\phi_V(\nu) = \frac{1}{\Delta\nu_D \sqrt{\pi}} H(a, u)$$

where

$$H(a, u) = \frac{a}{\pi} \int_{-\infty}^{+\infty} \frac{e^{-y^2}}{a^2 + (u - y)^2}$$

is called the Hjerting function, and

$$a = \frac{1}{4\pi\Delta\nu_D}; u = \frac{\nu - \nu_0}{\Delta\nu_D}$$

For the comparison, Lorentzian and Gaussian line shape functions, are shown in Fig. 2.6.
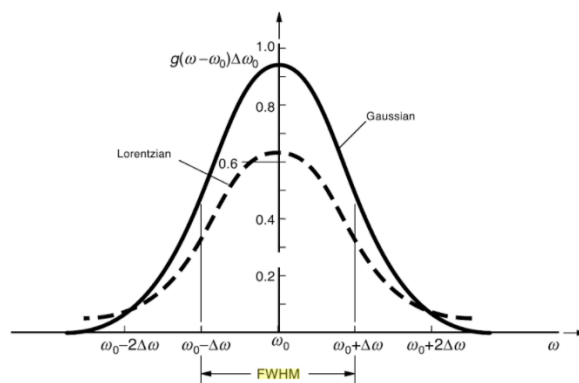
Figure 2.6 – Lorentzian and Gaussian line shape function profiles [65].

2.2.5 Calculations of a Doppler width for a triple ^{13}C ethyl cyanide

As was pointed out earlier, the spectral resolution of Lille spectrometer is limited by the Doppler width, which is in principle easily computable. In real experiments the Doppler broadening dominates over all other broadening mechanisms. At MM-wave and THz ranges Doppler broadening is most significant at low pressure, high temperatures and at high frequencies, with collision being relatively negligible. The line width is determined by the Doppler width in the low-pressure limit and by pressure broadening at higher pressures. However, at pressures, high enough, collisional (pressure) broadening becomes significant. The line width of molecular transitions is then determined by the Doppler width in the low-pressure limit and by pressure broadening at higher pressures. Molecular spectral lines, obtained experimentally, possess line profile which contains the effects of all broadening mechanisms. Such line profile is reasonably well described by Voigt function. Below, an example of measuring a Doppler width from experiment for triple ^{13}C-substituted ethyl cyanide, $^{13}CH_3{}^{13}CH_2{}^{13}CN$, will be given.

While investigating, for example, unstable species, to obtain the spectra we need to quickly optimize experimental conditions and to sweep (scan) frequency *fast*. A proper choice of a frequency step is important since it affects the spectra recording, notably data acquisition rate (or sample rate). Frequency step should be rationally selected at each frequency range, to achieve high productivity of the experimental data. For that we need to estimate the Doppler width theoretically and/or experimentally. In order to correctly fit molecular line and to determine central line frequency, we need, as known, to have at least 10 points at line FWHM. Frequency step, to acquire 10 data points, equals FWHM/10. Example of measuring Doppler (and Lorentz) widths and corresponding

Table 2.4 – Doppler width for triple ^{13}C-substituted ethyl cyanide, $^{13}CH_3{}^{13}CH_2{}^{13}CN$, at 300 K, at a constant pressure, as a function of frequency range

ν_0, MHz	Line intensity	$\Delta\nu_D$, MHz	$\Delta\nu_L$, MHz	frequency step, to choose (optimum)
154422.1115	38.98	0.2514	0.5612	~25 kHz
162860.3445	49.24	0.2652	0.5738	
175095.3760	37.13	0.2852	0.5462	
185838.4119	74.29	0.3026	0.5876	
192995.2126	57.28	0.3142	0.5604	
202057.3913	13.98	0.329	0.5486	
...				
892521.8307	3.130	1.4534	1.0048	~90 kHz
909702.3781	1.731	1.4814	0.9512	
910925.4916	3.924	1.4834	1.0494	

frequency step, will be given on $^{13}CH_3{}^{13}CH_2{}^{13}CN$, which spectra have been recorded during the author's PhD. Table 2.4 lists the frequency transitions of $^{13}CH_3{}^{13}CH_2{}^{13}CN$ in a frequency range from 154 to 910 GHz, with measured the Doppler and Lorentz widths. Optimum frequency step for each frequency range, is given in the right column.

Doppler width is also a function of a pressure. At low pressures, pressure broadening can be neglected and spectra exhibit Doppler limited line widths, providing the high resolution required to separate spectral lines.

If the pressure is too low and the power emitted by radiation source is too high, saturation of the absorption lines may occur. This will result that [absorption] peak height will decrease and the line width will increase. To keep a spectral resolution without the loss in sensitivity, we need to reduce the pressure until other broadening factors, that do not depend on pressure (i.e. Doppler) become significant. As the pressure is reduced to the point at which the Doppler broadening becomes dominant, the line shape changes to the Maxwell-Boltzmann shape described earlier, and the peak of maximum intensity decreases directly with the decrease in pressure.

Considerations of Doppler width and pressure help to rationally choose experimental conditions and parameters, that depends on operating frequency of a spectrometer, for spectral recordings.

Chapter 3

Experimental Investigation of Terahertz Transmission. Determination of Properties of Dielectric and Semiconductors Materials, Related to Astronomical and Spectroscopic Instrumentation.

3.1 Overview of the work

Durind my PhD, I've worked one year in the instrumentation laboratory at LERMA where there are many set-ups operating at THz frequencies. In this chapter we will present experimental investigation of transmission properties of a number of important materials that can be used to design components in instrumentation for astronomy and spectroscopy in Terahertz frequency range. The experiments I carried out allowed me to get acquainted with THz instrumentation, to device experimental set-ups and change them according to the requirements, to get a feeling for measurement accuracies, sensitivities and difficulties and to come up with a data analysis scheme. Besides that the study of materials will be advantageous in order to minimize losses and increase the sensitivity of future instrument. Materials studied here include *High-density Polyethylene (HDPE)*, *high resistivity Silicon*, *Zitex* and *Mylar*. Their refractive indices and absorption coefficients will be determined. The work performed here is of particular interest for the instrumentation in radio astronomy, since HDPE is a material commonly used for the vacuum windows for cryostats, and Mylar is actively employed as a beam splitter in heterodyne receivers. Also, the current investigation will be helpful in general for the practical choice of materials with regard to their specific use in the THz range. Here we have developed an experimental setup that can be used to investigate various dielectrics and semiconductors around 609 GHz (∼500

μm, 20 cm^{-1}) and around 1.4 THz ($\sim$200 μm, 50 cm^{-1}); We propose a simple method for measuring their angular and/or frequency dependent transmission. The set-up can be applied as well for the studies at other frequencies. Careful attention in the current work was given to the investigation of polarization-independent transmission. To derive the optical properties of materials, we have applied a graphical fitting method. With the use of a numerical method in Matlab, we have improved on the accuracy of determination of the refractive indices and absorption coefficients.

3.2   Motivation for the current study

For good sensitivity, it is essential to reduce any losses, absorption or scatteres in astronomical receivers, as well as laboratory spectrometers. The optics can introduce losses and increase the receiver noise temperature, for example. Filters, windows, beam splitters, substrates, lenses, and other components (vacuum or cryogenic), employed in the instrumentation, are needed for low loss optics at THz frequencies. These components are generally made out of dielectric or semiconductor materials are used. In particular, polymeric materials have found numerous uses as lenses and windows materials. For example, windows for cryostats should have maximum transmission, low losses, and hold vacuum. For the efficient coupling of the radiation, e.g. from the radiation source to the gas cell and then to a detector in the spectrometer, at THz frequencies, an optical system, a combination of lenses and/or mirrors, should be designed, which uses appropriate materials. Beam splitter is the key component in modern Michelson Fourier-transform infrared (FTIR) spectrometers, and is also used as a diplexer in heterodyne receivers. A film for a beam splitter should be properly chosen for its transmission and reflection properties at the desired frequency.

3.3   Commonly used dielectric and semiconductor materials

High-density polyethylene (HDPE) is often used as window material in sub-millimeter instrumentation. Receivers that require cooled detector employ a cryostat with a thermally isolating vacuum. For the radiation to pass to a detector in cryostat, vacuum windows, transparent to incoming light, are needed. The vacuum window needs to have high transmission, be mechanically strong and Hold the vacuum. HDPE is also often used as a material for lens applications in the MM-wave, due to its isotropy, availability and easy machining.

Mylar is the trade name of DuPont for Polyethylene terephthalate (PET)-film, is a common choice for dielectric beam splitters. Mylar is chemically inert, mechanically stable and has a high transmission in THz range. Mylar films were available in thickness between 6 and 300μm.

Zitex is particularly useful as an IR blocking filter in front of bolometers. Filters are needed to minimize heating, i.e. IR radiation. Zitex is a sintered Teflon material from Saint-Gobain Performance Plastics, which relies on scattering. It is a porous Teflon sheet with a filling factor of 50%, and is manufactured in several varieties as a filter paper. Zitex G-104, investigated here, is made from sintered Teflon spheres with pore sizes ranging from 5 to 6μm, and has a thickness of 100μm.

Silicon is an attractive material for the use in THz range. Silicon might be an alternative for HDPE window, this material has good transmission properties, is very strong but fragile. Even if optical components from this material suffer from significant reflection losses, this can be overcome by an appropriate anti-reflection coating or anti-reflection grooves.

Given the importance of the materials, mentioned above, we (re-)investigated here the properties of [low-loss] materials, that are candidates for various applications at Terahertz frequencies.

3.4 Literature background

Some measurements of properties of dielectrics have been carried out in the submm- and THz range. Transmission and reflection measurements of the materials, investigated here, have been previously carried out using far-infrared Fourier transform spectroscopy (FTS). Numerous studies on polymers and various plastics such as HDPE been performed by a number of authors [66–69]. The properties of thin-film beam splitters have been investigated in the past with particular reference to Mylar. Its optical transmission and constants were studied by [70, 71]. Transmission properties of Zitex in submillimeter were reported by[72, 73]. Refractive indexes for semiconductors from transmission spectra have been determined in [74]. Optical properties of doped Silicon from 0.1 to 2 THz have been investigated by[75]. The refractive index and absorption coefficient can be determined from the transmission measurements by numerical methods with a high accuracy.

Data analysis using simultaneous determination of thickness and refractive index have been demonstrated in previous works [74, 76, 77]. We employed a similar approach using Matlab, to simultaneously derive (retrieve) the optical parameters (refractive index, absorption coefficient) and the thickness of the measured materials from transmission measurements.

Regardless that there are data available on the optical constants (refractive index and absorption coefficient) of many different materials studied at MM-wave and THz frequencies ([78, 79], for example), mostly, only single polarization measurements have been performed. Many previous works paid attention to the transmission properties only of TM polarization, while TE polarization has received very little attention [80].

Besides, a literature review shows sometimes considerable differences between the optical properties, measured on the same materials, especially at THz range. It is very preferable to have consistent data, when we want to buy the materials that have the same properties, from different suppliers, and to design components. The possible reason for that is the material properties might be different even if the samples are nominally from the same material, which can take place due to different fabrication processes or ageing of the material, which is especially relevant for polymers as HDPE and Mylar. In the case of semiconductors, Silicon for example, the doping and other impurities may give rise to different optical characteristics. More, systematic errors can occur in the measurements of optical constants by different techniques.

Although the transmission properties of materials mentioned above have been studied by many authors, the detailed investigation has remained incomplete. Our measurements were carried out at 600 GHz and 1.4 THz and pay particular attention to an angular and polarization dependent transmission. Our measurements allow as well for the determination of refractive index and absorption coefficient. Some available previous measurements we have included for comparison. In this work, we also developed a method which employs the monochromatic radiation source, operated in single linear polarization at frequencies 600-642 GHz and 1300-1500 GHz. in order to simultaneously accurately determine the thickness and the refractive indices of studied materials.

3.5 Theoretical description

Since the aim of this paper is to investigate the transmission properties of materials, short theory to treat the physical problem will be given below: the sample of materials, measured here, is considered as a [thin] slab surrounded by the air.

3.5.1 Transmission

The transmission of an incident electromagnetic plane wave through a thin dielectric slab of thickness d and refractive index n, surrounded by an air with refractive index, n_a, is well known from classical electromagnetic theory [81]. Samples investigated here are assumed to be homogeneous and isotropic thus classical Fresnel's formulas for transmission can be used.

A schematic representation of the physical problem is shown in Fig. 3.1. All surfaces are assumed to be plane parallel and optically smooth.

Light (radiation) incident on a dielectric material, is partially reflected, refracted and transmitted into (through) the material. The incident and reflected angles are related by Snell's law:
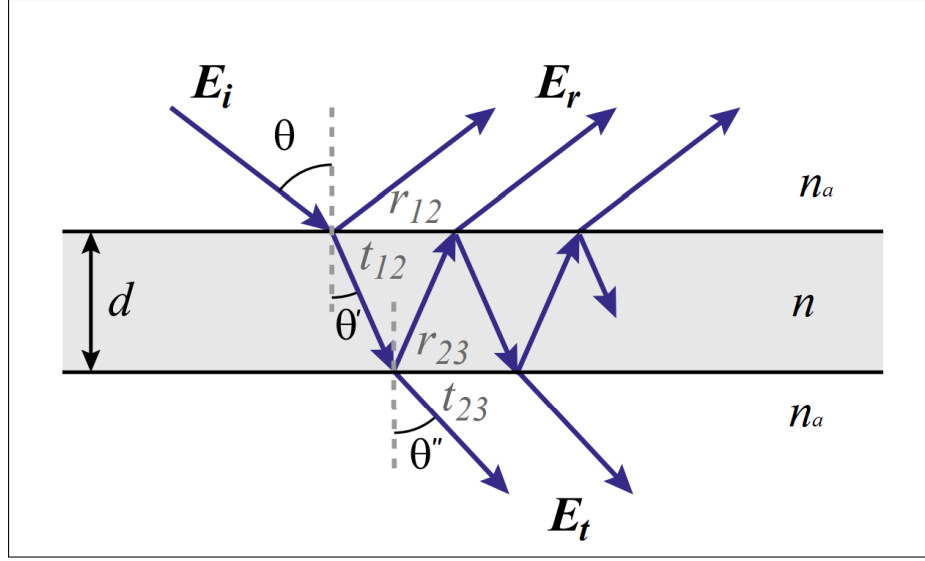
Figure 3.1 – Multiple reflection picture for the transmission through a thin dielectric slab. E denotes a wave amplitude. Only first and second reflection and transmission are taken into account.

$$n_a \sin\theta = n \sin\theta' = n_a \sin\theta''$$

where θ is the angle of incidence measured with respect to the normal, and θ' is the angle of refraction.

The intensity of radiation transmitted by a plane-parallel transparent plate is given by the Airy formula [81]. The transmission and reflection coefficients can be expressed in terms of the single-interface reflection (transmission) Fresnel coefficients r_{12} and r_{23} (t_{12} and t_{23}), as shown in Fig. 3.1, of summing the contributions from multiple partial reflections which depend on the polarization. If we assume that no absorption occurs, the overall reflection and transmission coefficients r and t, for the slab can be defined as [81]:

$$r = \frac{E_r}{E_i} = \frac{r_{12} + r_{23}\exp^{i2\phi}}{1 + r_{12}r_{23}\exp^{i2\phi}} \tag{3.1}$$

$$t = \frac{E_t}{E_i} = \frac{t_{12}t_{23}\exp^{i\phi}}{1 + r_{12}r_{23}\exp^{i2\phi}} \tag{3.2}$$

where E_i, E_t and E_r denote amplitudes of, respectively, incident, transmitted, and reflected waves; and ϕ is the phase difference accumulated by the radiation with the wavelength λ when it is passing through the plate, which is given by [81]

$$\phi = \frac{4\pi n d}{\lambda}\cos\theta' = \frac{4\pi d}{\lambda}\sqrt{(n^2 - n_a\sin^2\theta)} \tag{3.3}$$

If we considere that the slab is symmetric, in that case, $r_{23} = -r_{12}=r$, and $t_{12}t_{23} = 1 - r_{12}^2=1 - r^2$. Substituting 3.3 in 3.1 and 5.7 yields [81]:

$$r = \frac{r(1 - \exp^{i2\phi})}{1 - r^2 \exp^{i2\phi}}$$

$$t = \frac{(1 - r^2) \exp^{i\phi}}{1 - r^2 \exp^{i2\phi}}$$

Two cases of linear polarization of light are considered, namely one with electric field perpendicular to the plane of incidence, i.e., TE-polarization and one with electric field oscillating in the plane of incidence, i.e., TM-polarization. r, the reflection coefficient for the electric field, for each case of polarization, is given by:

$$r_{TE} = \frac{\sin(\theta' - \theta)}{\sin(\theta' + \theta)} \tag{3.4}$$

and

$$r_{TM} = \frac{\tan(\theta - \theta')}{\sin(\theta + \theta')} \tag{3.5}$$

The ratio of the intensity of the transmitted light (I_t) to the intensity if the incident light (I_i) is called transmittance (transmitted intensity) $T=\frac{I_t}{I_i}$. The reflectance (reflected intensity) is determined as $R=\frac{I_r}{I_i}=1 - T$, where I_r is the reflected intensity of the radiation. R and T can be expressed as

$$R = |r|^2 = \frac{2r^2(1 - \cos(\phi))}{1 + r^4 - 2r^2 \cos(\phi)}$$

$$T = \frac{\cos \theta''}{\cos \theta}|t|^2 = \frac{(1 - r^2)^2}{1 + r^4 - 2r^2 \cos(\phi)} \tag{3.6}$$

In practice, one usually multiplies T and R by 100 to obtain the percent transmittance (%T) or reflectance (%R), which ranges from 0 to 100%.

As seen from these equations 3.6, 3.4, 3.5 and 3.3, derived from the electromagnetic theory of light, transmittance depends on the refractive index n, the sample thickness d, wavelength λ, angle of incidence θ and polarization state of the incident electric field (TE- or TM-). The refractive index of a material n can be thus calculated from values of its transmittance T measured at several angles of incidence θ.

From the transmittance, one can calculate the quantity known as absorbance, A. Absorbance is the amount of light absorbed by a sample. It is calculated from T using the following equations:

$$A = -\log T \quad or \quad A = \log(1/T)$$

Transmittance and absorbance are inversely related. The more a particular wavelength of light is absorbed by a material, the less it is transmitted. Since the relationship between A and T is logarithmic, if 50% of radiation is transmitted by a sample (T is 0.5), 30% of it will be absorbed.

3.5.2 The absorption coefficient

The refractive index, in general, is complex. The complex index of refraction of a material takes into account its transmission and absorption. The losses are characterized by the absorption coefficient, α, which is related to the imaginary part of the complex refractive index ñ of the material

$$ñ(\nu) = n(\nu) + ik(\nu)$$

where n and k are respectively the real and imaginary parts of the complex refractive index ñ. $k(\nu)$ is called the extinction coefficient, it is usually associated with power loss and indicates the amount of absorption loss when the electromagnetic wave propagates (radiation passing) through the material:

$$k(\nu) = \frac{c}{4\pi}\frac{\alpha(\nu)}{\nu}$$

$\alpha = \frac{4\pi k(\nu)}{\lambda}$ (measured in cm^{-1}) describes the attenuation of the radiation intensity. If d and n are known, the absorption coefficient can be estimated from the general expression of the transmission.

Absorption coefficient α of a material is relate to the absorbance A as:

$$\alpha = \frac{A}{d}$$

ñ is also related to dielectric constant ϵ as ñ$=\sqrt{\epsilon}$. The dielectric losses in a material are characterised by the dielectric loss factor, $\tan\delta$, defined as

$$\tan\delta = \frac{Im\epsilon}{Re\epsilon} = \frac{2nk}{n^2 - k^2}$$

Equations for the refractive index n and the power absorption coefficient α, however, can be also solved analytically, and we find the following expressions [82]:

$$n(\nu) = \frac{1 - r(\nu)^2}{1 + r(\nu)^2 - 2r(\nu)\cos\phi(\nu)}$$

$$\alpha = \frac{4\pi\nu}{c}\frac{2r(\nu)\sin\phi(\nu)}{1 + r(\nu)^2 - 2r(\nu)\cos\phi(\nu)}$$

3.6 Experimental setup

The concept of the experimental set-up is quite simple and is illustrated in Fig. 3.2. It consists of 3 main parts: radiation source, material under investigation and a detection system.
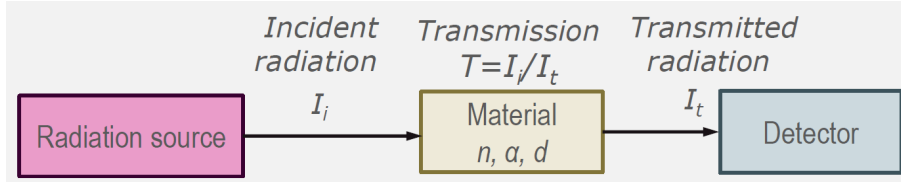
Figure 3.2 – General principle of transmission measurements (when $\theta=0$).

The radiation, emitted by a source, is incident on a sample of material and the transmitted power is measured by a detector. The radiation intensity after passing a material, I_t, of a thickness d, compared with the incident intensity I_i is determined as transmission: $T = I_t/I_i = \exp^{-\alpha d}$ and the absorption coefficient α is defined as $\alpha = -\frac{\log T}{d}$. The sample can be rotated around the [vertical] axis so that radiation is incident with different angles. To determine the refractive index of a material two methods are possible as follows from the theoretical formulas Eq. 3.3 and 3.6:

(a) variation of an incident angle θ with fixed frequency ν , $T = f(\theta)$ and

(b) variation ν with θ fixed, $T = f(\nu)$

In this way the angular and frequency dependence of the transmission of material can be investigated and the absorption coefficient can be determined as well.

The experimental set-up, developed for the transmission measurements in the present study is schematically shown in Fig. 3.3. For the radiation source, a microwave frequency synthesizer (Rohde & Schwarz 100A or Agilent E368A, depending on the configuration) is employed to drive the amplifier multiplier chains (AMCs) that consist of a cascade of frequency multipliers. Radiation, modulated at 81 Hz, is propagating from the feed horn of the AMC and registered by a Golay detector and then fed in to a lock-in amplifier (SR510). The signal is also displayed with an oscilloscope.
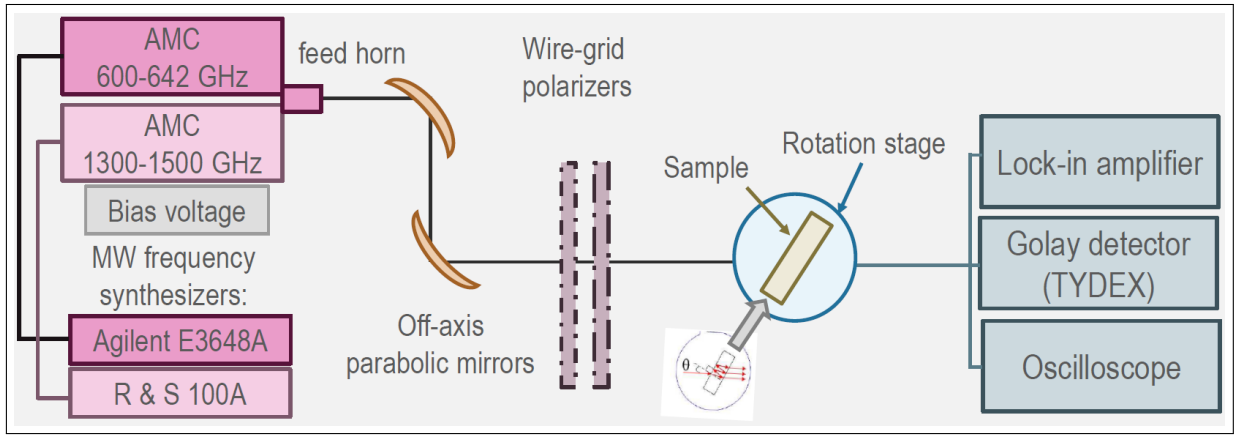
Figure 3.3 – Experimental set-up for the transmission measurements in the THz range

The sample of the material under investigation is placed in the holder on the rotation stage, it can be rotated to change the angle of incidence. Two parabolic mirrors were used as focusing elements to guide the radiation from the feed horn of the multiplier chain, through the material and to the QMC detector.

Two different AMCs from Radiometer Physics GmbH (RPG) and Virginia Diodes, Inc (VDI), covering the range 600-642 GHz and 1365-1498 GHz, respectively, have been used.

For the RPG chain (600-642 GHz), a signal from Agilent 83751A MW frequency synthesizer, operating in a 16.66-17.83 frequency range, is fed to an active sextupler, frequency doubler and tripler. The chain performs a frequency multiplication x36 (x6x2x3), it can be tuned to any monochromatic frequency between 600 and 642 GHz. Its schematic is shown at Fig.3.4. The same chain was employed for the tests of Schottky heterodyne receiver in Chapter 4 and its picture can be found there.

For the VDI chain (1300-1500 GHz), a signal from Rohde & Schwarz 100A MW frequency synthesizer, operating in a 13.5-15.625 frequency range, is fed to a cascade of frequency multipliers: doubler, two quadrupoles and tripler. The chain performs a frequency multiplication x96 (x2x4x4x3), and covers the 1365-1498 GHz frequency range with a peak output power of $\approx$ 40 µW. Its schematic is shown at Fig.3.5.

3.6.1 Thickness Measurement

The thickness of the material samples must be known as accurately as possible, since this quantity enters directly into the determination of the refractive index.

Mylar films we used in thickness 6, 9, 13, 25, 50, 100 μm, high-resistivity Silicon of a thickness ~300 μm and Zitex ~100 μm. These thickness values were claimed by the manufacturer and were taken without re-measuring.

Two HDPE samples with rough thickness of 1 mm and 2 mm and a diameter of 60 mm were cut from a plastic block. The thickness of the HDPE samples was measured
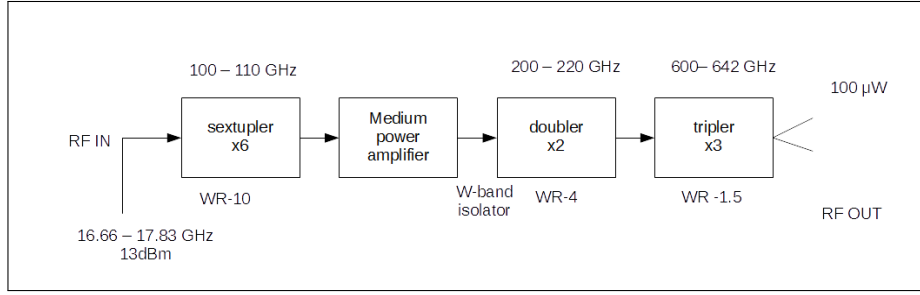
Figure 3.4 – Schematic of 600-642 GHz RPG multiplier chain, used for the transmission measurements
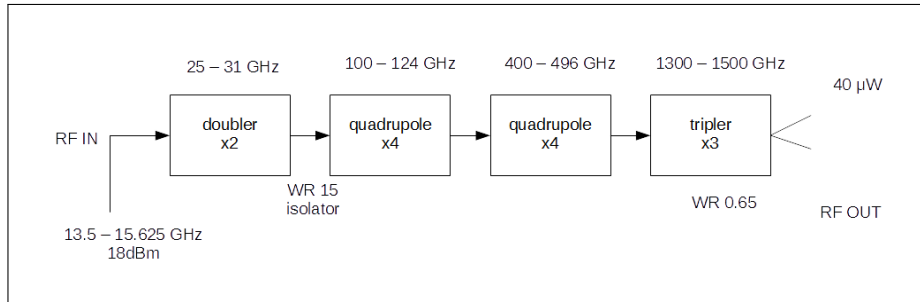
Figure 3.5 – Schematic of 1300-1500 GHz VDI multiplier chain, used for the transmission measurements

with a digital micrometer. We read $d = 1065$ μm and 1995 μm. The thickness accuracy, determined with a digital micrometer is to ± 1 μm. Our HDPE samples were somewhat wedged, with thickness variations across the surface of about 1-2 μm. For more accurate determination of the refractive index, it is necessary to fabricate (or buy) a plane parallel slap of constant and known thickness, since Fresnel relations we use for theoretical description, assume smooth surfaces. However, thickness variations of 1-2 μm are much smaller than the wavelength, 500 μm (at 600 GHz) and 214 μm at (1.4 THz), and satisfies the main purpose of the current study.

3.7 Experimental Procedure

All measurements have been carried out in air at room temperature. The set of transmission measurements have been performed in the following manner. The frequency of the radiation source was set to 609 GHz. The polarization was chosen to be $TM-$. One polarization grid was put after the feed horn of multiplier chain to eliminate any cross polarization. At first, the sample was removed, and the intensity of the incident radiation I_i, was measured with Golay detector. Then, the sample was put into the holder, placed normal to the radiation (at 0 °), and the transmitted power I_t was measured. Onwards, the power transmitted through a sample was measured at various angles of incidence θ (0 °-90 °) at fixed frequency 609 GHz. "Standing" waves, arising from the superposition

of incident and reflected waves, limitated the accuracy of transmission measurements. The amplitude of measured signal depended on at which position of the standing wave it was measured. That's why, we did measurements in the node [or anti-node] of the standing wave, where its amplitude is either minimum or maximum. For this, position of Golay detector was adjusted each time while performing the set of the measurements., i.e. changing the position of a sample in a holder on a rotation stage, setting the new frequency value, etc.

At second, the sample was rotated around the vertical axis with steps of 2° with respect to its previous position, so the radiation, emitted by a source, is passing the sample under different incident angles θ, the signal is registered by Golay detector, and the transmitted power is measured again.

After this set of measurements had been performed on each sample, the polarization of the radiation source was changed to be $TE-$ with the use of two polarization grids at 45° and 90° and procedure to measure angular dependent transmission at the same frequency, 609 GHz, was repeated again. The first polarization grid passes $\sqrt{2}$ of the polarization at 45°, the second grid passes $\sqrt{2}$ is TE.

In this way angular dependent transmission $T=f(\theta)$ of different materials was obtained. The similar set of measurements were made at a fixed frequency of 1.374 THz for $TE-$ and 1.440 THz for $TM-$ polarization. Two frequencies differ because the multiplier chain when operating in $TE-$ polarization didn't provide sufficient power, because of the use of two polarizing grids, that reduced the intensity of electromagnetic wave twice, so the frequency value was changed to another one with high output power.

3.8 Results and discussion

Maximum and minimum values of transmitted power were noted and the resulting value was averaged. Transmission plots T, as a function of incident angle θ, were then obtained by taking the ratio of the averaged value I_t of transmitted power to the averaged reference value I_i (without the sample). The studied samples are high resistivity Silicon, Zitex, HDPE (speciemens of 1 mm and 2 mm), and Mylar (6 specimens of different thickness 6, 9, 13, 25, 50, 100 μm). Some plots of measured angular dependent transmission at 609 GHz and 1374/1440 GHz of these materials are given at Fig.3.6, 3.7,3.8. Measurements are in very good agreement with the theoretical formulas. All other transmission data for these materials may be found in App. A.

Tables 3.1 and 3.2 lists the samples we measured and summarizes the values of their transmission.

In the current study, we used a curve-fitting technique in which the experimental data were compared with the data generated from a theoretical model, based on Fresnel's equa-

(a) TM-polarization

(b) TE-polarization, n=1.531-1.533, α=0.025

(c) TM-polarization

(d) TE-polarization, n=1.534-1.537, α=0.015-0.005
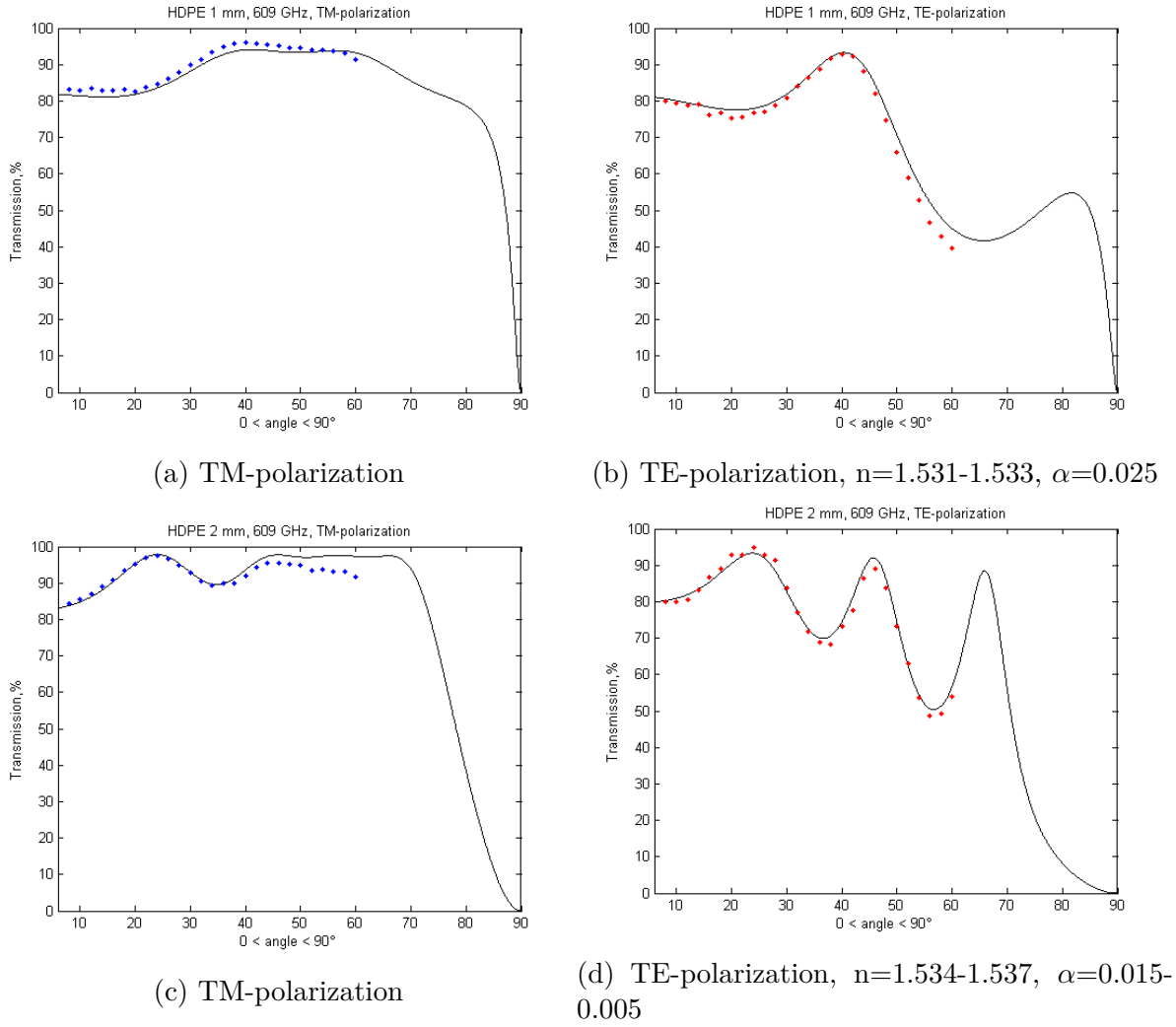
Figure 3.6 – Experimental transmission measurements for HDPE samples with a thickness of 1 mm (a, b) and 2 mm (c,d) at 609 GHz (represented by red and blue points) and the fitted theoretical curve (black), determined by Matlab.

tions. A developed graphical method permits the determination of the refractive index and absorption coefficient from the transmission data. A good visual fit was obtained by varying manually several parameters (refractive index, absorption coefficient) which enter the theoretical model. An approach was applied only to HDPE samples, since for other materials the uncertainty in determining n was not resolved because of the curve behaviour , more exactly no sufficient peaks were available to fit correctly curve properly.

Results of obtained values of refractive index n and absorption coefficient α for HDPE are presented numerically in Table 3.3 as best fit parameters for n and α. HDPE has a refractive index 1.52-1.53 and the absorption coefficient 0.005-0.040 mm^{-1} depending on the frequency. The agreement between the values determined in this work and previously published results obtained by other authors is remarkable good.

Table 3.1 – **Transmission of studied materials at 609 GHz**

Material	d	Polarization	T_{max},%	θ, °
HDPE	1 mm	TE	94	40
	1 mm	TM	95	40-60
	2 mm	TE	95	25;45
	2 mm	TM	98	25;45-60
Zitex	100 μm	TM	95	0-60
	100 μm	TE	90-95	0-40
Silicon	300 μm	TM	70-80	0-60
	300 μm	TE	70	0

Table 3.2 – **Transmission of studied materials at 1374/1440 GHz**

Material	d	Polarization	T_{max},%	θ, °
HDPE	1 mm	TE	90	30;50
	1 mm	TM	90	25;40-50
	2 mm	TE	90	multiple peaks
	2 mm	TM	90	multiple peaks
Zitex	100 μm	TM	95	0-50
	100 μm	TE	95	0-50
Silicon	300 μm	TM	99	40-50
	300 μm	TE	50	0

Table 3.3 – **Refractive index and absorption coefficient of HDPE samples at 609 and 1.4 THz, determined as the best fitted parameters from Matlab.**

Frequency, GHz	d	n	α, mm^{-1}	Polarization
609	1 mm	1.53	0.025	TE,TM
	2 mm	1.53	0.015	TE,TM
1374/1440	1 mm	1.52	0.040	TE,TM
	2 mm	1.52	0.020	TE,TM
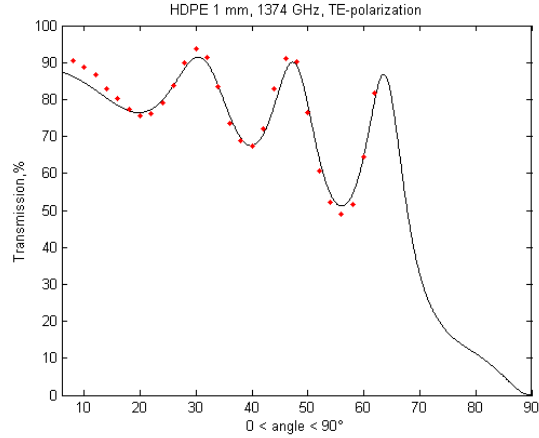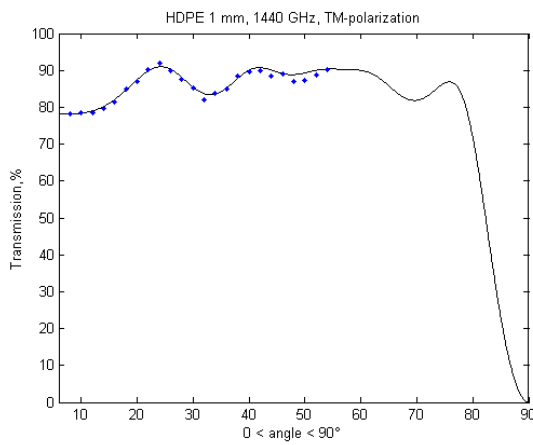
(a) TM-polarization, n=1.534-1.537, α=0.040

(b) TE-polarization, n=1.521-1.523, α=0.035-0.040
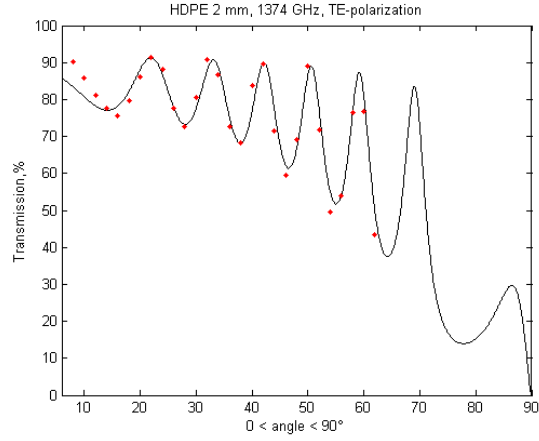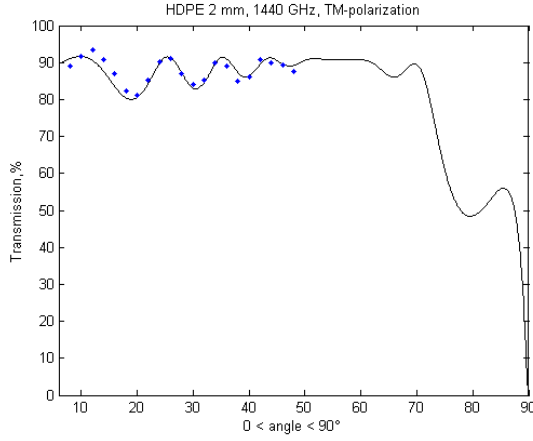
(c) TM-polarization, n=1.521-1.523, α=0.020

(d) TE-polarization, n=1.523-1.524, α=0.020

Figure 3.7 – Experimental transmission measurements for HDPE samples with a thickness of 1 mm (a, b) and 2 mm (c,d) at 1440 GHz (represented by red and blue points) and the fitted theoretical curve (black), determined by Matlab.

3.9 Practical suggestions for materials applications

For HDPE at 600 GHz and 1.4 THz frequency range, we suggest to choose the $TM-$ (horizontal) polarization of a radiation source if aimed to obtain maximum transmission. Even if T will be slightly changing depending on the incident angle, in a case of $TE-$ (vertical) polarization, maximum transmission will have multiple peaks and will vary up to 20-30%. For the Silicon, as follows obviously from the plots, it is also preferable to have $TM-$ polarization of electromagnetic wave. It is critically noticeable at 1.4 THz, leading to nearly 100% transmission in $TM-$ and 50% in $TE-$ polarization.

(a) TM-polarization, 609 GHz

(b) TE-polarization, 609 GHz

(c) TM-polarization, 1440 GHz

(d) TE-polarization, 1374 GHz
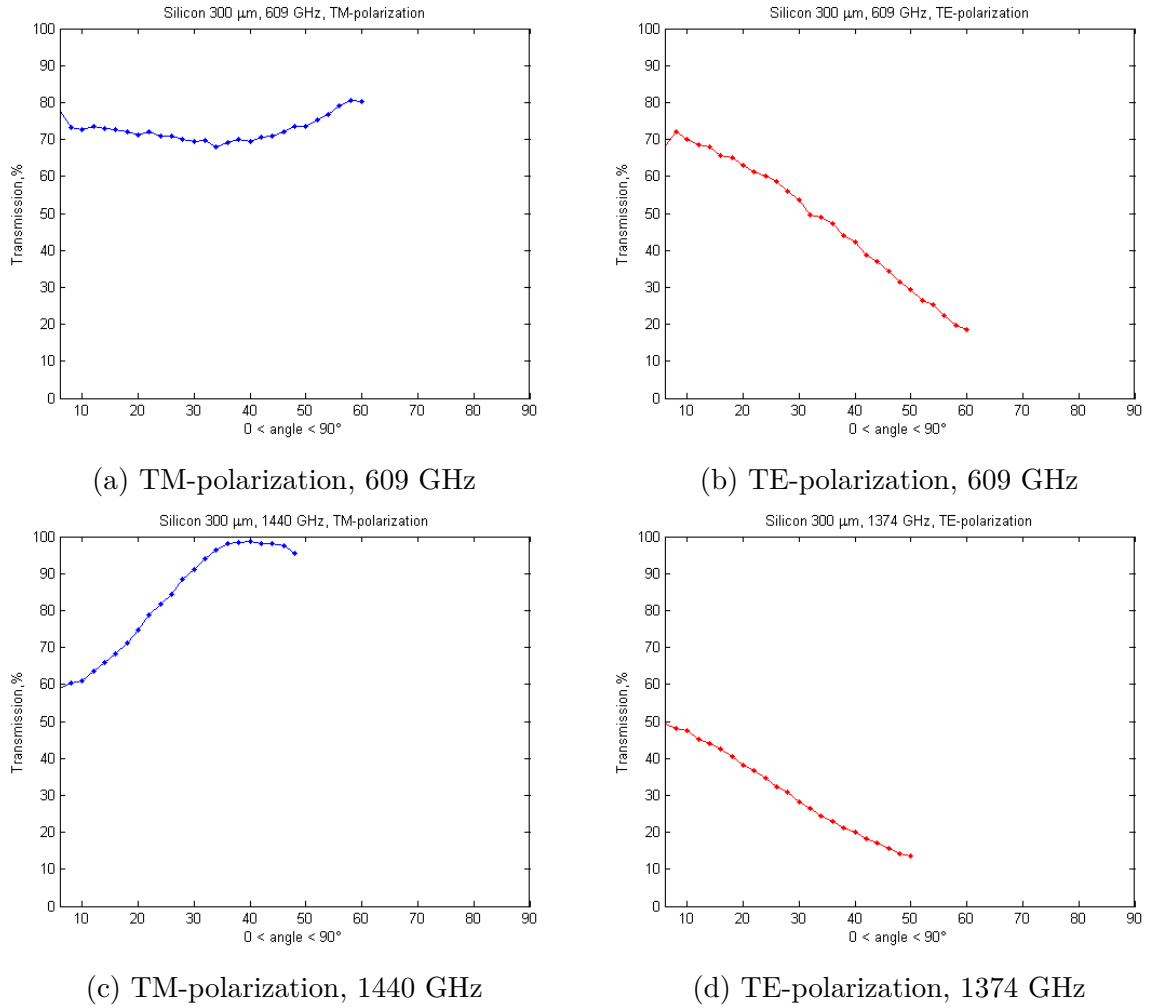
Figure 3.8 – Transmission measurements (represented by red and blue lines) for a Silicon of a thickness 300μm at 609 GHz (a,b) and 1.4 THz (c,d).

3.10 Error analysis

Theoretically, the precision in measuring transmission is dependent on the precision in the determination the thickness d, the angle precision θ, and frequency accuracy of the radiation source $f = \frac{c}{\lambda}$, according to Eqs. 3.6 and 3.3. The experimental precision is limited by a variety of factors including sample surface quality (either it has smooth or rough surfaces), changes of absorption in the ambient air, power stability of a radiation source, vibrations etc. In our measurements the uncertainty of the frequency of the MW frequency synthesizer, Agilent 83751A is of the order of 1 Hz, which we can neglect. Fluctuations, or drifts in power of the radiation source, or in the gain of the frequency multiplier or amplifier can also cause errors in transmission measurements. The angle θ is set manually with a visual precision corresponding to a value on the rotation stage, and is 1 °. Variations in the sample thickness d (1-2 μm in our case) also affects the accuracy

of the measurements.

The stability of the electronics is not within the scope of this work and is not discussed further. The possible drift in radiation power during the time required for a measurement was approximately linear with time and was corrected in data reduction. This effect was eliminated by making measurements symmetrically: I_i was measured first, then a series of transmission measurements of I_t were performed for different values of θ, followed by another measurement for I_t.

3.11   Fitting the measured fringe data

In the above analysis, we have fitted the data with theoretical curves, by adjusting different parameters (n, d and α) and selected values of those parameters for which the curve looks in the best agreement with the experimental data. Here we will briefly discuss and apply a method to do a retrieval of the index of refraction and the thickness of materials using numerical method with Matlab.

Thickness and refractive index are fundamental to the characterization of materials. Several methods to simultaneously determine thickness and refractive-index measurement have been proposed in the literature. Here, we will use method proposed in [76].

Setting $\phi(\theta) = 2m\,\pi$ (m = integer) in Eq. 3.3, the peak locations are determined as

$$\theta_m = \sin^{-1}\frac{1}{n_a}\sqrt{1 - (\frac{\lambda m}{2d})^2} \tag{3.7}$$

In principle, both n and d can be determined by comparing the experimentally measured maxima locations ("peak data") against those obtained by Eq. 3.7. The first peak is located very close to the normal incidence ($\theta = 0$), associated with the maximum value of m (m_{max}). The spacing between neighboring peaks gets smaller with increasing angle of incidence, and the last peak corresponds to the minimum value of m (m_{min}).

Accurate values of n and d cannot be simultaneously determined from a set of fringe data, unless the peak data are extremely accurate. In this work, we used two radiation sources with different frequencies, 609 and 1440 GHz in order to resolve the 2π-ambiguity, and to determine accurate values of n and d simultaneously.

Matlab was used to find accurate peaks from experimental transmission data for HDPE, $\theta_{exp,i}$ ($i = 1, 2, 3, \ldots, N$), which were compared with the peak locations calculated by Eq. 3.7, $\theta_{calc,i}$ ($i = 1, 2, 3, \ldots, N$).

In order to determine n and d to better than 10^{-3}, we calculated the sum of the squared error

$$S = \sum_i \mid \theta_{exp,i} - \theta_{calc,i} \mid^2$$

and plot the inverse $(1/S)$ as a function of n and d, for those around the roughly determined values with a digital micrometer, n_{rough} and d_{rough}. Figures 3.9a and 3.9b show the contour plots of $1/S$ for the fringes measured for HDPE samples, with TE-polarization, at frequencies of 609 and 1440 GHz, respectively. In each plot, provided that the experimental data are perfect, the $1/S$ plot would indicate a diverging peak at the real values of (n, d). The procedure was applied only for HDPE samples since the transmission curves have multiple peaks, while other materials give monotonically decreasing or increasing dependence of angular dependent transmission.

HDPE samples of two different thickness (1 and 2 mm) were used to make sure that the best fit parameters were independent of the sample geometry. The peaks indicated in Figs. 3.9a and 3.9b have their maxima at a common thickness of 1993 $\pm$ 0.1 μm. As a result, the refractive indices of HDPE are determined to be 1.5358 $\pm$ 0.0002 at 609 GHz and 1.5214 $\pm$ 0.0002 at 1440 GHz, respectively. Results are presented numerically in Table 3.4.

(a) 609GHz   (b) 1374GHz
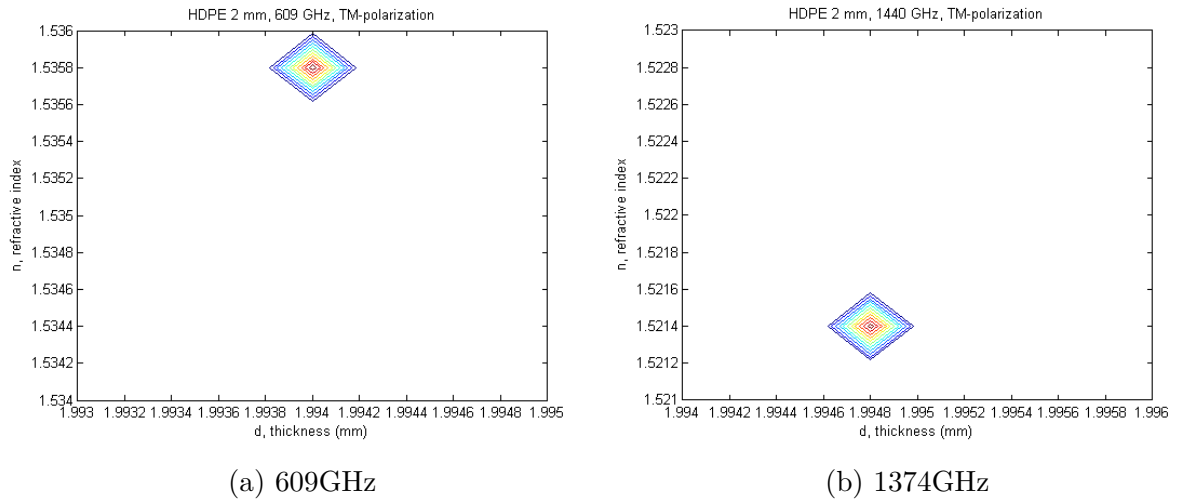
Figure 3.9 – Contour plots of 1/S versus (n, d) for HDPE sample of a thickness 2 mm at 609 (a) and 1440 GHz (b).

Table 3.4 – Refractive index of HDPE at 609 and 1440 GHz, determined from the Matlab contour plots.

f, GHz	d_{rough}, μm	n_{rough}	d,μm	n
609	1995	1.534-1.537	1993.8-1994.2	1.5356-1.5360
1440	1995	1.521-1.523	1994.6-1995.0	1.5212-1.5216

3.12 Conclusions. Characterization of materials for instrumentation

We have created an experimental set-up to study the angular dependency of the transmission T = f(θ) of a variety of materials: High-density Polyethylene (HDPE), high resistivity Silicon, Zitex and Mylar at 0.6 and 1.4 THz. The set-up's main components are amplifier multiplier chains (AMCs), driven by commercial microwave frequency synthesizer, the material under investigation and a Golay detector. This is one of the first experiments that can measure the transmission for both the TE and TM-polarization. The experimental set-up was optimized to minimize any standing waves and good quality data was obtained. From the data the refractive index and absorption coefficient of the dielectrics were determined using two different analysis methods. The numerical method allowed us to determine refractive indices of HDPE with uncertainties in the forth decimal place, and thickness to within 0.1 μ m. The results we obtained are consistent with prior measurements and validate our experimental and analysis approach.

The current study is important for practical applications in which detailed investigation of angular dependent transmission is required and accurate values of refractive indices of materials need to be known.

In a further step it would be interesting to study the transmission properties of materials also at higher frequencies (up to 2.7 THz) and to build an experiment to measure materials at cryogenic temperatures. These experiments would allow us to look at the value of the refractive index and the absorption coefficient with frequency and temperature.

Chapter 4

600 GHz Schottky heterodyne receiver for High-Resolution Molecular Spectroscopy with Lille Fast-Scan Fully Solid-State DDS Spectrometer

4.1 Overview

This chapter is dedicated to the development and testing a prototype of a 600 GHz Schottky heterodyne receiver, initially designed for space mission ESA JUICE [83] and its implementation with Lille fast scan DDS spectrometer. A 600 GHz Schottky heterodyne receiver, that will be described below, is a prototype of a receiver for ESA JUICE, including a state-of-the-art 520–620 GHz non-cryogenic Schottky solid-state mixer [84], provided by Alain Maestrini [1]. 600 GHz Schottky heterodyne receiver for JUICE was developed, designed and fabricated at LERMA [2], Observatoire de Paris in partnership with LPN [3] and CNRS [4]. It is based on MW frequency synthesizer, sub-harmonic Schottky diode mixer and a system of amplifier multiplier chains (AMCs). The design and main components of a Schottky heterodyne receiver will be described and its operation principle will be given. Further, the prototype will be integrated in the Lille fast-scan DDS spectrometer in PhLAM [5]. The performance of a 600 GHz Schottky heterodyne receiver with Lille fast-scan DDS spectrometer will be demonstrated by recordings of molecular spectra of CH_3CH_2CN in 600 GHz frequency range. CH_3CH_2CN spectra, measured with

---

[1] `alain.maestrini@obspm.fr`
LERMA, Observatoire de Paris, PSL Research University, CNRS, UMR 8112, Sorbonne Universités, UPMC Univ. Paris 06, F-75014 Paris, France
[2] Laboratoire d'Etudes du Rayonnement et de la Matière en Astrophysique et Atmosphères
[3] Laboratoire de Photonique et de Nanostructures
[4] Centre national de la recherche scientifique
[5] Le laboratoire de Physique des Lasers, Atomes et Molécules

Schottky heterodyne receiver during the tests will be analyzed and compared to those obtained with QMC InSb hot electron bolometer in a 600 GHz frequency range. The application of a 600 GHz Schottky heterodyne receiver to Lille fast-scan DDS spectrometer was a unique collaboration work, funded by ANR [6].

4.2   Introduction

The *development* and *improvement* of laboratory instruments - spectrometers, up to THz frequencies, is in a high demand. The sensitivity of the laboratory spectrometer can be mainly improved by applying heterodyne detection technique, employing more sensitive detector or the radiation source with lower phase noise.

QMC 4 K InSb hot electron bolometer (HEB) is currently employed with Lille fast-scan DDS spectrometer (further FSS) as a broadband detector up to 1.5 THz. It operates in cryostat and requires cryogenic cooling with liquid Helium. Usage of a cryostat increases the complexity of the spectrometer. Cryostat, being bulky and heavy, when filled with liquid Helium (and Nitrogen) makes the mechanical and optical alignment a spectrometer pretty inconvenient. Besides, liquid Helium is quite expensive. Liquid Nitrogen has an affordable price, so it is often used in a first stage to cool to 77 K and reduce consumption of Helium, but liquid Helium, to achieve 4 K, required for bolometer operation, is necessary. Below 600 GHz, room-temperature VDI zero bias Schottky diodes detectors can be used to provide reasonably good level of sensitivity for molecular laboratory spectroscopy. But at frequencies above 600 GHz, the highest sensitivities in laboratory spectrometer can be only nowadays achieved with the use of cryogenic bolometers.

For the observation of interstellar molecular lines in the THz region, instruments using high resolution heterodyne spectrometers, like HIFI, are predominantly used. *In general,* heterodyne detection has a number of advantages as compared to direct detection. Direct detectors (that are bolometers or zero bias Schottky detectors, for example) can operate over a broadband frequency range, while heterodyne receivers have a narrow band detection bandwidth. For frequencies above 200 GHz, there are no commercially available amplifiers. In a heterodyne receiver the incoming signal (at hundreds GHz or a few THz) is down-converted to a significantly lower frequency (a few MHz or GHz) that can be amplified by low-noise amplifiers, that are commercially available. Also, the output signal of a heterodyne receiver can be divided into many channels without adding a significant amount of noise.

Therefore we have decided to develop a new compact room temperature detector, heterodyne receiver, which operates in a 600 GHz frequency range, and provides level of sensitivity, comparable to those of Helium-cooled bolometers - and to apply it for

---

[6]French National Agency for Research

laboratory molecular spectroscopy in PhLAM.

A 600 GHz Schottky heterodyne receiver (further SHR) for European Space Agency (ESA) Jupiter Icy Moons Explorer (JUICE) [85] was designed at LERMA, Observatoire de Paris in partnership with LPN-CNRS (Laboratoire de Photonique et de Nanostructures). Space mission like JUICE require very sensitive instruments. In addition, components should be state-of-the-art, highly reliable and meet the instrument requirements for sensitivity. A 600 GHz SHR for JUICE has a DSB (double side band) noise temperature of 1000-1500 K at a room temperature, which makes it the most sensitive up to date solid-state non-cryogenic heterodyne receiver at 600 GHz frequency range. The developed Schottky receiver has also the advantage of being compact and non-cryogenic. It is considered to provide high level of sensitivity for laboratory molecular spectroscopy in PhLAM, University of Lille, in a 600 GHz frequency range.

It should be noted that the heterodyne [sub-millimiter-wave] spectroscopy in the laboratory has been performed in the past (1980-ies) in PhLAM in the 74 -400 GHz [86, 87] and 600-2500 GHz [88] frequency ranges. At the time, klystron, Gunn diode and frequency synthesizers were commonly used as local oscillators and whisker-contacted Schottky diodes as mixers, which were very sensitive devices up to 3 THz, but not easy to handle (quite difficult diode's adjustment procedure to make a contact). The sensitivity of the mixer and performance of the LO source is critical. For the last 20 years, GaAs Schottky barrier diodes have been used as the mixing elements in a frequency range from 100 GHz up to a few THz. The recent improvements in fabrication technology of planar Schottky diodes made possible the development of sensitive mixers and frequency multipliers, that can be designed to cover the frequency ranges up to 3 THz, need very little power to be pumped and are more robust.

Therefore the application of a prototype of a 600 GHz SHR, initially designed for ESA JUICE, is of great interest for the laboratory molecular spectroscopy, in the context of its capability to achieve a high sensitivity, room temperature operation and compactness.

Combination of two state-of-the-art instruments: non-cryogenic solid-state 600 GHz Schottky [space] heterodyne receiver with unprecedented sensitivity - 1000-1500 K at a room temperature, and Lille fast scan fully solid state DDS spectrometer that provides high sensitivity and spectral resolution with high accuracy fast frequency scan *possibly can be* a next generation of state-of-the-art instruments for laboratory molecular spectroscopy - superior in its operation characteristics and unique in its design.

4.3   Heterodyne Receivers

The heterodyne detection principle was invented in 1918 by E. H. Armstrong to enhance the frequency selectivity of the radio systems. Up to the present day heterodyning (i.e.

frequency conversion) is commonly used in signal processing, telecommunication, cell phones and so on. The heterodyne principle is commonly used in astronomy for high spectral resolution observations. In high frequency receivers the heterodyne principle is used for down-converting the radio frequency (RF) signal to a lower frequency in order to use commercially available low noise, cheap, electronics for the signal amplification.

Here the concepts of heterodyne receivers, typically used in astronomy, will be presented.

4.3.1 Basic Components and Characteristics of Heterodyne Receivers

The heterodyne receiver scheme is shown in Fig. 4.1. A radiation from the source at ν_S is combined with a signal from local oscillator (LO) at ν_{LO} on a mixer, where the difference between the source and LO frequencies, intermediate frequency (IF), $\nu_{IF} = \nu_{LO} - \nu_S$, is generated. The major components of heterodyne receiver are:

- A local oscillator (LO) that delivers the reference frequency to the mixer.

- A mixer that creates the beat frequency between the RF signal the LO. The mixer delivers an output at the intermediate frequency (IF).

- Optics (feed horns, beam splitters, lenses, diplexers) to couple the radiation from the RF and LO signal onto the mixer.

- A back-end

The back-end deals with the downconverted IF signal. Its components are:

- An IF chain with amplifier(s) and filter to process the signal generated by the mixer.

- A detector for the detection of the IF signal (to measure the IF power). The choice depends on the application. For absorption spectroscopy, where FM technique is applied, a diode detector is used. For other types of measurements, a power meter can also be used. The IF signal can be displayed as well on a spectrum analyzer.

The mixer, local oscillator, optics and first IF amplifier are the most important components of the heterodyne receiver since they determine its sensitivity.

The sensitivity of a heterodyne receiver depends on:

- Quality of the mixer: its noise performance and conversion efficiency.

- Noise introduced into the system (e.g. power level and stability of the LO)

- Efficiency of the coupling of the signal radiation to the detector element.
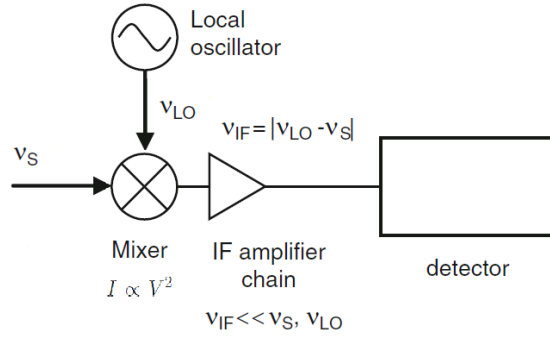
Figure 4.1 – Scheme of a heterodyne receiver.

Spectral resolution, achieved by a heterodyne receiver is determined by

- Linewidth (should be narrow enough) and frequency stability of the LO.

- IF processing, including spectrometer.

In general, heterodyne detection offers higher spectral resolution.

4.3.2 Heterodyne Detection Theory

A heterodyne receiver often down-convert the radio frequency (RF) signal to a lower intermediate frequency (IF) in mixer. The RF signal at frequency ν_S is combined (mixed) with a reference signal at a well known, fixed frequency ν_{LO}, produced by the local oscillator (LO). The LO operates at a frequency near to that of the RF signal.

A mixer is a non-linear device, i.e. an element with a non-linear relation between input voltage and output current. Mixer receives signals from both the source (RF) at ν_S and a local oscillator at ν_{LO}.

If we apply both a signal from the source (RF), $V_{RF} \sin(2\pi\nu_S t)$ and a local oscillator (LO) $V_{LO} \sin(2\pi\nu_{LO} t)$ as their sum U at the input of a mixer, the output $I \sim U^2$, up to 2rd order, will be:

$$
\begin{aligned}
I &= \alpha[V_{RF} \sin(2\pi\nu_S t) + V_{LO} \sin(2\pi\nu_{LO} t)]^2 \\
&= \alpha V_{RF}^2 \sin^2(2\pi\nu_S t) + \alpha V_{LO}^2 \sin^2(2\pi\nu_{LO} t) \\
&\quad + 2\alpha V_{RF} V_{LO} \sin(2\pi\nu_S t) \sin(2\pi\nu_{LO} t)
\end{aligned}
$$

Using a trigonometric formulae, the output can be written the following:
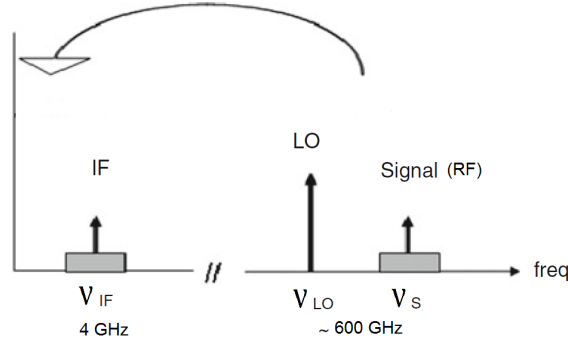
Figure 4.2 – Frequency conversion process: In heterodyne receivers, the detected signal with THz frequencies (600 GHz) is down−converted to much lower frequencies (1–30 GHz), intermediate frequency (IF), where it is amplified by low−noise amplifiers.

$$I = \frac{1}{2}\alpha(V_{RF}^2 + V_{LO}^2) \qquad \text{(DC component)}$$

$$-\frac{1}{2}\alpha V_{RF}^2 \sin(2\pi 2\nu_S t + \frac{\pi}{2}) \quad \text{(2nd harmonic of signal)}$$

$$-\frac{1}{2}\alpha V_{LO}^2 \sin(2\pi 2\nu_{LO} t + \frac{\pi}{2}) \quad \text{(2nd harmonic of LO)}$$

$$+\alpha V_{RF} V_{LO} \sin[2\pi(\nu_S - \nu_{LO})t + \frac{\pi}{2}] \qquad \text{(difference frequency)}$$

$$-\alpha V_{RF} V_{LO} \sin[2\pi(\nu_S + \nu_{LO})t + \frac{\pi}{2}] \qquad \text{(sum frequency)}$$

The output consists of the superposition of several components at different frequencies (Fig. 4.2): a DC signal, signals at twice the signal and the local oscillator frequencies, and two components at the difference and the sum of signal and oscillator frequencies. By use of an appropriate bandpass filter, usually the high frequency terms are filtered out and, only desired, low-frequency component of a signal is kept.

Fundamentally, two frequencies are transferred to the IF chain, ν_{LO}-ν_{IF} and ν_{LO}+ν_{IF}, called the lower side band (LSB) and the upper side band (USB), respectively. If a mixer is operated in a way that both side bands are present, it is called a double-side band (DSB) mixer. If one sideband is suppressed, for example by a filter, only one side band is down-converted and it is a single-sideband (SSB) mixer. Usually at the output of the mixer, the signal at a frequency, called the "intermediate frequency" (IF), a difference between ν_S and ν_{LO}: $\nu_{IF} = \nu_S$ - ν_{LO} is kept, thus in a lower frequency range. This IF signal is then further amplified and analyzed.

1 Local oscillators

The LO must produce a monochromatic reference signal. Mainly, the choice depends on a frequency range. At MM-wave and THz ranges, the LO, in principle, might be any radiation source such as those described in some details in Sec. 1.4. They include radiation sources, based on MW frequency synthesizers and frequency amplifier multiplier chains (AMCs), gas lasers, quantum-cascade lasers (QCL), BWOs etc. The characteristics, required for the LO to be used in a heterodyne receiver, are quite the same as for frequency radiation sources for high-resolution spectroscopy, introduced in Chapter 1. The LO power needs to be sufficient to drive ("to pump") the mixer into the optimum operating [non-linear] region. This depends on the type of mixer (SIS, HEB or Schottky) and the operation frequency. For a Schottky diode mixer, for example, the required LO power is typically in the order of several mW, while for SIS and HEB mixers it is in the order of 10 μW and 1μW, respectively. The requirement of the LO power stability also depends on the mixer. Schottky diodes are relatively insensitive against power fluctuations, while the performance of a HEB mixer is much more critical to power fluctuations.

2 Frequency Mixers

Mixers are essential parts of any heterodyne receiver and its choice is crucial for the heterodyne receiver sensitivity. At present there are three main technologies for the mixer devices at MM-wave and THz frequencies: Superconductor-Isolator-Superconductor (SIS) junctions [90, 91]), hot-electron-bolometer (HEB) mixers [89, 92–95], and Schottky diodes [96–98]. They are illustrated in Fig. 4.3. Table 4.1 lists the key characteristics of modern mixer technologies at sub-millimeter frequencies. SIS mixers (Fig. 4.3c) provide excellent sensitivity approaching the quantum limit in the sub-millimetre regime up to $\approx$ 1.3 THz. The non-linear mixing element is an SIS tunnel junction, formed by two superconductors (typically Nb) separated by a very thin insulating layer. Hot-electron-bolometer mixers (Fig. 4.3b) are the most sensitive for frequencies above $\approx$ 1.3 THz and up to $\approx$ 6 THz. HEB are simply thermal detectors which can also be used as mixers if local oscillator radiation is applied. An HEB mixer device consists of a very thin bridge of superconducting material (typically NbN) on a silicon substrate. Schottky mixers (Fig. 4.3a) have the general disadvantage of being significantly less sensitive than those using SIS or HEB mixers. But on the other hand, their major advantage is the fact that they can be operated at room temperature (although they are often cooled to lower temperatures to improve the noise performance). The two most common design for Shottky mixers employ a pair of planar Schottky diodes, either in an anti-parallel or in an open loop configuration. They are usually integrated into waveguides, and horn antennas are used
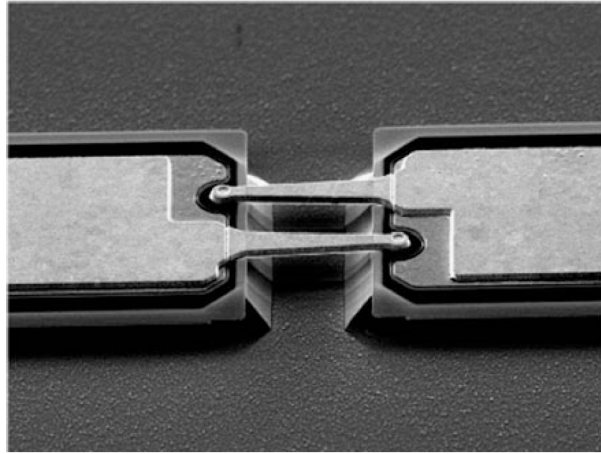
(a) Planar Schottky diode mixer (Courtesy B. Ellison, RAL)
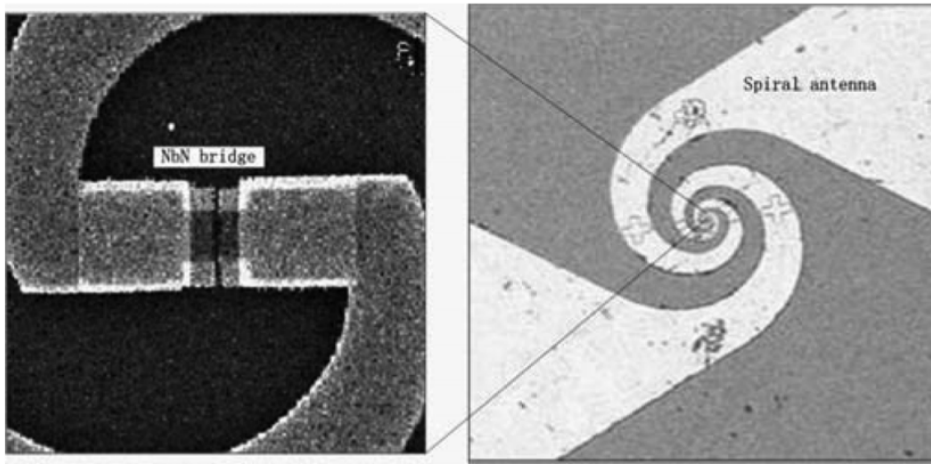
(b) HEB mixer chip with the NbN bridge [89]
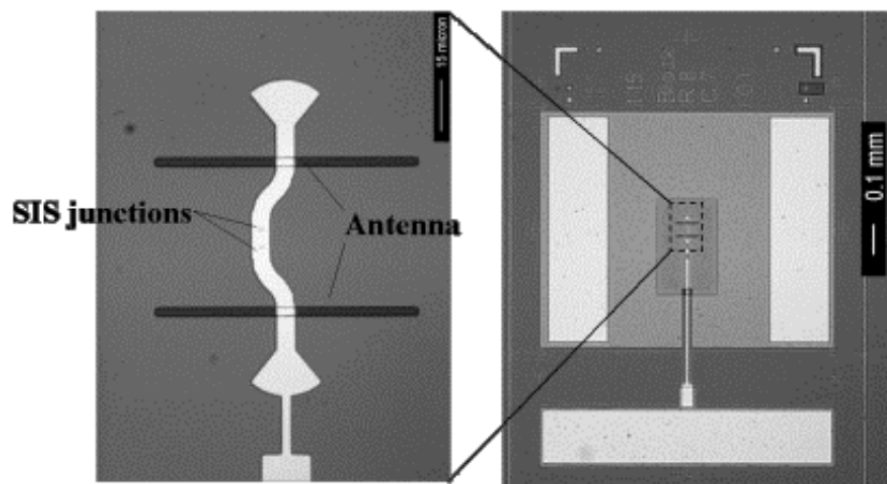
(c) SIS mixer chip layout. The two SIS junctions are coupled to a double slot antenna [90]

Figure 4.3 – Examples of mixers for sub-millimetre frequencies.

Table 4.1 – Key characteristics of sub-millimeter/far-infrared mixer technologies (status 2012)

	SIS	HEB	Schottky
RF range	up to ≈ 1.3 THz	1.3 to 5 THz	up to 3 THz
Sensitivity[a]/T_{min}	excellent: ≈ 2 to 6	medium: ≈ 4 to 10	poor: ≈ 20 to 40
LO power requirement	low: ≈ 1 μW	very low: ≤ 1 μW	high: ≈ 1 mW
Operating temperature	$\leq$ 4K	$\leq$ 4K	70 to 300 K

Notes. [a] in units of $T_{min}=h\nu k_B$, the minimum achievable noise temperature for DSB receiver, with h the Plank constant ($6.626 \cdot 10^{-34}$ $J \cdot s$), ν the receiver input frequency and k_B the Boltzmann constant ($1.381 \cdot 10^{-23}$ J/K)

for the radiation coupling.
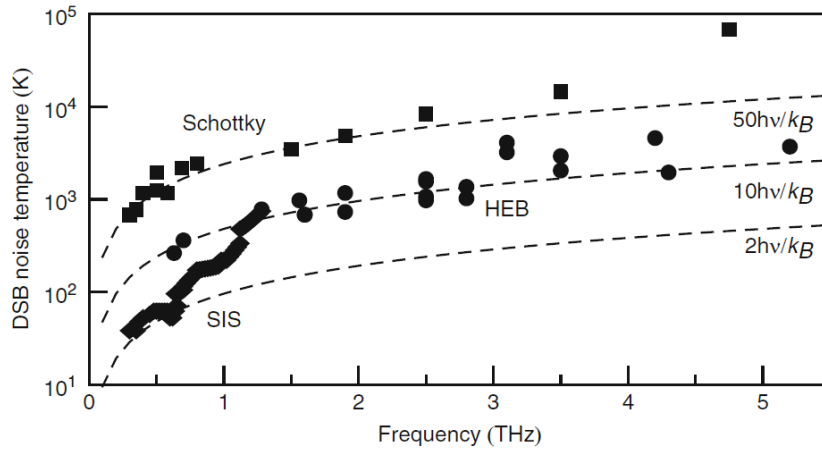
Figure 4.4 – DSB noise temperatures achieved with Schottky diode mixers (squares), SIS mixers (diamonds), and HEBs (HEB, circles) [7]

DSB noise temperatures achieved with different types of mixers, discussed in Sec. 2 are presented in Fig. 4.4.

4.4 Sensitivity of Heterodyne Detection

The noise sources in a heterodyne receiver are highlighted at Fig.4.5. The parameters, used to characterize a mixer, are the conversion loss L_M (or mixer gain, $G_M=1/L_M$) and the mixer noise temperature T_M. The conversion loss is defined as the power level (the amplitude) of the input RF signal, divided by the power amplitude at the IF signal output. In a heterodyne receiver the mixer is usually followed by an IF amplifier with a gain G_{IF}. It is characterized by a noise temperature T_{IF}. The noise temperature at the output of the IF amplifier is $G_{IF}T_{IF}$.

The receiver noise temperature T_{sys} is defined as the increase of signal noise temperature, which is required to generate the same output noise as would be generated by a
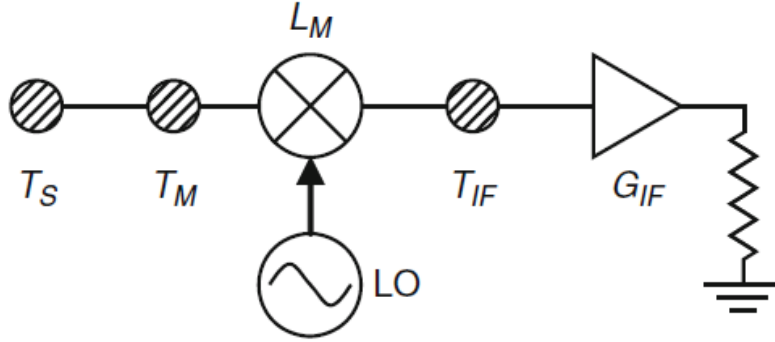
Figure 4.5 – A noise model of a heterodyne receiver. The noise sources (the noise temperature of a signal, T_S, the mixer, T_M, and IF amplifier T_{IF}) are assigned to the input of each component and are symbolized by hatched circles

noiseless receiver, i.e.

$$T_{sys} = T_M + L_M T_{IF}$$

4.4.1 Receiver Noise Temperature

The sensitivity of a heterodyne receiver, or the receiver (system) noise temperature T_{sys} is measured in Kelvin, units commonly used by astrophysicists community, it corresponds to the noise power P (in Watts) in a given bandwidth:

$$T_{sys} = \frac{P}{k_B \Delta\nu}$$

where $\Delta\nu$ is the (resolution) bandwidth (in Hz) over which that noise power is measured. The lower noise temperature, the more sensitive receiver.

Neglecting all additional noise sources a heterodyne system has a natural limit, the so-called quantum limit T_{lim} which is the minimum noise contribution of a mixer in an ideal system which limits the sensitivity of any heterodyne receiver:

$$T_{sys}^{lim} = \frac{h\nu}{k_B}$$

The receiver noise temperature T_{sys} determines the sensitivity of the receiver, i.e. its minimum detectable power or minimum detectable temperature in a given integration time τ and bandwidth B. The minimum detectable temperature difference T_{min} of a system with a noise temperature T_{sys} is given by "radiometer equation." [7]

$$\Delta T_{min} = \frac{T_{sys}}{\sqrt{\tau B_H}}$$

where B_H is the detection bandwidth (in Hz) defined by the bandwidth of the IF amplifier chain, τ is the integration time (in s).

4.4.2 Heterodyne Receivers for Astronomy

Heterodyne receivers play an important role in astrophysics, investigation of the Earth's and planetary atmospheres, and remote sensing applications [84, 99, 100]. This particular kind of receivers are primarily employed in THz and MM-wave instruments in ground-based astronomical telescopes and space- or airborne missions. The state-of- the-art technical performance and outstanding sensitivity makes heterodyne receivers essential instruments for the astronomical observations of stars, planets, comets, galaxies and other objects that are million light-years away from Earth. Below, the major examples of past, present and future astronomical THz heterodyne receivers will be given.

The Heterodyne Instrument for Far Infrared (HIFI) on ESA's [7] Herschel Space Observatory covered a frequency range from 0.48 to 1.28 THz and from 1.4 to 1.9 THz, its receivers used SIS and HEB mixers with multiplier based local oscillators (LOs). Data, obtained with HIFI, allowed to study in details the chemical composition and evolution of molecular clouds in the ISM. Through the astronomical observations, carried out by HIFI, different species of molecules, interstellar atoms and ions were identified. HIFI campaign allowed the development of all-solid-state frequency sources that are commercially available (VDI, RPG).

Another astronomical heterodyne receiver is the German Receiver for Astronomy at THz Frequencies (GREAT) [101], which is now in operation on Stratospheric Observatory for Infrared Astronomy (SOFIA) [102]. GREAT covers three frequency bands from 1.3 to 1.9, 2.5 to 2.7, and at 4.7 THz. It consists of HEB mixers and of LOs which are multiplier sources (below 3 THz) and QCL (at 4.7 THz).

All major ground-based submm/THz telescopes are now equipped with heterodyne receiver arrays. The Atacama Large Millimeter Array (ALMA) is composed of hundreds of heterodyne receivers covering the frequency range from 84 to 950 GHz.

Heterodyne receivers, using sub-millimetre Schottky mixers, have been used in the SWAS [8] [103, 104], ODIN satellite [105] and Rosetta-MIRO [9] astronomical space missions, launched in 1998, 2001, and 2004, respectively.

ESA Jupiter Icy Moons Explorer (JUICE) [83] is the next space mission, planned

---

[7]The European Space Agency

[8]The Submillimeter Wave Astronomy Satellite

[9]Microwave Instrument for the Rosetta Orbiter

for launch in 2022 and arrival at Jupiter in 2030. It is intended to observe Jupiter and its icy moon atmospheres which are thought to have oceans of liquid water. JUICE will spend at least three years making detailed observations of the giant gaseous planet Jupiter and three of its largest moons, Ganymede, Callisto and Europa. SWI (Sub-millimeter Wave Instrument) [106] is a heterodyne spectrometer on board JUICE, working in two spectral ranges 1080-1275 GHz and 530-601 GHz will investigate the temperature structure, composition and dynamics of Jupiter's stratosphere and troposphere, and the exospheres and surfaces of the icy moons. The non-cryogenic heterodyne receivers for SWI-JUICE are currently being developed by[107, 108], that are based on sub-harmonic Schottky diode mixer pumped by frequency amplifier multiplier LO chains, and one of the prototypes could be used for the spectroscopic applications and it will be the subject of current investigation here.

4.5 LERMA 600 GHz SHR Prototypes Sensitivity
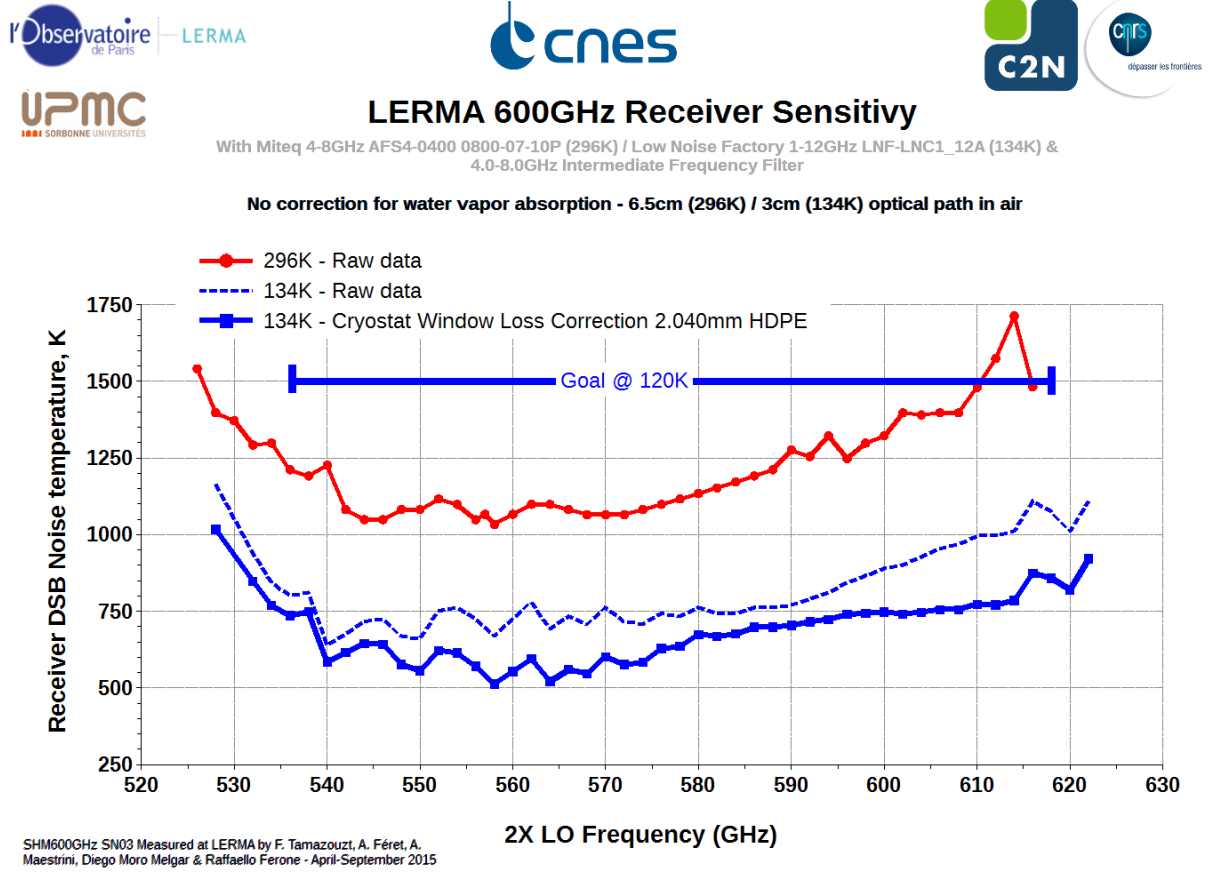
Figure 4.6 – 600 GHz Schottky receiver's sensitivity. Plot is kindly provided by A. Maestrini.

600 GHz SHR prototypes are the most sensitive to date with a DSB receiver equivalent noise temperature in the range of 1000 K-1500 K at room temperature (Fig. 4.6), which is enough for laboratory spectroscopy applications. It is state of the art instrument that is able to provide high sensitivity for planetary space missions like JUICE.

The mixer for a 600 GHz SHR was designed and fabricated by LERMA-LPN [84]. It features a pair of planar Schottky diodes in an anti-parallel configuration, integrated onto a GaAs membrane and coupled to waveguide using the LERMA-LPN process. The LERMA-LPN fabrication process use electron beam lithography, combined with conventional epitaxial layer design, similar to that described in [109]. The epitaxial layers are grown by MBE (Molecular Beam Epitaxy) on a semi-insulating 500- -thick GaAs substrate. Detailed design and fabrication of 520-620 GHz sub-harmonic mixer are given in [84]. The sub-harmonic mixer is illustrated in Fig. 4.7. Its fabrication is very challenging, the dimensions are of order a few micrometers. At 600 GHz the preferred choice is the

sub-harmonic mixer, allowing use of a LO signal at half the RF frequency.
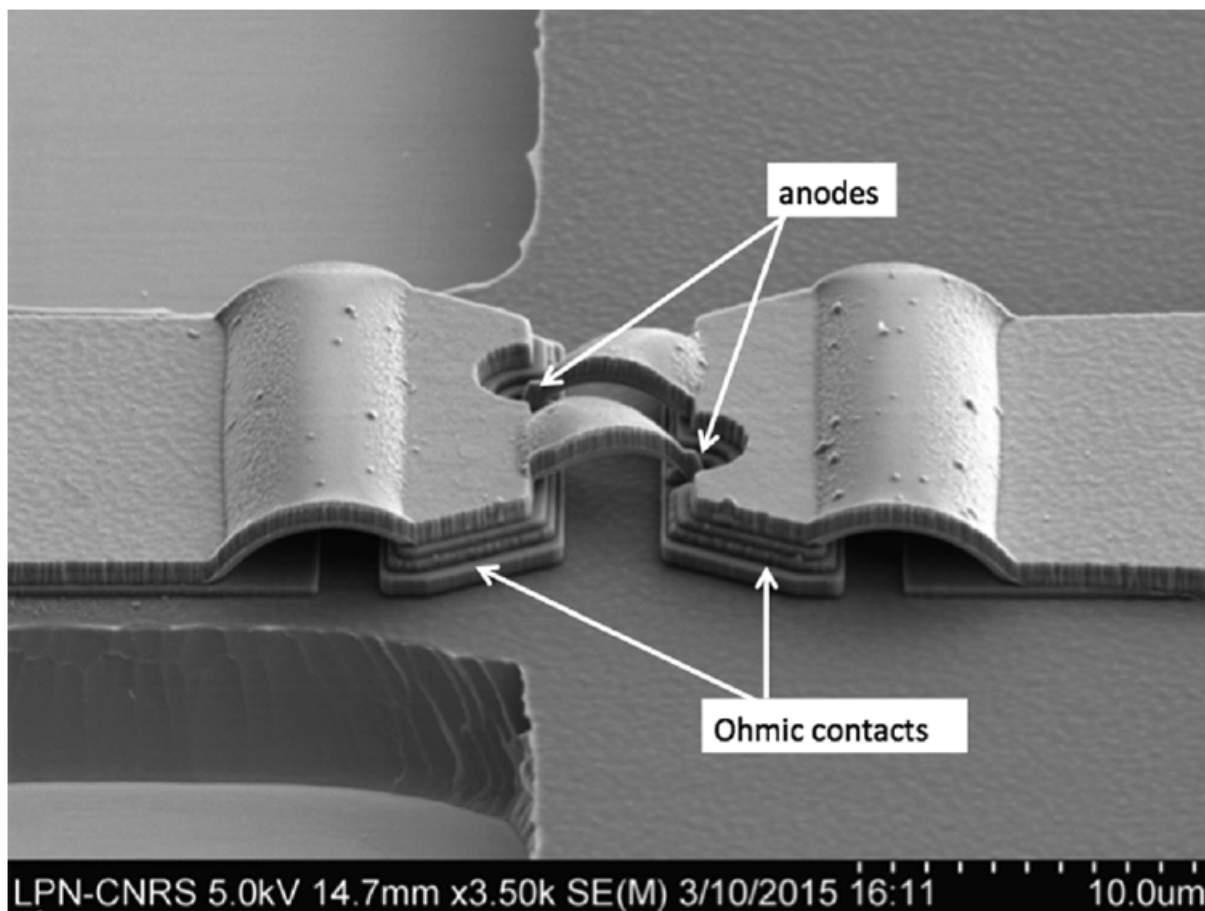
Figure 4.7 – Sub-micron Schottky diodes of 520-620 GHz mixer. Fabrication: Dr. L. Gatilova (LERMA). Growth: Dr. A. Cavanna (LPN). Photo Courtesy and copyright to [110].

4.6 Preliminary tests of a 600 GHz Schottky receiver prototype in LERMA

Preliminary tests of a 600 GHz Schottky receiver prototype are needed before it will be integrated in a laboratory spectrometer in Lille. The tests, to be presented here, don't aim to perform high-resolution laboratory molecular spectroscopy, but rather to check the principal ability of LERMA SHRs to detect molecular absorption lines in a 600 GHz frequency range and to obtain some preliminary results of representative spectra. For the implementation of a 600 GHz SHR with Lille fast-scan DDS spectrometer and the high-resolution spectra recordings see Section 4.8. For the tests performed below, a prototype of non-cryogenic solid state SHR, developed in LERMA for the space mission JUICE, was used. Although, this prototype slightly differs in configuration of LO chain from the receiver, used for the tests with Lille spectrometer, both prototypes are built on the similar components with the similar sensitivity of Schottky mixer. Besides, in the time it has not

been decided which prototype will be employed in the final set up with spectrometer in Lille, the current, available one, was tested. Moreover, an experimental measuring set-up we built in LERMA will allow in perspective to perform further characterization of the radiation sources and heterodyne receivers, that are being currently developed, designed and fabricated in LERMA, for their applications to molecular spectroscopy, in particular in PhLAM.

4.6.1 Experimental set-up

Fig. 4.8 shows a schema of the experimental set-up, built in LERMA, for testing a prototype of a 600 GHz SHR. The set-up, however, is similar, but rather in some 'primitive' form, to a conventional absorption spectroscopy. It consists of a radiation source, gas cell filled with a gas, and a SHR with the back-end: IF chain, detection and data acquisition systems.

Radiation source (RF signal) is based on Agilent 83751A MW frequency synthesizer, operating in a 16.66-17.83 frequency range, and a custom system of amplifier multiplier chains (AMCs) from RPG: active sextupler, frequency doubler and tripler. It's shown at Fig. 4.9. The chain performs a frequency multiplication x36 (x6x2x3), and covers the 600-642 GHz frequency range with a typical output power of $\approx$ 100 µW (additional information can be found in Appendix B).

Off-axis parabolic metal mirrors (before) and the focusing Teflon lens (after) the gas cell were mounted to optically focus radiation, which propagates from the feedhorn of a radiation source, passes through the absorption gas cell, filled with the methanol gas, CH_3OH, and reaches the SHR. The gas cell, used for the measurements, was developed by IAS-Orsay [10] and ENS[11]-LERMA for HIFI campaigns. The gas cell is in a multi path configuration, it has a total path length of 128 cm in a very compact (less than 30 cm high and 15 cm in diameter) configuration. The optics (mirrors) to guide the radiation beam, are located inside the gas cell. Its drawing design and technical description is detailed in Appendix B as a part of HIFI gas cell manual [111]. The cell is connected to two pumps: one primary pump, allowing to go down to about 0.1 mbar and one secondary (Turbo) pump to achieve vacuum as low as some 10^{-5} mbar.

45-degree grating was mounted after the gas cell to split the radiation in two directions. In a first stage, the output RF signal (designated by red arrows), after passing the gas cell, was detected by QMC pyroelectric detector. In this case, Agilent 83751A was internally modulated with 10 Hz according to the requirment of pyroelectric detector (its operation principle was discussed in Chapter 1). The RF signal is then fed to a lock-in amplifier

---

[10]Institut d'Astrophysique Spatiale - Université Paris-Sud
[11]l'École Normale Supérieure
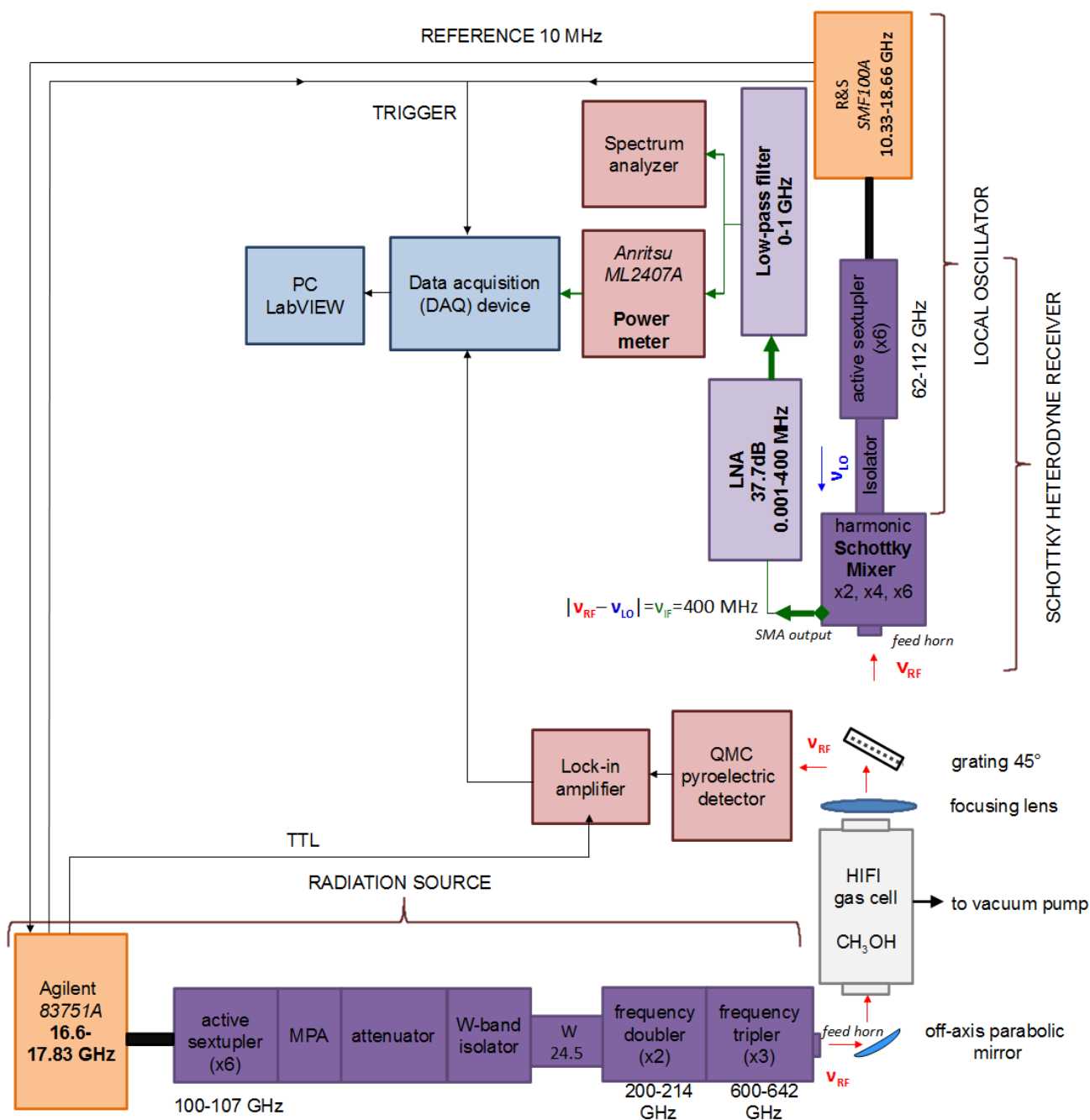
Figure 4.8 – Experimental set-up in LERMA for the preliminary tests of a 600 GHz SHR prototype, coupled with the HIFI gas cell.

and displayed at oscilloscope. The experimental set-up has been properly aligned. The optical and mechanical adjustment between RPG chain, off-axis parabolic mirror, HIFI gas cell, focusing lens, and a QMC pyroelectric detector has been performed to obtain the maximum output signal.

After the alignment have been done with QMC detector, the further attention was given only to the second configuration of a set-up. i. e. the one with SHR. 45-degree
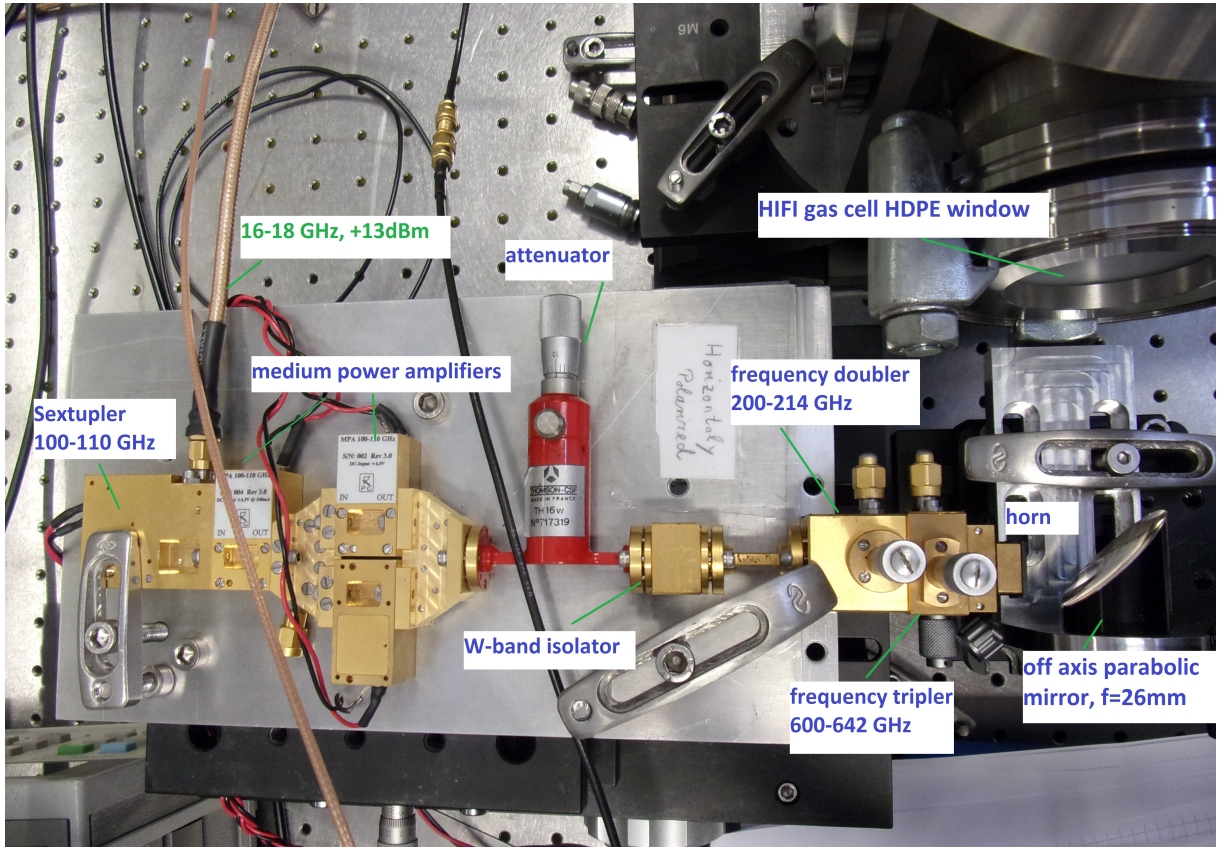
Figure 4.9 – Custom system of amplifier-multiplier chains (AMCs), used as components of radiation source (600–642 GHz) for a set-up at Fig. 4.8.

grating was removed, and Agilent 83751A was no longer modulated. A prototype of a 600 GHz SHR for JUICE, employed in the current set-up configuration, is shown at Fig. 4.10. It is composed of the Rohde & Schwarz SMF100A MW frequency synthesizer, operating in a 10.33-18.66 GHz frequency range that drives the LO - an active sextupler (x6, 62-112 GHz). Schottky mixer operates at even (2nd, 4th, 6th) harmonics of the LO output. R&S SMF100A also provides the 10 MHz frequency reference for the Agilent 83751A. The IF signal at ν_{IF}=400 MHz was amplified by LNA by a gain of $\approx$ 37 dB. The low-pass filter with a band of 0.001-1 GHz was mounted after. The detected IF signal was measured by an Anritsu ML2407A power meter. The IF amplitude was displayed as well at spectrum analyzer.

The MW frequency synthesizers, Agilent 83751A and Rohde & Schwarz SMF100A, used to drive radiation source (RPG chain) and the LO of a SHR, respectively, were swept at the same time, but with a frequency offset of the ν_{IF}=400 MHz. Their sweeps were synchronized by the auxiliary interface. The swept frequency values of the LO of a Schottky heterodyne receiver and AMCs radiation source were stored as x-data. The detected IF signal was converted to a digital value by use of the Anritsu MA2470A diode
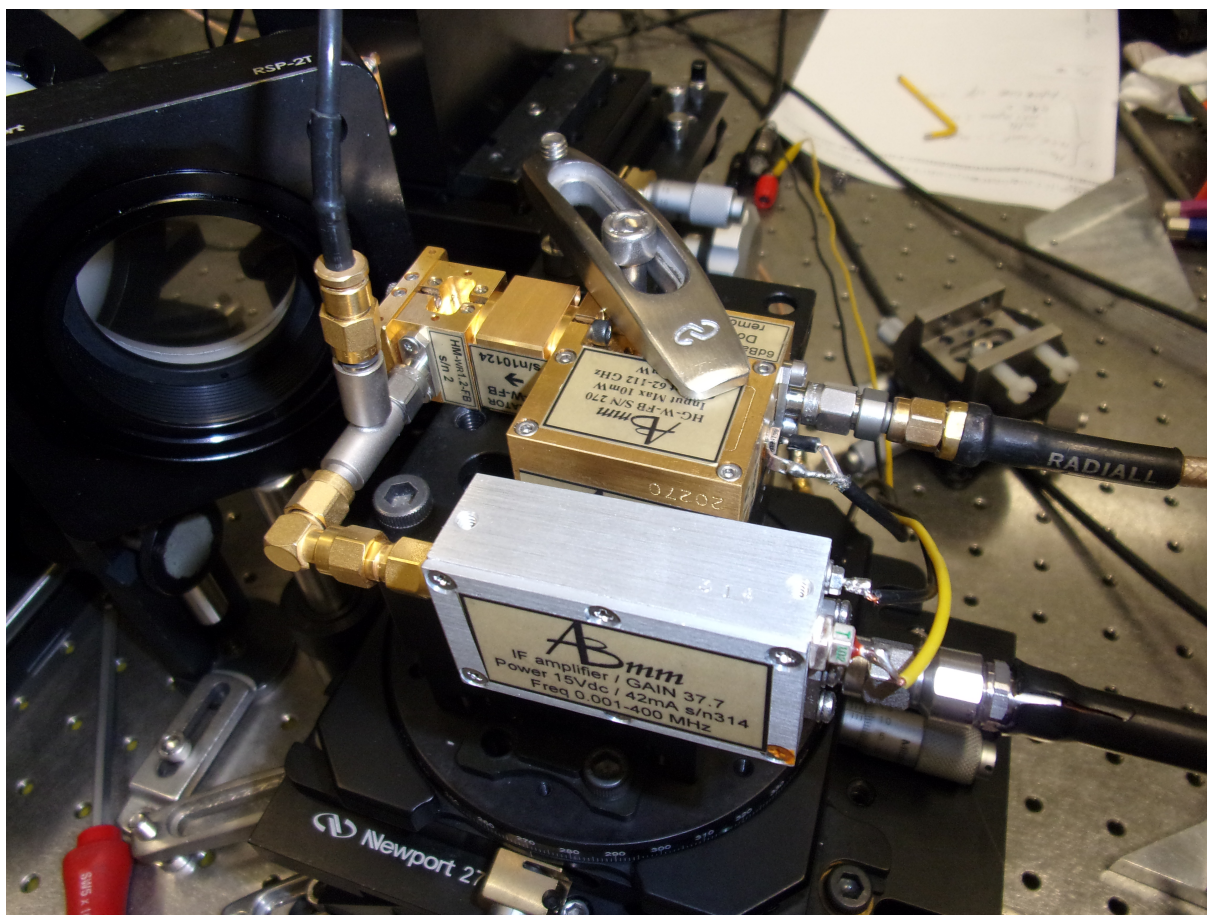
Figure 4.10 – A prototype of a SHR, used for the tests with a set-up at Fig. 4.8.

power sensor, and recorded as y-data. The recorded (x,y) pairs of data corresponding to frequency value and IF amplitude were further acquired by DAQ and processed with the computer (Labview program). The control of frequency synthesizers was also carried out by LabView software.

To test the performance of a 600 GHz Schotky heterodyne receiver for its possible application to molecular spectroscopy, two lines of methanol CH_3OH in 600 GHz frequency range, listed at Table 4.2, were chosen for the preliminary tests. Data for transitions of CH_3OH were taken from the JPL spectroscopic Catalog (https://spec.jpl.nasa.gov/) [112, 113]. CH_3OH is a typical example of a complex asymmetric top molecule. The choice of CH_3OH was made because of its well-studied rotational-torsional spectra [114] in the 600 GHz frequency range of interest, its availability and ease of use. Later on, if the spectroscopic tests on the strong methanol lines are successful, a 600 GHz SHR's prototype can be applied to the high-resolution studies of other molecules, including those of astrophysical interest.

The measurements in LERMA were performed in a simple and straightforward manner. Again, neither measurement procedure or experimental set-up for the current tests

Table 4.2 – Transition frequencies, intensities and quantum numbers of methanol absorption lines, CH$_3$OH from JPL Catalog, used for the test performance of a SHR in LERMA.

FREQ [a]	LGINT [b]	QN′ [c]	QN″ [d]
601849.079	-3.2726	13 1 0	12 2 0
602233.093	-3.1062	9 1 0	8 0 0

Notes. [a]Frequency of the line in MHz. [b]Base 10 logarithm of the integrated intensity in units of nm^2 MHz at 300 K. [c] Quantum numbers for the upper state. [d]Quantum numbers for the lower state.
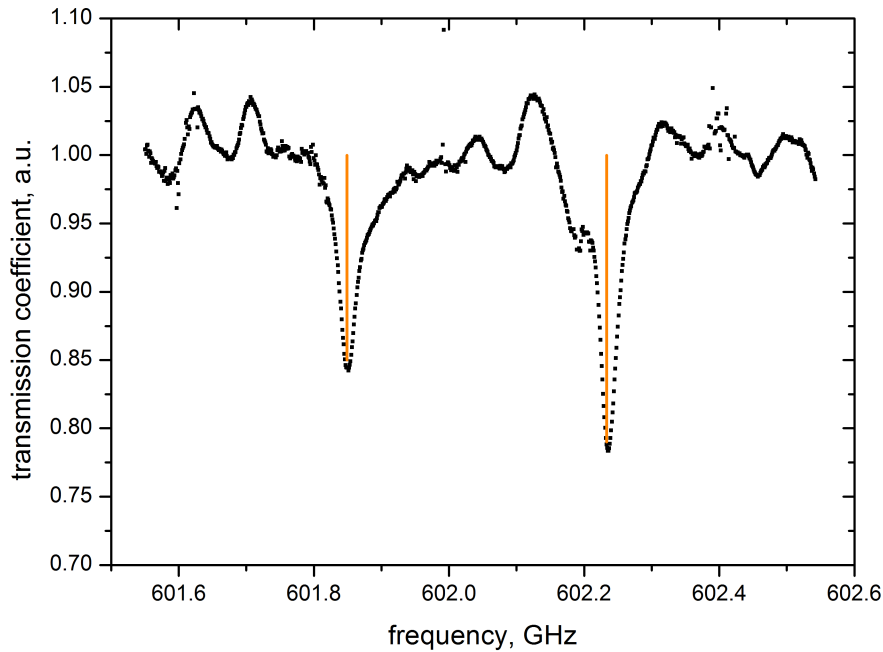
Figure 4.11 – CH$_3$OH normalized representative spectra, taken with the H polarization between 601.5 to 602.6 GHz in steps of 1 MHz at an average gas cell pressure of 32 μbar. CH$_3$OH transition frequencies from JPL catalogue are shown as orange sticks to demonstrate the correspondence of the frequency predictions.

didn't fully use the techniques usually applied for the high-resolution molecular spectroscopy (most importantly, frequency modulation of a radiation source with subsequent lock-in detection), but the experimental set-up, built here, consists of the identical components, as of those employed in absorption spectrometers: radiation source, absorption cell filled with a gas, and a detection system.

The radiation source (Agilent 83751A frequency synthesizer with the RPG AMC) was swept between 601.8 and 602.03 GHz with a frequency step of 1 MHz (as well as R&S SMF100A with the LO of Schottky receiver, but with an off-set of 400 MHz), where methanol lines, listed at Table 4.2, should normally appear. At first, the frequency scan
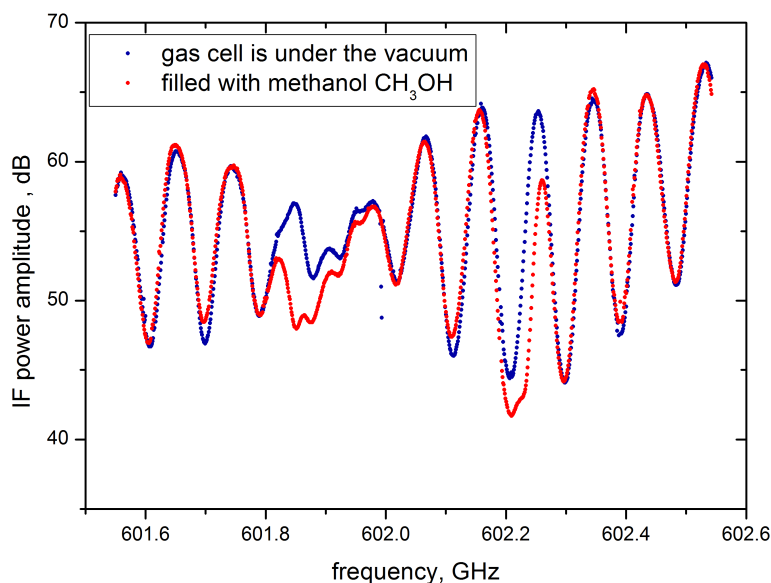
Figure 4.12 – Two plots represent IF signal amplitude taken through a filled with CH_3OH (in red) and an empty cell (in blue) while frequency sweeping.

was made without CH_3OH in a gas cell, i.e. under a vacuum, to obtain a 'baseline', that in general is a complex function: it represents variations of power of the radiation source with a frequency, the transfer function of a gas cell (for example, variation of the transmission coefficient with a frequency of the materials, used for the gas cell windows etc.), different frequency response of the detector system (Schottky mixer inconstant conversion loss, LO power instability, variations in IF amplifier gain etc.). Then a frequency scan, at the same experimental conditions, was performed again, but with a methanol in the gas cell, and the variation of IF signal power versus frequency was recorded. Then the fraction between the two data sets in IF power, obtained with and without the methanol in a gas cell, a transmission coefficient, was calculated. The corresponding plot is given at Fig. 4.11. It represents a CH_3OH spectra, taken in absorption with LERMA 600GHz SHR; CH_3OH transition frequencies from JPL catalog are inserted as lines for visual comparison. The value of transmission coefficients of two [strong] observed CH_3OH lines is remarkably good considering the fact that both corresponds to the relative intensities of CH_3OH from Table 4.2, as well as experimental transition frequencies match those from JPL catalog. Precise values of central frequencies of a recorded molecular spectral lines with SHR will be calculated in the next Section, since here the main goal was to observe molecular lines and to obtain preliminary accordance with those from spectroscopic catalogue.

Example of transmission measurements, performed with SHR in LERMA through HIFI gas cell at 600 GHz frequency range, is also presented in Fig. 4.12. Plot give the

variation of IF signal amplitude during the frequency scan. Two data sets were taken when radiation passes through an empty gas cell, i.e. under the vacuum (in blue) and when the cell is filled with CH_3OH (in red). As can be seen from the plot, since frequency modulation (with a subsequent lock-in detection) technique has not been applied, the presence of standing waves, and given the current level of high-resolution laboratory molecular [absorption] spectroscopy, the spectra we recorded is likely of a representative character.

However, even despite the fact that the current experimental set-up, built in LERMA cannot compete with high resolution and sensitive laboratory instruments - spectrometers, it allowed to *"spectroscopical"* test a prototype of a 600 GHz SHR, developed for a space mission JUICE, and to obtain first molecular spectra in laboratory with such kind state-of-the-art instrument.

4.7 Tests of Lille fast-scan DDS spectrometer with 600 GHz SHR

4.7.1 Configuration of a 600 GHz SHR

A series of spectroscopic measurements, even in a small frequency range of 1 GHz, presented in Sec. 4.6, have been successfully preliminarily performed in LERMA on methanol CH_3OH to test 600 GHz SHR prototype capability to observe [absorption] molecular lines in 600 GHz frequency range. Therefore the prototypes of 600 GHz SHRs can now be further applied for high-resolution molecular spectroscopy, and in particular in PhLAM with FSS.

The schematic block diagram of a 600 GHz SHR, tested with FSS is shown at Fig. 4.13 and its photo picture is presented at Fig. 4.14.

1 Local Oscillator (LO)

The LO chain of a 600 GHz Schottky receiver is entirely based on waveguide solid-state components. Basics of a waveguide technique were discussed earlier in Sec. 1.5.2. The LO chain to assemble a SHR consists of MW frequency synthesizer and frequency amplifier multiplier chains (AMCs), specially designed and fabricated, or, depending on a particular component, purchased from commercial suppliers. General design and operation principle of AMCs was introduced previously in details in Chapter 1.

The LO chain of a 600 GHz Schottky receiver is composed of commercially available Agilent 83711B microwave frequency synthesizer, referenced to a 10 MHz (Rb), followed by an active sextupler from RPG [12] and a cascade of two successive frequency doublers from RPG and LERMA, respectively. Agilent 83711B operates in a frequency range of

---

[12]Radiometer Physics GmbH
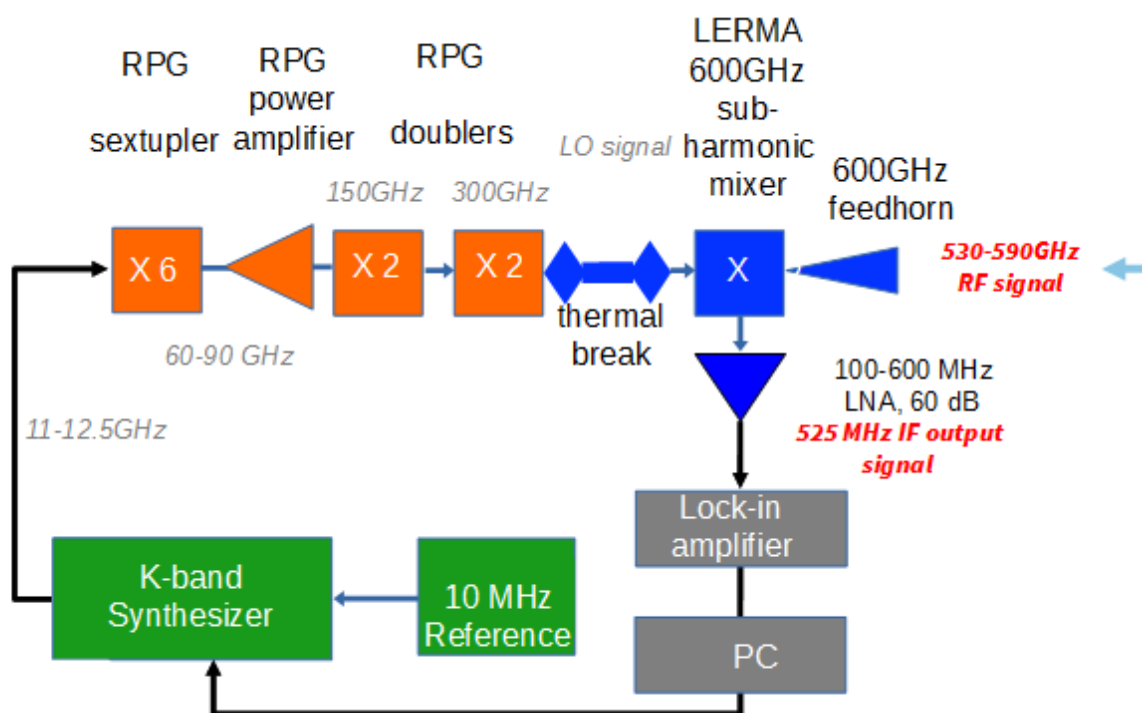
Figure 4.13 – Schematic block diagram of a prototype of a 600 GHz SHR for JUICE [84], tested with FSS (up to now configuration is not final).
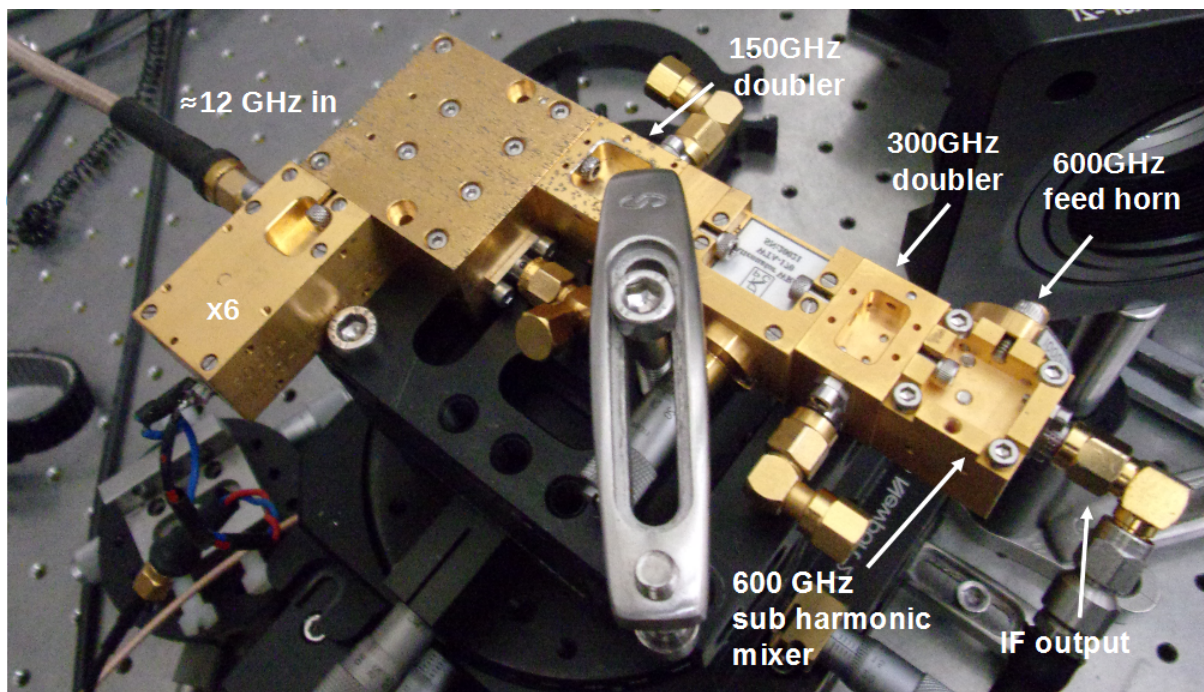
Figure 4.14 – 600 GHz SHR prototype, used for the tests with FSS. Some of the LO components will be replaced soon for the final tests.

about 11-12.5 GHz (K-band), this signal is multiplied by 6 and amplified by a gain of 10dB with an active sextupler, that is a frequency multiplier (x6) + medium power amplifier, and will be in the 66-75 GHz frequency range, then it is fed to a cascade of two frequency doublers (x2x2), that allow to reach consistently 132-150 and 264–300 GHz frequency range. At the output of a 150 GHz doubler a power of approximately 26 mW is provided. The maximum LO power output is approximately 7-8 mW. The LO chain performs a frequency multiplication by 24 (x6x2x2). An isolator is placed after the 150 GHz doubler that allow the radiation power to pass in one direction only. It is also prevents power reflections that arise in one part of the receiver from affecting its other parts. Tunable attenuator with attenuation range 0-40 dB is placed after isolator, that can be used to reduce the amplitude of an input signal that is fed to a 300 GHz doubler.

Sextupler (full band WR.12, 60-90 GHz, output power +6dBm), medium power amplifier (100-130 GHz, Gain 10dB), tunable attenuator (WR6.5, 110-170 GHz), isolator (>20 dBm), and 130–154 GHz frequency doubler (WR 6.5, output power +17 dBm) modules were developped or purchased from RPG. The stage of 300 GHz frequency doubler was designed and fabricated at LERMA-LPN [110]. The data sheets on these components can be found in App. B.

2 Sub-Harmonic Mixer (SHM)

The mixer down-converts the RF signal to IF. (Theory of the mixers operation were given in Sec. 4.3.2). The mixer for a 600 GHz SHR operates at the 2nd harmonic of the LO output, means it is subharmonically pumped by the LO. The RF signal is coupled to a mixer with a feed horn. Waveguide of a mixer has a output with SMA [13] coaxial connector, that is suitable for use from DC to 18 GHz.

3 IF chain

The down-converted IF signal, coming out from the mixer output, at ν_{IF}=525 MHz was amplified by low-noise amplifier (LNA, 100 to 600 MHz, by a gain of 60 dB). A band-pass filter (with a passband of 525±40 MHz), was mounted after. For the detection of the IF signal, HP Schottky power diode detector (0.01-33 GHz) was used; the IF amplitude was also displayed at spectrum analyzer. Due to the delay in the equipment delivery, the 600 GHz SHR, tested with Lille spectrometer, was not in the optimal configuration: LO chain for the receiver was not specially designed for the current prototype; the IF chain was assembled from the available elements at time in a laboratory, amplifier and filter were ≈ 20 y.o. IF amplifier we used was that for the phase-lock loop from BWO and low pass

---

[13]SubMiniature version A

band filter was of unknown manufacturer. For the future (final) tests, some of the part of the LO chain will be replaced and for the IF chain the modern elements with superior characteristics will be purchased.

4.7.2 Experimental set-up of Lille spectrometer

Experimental set-up for the tests of a 600 GHz SHR with FSS molecular spectroscopy is given at Fig. 4.15 and its front-end is illustrated in Fig.4.16. The Lille spectrometer configuration for the tests with SHR, performed here, in general was similar to those for the standard operation, described in the Chap.2, with the detection system replaced by 600 GHz SHR, described in Sec. 4.7.1 and presented at Fig. 4.13 and 4.14.
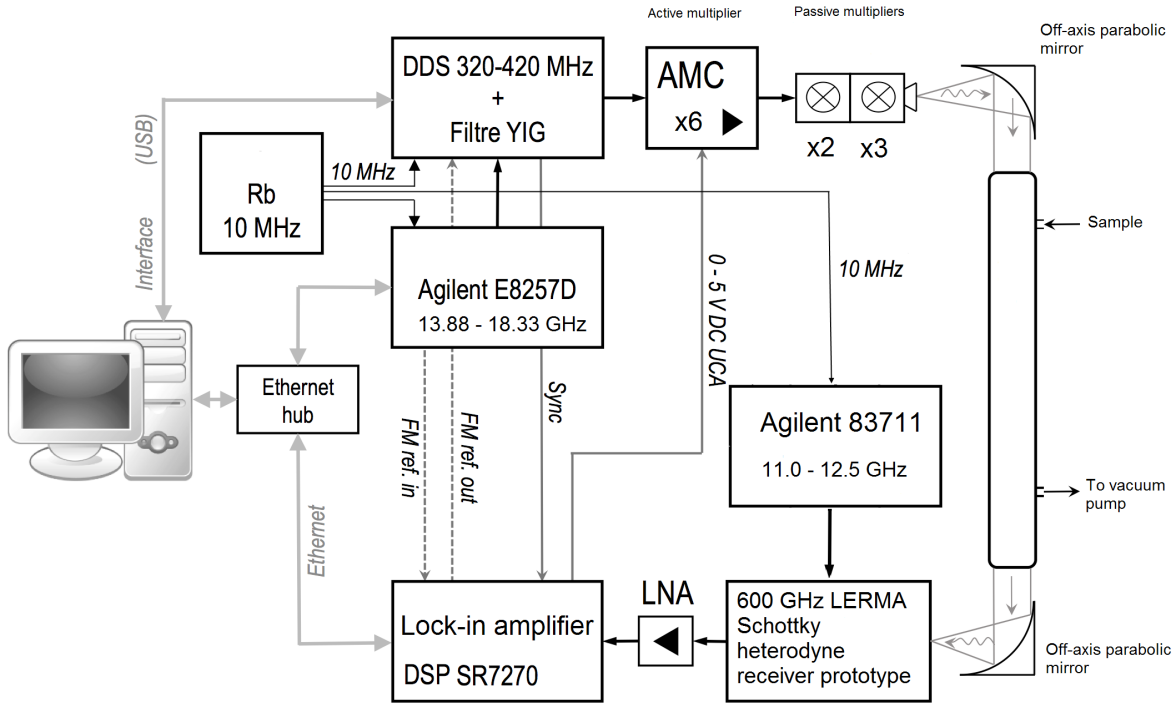
Figure 4.15 – Experimental schema of Lille non-cryogenic fast scan heterodyne spectrometer in PhLAM, fully built on solid state devices (test configuration).

The prototype of the 600 GHz LERMA SHR, employed in the current set-up, covers the 530-590 GHz frequency range. Radiation source of a spectrometer in the curent configuration covers the 500-660 GHz range. The chain performs a frequency multiplication in total by 36 (x6x2x3). More detailed operation principle of AMCs and Lille spectrometer can be found, respectively, in Chapter 1 and 2.

All the components of spectrometer set-up were properly aligned. Multiplier chain, gas cell and SHR were adjusted mechanically to each other in height. Water level ruler was also used to re-check if the optical table level is right. Components of a spectrometer:
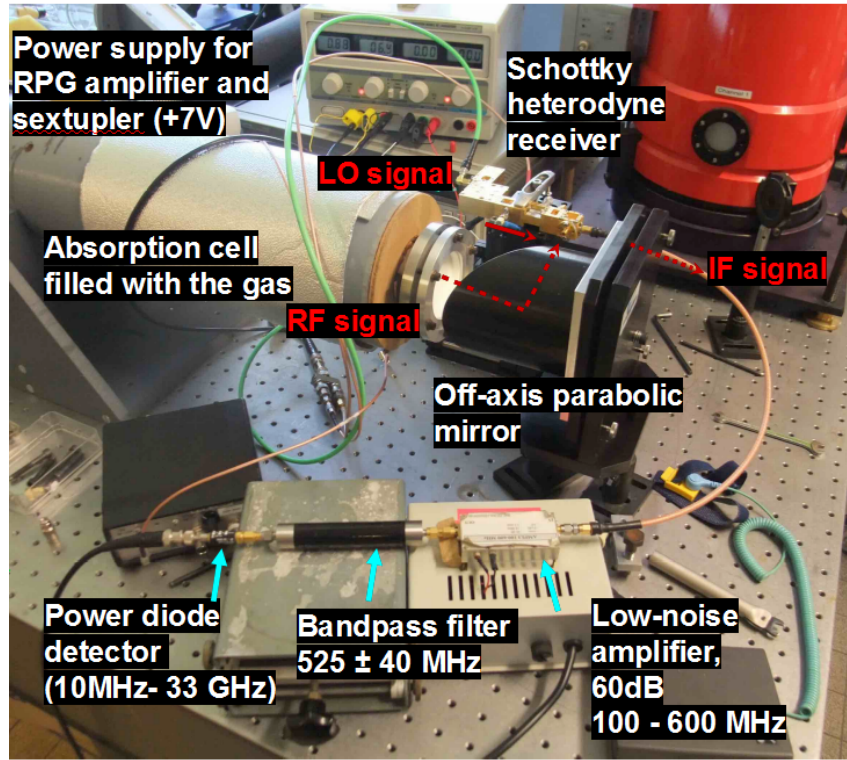
Figure 4.16 – Front-end of Lille fast scan heterodyne spectrometer in PhLAM (test configuration).

feed horns of multiplier chain and Schottky receiver, input/output windows of gas cell were approximately aligned to be on the same axis (in the center). The focusing system consisted of two off-axis parabolic mirrors, one placed after the feed horn of the multiplier chain to guide the radiation in a gas cell and the second one - to feed the RF signal to Schottky receiver, and then couple it to a mixer with the signal, produced by a LO chain. After the spectrometer was set up, the alignment of each component was repeated to obtain maximum IF signal.

4.8 Measurements of CH$_3$CH$_2$CN absorption spectra

For the spectroscopic studies with Lille fast scan heterodyne spectrometer, we took ethyl cyanide, CH$_3$CH$_2$CN, complex organic molecule, abundunt in the ISM, which is well studied in a laboratory up to THz range (for example [115]).

The molecular spectra, to be presented here, was recorded with 600 GHz SHR. The radiation source was frequency modulated with f_{mod}=30.5 kHz and f_{dev}=15.0x36=540 kHz. The sweep was made between 530 and 590 GHz with a frequency step of 81 kHz. 60 GHz spectra was recorded in 52 min. Examples of CH$_3$CH$_2$CN spectra, recorded with FSS and 600 GHz SHR, are given at Fig. 4.17a. CH$_3$CH$_2$CN produces quite dense and reach spectrum. R branches (ΔJ=+1) can be clearly observed. Fig. 4.17b shows
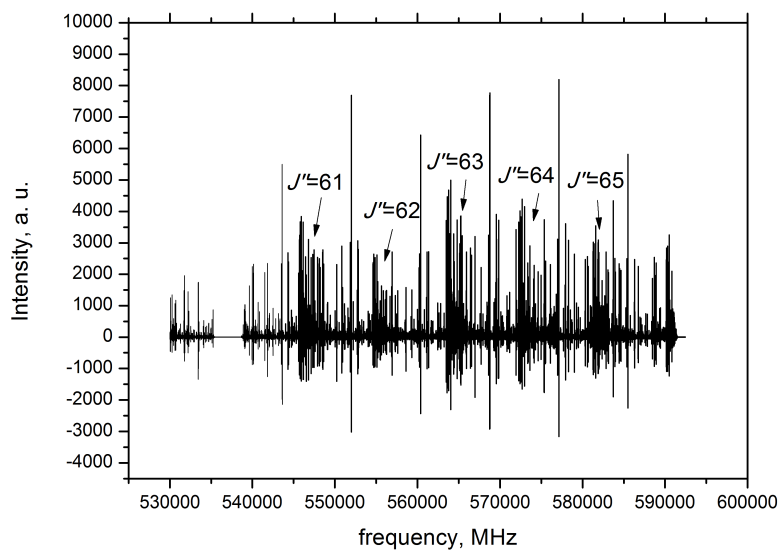
(a)
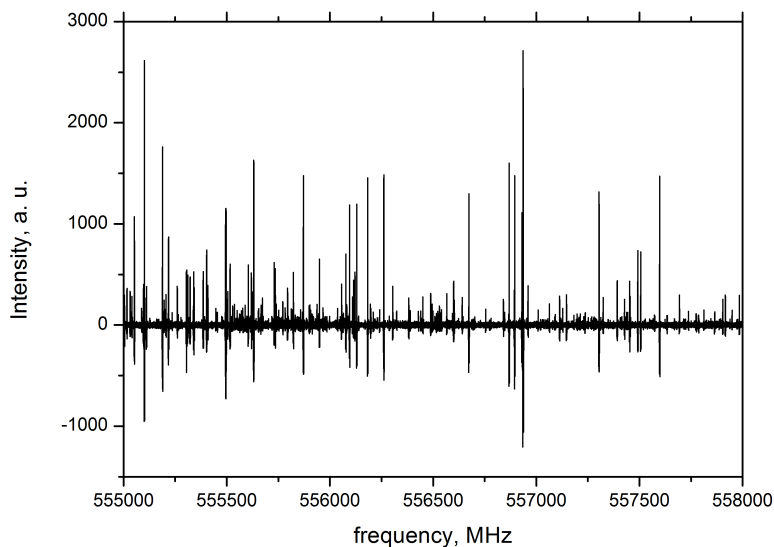
(b)

Figure 4.17 – Spectra of ethyl cyanide, CH_3CH_2CN, recorded with FSS and 600 GHz SHR between 530 and 593 GHz (a) and in a detailed range between 555 and 558 GHz (b).

spectra of CH_3CH_2CN in the detailed 555-558 GHz frequency range. Some of the observed transitions are indicated in Fig. 4.18 along with the prediction transitions from JPL catalog. As seen, experimental spectra and predictions from JPL catalogue are in good agreement.

86
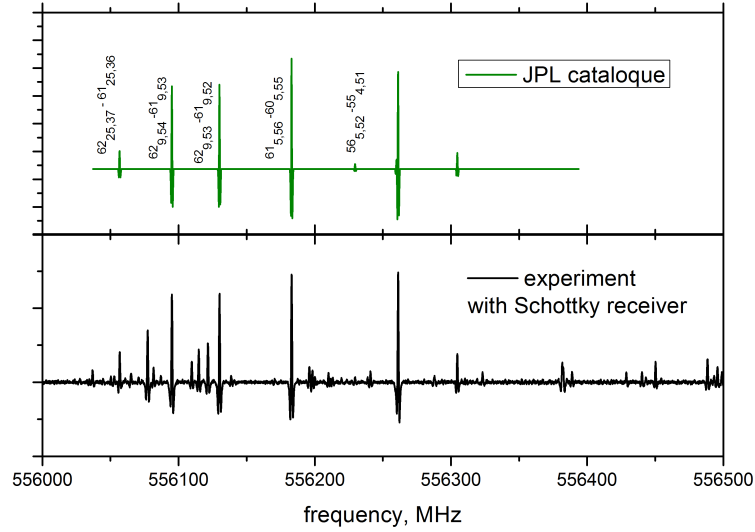
Figure 4.18 – Observed transitions are given along with those from JPL cataloque.

4.9 Sensitivity of 600 GHz SHR for the absorption spectroscopy with FSS

Here we will calculate and discuss sensitivity, achieved experimentally with FSS with SHR in a 600 GHz frequency range. Qualitative comparison of signal-to-noise ratios (SNR) of molecular lines, recorded with SHR and QMC bolometer, will be also presented.

4.9.1 Noise Theory Background for the Absorption Spectroscopy

A good discussion on spectroscopic detection and fundamental limits of absorption spectrometers is given in [116], some of its considerations will be applied to analysis here.

Absorption spectroscopy deals with a detection of small change of power $[P(\nu)/P_0]$ of a large signal [emitted by a radiation source, P_0] (Eq.1.1) due to absorption in a presence of some molecule [with absorption coefficient, α] in a gas cell. The signal to be detected consists of a small variation in the source power. Usually it is easy to detect *this* power level and compare it to the noise floor (that of the detector and radiation source, in the absence of molecule, i.e. when the gas cell is under the vacuum) and to determine a signal-to-noise ratio (SNR) of a molecular line.

The sensitivity limitations for [microwave] absorption spectrometers were first discussed by [117]. When a radiation source emits rather high power, the theoretical minimum for detectable change in power, i.e. the smallest detectable signal P_{min}, is proportional to the square root of the *receiver noise temperature, T* and the *power, received by a detector*:

$$P_{min} = 2\sqrt{k_B T \Delta\nu P_{rx}} \tag{4.1}$$

where k_B is Boltzmann's constant, T is the receiver's noise temperature in the absence of signal power (that is dependent on the frequency), $\Delta\nu$ is the detection bandwidth and P_{rx} is the received signal power. Eq. 4.1 is valid in a Rayleigh-Jeans limit, i.e. when $h\nu << k_B T$. The Rayleigh–Jeans law agrees at frequencies, up to sub-millimeter (~ 6 THz for T=300 K). From Eq. 4.1 it follows that the sensitivity of heterodyne receiver for absorption spectroscopy is proportional to the square root of the radiation source power P_{rx}. This term is often not taken into account when discussing the sensitivity of absorption spectrometers. However, the fundamental spectroscopic sensitivity limit is determined by the signal power, multiplied by receiver's noise temperature, $P_{rx} \cdot T$. Receiver noise temperature and noise sources in a heterodyne receiver were discussed in Sec. 4.4. The derivation Eq.4.1 is based on the Rician probability distribution of signal detection as described by Levanon in the context of radar detection [118]

We can determine signal-to-noise-ratio (SNR), achieved with a spectrometer as:

$$SNR = \frac{P_{rx}}{P_{min}} \tag{4.2}$$

Practical example: If we apply a 600 GHz Schottky receiver prototype for JUICE that has noise temperature T of ~ 1250 K in 530-590 GHz frequency range as seen from plot at Fig. 4.6, and given that at 500-660 GHz frequency range radiation source emits power of P_{rx} of $\sim 30~\mu$ W, provided by VDI (as summarized in Table 2.1). In a bandwidth of 1 kHz (typical time measurement with lock-in amplifier is 1 ms, results in detection bandwidth of 1 kHz), FSS will be able to detect a minimum detectable signal of $P_{min} \approx 5 \cdot 10^{-11}$ W, and achieve a SNR $= \frac{P_{rx}}{P_{min}}$ of $\approx 6 \cdot 10^5$.

SNR value in Eq. 4.2 can be easily re-calculated for different values of P_{rx}. Since we know the powers, emitted by the radiation sources of FSS (Output powers are provided by VDI in Table 2.1), we can estimate P_{min} and SNR for a given frequency range

The minimum detectable absorption in [absorption] spectroscopy is given by the following equation:

$$P_{min} = P_{rx}(1 - \exp^{-\alpha_{min}L})$$

where α_{min} is the minimum detectable gas absorption in cm^{-1} and L is the length of the absorption cell in cm.

For the small absorptions we can write

$$P_{min} \approx P_{rx} \alpha_{min} L$$

Minimum detectable absorption coefficient α_{min}, that could be (theoretically) measured is equal to

$$\alpha_{min} = \frac{P_{min}}{P_{rx} L} = \frac{1}{SNR \cdot L}$$

in a 2 m (200 cm) length absorption gas cell and theoretically achieved SNR of $\approx 6 \cdot$ 10^5 with 600 GHz SHR, calculated above, α_{min}, that could be theoretically measured with FSS, is of $\sim 1 \cdot 10^{-8}$ cm^{-1}.

The ultimate sensitivity of FSS with 600 GHz SHR for JUICE, estimated here, is α_{min} = $1 \cdot 10^{-8}$ cm^{-1}. This value takes into account only the detector (receiver) characteristics. The experimental sensitivity of spectrometer depends on several other factors, including the performances of all elements that introduce noise (radiation source, lock-in amplifier, data acquisition system). That's why we will not achieve the same level of sensitivity; the experimental sensitivity of Lille spectrometer with 600 GHz SHR for JUICE will be estimated on an example of CH_3CH_2CN molecule in Section 4.9.3. In the next section, we will try to compare theoretically sensitivity of SHR and 4 K QMC bolometer.

4.9.2 Comparing heterodyne and incoherent detector sensitivity

All radiation detection systems in THz range can be divided into two groups: incoherent detection systems (direct detection), which allow only signal amplitude detection and which, as a rule, are broadband detection systems such as bolometers or zero bias Schottky diodes (both were introduced in Chapter 1), and coherent detection systems, heterodyne receivers, which allow detecting not only the amplitude, but also the phase of a signal.

Direct detectors are preferably used in those applications where sensitivity is more important than the spectral resolution. Among the direct detectors, low−temperature bolometers currently offer the highest sensitivity at sub-millimiter wavelengths, providing background limited performance. The sensitivity of a bolometer is usually specified in terms of its noise equivalent power, NEP.

We will now compare the sensitivity of a bolometer with that of a heterodyne receiver operating at the same frequency in terms of signal to noise ratios. The signal to noise ratio obtained by the bolometer [119] is given by

$$SNR_B = \frac{P \Delta t^{1/2}}{NEP}, \tag{4.3}$$

where P is the signal power received through a submillimeter bandwidth, B_B, defined

by the band-pass filter and Δt is the integration time and NEP is bolometer noise equivalent power (W Hz$^{-1/2}$). Assuming that the radiation source temperature, T_S, is high enough for the Rayleigh-Jeans limit to apply, the signal input power may be written as

$$P = mk_B T_S B_B \tag{4.4}$$

where

m=1 or 2, depending on whether single or dual polarization detection

B_B=predetection bolometer bandwidth (Hz)

Substituting Eq. 4.4 in Eq. 4.3 gives the expression for bolometer signal-to-noise ratio (SNR_B)

$$SNR_B = \frac{mk_B T_S B_B (\Delta t)^{1/2}}{NEP} \tag{4.5}$$

The signal-to noise ratio for heterodyne receiver (SNR_H) would be [120]

$$SNR_H = \frac{T_S}{\Delta T_{min}} = \frac{T_S (B_H \Delta \tau)^{1/2}}{T_{sys}} \tag{4.6}$$

where T_{sys} is the noise temperature of the receiver and B_H is the detection bandwidth.

Assuming that we observe the same source and integrate over the same time period, taking the ratio of Eq. 4.6 and 4.5, yields [121]

$$\frac{SNR_H}{SNR_B} = \frac{NEP(B_H)^{1/2}}{mk_B B_B T_{sys}} \tag{4.7}$$

Suppose we have two systems, bolometer and heterodyne receiver, operating in a 600 GHz frequency range. 4 K InSb HEB has a typical value of NEP=10^{-12} W Hz$^{-1/2}$, according to QMC Ltd., and an input bandwidth B_B=1500 GHz. A prototype of 600 GHz SHR, investigated in a current work has a noise temperature, T_{sys} of $\sim$ 1250 K at a room temperature (Fig. 4.6) and a bandwidth of about 1 GHz. Substitutions of these values into Eq. 4.7 shows that 4K QMC bolometer with NEP=10^{-12} W Hz$^{-1/2}$ is more sensitive than SHR with $T_{sys} = 1250$ K by about a factor of 3 (if one polarization is detected, i.e. if m=1).

4.9.3 Sensitivity of FSS, achieved experimentally with SHR in 600 GHz frequency range

In order to estimate sensitivity of the spectrometer, we need to know absolute value of molecular line intensity (INT_{abs}). The predictions for CH$_3$CH$_2$CN can be taken from

spectral line catalogs, such as JPL or CDMS, where the units of line intensity are given in [$nm^2 \cdot MHz$], that are based on the integral of the absorption cross-section over the spectral line shape. For example, CDMS provides base 10 logarithms of the integrated intensity (LGINT) at 300 K, while the experiment gives the absolute intensity of a molecular line. The intensity of molecular line in nm^2 MHz is converted by exponentiation with base 10 the CDMS intensity with the formula:

$$INT_{abs} = 10^{LGINT},$$

Knowing the experimental value of absolute intensity INT_{abs} of a molecular line, one may calculate intensity LGINT, corresponding to CDMS intensity units, and vice versa. Example is given in Table 4.3.

Table 4.3 – Transition frequency, intensity and quantum numbers of ethyl cyanide (propionitrile), CH_3CH_2CN, line from the CDMS Catalog, are given along with those derived from the experiment.

FREQ [a]	LGINT [b]	QN′[c]	QN″[d]	FREQ$_{exp}$ [e]	INT$_{abs}$ [f]
552000.7373	-2.5380	64 1 64	64 0 64	552000.7191	2.897344 10^{-3}

Notes. [a]Frequency of the line in MHz. [b]Base 10 logarithm of the integrated intensity in units of nm^2 MHz at 300 K. [c] Quantum numbers for the upper state.[d]Quantum numbers for the lower state. [e] value from the fit. [f] Intensity in absolute units, $INT_{abs}=10^{LGINT}$

The sensitivity of the spectrometer can be estimated from the measurement of a weak line. For lines with known intensity $INT(T)$ [nm^2MHz] from the spectroscopic catalog (JPL, CDMS), at a temperature T (for 300 K), the peak absorption coefficient α_{max} [cm^{-1}] can be evaluated in the thermal Doppler limit at the same temperature T to be [122]

$$\alpha_{max}[cm^{-1}] = 151.194 \cdot \frac{INT(T) \cdot p}{\Delta\nu_D/2} \tag{4.8}$$

where p is the partial pressure of the molecule in $Torr$, $\Delta\nu_D$ is the Doppler full-width at half-maximum (FWHM) of the line in MHz.

To determine Doppler FWHM and transition frequency of molecular line, we need to fit it with suitable line profile. Home made software, developed in Lille, Spectrum Explorer[14], was used during the thesis to fit lines with Voight profile and analysis of spectra in general. A few weak lines, observed in 530-590 GHz frequency range, were found and the peak absorption coefficient α_{max} [cm^{-1}] was calculated with a Eq. 4.8. The values are summarized in Table 4.4.

---

[14]Spectrum Explorer 6.8 © Roman Motiyenko (PhLAM, USTL)
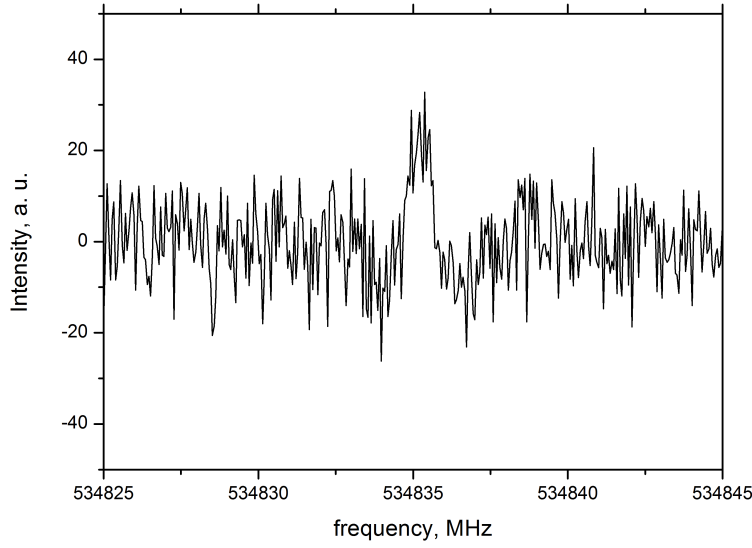
Figure 4.19 – The weak line of CH_3CH_2CN with SNR $\approx$ 2, measured with Lille fast-scan spectrometer and SHR in 600 GHz frequency range (with 81 kHz frequency step, 30.5 kHz frequency modulation and 540 kHz deviation). Acquisition time is 4 ms.

Table 4.4 – Estimation of sensitivity of FSS with SHR in a 600 GHz frequency range, using the molecular transitions of ethyl cyanide, CH_3CH_2CN at T=300 K and p=25 μbar (0.02 Torr)

ν_0 [MHz]	$LGINT$[nm^{2}MHz]	INT[nm^{2}MHz]	$\Delta\nu_D/2$ [MHz]	α_{max} [cm^{-1}]
534835.1834	-5.3886	4.09$\cdot 10^{-6}$	0.4393	2.82 $\cdot 10^{-5}$
550157.7558	-4.5745	2.66$\cdot 10^{-5}$	0.4519	1.79 $\cdot 10^{-4}$
553754.2563	-4.274	5.32$\cdot 10^{-5}$	0.4548	2.94 $\cdot 10^{-4}$
571290.5150	-4.5556	2.78$\cdot 10^{-5}$	0.4692	1.80 $\cdot 10^{-4}$
582708.0962	-3.6159	2.42$\cdot 10^{-4}$	0.4786	1.53 $\cdot 10^{-3}$
584097.4166	-3.8995	1.26$\cdot 10^{-4}$	0.4797	7.99 $\cdot 10^{-4}$

One of the weakest lines with SNR $\approx$ 2, measured with Lille spectrometer in 600 GHz frequency range with SHR was $84_{1,83} \leftarrow 84_{0,84}$ rotational transition of CH_3CH_2CN at 534835.1834 MHz, showed at Fig. 4.19 with $\alpha_{max} = 2.82\cdot10^{-5}$ cm^{-1} over an absorption path of 2 m.
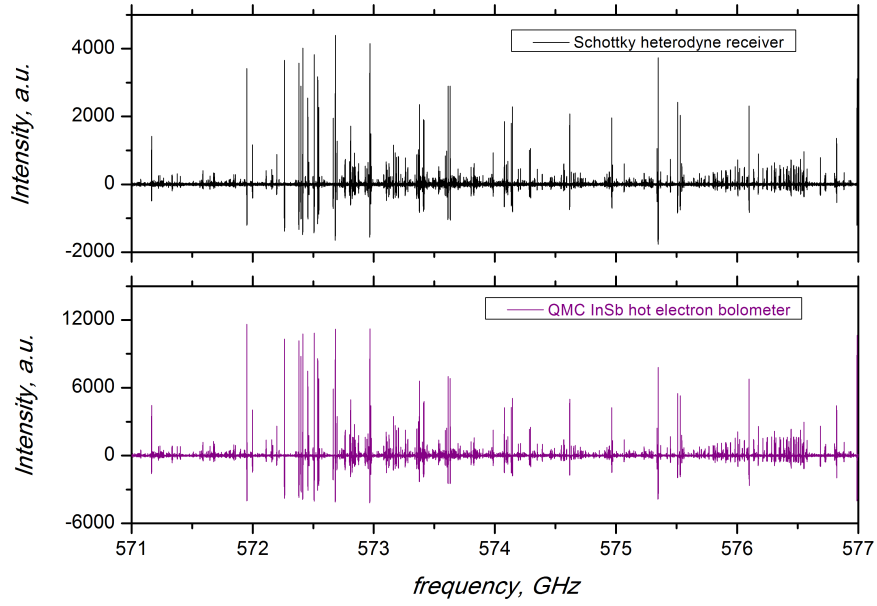
(a)
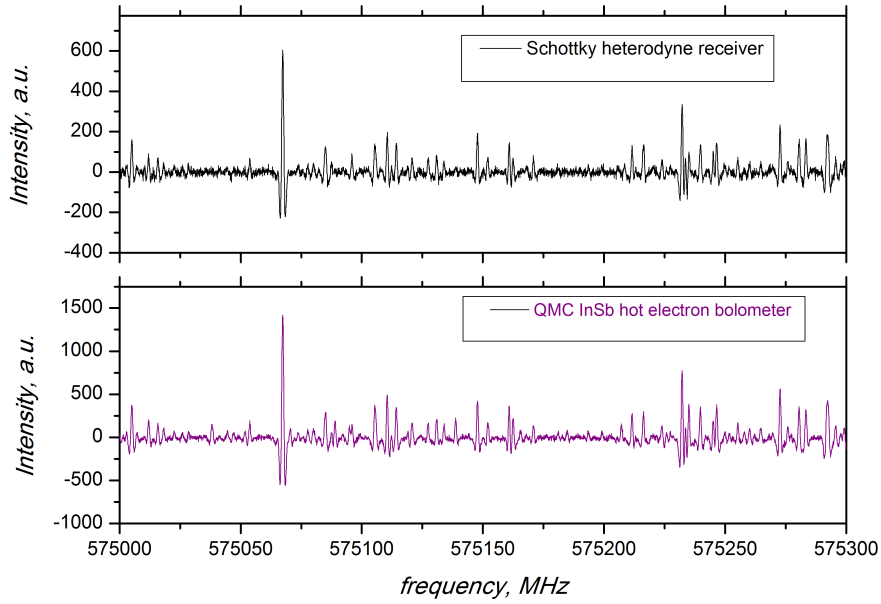
(b)

Figure 4.20 – Spectra of ethyle cyanide CH_3CH_2CN, recorded with Lille's fast scan spectrometer and [room temperature] SHR (in black) and [helium-cooled] QMC InSb bolometer (in purple) between 571 and 577 GHz (a) and in a detailed frequency range of 300 MHz (b) at the same experimental conditions.

4.9.4 Experimental comparison of sensitivities of SHR and QMC InSb HEB in terms of signal-to-noise ratio (SNR) of molecular lines, recorded with FSS in 600 GHz frequency range

The comparison of sensitivities of SHR and QMC INSb HEB, achieved with FSS in 600 GHz frequency range, will be presented here. The CH_3CH_2CN spectra were recorded with FSS over 530-590 GHz frequency range with QMC InSb HEB and SHR at the same experimental conditions: with a frequency step of 81 kHz, 30.5 kHz frequency modulation and 540 kHz deviation and acquisition time of 4 ms. Sensitivity of a spectrometer will be estimated in terms of signal-to-noise-ratio of the recorded molecular line.

In science and engineering, the signal-to-noise ratio, SNR, is a measure that compares the level of a desired (useful) signal to the level of background noise. Generally noise can be defined as the unwanted part of the signal, in our case it's the regions where no molecular features are observed. The SNR in the simple form can be defined as the ratio of signal power in the presence of molecular line to noise power.

$$SNR_{(mol.line)} = \frac{P_{signal}}{P_{noise}}$$

SNR is most often expressed in decibels (dB). When we perform measurements with Lille spectrometer, the signal, is recorded in [milli]volts. If we denote the signal level Vs when we observe molecular line, and the noise level Vn, then the signal-to-noise ratio of a molecular line, SNR, in decibels, can be given by:

$$SNR_{(mol.line)} \quad [dB] = 20\log(V_S/V_N)$$

If $V_s = V_n$, then SNR = 0. SNR of 2 (3 dB) is considered as the boundary between low and high SNRs, and in spectroscopy we use the same criteria for molecular lines.

Mathematically, SNR can be defined as the mean signal $\bar{S}$ in the presence of molecular line and the standard deviation of the noise σ_N where no molecular line is observed:

$$SNR_{(mol.line)} = \frac{\bar{S}}{\sigma_N}$$

As can be seen from Figs. 4.20, CH_3CH_2CN produces very rich and dense spectra. For the correct estimation of SNR, we need to find a well-isolated single molecular line, which was not easy given the molecule we choose for the tests. Regardless, a few suitable molecular lines as those shown at Fig. 4.21 were found. Obviously, CH_3CH_2CN spectra recorded with SHR, seems to be *"noisier"* than those recorded with QMC InSb HEB. To
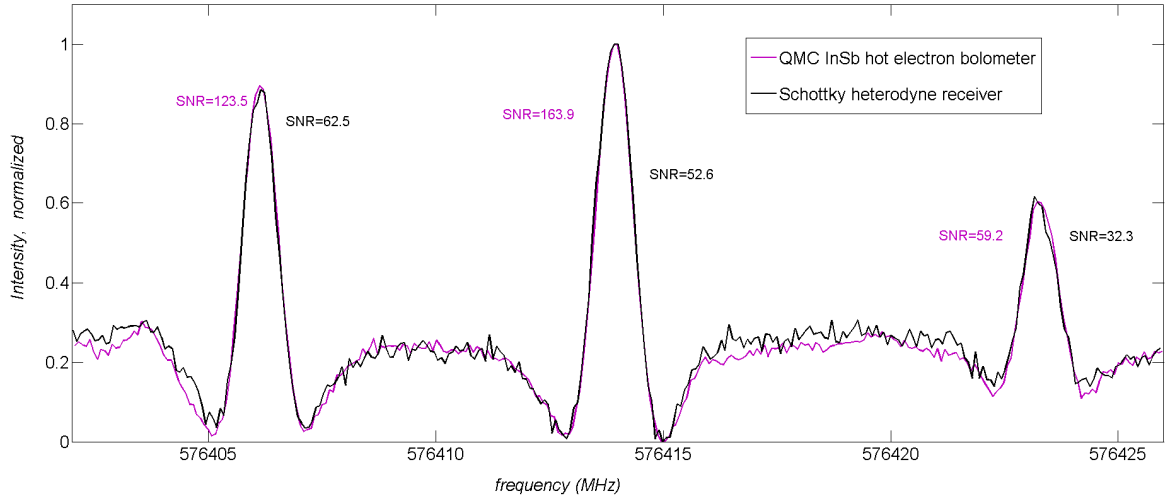
Figure 4.21 – Example of recorded modulated absorption lines of CH_3CH_2CN near 576 GHz a with a frequency step of 81 kHz, 30.5 kHz frequency modulation and 540 kHz deviation. Measurements with QMC InSb HEB are given in purple and SHR in black. Each scan shows 4 co-added 1 ms sweeps (acquisition time is 4 ms per data point). Calculated SNR for both detectors are indicated aside.

estimate mathematically the signal and noise levels of molecular lines we performed the following procedure. First, the intensity values of each and the same chosen molecular line (corresponding to data voltage acquired from the lock-in amplifier), recorded with SHR and QMC InSb HEB, were normalized to [0,1] as $Int_{norm} = (Int_{abs}-Int_{min})/(Int_{max}-Int_{min})$. The line then was fitted to a 8-Term Gaussian Model in MatLab (Fig. 4.24) to determine three parameters: central frequency ν_0, standart deviation of noise σ_N, and mean intensity of the line $\bar{S}$ (which we took as 1 for SNR calculation since the value doesn't really affect the precision of results, required for the objects of the current study). Gaussian model to fit peak of a molecular line is given by

$$y = \sum_{i=1}^{n} a_i e^{[-(\frac{x-b_i}{c_i})]}$$

where a is the amplitude (line intensity in our case), b is the centroid (location, i.e. frequency of a line), c is related to the peak width, n is the number of peaks to fit. The number of terms can vary from 1 to 8. Here we used a 8-term gaussian model since it describes reasonably well spectral lines.

For a 8-term gaussian model we need sufficient number of data points to make a curve fitting and to define accurately the peak. The regions to estimate the noise should be separated from the line peak and other molecular features that could be present close. The examples of 8-term gaussian fit of molecular lines performed with Matlab, with

95

corresponding residuals (that are experiment minus fitted values) are given in Figs. 4.24. These residuals represent noise. The standard deviation of noise σ_N (residuals) was also determined by Matlab and used for SNR calculations. A procedure were performed for a number of lines. The obtained parameters: ν_0, σ_N, determined from the fit, and calculated signal-to-noise ratios of molecular lines as $SNR=1/\sigma_N$, recorded with Lille spectrometer either with SHR or QMC InSb HEB are summarized in Table 4.6.
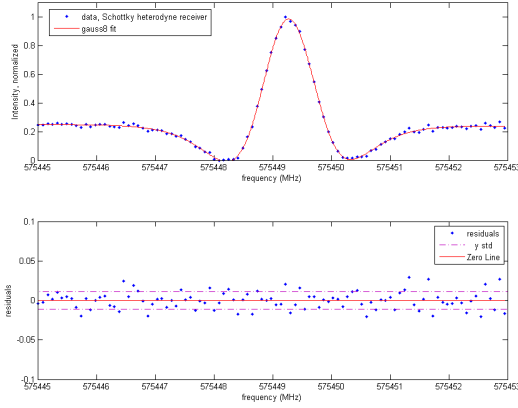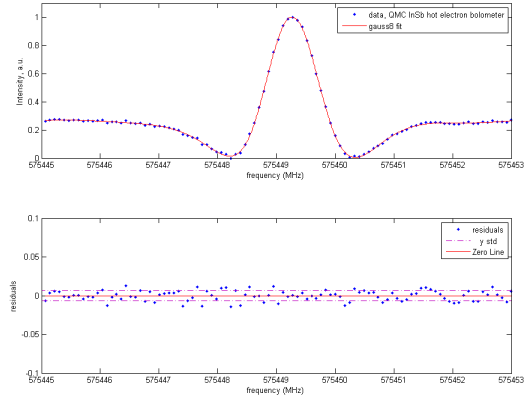
Figure 4.22 – (a)   Figure 4.23 – (b)

Figure 4.24 – Observed transition of CH_3CH_2CN, (frequency values are given in MHz), recorded with QMC InSb HEB (a) and SHR (b), are given with noise standard deviation (residuals of the fit).

Table 4.5 – Comparison of SNR of molecular line of CH_3CH_2CN from Fig.4.24, recorded with SHR and QMC InSb HEB.

	SHR	QMC InSb HEB
ν_0, MHz	575449.266	
σ_{Noise}	0.0110	0.0065
SNR	91	153
ratio	1.7	

SNR values for SHR are ranged from 50 to 150. We also calculated the ratios between SNR of the same molecular line, recorded with SHR and QMC InSb HEB (the right column). One of the reasons the ratio in SNR values differs for different molecular lines is that sensitivity of SHR, as seen from 4.6 may vary with frequency, the same is explained in a case of QMC InSb HEB, its NEP is frequency dependent. However, the average value ≈ 1.9 indicated that SHR provides the same level of sensitivity as QMC InSb HEB, which was previously theoretically derived (by a factor of 3) in Sec. 4.9.2. The sensitivities, achieved experimentally with these two detectors in their configugations with

Table 4.6 – Estimation of SNR of molecular lines of ethyl cyanide, CH_3CH_2CN, recorded with FSS (at 300 K and 25 μbar), in its configuration with SHR and QMC InSb HEB.

	ν_0, MHz (from the fit)	σ_{Noise}	$SNR_{mol.line}$	ratio
SHR	575449.266	0.01106	90.91	1.7
QMC HEB	575449.266	0.00653	153.19	
SHR	576413.942	0.01861	53.74	1.4
QMC HEB	576413.942	0.0133	75.2	
SHR	579710.764	0.0140	71.43	1.8
QMC HEB	579710.764	0.0079	126.58	
SHR	580938.550	0.0073	136.99	2.0
QMC HEB	580938.564	0.0036	277.77	
SHR	581068.644	0.0067	149.25	2.2
QMC HEB	581068.750	0.0031	322.58	
SHR	582572.912	0.0154	64.94	1.5
QMC HEB	582572.888	0.0105	95.24	
SHR	588377.482	0.0121	82.65	2.6
QMC HEB	588377.522	0.0047	212.77	

Lille spectrometer in 600 GHz frequency range, are of the same order in terms of SNR. But SHR has an advantage of being compact and operated at room temperature. Employing developed SHR with FSS, we got rid of the need to use liquid helium as in the case with QMC HEB, but we kept the sensitivity and other spectrometer's parameters as frequency accuracy, frequency sweeping speed, at the same level.

4.10 Conclusions

The previous configuration of FSS in PhLAM required to use a cryogenic cooling of QMC InSb HEB by liquid helium above 400 GHz. InSb HEB operates up to 2.7 THz and is now used in almost all of spectroscopic groups to achieve the highest sensitivity. Room temperature VDI Zero bias Schottky diode detectors are available to configure spectrometers to achieve good sensitivity at frequencies up to 400 GHz. There are no currently commercially available sensitive non-cryogenic detectors [for laboratory molecular spectroscopy] that operate in a 600 GHz frequency range that can be purchased from suppliers and be employed in laboratory spectrometer to obtain sensitive spectroscopic data. That's why we [LERMA-LPN, PhLAM] have developed a sensitive, compact and non-cryogenic 600 GHz SHR, and tested it later with Lille spectrometer.

The development of *such receiver*, initially intended for the space -based mission JUICE, was possible due to the technological advances in solid state multiplier sources and fabrication in planar Schottky diode mixers that offer high sensitivity for frequencies up to 3 THz, and operate at room temperature. A 600 GHz non-cryogenic Schottky solid-

state heterodyne receiver, described here, is based on a 600 GHz sub-harmonic Schottky diode mixer, designed and fabricated at LERMA-LPN, pumped by amplifier multiplier chains, purchased from RPG.

After the preliminary tests in LERMA were performed, 600 GHz SHR was integrated with FSS in PhLAM. It is the first combination of a such compact non-cryogenic SHR and Lille fast-scan DDS spectrometer. The performance of a spectrometer was demonstrated by recording of the molecular spectra of CH_3CH_2CN. Sensitivity of the spectrometer in a 600 GHz frequency range was estimated from the measurement of weak CH_3CH_2CN lines, and in terms of signal-to-noise ratio, and compared to those achieved with QMC InSb HEB. Compact room-temperature 600 GHz SHR provides the same order of sensitivity and frequency accuracy for Lille spectrometer, as QMC InSb HEB, but, in comparison with QMC that required cryogenic cooling and was not very convenient to use. Developed 600 GHz SHR is a now a competitive alternative to QMC InSb HEB for the laboratory molecular spectroscopy.

Part II

Laboratory Molecular Spectroscopy

Chapter 5

Theoretical Background

5.1 Overview

The Part II of the thesis deals with the laboratory molecular spectroscopy, it will consist of two chapters. In the current work the rotational spectra of molecules of astrophysical interest, methoxyisocyanate CH_3ONCO and triple- ^{13}C isotopologue of ethyl cyanide, $^{13}CH_3^{13}CH_2^{13}CN$, have been recorded and highly accurate sets of spectroscopic constants of these two molecules have been obtained. The results of this analysis will be presented in the next chapter. In the following chapter, the theoretical background, needed for the analysis of the molecular spectra will be given. The fundamentals of quantum mechanics that are important for the spectroscopy will be briefly introduced.

The author of this thesis does not intend to describe all available theoretical methods of rotational spectroscopy. Only the key aspects of the theory that are essential for dealing with measured experimental data will be presented.

Description of theoretical methods used in rotational and rotation-vibration spectroscopy can be found in the excellent monograph of Gordy and Cook [123], as well as in the book of Papoušek and Aliev [124]. The books of Townes and Schawlow [125], and Kroto [126] are sources for further reading on theoretical spectroscopy.

5.2 Introduction

The study of molecular spectra starts with classical expressions of the quantum mechanics. In rotational spectroscopy we measure the energies of transitions between rotational states of molecules. The energy levels of a molecule are eigenvalues of Hamiltonian operators that can usually be expressed in terms of the operators of the angular moments. Then we accurately determine the molecular spectroscopic parameters by fitting the frequencies of molecular lines. A detailed knowledge of transition frequencies is thus essential for the

study of high-resolution molecular spectra.

5.3 Vibration-Rotation Hamiltonian

5.4 The molecular Hamiltonian

A quantum mechanical system, such as a molecule, is described by its Hamilton operator or Hamiltonian H. The quantised energy levels E of this system, from which transition frequencies can be derived, are obtained by solving the stationary Schrödinger equation:

$$H\psi = E\psi$$

The wave function ψ may be referred to as eigenfunction and the associated energies E as the eigenvalues.

The Hamiltonian H for a molecule, composed of atoms and electrons, is the sum of the quantum mechanical equivalent of the kinetic energy T, and the potential energy V:

$$H = T + V$$

5.4.1 Potential energy surface

In Born-Oppenheimer approximation it is assumed that vibrating nuclei move so slowly compared with electrons so the movements of electrons and nuclei can be separated, and Schrödinger's equation can be solved independently for nuclei and electrons. Here we will deal only with the 'nuclear' Hamiltonian, which consists of vibrational and rotational contributions and is called rotation-vibration Hamiltonian. The energy levels of the molecular rotation-vibration Hamiltonian are given by the eigenvalues of

$$H = T_n + V$$

where T_n is the kinetic energy of the nuclei and V the potential energy:

$$V = V_{nn} + E_e$$

where V_{nn} is sum of the energy of electrostatic nucleus -nucleus potential energy, and E_e is the eigenvalue of the electronic Hamiltonian, assuming that the nuclei are fixed ("frozen").

Each eigenvalue of V is a function of the nuclear coordinates that represents the

effective potential energy function for the motion of the nuclei in particular electronic state. A potential energy surface relate the energy of a molecule with its geometry (bond lengths, bond angles). For the most of the spectroscopic applications, if a molecule is near the equilibrium position, we can consider that it makes the harmonic movements of small amplitude. Then the analytical expansion of the potential energy around the equilibrium position can be expressed as

$$V(Q) = \frac{1}{2} \sum_k \lambda_k Q_k^2 + \frac{1}{6} \sum_k \Phi_{klm} Q_k Q_l Q_m + \frac{1}{24} \sum_k \Phi_{klmn} Q_k Q_l Q_m Q_n + ... \qquad (5.1)$$

where the minimun is taken as the energy zero, and λ_k, Φ_{klm}, Φ_{klmn}, ..., are respectively the quadratic, cubic, and quartic force constants; these terms are the potential energy derivatives of the second, third, and fourth order of the potential energy surfaces with respect to the normal coordinates Q_k of the nuclei.

5.4.2 Expansion of Hamiltonian

The complete vibration-rotation Hamiltonian of a molecule, according to Watson [127] has a form:

$$H_{rv} = \frac{\hbar^2}{2} \sum_{\alpha\beta} (J_\alpha - \pi_\alpha) \mu_{\alpha\beta} (J_\beta - \pi_\beta) + \frac{1}{2} \sum_k P_k^2 + V(Q) + U$$
$$U = -\frac{\hbar^2}{8} \sum_\alpha \mu_{\alpha\alpha} \qquad (5.2)$$

where J_α the component of total angular momentum about the center of mass along the rotating direction α, π_α the vibrational operator usually described as the component of the vibrational angular momentum along the rotating direction α, $\mu_{\alpha\beta}$ the $(\alpha\beta)$-component of a reciprocal inertia tensor, and P_k the momentum conjugate to normal vibration coordinate Q_k. For a non-linear molecule the $\alpha\beta$ sums in Eq. 5.2 run over all three components x, y, z of the rotating axes, and k sums over the (3N-6) normal modes. A normal mode is one in which all the nuclei undergo harmonic motion, have the same frequency of oscillation and move in phase but generally with different amplitudes. In approximation each of the vibrations of a molecule can be regarded as harmonic.

The form of Hamiltonian Eq. 5.2 can be simplified by expanding the rotational tensor of inertia $\mu_{\alpha\beta}$ as [127]

$$\mu_{\alpha\beta} = (I_\alpha)^{-1} [I_\alpha \delta_{\alpha\beta} - \sum_k a_k^{\alpha\beta} + \frac{3}{4} \sum_{k,l,\gamma} a_k^{\alpha\gamma} Q_k I_\gamma^{-1} a_l^{\gamma\beta} Q_l - ...](I_\beta)^{-1} \qquad (5.3)$$

With the use of expansions of the potential energy V (Eq.5.1) and the rotational tensor $\mu_{\alpha\beta}$ (Eq. 5.3) the complete vibration-rotation Hamiltonian (Eq. 5.2) for a non-rigid molecule can be expanded in powers of the vibrational operators π_α, and the rotational operators J_α and written in a compact form as [128]

$$H_{rv} = \sum_{m,n} H_{mn}$$

$$
\begin{aligned}
H_{rv} = &\ H_{20} + H_{30} + H_{40} + ... \quad \text{(vibrational terms)}\\
&+H_{21} + H_{31} + H_{41} + ... \qquad \text{(Coriolis terms)}\\
&+H_{02} + H_{12} + H_{22} + ... \quad \text{(rotational terms)}
\end{aligned}
\tag{5.4}
$$

Hamiltonian H_{rv} is thus the sum of terms of degree m in the vibrational operators π_α and of degree n in the rotational operators J_α. Terms H_{mn} have matrix elements of order $\kappa^{m+n-2}\,\omega_v$, κ being the Born-Oppenheimer expansion parameter$(m_e/m_n)^{1/4} \simeq \frac{1}{10}$ [129], where m_e is the electron mass, m_n is a typical nuclear mass and ω_v a typical vibration frequency.

Expressions for various terms H_{mn} in the expansion Eq. 5.4 of the vibration-rotation Hamiltonian can be found in [130]. Here only some important terms of Hamiltonian: rigid-rotor H_{02} term, the harmonic oscillator term H_{20} will be presented.

The term H_{02} of rotational rigid-rotor has a form

$$H_{02} = \sum_\alpha B_\alpha^e J_\alpha^2 \tag{5.5}$$

where rotational constant B_α^e is given by

$$B_\alpha^e = \hbar^2 \mu_{\alpha\alpha}^e/2hc = \hbar^2/2hcI_\alpha^e \tag{5.6}$$

Harmonic oscillator term H_{20} is written as

$$H_{20} = \frac{1}{2} \sum_k \omega_k (Q_k^2 + P_k^2)$$

where P_k is the vibration moment conjugated to the normal mode Q_k, with the harmonic vibration frequency ω_k of the kth normal mode.

5.4.3 Van Vleck Transformation

The matrix elements of the vibration-rotation Hamiltonian are expressed in the basis of the eigenstates of the harmonic oscillator and the rigid rotator. Each matrix block for a given J is infinite as a function of the quantum numbers of vibration. In order to determine approximate eigenvalues of the vibration-rotation Hamiltonian [Eq. 5.4], approaches, based on perturbation theory, are applied to the expansion of this Hamiltonian in a power series of products of vibrational and rotational operators. The detailed calculations will not given here and the relationship of the parameters in the Hamiltonian, obtained after transformation to those in original can be found in [131]. Those coefficients are adjusted as empirical parameters to fit observed spectra. Here is a very brief summary of Van Vleck's principle for transformation will be given.

Assuming that the terms of Hamiltonian H is separated into terms of different orders of magnitude with parameter λ as

$$H = H_0 + \lambda H_1 + \lambda^2 H_2 + ...,$$

If we transform the Schrödinger equation $H\psi = E\psi$ to

$$\tilde{H}\phi = E\phi, \quad \tilde{H} = \exp^{iS} H \exp^{-iS}, \quad \phi = \exp^{iS}\psi \tag{5.7}$$

where S is a Hermitian operator so that $\exp^{iS}$ is unitary. If the transformed Hamiltonian $\tilde{H}$ is diagonal in some basis ϕ, then the diagonal elements of E are the eigenvalues of H, and the eigenfunctions of H are $\psi = \exp^{iS}\phi$. In general the matrix of $\tilde{H}$ is not completely diagonal, but has a block-diagonal form. By a further transformation $U \tilde{H} U^{-1}$ with a unitary operator U, blocks can be algebraically diagonalized. What is achieved by transformation of Eq. 5.7 is a kind of separation of the vibration-rotation Hamiltonian for an individual vibrational level.

Applying a transformation of Eq. 5.7 by operator $\exp^{i\lambda S_1}$ the Hamiltonian can be written as:

$$\tilde{H}^{(1)} = \exp^{i\lambda S_1} H \exp^{-i\lambda S_1} = \tilde{H}_0 + \lambda\tilde{H}_1 + \lambda^2\tilde{H}_2 + \lambda^3\tilde{H}_3...,$$

The operator S_1 should be chosen such as $\tilde{H}_0 = H_0$ and to bring H_1 to block-diagonal form.

The Hamiltonians $\tilde{H}^{(2)}$, $\tilde{H}^{(3)}$,..., etc. can thus be derived systematically by successive transformations of Eq. 5.7 by operators $\exp^{i\lambda S_2}$, $\exp^{i\lambda S_3}$,... etc. In this way the vibration-rotation Hamiltonian can be transformed to a set of block-diagonal Hamiltonians for an

individual vibrational level.

5.4.4 Rotational energy levels

In order to take into account the rotation of the molecules investigated in this thesis, we have to consider the components of the rotational angular momentum in the laboratory fixed system and in the fixed axis system, related to the molecule.

1 Rotational angular momentum

The quantum operators corresponding to the rotational angular momentum components in the laboratory, J_X, J_Y, and J_Z, satisfy the commutation rules:

$$\left[J_X, J_Y \right] = i\hbar J_Z, \quad \left[J_Y, J_Z \right] = i\hbar J_X, \quad \left[J_Z, J_X \right] = i\hbar J_Y$$

where $\hbar$ is the Planck constant divided by 2π. The components of the rotational angular momentum in the molecule fixed axis system are denoted J_x, J_y and J_z. These operators satisfy the commutation rules:

$$\left[J_x, J_y \right] = -i\hbar J_z, \quad \left[J_y, J_z \right] = -i\hbar J_x, \quad \left[J_z, J_x \right] = -i\hbar J_y$$

The components of the angular momentum, whether in the fixed or molecular systems, commute with the total angular momentum operator, $\mathbf{J}^2 = J_X^2 + J_Y^2 + J_Z^2 = J_x^2 + J_y^2 + J_z^2$. In the following, a dimensionless angular momentum will be used and the factor $\hbar$ in the expression of the components of the angular momentum will be ignored.

We use the rotational wave functions, noted $\mid J,\ K,\ M\ \big\rangle$, which are eigenfunctions of the total angular momentum $\mathbf{J}^2$, its projection J_Z along the laboratory axis Z and its projection along the z axis of the molecular axis system J_z. These wave functions meet the conditions:

$$\mathbf{J}^2 \mid J, K, M \big\rangle = J(J + 1) \mid J, K, M \big\rangle$$

$$J_Z \mid J, K, M \big\rangle = M \mid J, K, M \big\rangle$$

$$J_z \mid J, K, M \big\rangle = k \mid J, K, M \big\rangle$$

where J, M and K are the quantum numbers corresponding to the operators $\mathbf{J}^2$, J_Z, J_z and $-J \leq K,\ M \leq J$.

The wave functions corresponds to the following relation:

$$J_{\pm} \mid J, K, M \rangle = \sqrt{J(J+1) - K(K \mp 1)} \mid J, K \mp 1, M \rangle$$

where $J_{\pm} = J_x \pm iJ_y$. In the case of the isolated molecule, the rotational energy does not depend on the quantum number M and, for simplicity, the notation $\mid J, K \rangle$ is used instead of $\mid J, K \mp 1, M \rangle$.

2 Basis functions

Table 5.1 – The representations corresponding to the identification of the molecule-fixed x, y and z axes with the molecule-fixed a, b, c inertial axes defined such as $I_a < I_b < I_c$

	I^r	II^r	III^r	I^l	II^l	III^l
x	b	c	a	c	a	b
y	c	a	b	b	c	a
z	a	b	c	a	b	c

The eigenstates and eigenvalues of the asymmetric Hamiltonian rotor are retrieved by diagonalization of matrix associated to the standard base $\mid J, K \rangle$. Different ways can be chosen for the orientation of the body-fixed axis (x, y, z) reference system for the symmetric rotor relative to the (a, b, c) inertia axes of the molecule.

These are shown in Table 5.1. Since asymmetric rotor molecules are either oblate-like or prolate-like in their behaviour, the most commonly used representations are type I ($a = z$) for near-prolate molecules, and type III ($c = z$) for near-oblate ones. Since the type II representations correspond to neither of the symmetric top limiting cases they are almost never used. For the type I representation the most commonly used is the I^r, right-handed one, where (a, b, c) are associated with (z, x, y). For the oblate representation both III^r, where (a, b, c) are associated with (x, y, z), and III^l, where (a, b, c) are associated with (y, x, z), are used.

3 Rotational energy

Molecules studied during the current thesis are asymmetric top molecules (for an asymmetric top molecule the rotational motion is free so the Hamiltonian will have kinetic energy operators along the a, b, and c rotational axes). There are no closed formulae for rotational term values of asymmetric top molecules. Instead, energy values can be determined accurately only by a matrix diagonalization for each value of J. For relatively low values of J one can find the energy levels in [123] (Table 7.7)

The rotational Hamiltonian of an asymmetric top molecule is given by Eq. 5.5. The three principal rotational constants B_α^e (Eq. 5.6) are noted as $B_a = A$, $B_b = B$ and $B_c = C$ and ordered by the relation $A \geq B \geq C$.

The labeling of the asymmetric top energy levels is made by considering a smooth variation from the prolate to the oblate top limit. This is often plotted in terms of the Ray asymmetry parameter, $\kappa = (2B\text{-}A\text{-}C)/(A\text{-}C)$, which varies from -1 in the prolate limit to +1 in the oblate limit: Fig. 5.1.
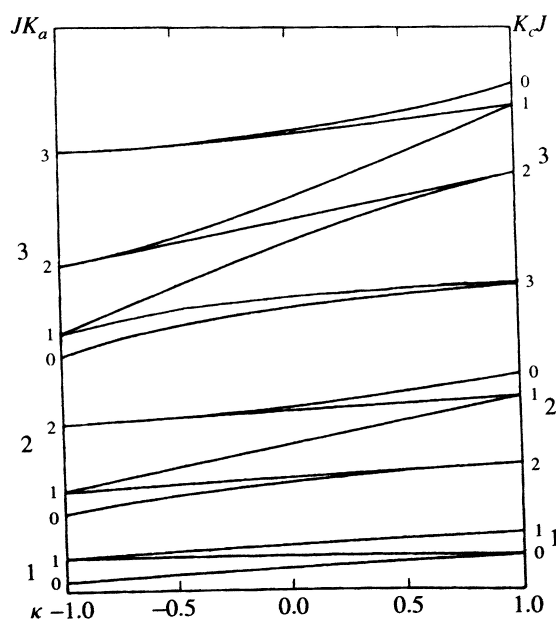
Figure 5.1 – Assymetric top correlation diagram plotted using the Ray asymmetry parameter κ.

Asymmetric top rotational states are labelled by the value of J with subscripts K_a, K_c with $K_a + K_c = J$ or $J + 1$, where K_a and K_c correspond to the quantization of the projection of the total angular momentum along the a axis or the c axis, in the prolate or oblate top limits, respectively.

As J increases, the energy levels with low values of K_a, e.g. 0 and 1, having the same oblate top quantum number, K_c, tend to become degenerate. This corresponds to the limit when the molecule is spinning mainly about the axis of the largest moment of inertia. The reverse type of limiting behaviour occurs when K_a is large and K_c is small; the molecule then rotates mainly about the axis of the least moment of inertia. This means that asymmetric top molecule can behave like both of the limiting symmetric rotor cases, but the intermediate energy levels of a given value of J correspond to the classical motion about all the inertial axes.

Equation of the eigenvalues of rotational Hamiltonian H_{rot} has the form:

$$H_0^{rot} \mid J, K_a K_c \rangle = E_{(J K_a K_c)}^{rot} \mid J, K_a K_c \rangle$$

In the case of "prolate" top $A > B = C$ and the expression for rotational energy has form:

$$E^{rot}(J, K_a) = (A - B)K_a^2 + BJ(J + 1)$$

In the case of an "oblate" top $A = B > C$ and the rotational energy is:

$$E^{rot}(J, K_c) = (C - A)K_c^2 + BJ(J + 1)$$

4   Rotational selection rules

For a transition between two rotational states to be allowed, the matrix element of at least one of the components of the dipole moment in the fixed laboratory axis must be not zero. It is the one along the laboratory axis Z is usually considered. The condition is written as:

$$\left\langle J' K_a' K_c' \mid \mu_Z \mid J'' K_a'' K_c'' \right\rangle \neq 0$$

where vibrational quantum numbers of the two states are labelled using the signs $'$ and $''$ and μ_Z is the component of the dipole moment along the of the laboratory axis Z.

Rotational selection rules give conditions on variations in $\Delta J = J' - J''$, $\Delta K_a = K_a' - K_a''$, $\Delta K_c = K_c' - K_c''$ according to the μ_β component of the dipole moment as:

ΔJ	ΔK_a	ΔK_c	β
$0, \pm 1$	even	odd	a
$0, \pm 1$	odd	odd	b
$0, \pm 1$	odd	even	c

Depending on the component of the dipole moment, the rotational transitions will be of type a, b, or c.

For example, for a type a near-symmetric top the selection rules are:

$$\Delta J = 0, \pm 1 \quad \Delta K_a = 0, \quad \Delta K_c = \pm 1$$

5.4.5   Asymmetric rotor molecules

According to Watson, the rotational Hamiltonian for asymmetric top molecules is composed in terms of angular momentum operators J^2, J_z^2 and $J_\pm = J_x \pm J_y$ and has the following form:

$$H_{rot} = H_{02} + H_{04} + ...$$

where H_{02} is the rigid-rotor energy term:

$$H_{02} = \frac{1}{2}(B_x + B_y)J^2 + \frac{1}{2}(2B_z - B_x - B_y)J_z^2 + \frac{1}{4}(B_x - B_y)(J_+^2 + J_-^2)$$

H_{04} is the quartic centrifugal distortion term:

$$H_{04} = T_{400}J^4 + T_{220}J_z^2 J^2 + T_{040}J_z^4 + T_{202}(J_+^2 + J_-^2)J^2 + \frac{1}{2}T_{022}\left\{J_z^2, (J_+^2 + J_-^2)\right\} + T_{004}(J_+^4 + J_-^4)$$

in which B_α and T_{ijk} are the cartesian and cylindrical components of rotational and centrifugal constants, respectively.

As have been shown by Watson, of the six quartic centrifugal distortion constants T_{ijk}, only five combinations are experimentally determinable

$$\tilde{T}_{400} = -\tilde{D}_J = T_{400} - \frac{1}{2}s_{111}(B_x - B_y)$$

$$\tilde{T}_{220} = -\tilde{D}_{JK} = T_{220} - 3s_{111}(B_x - B_y)$$

$$\tilde{T}_{040} = -\tilde{D}_K = T_{040} - \frac{5}{2}s_{111}(B_x - B_y)$$

$$\tilde{T}_{022} = 2\tilde{R}_5 = T_{022} - s_{111}(2B_z - B_x - B_y)$$

$$\tilde{T}_{004} = \tilde{R}_6 = T_{004} - \frac{1}{4}s_{111}(B_x - B_y)$$

$$\tilde{T}_{202} = -\delta_J = T_{202}$$

In order to keep only uniquely determinable parameters, we need to use a reduction, which in principle is applied to eliminate (or fix) the removable terms. In spectroscopy, for asymmetric rotor molecules, we use two principal reductions, the A and S.

1 A-reduction

The most often used reduction, proposed by Watson, is A-reduction (or asymmetric). It involves choosing s_{111} so that $\tilde{T}_{004}=\tilde{R}_6=0$, hence

$$s_{111} = -\frac{4T_{004}}{B_x - B_y}$$

The A-reduction is used for asymmetric tops, i.e. in the case when the rotation constants have quite different values.

The Hamiltonian for an *A*-reduced Hamiltonian up to the fourth power in angular momentum is given by the following equation

$$H_{rot}^{(A)} = \frac{1}{2}(B_x + B_y)\boldsymbol{J}^2 + [B_z - \frac{1}{2}(B_x + B_y)]J_z^2 - \Delta_J\boldsymbol{J}^4 - \Delta_{JK}\boldsymbol{J}^2J_z^2 - \Delta_K J_z^4 +$$
$$+[\frac{1}{4}(B_x - B_y) - \delta_J\boldsymbol{J}^2](J^{+2} + J^{-2}) - \frac{1}{2}[\delta_K J_z^2, J^{+2} + J^{-2}]_+...,$$

(5.8)

where $[]_+$ is the anti-commutator.

2 S-reduction

For very slightly asymmetric tops, it is preferable to employ S-reduction. In this case $\tilde{R}_5=0$ which requires

$$s_{111} = \frac{T_{022}}{2B_z - B_x - B_y}$$

The Hamiltonian for an *S*-reduced Hamiltonian up to the fourth power in angular momentum is as follows:

$$H_{rot}^{(S)} = \frac{1}{2}(B_x + B_y)\boldsymbol{J}^2 + [B_z - \frac{1}{2}(B_x + B_y)]J_z^2 - D_J\boldsymbol{J}^4 - D_{JK}\boldsymbol{J}^2J_z^2 - D_K J_z^4 +$$
$$+[\frac{1}{4}(B_x - B_y) + d_1\boldsymbol{J}^2](J^{+2} + J^{-2}) + d_2[J^{+4} + J^{-4}]_+...,$$

(5.9)

and *S*-reduction is preferred for molecules close to the symmetric top, i.e. when two rotational constants are nearly equal.

5.5 Perturbations in Spectra

One of the main complications responsible for difficulties in the analysis of rotational spectra of molecules is the existence of perturbations, of which the most common are those due to Coriolis interaction, Fermi or Darling-Dennison resonances. Another problem is the interference between vibrational excited states. In the current thesis, analysis of the Coriolis interaction has been carried out, below, only this type of resonance will be shortly described.

5.5.1 Molecular vibrations

For the study of resonances, such as Coriolis or Fermi, occurring in the spectrum, it is necessary to consider molecular symmetry and the type of vibrations. Main terms and

definitions will be given below.

All molecules vibrate unless they are at zero degrees Kelvin. A molecule can vibrate in many ways. The vibrational motion of a molecule is described by fundamental frequencies, denoted ω_i, corresponding to different types of vibration. The vibrational motions of atoms can be expressed as fundamental vibrational modes of the molecule, known as normal modes.

Every atom has 3 degrees of freedom (the 3 dimensions of space) leading to $3N$ degrees of freedom for an N -atomic molecule. Of these degrees of freedom, three describe rotation around a centre of mass, which does not correspond to any vibrational motion. A further three degrees of freedom describe a translational motion. Thus, in general an N-atomic molecule has $(3N - 6)$ vibrational modes. Methoxy isocyanate and ethyl cyanide, studied during this thesis, has $(3N - 6)=18$ and $(3N - 6)=21$ vibrational modes, respectively. These vibrational motions are referred to as the normal modes of vibration (or normal vibrations) of the molecules; in general a normal vibration is defined as a molecular motion in which all the atoms oscillate with the same frequency and pass through their equilibrium positions simultaneously.

5.5.2   Symmetry of Molecules

The symmetry is described in group theory in terms of point groups. Since this chapter is about molecular spectroscopy rather than group theory, only outline of the theory necessary to understand basic terms will be given. The reader who desires to study the subject more thoroughly should look into literature of group theory.

Molecules possess some symmetry. The application of group theory to molecular systems is based on the fact the Schrödinger equation for a physical system is invariant with respect to symmetry transformations of the system. The groups which may be used for the non-rotating molecule are the molecular point groups. Symmetry properties of molecules is essential to solve the eigenvalue equation Hamiltonian. The study of symmetry properties is also important in understanding of molecular vibrations, it can be used to determine the number of fundamental frequencies, their degeneracies, the selection rules, the possibility and type or perturbations due to resonance, and other useful information.

1   Elements of Symmetry

For molecules any possible symmetry operations are rotation through a definite angle about some axis, and reflection in some plane. The symmetry of a molecule is determined by all the possible rearrangements after which its configuration stays unchanged means the center of mass must remain unmoved by any symmetry operation and therefore lies on all symmetry elements. If the molecule is unchanged by reflection in some plane, this

plane is said to be a plane of symmetry. All of the symmetry operations that apply to a molecule constitute its point group. The elements of the point group of the molecule are interpreted as rotating and/or reflecting the vibronic coordinates with respect to the molecule-fixed axes. It is the point group to which the molecule belongs that designates its symmetry and which we used in spectroscopy.

2   The Point Group Symmetry of Molecules

Molecular point groups are used to help understand the behavior of molecules. Point group symmetry is based on the shape of a molecule in its equilibrium configuration.

The group theory makes it possible to show that there exists, for each point group, fundamental modes of transformation of physical quantities with respect to operations of symmetry of the group. Representations of fundamental modes are called irreducible representations. A type of symmetry is defined by the array of characters in an irreducible representation.

Each point group has an associated character table. The methoxy isocyanate and ethyl cyanide molecules investigated during this thesis belong to the C_s point group. The symmetry operations of the C_s point group are: the identity E and a mirror plane σ. The identity operator E is the simplest operator which leaves the molecular configuration unchanged, i.e. $\sigma^2{=}E$.

Table 5.2 gives the character table for group C_s. Each of the rows of numbers in a character table represents a symmetry label; the technical name for such a symmetry label is an 'irreducible representation'. Each of the numbers in an irreducible representation is called a 'character' and these numbers can be different from $+1$ or -1. In general they are the sum of the diagonal elements of a matrix having as dimension the character given under the identity operation E for that irreducible representation. If we chose the z axis as the main axis of symmetry of the molecule, Table 5.2 gives the properties of the T_x, T_y and T_z components on the x, y or z axes of any polar vector (like the dipole moment μ), those of any axial vector (R_x, R_y and R_z) as **J**. Finally, the type of symmetry (A' or A'') of the T_Z component of a polar vector on the "fixed" laboratory axis Z is given. For example, the C_s point group of methoxyisocyanate and ethyl cyanide molecule has the labels A' and A''; the states of these molecules are therefore of these two symmetry types.

Table 5.2 – Character tables for C_s point group.

C_s	E	σ_{xz}	
A'	1	1	T_x, T_z, R_y
A''	1	-1	T_y, R_x, R_z

3 Labeling Vibrational States

Harmonic vibrations of the C_s point group are labelled according to their symmetry properties as belonging to one of the two irreducible representations A' and A'' . Each motion is labelled symmetric or antisymmetric. Those properties belonging to irreducible representation A' are symmetric to both the identity operation E as well as reflection through the mirror plane σ. Those properties belonging to irreducible representation A'' are symmetric with respect to the identity operation E but antisymmetric with respect to reflection through the mirror plane σ.

For example, if we rotate the vibrating molecule by 180° the vibration is quite unchanged in character - it is called a symmetric vibration. If rotation produces a vibration which is in anti-phase with the original and so this motion is described as the asymmetric. Vibrations are labelled: ν_1, ν_2, ν_3 and so on. By convention it is usual to label vibrations in decreasing frequency within their symmetry type.

For example, methoxyisocyanate has the three lowest symmetry modes: skeletal torsion ν_{18}, bending ν_{11}, and the methyl torsion ν_{17}. In the in plane bending mode (ν_{11}) the CONC bond simultaneously bend whereas in the antisymmetric out of plane skeletal torsion mode the CONC bond contracts. Clearly the molecule undergoing the bending vibration 'looks the same' after each of the point group operations; the 'symmetry coordinate' describing the motion is multiplied by +1 by each symmetry operation. Thus each of these two vibrational states has symmetry A'. However, for the skeletal and methyl torsion mode (ν_{18} and ν_{17}) the symmetry operations interchange so that the symmetry coordinate is multiplied by -1. Means these modes will be of symmetry A''.

For the purpose of understanding which vibrational states can be excited it is important to know the symmetry labels for the components of the 'dipole moment' μ_Z; these are always given in point group character tables (the notation T_Z is used instead of μ_Z.)

In this way, for any molecule once we have the character table of the point group we can determine the symmetry of the normal vibrational modes and the symmetry of any vibrationally excited state and determine which pairs of levels can interact with each other.

5.5.3 Hamiltonian

At zero order, the rotation and vibration are well separated ($H_0 = H_0^{vib} + H_0^{rot}$). The eigenstates of H_0 are the product of vibrational eigenstate of H_0^{vib} denoted as $\mid \nu_1, \nu_2, ... \nu_{18} \rangle_0$ and the rotational eigenstate of H_0^{rot}, denoted as $\mid J, K_a K_c \rangle_0$:

$$\mid \nu_1, \nu_2, ... \nu_{18} \quad J, K_a K_c \rangle_0 = \mid \nu_1, \nu_2, ... \nu_{18} \rangle_0 \mid J, K_a K_c \rangle_0$$

Example will be given on molecule CH_3ONCO that has 18 normal modes of vibration. CH_3ONCO fundamental frequencies ω_i and the types of symmetry of the different modes normal vibration values can be found in Chapter 6.

The zero-order vibrational Hamiltonian of CH_3ONCO, H_0^{vib}, is a tensorial product of 18 non generated harmonic oscillators. Each corresponding vibrational eigenstate, $\mid \nu_1, \nu_2, ...\nu_{18}\big\rangle_0$ is the product of 18 $\mid \nu_i\rangle$ harmonic oscillators eigenstates. Each associated eigenvalue is the sum of 18 associated eigenvalues:

$$E_0^{vib} = \omega_1\left(\nu_1 + \frac{1}{2}\right) + \omega_2\left(\nu_2 + \frac{1}{2}\right) + ... + \omega_{18}\left(\nu_{18} + \frac{1}{2}\right)$$

The eigenstates of H_0 can also be classified using the two irreducible representations of C_s group, their type of symmetry Γ ($\Gamma = A'$ or A'') depends on the parity of the rotational and vibrational quantum numbers and is obtained by multiplication of the types of symmetry of the vibrational state and of the rotational level:

$$\Gamma\left(\mid \nu_1 \quad \nu_2...\nu_{18} \quad J \quad K_a \quad K_c\big\rangle_0\right) = \Gamma\left(\mid \nu_1 \quad \nu_2...\nu_{18} \quad \big\rangle_0\right) \otimes \left(\mid J \quad K_a \quad K_c\big\rangle_0\right)$$

Further, it is possible to calculate the matrix elements of the operators of the Hamiltonian using a symmetry adapted basis defined from the $\mid J \quad > K\rangle$ and $\left(\mid \nu_1 \quad \nu_2...\nu_{18} \quad \big\rangle_0\right)$.

1 Symmetry of vibrational states

The type of symmetry of a particular vibrational state $\mid \nu_1 \quad \nu_2...\nu_{18} \quad \rangle$ is given by the direct product of the types of symmetry of its each vibrational state $\mid \nu_i\rangle$:

$$\Gamma\left(\mid \nu_1 \quad \nu_2...\nu_{18}\rangle\right) = \Gamma\left(\mid \nu_1\rangle\right) \otimes \Gamma\left(\mid \nu_2\rangle\right) \otimes ... \otimes \Gamma\left(\mid \nu_{18}\rangle\right)$$

The eigenfunctions of one dimension harmonic oscillator $\mid \nu_i\rangle$, are Hermite's polynomes, $H_v(q_i)$. If the sign $q_i \rightarrow -q_i$ changes, the $\mid \nu_i\rangle$ wavefunction changes as:

$$q_i \rightarrow -q_i \quad H_{v_i}(q_i) \rightarrow H_{v_i}(-q_i) = (-1)^{v_i} H_{v_i}(q_i)$$

The symmetry type of the $\mid \nu_i\rangle$ vibrational wave function according to C_s thus depends on the i and v_i values.

2   Selection rules

The intensity of an electric dipole moment transition between two levels $| \begin{array}{ccccc} \nu_1' & \nu_2'...\nu_{18}' & J' & K_a' & K_c' \end{array} \rangle$ and $| \begin{array}{ccccc} \nu_1'' & \nu_2''...\nu_{18}'' & J'' & K_a'' & K_c'' \end{array} \rangle$ is proportional to the square of the transition moment matrix element:

$$| \left\langle \begin{array}{ccccc} \nu_1' & \nu_2'...\nu_{18}' & J' & K_a' & K_c' \end{array} \right| \mu_Z \left| \begin{array}{ccccc} \nu_1'' & \nu_2''...\nu_{18}'' & J'' & K_a'' & K_c'' \end{array} \right\rangle |^2$$

where μ_Z is the component on the laboratory axis Z of the molecule electric dipole moment μ. In order this matrix element be non-zero, the following conditions must be met:

- $\Delta J = 0, \pm 1$

- For a C_s type molecule:

$$\Gamma\left(| \begin{array}{ccccc} \nu_1' & \nu_2'...\nu_{18}' & J' & K_a' & K_c' \end{array} \rangle \right) \otimes \Gamma\left(| \mu_Z \rangle \right) \otimes \Gamma\left(| \begin{array}{ccccc} \nu_1'' & \nu_2''...\nu_{18}'' & J'' & K_a'' & K_c'' \end{array} \rangle \right)$$

Since $\Gamma\left(| \mu_Z \rangle \right) = A''$

$$\Gamma\left(| \begin{array}{ccccc} \nu_1' & \nu_2'...\nu_{18}' & J' & K_a' & K_c' \end{array} \rangle \right) \otimes \Gamma\left(| \begin{array}{ccccc} \nu_1'' & \nu_2''...\nu_{18}'' & J'' & K_a'' & K_c'' \end{array} \rangle \right) = A''$$

3   Resonance conditions

Interactions can couple energy levels belonging to different vibrational states with rather close energy. These resonances must be accurately taken into account. Let us consider two states $| \nu_1 \rangle$, $| \nu_2 \rangle$ with energies $E_{v_1}^0$, $E_{v_2}^0$. The resonance conditions for states are:

- same value of J quantum number

- symmetry conditions

- close energy levels

5.5.4   Coriolis coupling

A Coriolis force occurs in the case of a rotating and vibrating molecule. As the rotating molecule vibrates, its rotation is slowed down and as the molecule contracts its rotation

is speeded up by Coriolis forces. Such changes in rotational velocity are attributed to the law of conservation of angular momentum - as molecule expands its moment of inertia increases and hence it must slow down in order to conserve angular momentum. This is the reason the resonance-type terms involving the difference between two frequencies are called Coriolis terms.

Quantum mechanically speaking, Coriolis interactions are caused by the coupling of the total angular momentum J_α and the vibrational angular momentum π_α (Eq. 5.2). Coriolis forces represent a coupling of the modes of vibrations in the rotating molecule. When two vibrational states coupled by the Coriolis interaction come accidentally close in energy, the rotational levels in both states are seriously perturbed and the analysis of the rotational spectrum in such case may be complicated.

1 Coriolis interactions

According to Jahn's rule [132], if the product of the symmetry species of the two vibrational states contains the species of rotation

$$\Gamma(q_k) \times \Gamma(q_l) \in \Gamma(J_\alpha)$$

Coriolis interaction takes place between the modes ω_k or ω_l, or between the states (ν_k, ν_l) and $(\nu_k + 1, \nu_l - 1)$. If the states (ν_k, ν_l) and $(\nu_k + 1, \nu_l - 1)$ are close in energy, the Coriolis interaction has to be included in matrix to be diagonalized numerically.

Coriolis perturbations arise from the terms H_{21}, H_{31}, H_{41} etc. of the expansion of the vibration-rotation Hamiltonian given in Eg. 5.4. H_{21} term are the simplest type of vibration-rotation interaction, have been discussed by [124]. It is given by:

$$H_{21} = \sum_{kl} -2(\frac{\omega_l}{\omega_k})^{1/2} \sum_{\alpha} B_\alpha^e \zeta_{kl}^\alpha J_\alpha q_k p_l \tag{5.10}$$

where $\zeta_{k,l}^\alpha$ is the Coriolis zeta constant, B_e^α are the rotational constants, ω_k, ω_l are harmonic frequencies (in wavenumbers) of the participating modes.

2 Hamiltonian

In a case of the Coriolis interaction between vibrational states, labelled for example as vv, $v'v'$, $v''v''$, the Hamiltonian for the coupled fit can be constructed in a block form [133]

$$H = \begin{pmatrix} H_{vv}^{rot} & H_{v'v}^{Cor} & H_{v''v}^{Cor} \\ H_{vv'}^{Cor} & H_{v'v'}^{rot} + \Delta E_{v,v'} & H_{v''v'}^{Cor} \\ H_{vv''}^{Cor} & H_{v'v''}^{Cor} & H_{v''v''}^{rot} + \Delta E_{v',v''} \end{pmatrix}$$

where the diagonal blocks consist of the rotational Hamiltonian for the each appropriate state , H_{vv}^{rot}, $H_{v'v''}^{rot}$ etc., augmented by the vibrational energy difference $\Delta E^{v,v'} = E_{v'} - E_v$, $\Delta E^{v',v''} = E_{v''} - E_{v'}$ between unperturbed states. H_{vv}^{rot}, $H_{v'v''}^{rot}$ etc. blocks are set up using Watson's *A*- or *S*-reduced asymmetric rotor Hamiltonian, presented in Eqs. 5.8 and 5.9. The off-diagonal blocks $H_{vv'}^{Cor}$, $H_{v'v''}^{Cor}$ represent the Coriolis interaction. The leading terms of the Coriolis interaction result from the H_{21} (Eq. 5.10) and H_{22} terms (expression for this may be found in [124]) of the vibration–rotation Hamiltonian of Eq. 5.4, and $H_{vv'}^{Cor}$, $H_{v'v''}^{Cor}$ can be written, following [133] as

$$H_\alpha^{Cor} = i(G_\alpha + G_\alpha^J \mathbf{J}^2 + G_\alpha^K J_z^2 + G_\alpha^{KK} \mathbf{J}^4 + ...)J_y + \\ + (F_{\beta\gamma} + F_{\beta\gamma}^J \mathbf{J}^2 + F_{\beta\gamma}^K J_z^2 + ...)(J_z J_x + J_x J_z) \tag{5.11}$$

where α, β, γ are permutations of a, b, c and are chosen according to the type of the Coriolis interaction.

The G_α parameters (first-order Coriolis interaction constant) are related to the Coriolis zeta constant $\zeta_{k,l}$ in expression for H_{21} through

$$G_\alpha = B_\alpha \zeta_{k,l}^\alpha [(\omega_k/\omega_l)^{1/2} + (\omega_k/\omega_l)^{1/2}] \tag{5.12}$$

F parameters are the second-order Coriolis constants, arising from the H_{22} terms.

Using the block-form of the Hamiltonian matrix, with the given expressions, the experimental data for the interacting vibrational states can be introduced in a fit leading to the determination of a set of rotational (B_α), centrifugal and Coriolis constants (G, F), as well as vibrational energies between states (E).

5.5.5 Multiple state fitting

This section will describe in some detail how to fit simultaneously different states, which was the case of methoxyisocyanate. First, the states were fit independently in each case, and their results were combined with adding interaction parameters and energy separation between states.

The analysis of the molecular spectra obtained in this work, spectroscopic predicting and fitting computer programs SPFIT (Spin fitting) and SPCAT (Spin Cataloging) by Herbert Pickett was employed [134]. The example of multiple state fitting will be given according to the operators codes in SPFIT.

Example of parameter types for asymmetric rotors with Coriolis coupling employed in SPFIT are given in Table 5.3. Operators that are off-diagonal between defined states are coded with $v' \neq v$.

Table 5.3 – Parameter identifiers for Coriolis interactions ($v<->v'$) in SPFIT.

$E_{v'}$	$v'v'$				
G_c	$6000vv'$	G_a	$2000vv'$	G_b	$4000vv'$
G_c^J	$6001vv'$	G_a^J	$2001vv'$	G_b^J	$4001vv'$
G_c^K	$6010vv'$	G_a^K	$2010vv'$	G_b^K	$4010vv'$
F_{ab}	$6100vv'$	F_{bc}	$2100vv'$	F_{ca}	$4100vv'$
F_{ab}^J	$6101vv'$	F_{bc}^J	$2101vv'$	F_{ca}^J	$4101vv'$
F_{ab}^K	$6110vv'$	F_{bc}^K	$2110vv'$	F_{ca}^K	$4110vv'$

As was indicated above, vibrational states are defined as vv, $v'v'$, $v''v''$ etc. For example, usually the ground state is labelled 00, the first vibrational state 11, the second 22 etc.

For the data sets of transitions for the ground (00) and one vibrational state (11), to the first order, analysis will require the value of vibrational energy of state (11), E_{11}, Coriolis coupling constants, G_a^{01}, G_b^{01}, or G_c^{01}, depending on a type of interaction, and rotational constants for every state (i.e. A^{00}, B^{00}, C^{00}, A^{11}, B^{11}, C^{11}). Distortion constants for vibrational state can be fixed to those of the ground state, if previously determined from the fit. The energy value between states, E_{11} can be fixed to a value, calculated from the *ab initio*, for the first fitting stage, and can be released after the simultaneous coupled fit of states (00) and (11) has been performed. Coriolis coupling constants (G_a^{01}, G_b^{01}, G_c^{01}) can be initially derived with the use of Eq. 5.12 to be included in a global fit. Manually adjusting the fixed value of E_{11}, values of G_α^{01} parameters can be found with the minimum standard deviation σ of the fit. In such a manner the observed transitions from different states could be fit simultaneously to within experimental uncertainties. The analysis of spectra with the Coriolis interactions is often difficult because the Coriolis interaction parameters $G_\alpha^{vv'}$, $F_{\alpha\beta}^{vv'}$, may be correlated with the related rotational constants B_α corresponding to rotation about the coupling axis. The criterion of 10σ is typically used in order to avoid force-fitting transitions which are assigned with confidence but may not yet be treatable with the present Hamiltonian model. The treatment of a coupled N-state fit allows a precise determination of the vibrational energies of each state, based entirely on the perturbations in frequencies of rotational transitions.

Chapter 6

High Resolution Spectroscopy of Molecules of Astrophysical Interest

6.1 Introduction

This chapter will present the results of the laboratory work on spectroscopic studies of two molecules of astrophysical interest, methoxyisocyanate CH_3ONCO and triple- ^{13}C isotopologue of ethyl cyanide, $^{13}CH_3^{13}CH_2^{13}CN$, carried out by the author during the doctoral research in PhLAM. The laboratory rotational spectra of CH_3ONCO and $^{13}CH_3^{13}CH_2^{13}CN$ have been recorded with the Lille's fast DDS solid-state spectrometer and analyzed in the millimeter- and sub-millimeter ranges.

The main objective of the current studies is to obtain accurate spectroscopic constants of CH_3ONCO and $^{13}CH_3^{13}CH_2^{13}CN$, molecules that are expected to be present in the ISM and to provide reliable predictions up to the THz range to enable their astronomical detection. The detection of these molecules by their rotational and ro-vibrational spectra should provide some information on the formation pathways of interstellar molecules.

The choice of the new molecule to be studied in the laboratory and searched by astronomers in the ISM is usually made by analogy with previously detected molecules. Methoxy substituted derivatives, isotopologues and vibrational exited states, for example, could be suggested as logical candidates for further laboratory and observations studies.

This section is organized as follows. The $^{13}CH_3^{13}CH_2^{13}CN$ will be presented in Sect. 6.2 and CH_3NCO in Sect. 6.3.

6.2   Ethyl cyanide, triple ^{13}C - substituted, ^{13}CH$_3$^{13}CH$_2$^{13}CN

6.2.1   Astrophysical interest

With the Atacama Large Millimeter/submillimeter Array (ALMA), it is now possible to search for the isotopologues of complex and less abundant species.

A recently published astronomical detection of all three doubly ^{13}C-substituted ethyl cyanides toward Sgr B2(N2) [135] was the motivation to investigate triple ^{13}C isotopic species that are expected to be also present in the ISM.

Observations of isopotologues of ethyl cyanide may provide useful clues to the chemical pathways leading to their formation. Measurements of isotopic fractionation may help to constrain formation pathways of molecules since isotopic fractionation is sensitive to physical conditions such as density and temperature.

Besides, in many cases, the emission of the main isotopologue is optically thick, which leads to difficulties in the determination of column densities and the observations of the denser parts of the molecular clouds. And the observation of isotopologues could help to study the mass distribution in a molecular cloud.

The studies on rotational spectrum of ^{13}CH$_3$^{13}CH$_2$^{13}CN will be reported in a form of an already published article, and will be given below.

Astronomy & Astrophysics

The millimeter and sub-millimeter rotational spectrum of triple ^{13}C-substituted ethyl cyanide[⋆]

A. O. Pienkina[1], L. Margulès[1], R. A. Motiyenko[1], H. S. P. Müller[2], and J.-C. Guillemin[3]

[1] Laboratoire de Physique des Lasers, Atomes, et Molécules, UMR CNRS 8523, Université de Lille I,
 59655 Villeneuve d'Ascq Cedex, France
 e-mail: laurent.margules@univ-lille1.fr
[2] I. Physikalisches Institut, Universität zu Köln, Zülpicher Str. 77, 50937 Köln, Germany
[3] Institut des Sciences Chimiques de Rennes, École Nationale Supérieure de Chimie de Rennes, CNRS, UMR 6226,
 11 allée de Beaulieu, CS 50837, 35708 Rennes Cedex 7, France
 e-mail: jean-claude.guillemin@ensc-rennes.fr

ABSTRACT

Context. A recently published astronomical detection of all three doubly ^{13}C-substituted ethyl cyanides toward Sgr B2(N2) motivated us to investigate triple ^{13}C isotopic species that are expected to be also present in the ISM.
Aims. We aim to present an experimental study of the rotational spectrum of triple ^{13}C-substituted ethyl cyanide, ^{13}CH$_3^{13}$CH$_2^{13}$CN, in the frequency range 150–990 GHz. We want to use the determined spectroscopic parameters for searching for ^{13}CH$_3^{13}$CH$_2^{13}$CN in ALMA data. The main objective of this work is to provide accurate frequency predictions to search for this molecule in the Galactic center source Sagittarius B2(N) and to facilitate its detection in space.
Methods. The laboratory rotational spectrum of ^{13}CH$_3^{13}$CH$_2^{13}$CN has been recorded with the Lille's fast DDS solid-state spectrometer between 150 GHz and 990 GHz.
Results. More than 4000 rotational transitions were identified in the laboratory. The quantum numbers reach $J = 115$ and $K_a = 39$. Watson's Hamiltonian in the A and S reductions were used to analyze the spectra. Accurate spectroscopic parameters were determined. The rotational spectra of the ^{13}C containing species CH$_3$CH$_2$CN have been assigned, thus allowing the determination of the rotational and centrifugal distortion constants

Key words. molecular data – submillimeter: ISM – ISM: molecules – techniques: spectroscopic – line: identification – methods: laboratory: molecular

1. Introduction

Millimeter and submillimeter observations (Belloche et al. 2013, 2016) revealed that a remarkably rich chemistry occurs in the dense molecular clouds. Much of the molecular data gathered over the last 30 yr from laboratory experiments and quantum-chemical calculations have been summarized by Schoier et al. (2005). Complex organic molecules such as HCOOCH$_3$ (methyl formate), CH$_3$OCH$_3$ (dimethyl ether), CH$_3$CH$_2$OH (ethyl alcohol), CH$_2$CHCN (vinyl cyanide), and CH$_3$CH$_2$CN (ethyl cyanide) have been recognized in hot cores (Gibb et al. 2000a; Johnson et al. 1977) of massive star-forming regions such as Orion KL (Friedel & Widicus Weaver 2012), and Sgr B2 (Nummelin et al. 1998, 2000; Hollis et al. 2003; Müller et al. 2008).

Ethyl cyanide is an abundant molecule observed in hot molecular clouds. The core in Sgr B2, designated the Sgr B2(N) Large Molecule Heimat source or Sgr B2(N-LMH) by Snyder (2006), has the highest column densities of CH$_3$CH$_2$CN of all sources studied so far ($\sim$9.6 $\times$ 10^{16} cm^{-2}) (Miao et al. 1995; Kuan et al. 1996; Miao & Snyder 1997). Formation mechanisms

for CH$_3$CH$_2$CN and other COMs were discussed by Laas et al. (2011), Garrod et al. (2008), Belloche et al. (2009, 2014).

The first spectroscopic detection of ethyl cyanide in Titan's atmosphere, obtained with the Atacama Large Millimeter Array (ALMA), was recently reported by Cordiner et al. (2015). CH$_3$CH$_2$CN has also been observed in the coma of comet Halley (Altwegg et al. 1999), in regions of low-mass star formation (Bottinelli et al. 2007; Cazaux et al. 2003) and in high mass young stellar objects (YSOs; Bisschop et al. 2007). Observation of this molecule and its isotopologues is necessary for the comprehension of molecular cloud chemistry.

The relative natural abundance ratio of ^{13}C is about 1% of ^{12}C and is constant on the Earth. The dense clouds of the ISM contain many gas-phase organic molecules that are characterized by large deuterium enrichment compared to the terrestrial standart. Carbon fractionation is also observed and measured in ISM molecules but is less pronounced due to the smaller differential between ^{13}C and ^{12}C atomic masses. Deriving ^{13}C isotopic fractionation of the molecules by observations is one of the promising methods to constrain their main formation mechanism. The derived abundance ratios of mono-, double and triple- ^{13}C isotopologues can give suggestions about fractionation mechanisms and the origin of the fractionated carbon.

The rotational spectrum of ethyl cyanide has been measured many times in the microwave, millimeter and sub-millimeter

---

⋆ Full Table 3 is only available at the CDS via anonymous ftp to cdsarc.u-strasbg.fr (130.79.128.5) or via http://cdsarc.u-strasbg.fr/viz-bin/qcat?J/A+A/601/A2

ranges (Lovas 1982; Pearson et al. 1994) and (Fukuyama et al. 1996; Brauer et al. 2009; Fortman et al. 2010a,b). The rotational spectra of deuterated, mono-^{13}C, and -^{15}N containing isotopologs of ethyl cyanide (Margulès et al. 2009, 2016; Richard et al. 2012; Heise et al. 1974), as well as vibrationally excited ethyl cyanide (Gibb et al. 2000b; Heise et al. 1981; Mehringer et al. 2004; Daly et al. 2013; Belloche et al. 2013, 2016) have also been investigated and successfully detected in the ISM.

A recent laboratory spectroscopic investigation (Margulès et al. 2016) deals with the spectra and space identification of three double ^{13}C isotopologs studied in their ground vibrational states. However, no experimental data are available and there has been no study of the ethyl cyanide containing three ^{13}C atoms.

The present work is motivated by the relatively high abundance of ethyl cyanide in star-forming regions such as OMC-1 and Sgr B2 where other isotopologs have been observed. Our microwave studies of ethyl cyanide were extended to further isotopic species of this molecule. Since all three double-^{13}C ethyl cyanide isotopologs have already been detected in Sgr B2, we expect that ^{13}CH$_3^{13}$CH$_2^{13}$CN will also be observable. The characterization of isotopologs is also important from an astronomical point of view for determining isotope abundance ratios and the observations of the denser parts of the molecular clouds. Although many isotopic varieties containing ^{13}C have been spectroscopically characterized to allow their astronomical detection (i.e., for methyl formate Carvajal et al. 2009), the ^{13}C isotopologs of many other species cannot be identified in the ISM due to their lack of spectral recordings.

Several spectroscopic investigations were performed in support of this study, for example on iso-propyl cyanide (Müller et al. 2011), anti-ethanol with one ^{13}C (Bouchez et al. 2012), 2-aminopropionitrile (Møllendal et al. 2012), and n-butyl cyanide (Ordu et al. 2012). In addition, a number of spectroscopic studies have been prompted by the results of these line surveys, for example, on methyleneaminoacetonitrile (Motiyenko et al. 2013), aminoacetonitrile (Motoki et al. 2013), and 1,2-propanediol (Bossa et al. 2014).

This paper is organized as follows. The ^{13}CH$_3^{13}$CH$_2^{13}$CN synthesis and spectrometer description are reported in Sect. 2. The assignment of measured transitions and obtained spectroscopic parameters are presented in Sect. 3 and conclusions are given in Sect. 4.

2. Experimental details

2.1. Synthesis

Triethylene glycol (20 mL), potassium cyanide-^{13}C (K^{13}CN, 0.71 g, 10.7 mmol), and iodoethane-^{13}C$_2$ (1 g, 6.4 mmol) were introduced into into a three-necked flask equipped with a stirring bar, a reflux condenser, and a nitrogen inlet. The mixture was heated to 110 °C and stirred at this temperature for one hour. After cooling to room temperature, the flask was fitted on a vacuum line equipped with two U-tubes. The high boiling compounds were condensed in the first trap cooled at −30 °C and propanenitrile-^{13}C$_3$ (^{13}CH$_3^{13}$CH$_2^{13}$CN) was selectively condensed in the second trap cooled at −90 °C. Yield: 90% based on iodoethane. The nuclear magnetic resonance data (NMR) are given in Appendix A.

2.2. Measurements with Lille's fast scan DDS spectrometer

The spectra of triple ^{13}C ethyl cyanide were recorded in the ranges 150–330, 400–660, 780–990 GHz using a fully solid-state spectrometer. The spectrometer based on the direct digital synthesizers (DDS), described in detail by Alekseev et al. (2012), was used to measure millimeter and submillimeter wave spectra of the ^{13}CH$_3^{13}$CH$_2^{13}$CN which is thought to be present in detectable abundances in the ISM. The Lille spectrometer provides high-precision and fast-scan measurements. This system covers the 150–990 GHz range with small gaps and uses frequency multiplier chains from VDI Inc. to multiply the frequency of the radiation generated by an Agilent synthesizer operating around 12–20 GHz. A stainless absorption cell of approximately 2 m was used. The spectrometer was equipped with a 4.2 K He cooled QMC bolometer. The measurement accuracy is estimated at 30 kHz or 50 kHz depending on the frequency range.

3. Results

Ethyl cyanide and its isotopologs are asymmetric tops. Watson's A-reduced Hamiltonian in the I^r representation has been used. The rotational spectra were predicted and fit employing the SPCAT and SPFIT programs. ^{13}C isotopic substitution changes the reduced mass leading to a change in the moment of inertia and thus affecting the rotational spectrum. The ^{13}CH$_3^{13}$CH$_2^{13}$CN dipole moment was assumed to be unchanged upon isotopic substitution, and the values determined for ethyl cyanide given in (Kraśnicki & Kisiel 2011) of μ_a = 3.816 D and μ_b = 1.235 D were used.

3.1. Computational details: Theoretical prediction of the rotational spectra

Initially, ^{13}CH$_3^{13}$CH$_2^{13}$CN spectroscopic parameters (the ground-state rotational and the centrifugal distortion constants) have been theoretically evaluated with the Density functional theory (DFT) calculations at the B3LYP level of theory with a 6-311++g(3df, 2pd) basis set. The calculations were performed using Gaussian 09 suite of programs (Frisch et al. 2009). The theoretically optimized and experimental geometries (the bond angles, lengths and dihedrals), as well as the calculated and experimental frequencies are slightly different principally due to the use of finite basis sets, incomplete incorporation of electron correlation and the neglect of anharmonicity effects (Scott & Radom 1996). However, good agreement between the calculated and experimental frequencies can be obtained by applying scale factors.

The results of the performed DFT calculations may be sufficient to provide initial assignment of the recorded spectra. In this work, in order to obtain more accurate spectroscopic parameters for the prediction of the ^{13}CH$_3^{13}$CH$_2^{13}$CN rotational spectra, we used scaling factors based on the experimental data taken from the previous study of doubly ^{13}C-substituted isotopic species of ethyl cyanide (Margulès et al. 2016). We performed the following procedure. In a first step we calculated the "offsets", that is, the differences between the theoretical and experimental values for the rotational constants A, B, C and centrifugal distortion constants for ^{13}CH$_3$CH$_2^{13}$CN, ^{13}CH$_3^{13}$CH$_2$CN and CH$_3^{13}$CH$_2^{13}$CN from Margulès et al. (2016) (Table 1). The experimental errors for all three isotopologues are close to each other, with an average of 1.925% for rotational constant A and less than 0.5% for B and C. Then from our theoretical rotational constants A, B, and

Table 1. An example calculation of the offset value (the difference between calculated and observed rotational constants for $^{13}CH_3CH_2^{13}CN$).

Parameter (MHz)	B3LYP/6-311G ++(3df, 2pd)[a]	Experimental data[a]	Theory-experiment =offset (MHz)	Offset/experiment[b],%
A	27 840.439	27 314.27505(23)	526.16395	1.926
B	4556.6459	4572.983663(31)	−16.337763	−0.357
C	4114.3195	4112.858906(28)	1.460594	0.036

Notes. [a] Experimental data and DFT calculations are from Margulès et al. (2016), [b] experimental error.

Table 2. Determination of the rotational constants of $^{13}CH_3^{13}CH_2^{13}CN$ using the offset method which is based on the DFT calculations and previous experimental data for doubly ^{13}C-substituted isotopic species of ethyl cyanide.

Parameter (MHz)	B3LYP/6-311G ++(3df, 2pd)[a]	Scaled value[b]	Scaled value[c]	Scaled value[d]	Experimental data (this work)
A	27 206.198	26 680.0348	26 685.9764	26 691.67745	26 689.77113(20)
B	4542.2798	4558.64176	4558.130091	4559.150643	4558.824828(34)
C	4088.5480	4087.06373	4085.856899	4086.646415	4086.837211(35)

Notes. [a] Result of the DFT calculations, this work, [b] from $^{13}CH_3CH_2^{13}CN$, [c] from $CH_3^{13}CH_2^{13}CN$, [d] from $^{13}CH_3^{13}CH_2CN$.

C for $^{13}CH_3^{13}CH_2CN$ isotopologue we subtracted corresponding offset values of $^{13}CH_3CH_2^{13}CN$ (Table 2). The rotational constants resulting from this computational technique are compared with the experimental values in Table 2. The agreement between offset rotational constants and experimental ones is excellent (experimental error for A, B, C is less than 0.05%). It is interesting to note that offsets from $^{13}CH_3^{13}CH_2CN$ proved to give a more precise determination of rotational constants and the centrifugal distortion constants among other double ^{13}C-substituted species (with an experimental error less than 0.001% for A, B, C). This approach provided significantly more accurate parameters and is simple and straightforward.

3.2. Assignment and analysis

Given that all three sets of rotational constants have similar accuracy, one may use any of them for initial spectral assignment. In our case we used the set of constants scaled from $^{13}CH_3^{13}CH_2CN$ isotopic species. The scaled constants allowed a very accurate calculation of rotational transition frequencies. The lines involving low K_a and $J \leq 30$ transitions were predicted to be better than 5 MHz. Thus, the offset method is very efficient for derivation of rotational constants of isotopologues when the parent species have been previously investigated.

By adding new identified transitions to the fit we cyclically improved the predictions. The analysis was strict and straightforward even given the fact that the triple ^{13}C isotopologue shows a very dense and intense spectrum. Transitions with high K_a values sometimes were difficult to assign because of weakness or line blending. Over 4000 lines have been assigned and fitted with Watson's type A-and S-reduced Hamiltonian in I^r representation (Watson 1977) to a set of spectroscopic parameters. Table 4 lists all of the experimental rotational constants determined in the A- and S-reduction, and these are compared to the values from the theoretical calculations and to the experimental values of the main isotopologue from (Brauer et al. 2009). Both A- and S-reduction analyses from the present work demonstrate good similar results, with the S-reduction giving a slightly better rms than A-reduction (0.686 vs. 0.699 and 28.2 vs. 28.9) but S-reduction allowed to determine two additional parameters (l_4 and P_{JJK}). While all spectroscopic parameters of the
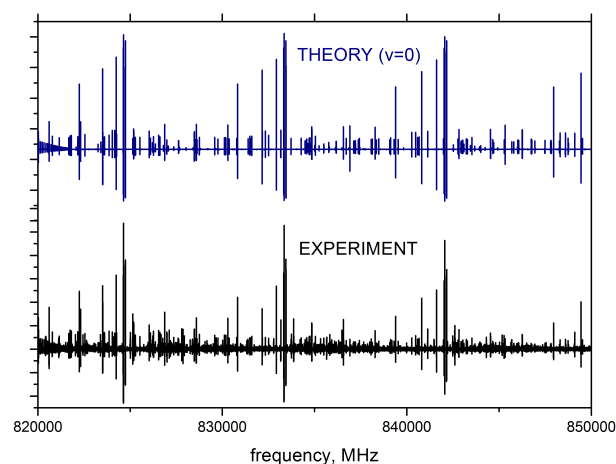
Fig. 1. Predicted (in blue) and observed (in black) rotational spectrum of $^{13}CH_3^{13}CH_2^{13}CN$ between 820 and 850 GHz. A slight inconsistency between predicted and observed spectrum, which may be visible for some strong lines, is due to source power and detector sensitivity variations.

$^{13}CH_3^{13}CH_2^{13}CN$ have been firmly determined with small relative uncertainties, some parameters were just barely determined, most notably l_{JK} and l_{KJ}. However, the values of these parameters appear to be reasonable in comparison with the corresponding values of the parent isotopic species. Figure 1 demonstrates generally good agreement between the $^{13}CH_3^{13}CH_2^{13}CN$ experimental spectra and the spectra predicted by the SPCAT program (the simulation is based upon the spectroscopic constants determined in this work). The complete list of measured rotational transitions of the ground state, presented in Table 3, is available at the CDS. Here, only a part of Table 3 is shown as an example.

4. Conclusions

Ethyl cyanide is a particularly abundant molecule in hot-core sources. In this study we have characterized the rotational spectrum of triply substituted ^{13}C ethyl cyanide for the first time. We measured and assigned about 4000 rotational lines of the $^{13}CH_3^{13}CH_2^{13}CN$ isotopologue in the frequency range from 150 to 990 GHz. The assigned lines involve rotational transitions

Table 3. Assigned rotational transitions of the ground state of $^{13}CH_3^{13}CH_2^{13}CN$.

J''	K_a''	K_c''	J'	K_a'	K_c'	Measured frequency (MHz)	Residual (MHz) A-reduction	Residual (MHz) S-reduction	Uncertainty (MHz)
38	3	36	38	2	37	200 285.7630	0.01376	0.00920	0.03000
57	4	53	57	3	54	229 870.1240	−0.04137	−0.02990	0.03000
52	5	48	52	4	49	238 942.8590	−0.04531	−0.03905	0.03000
63	4	59	63	3	60	282 864.5950	−0.02369	−0.00167	0.05000
73	3	70	72	4	69	616 550.5840	0.02133	0.01972	0.03000
91	12	80	90	12	79	785 668.5260	0.03476	0.03500	0.05000
103	8	95	102	8	94	895 732.2800	0.02518	−0.02945	0.05000
89	8	81	88	8	80	781 808.6790	−0.01659	−0.03092	0.03000
46	5	42	45	4	41	515 758.6710	0.00861	0.00848	0.03000
19	4	16	19	3	17	156 257.6970	−0.01303	−0.01426	0.03000
27	3	25	26	2	24	293 107.0420	−0.00584	−0.00657	0.03000

Notes. The full Table is available at the CDS.

Table 4. Spectroscopic parameters of triple ^{13}C isotopologue $^{13}CH_3^{13}CH_2^{13}CN$ of ethyl cyanide compared to normal species CH_3CH_2CN and calculated values.

Parameter (MHz)	$CH_3CH_2CN^a$ A-Reduction	$^{13}CH_3^{13}CH_2^{13}CN^b$ A-Reduction	Parameter (MHz)	$CH_3CH_2CN^c$ S-Reduction	$^{13}CH_3^{13}CH_2^{13}CN^d$ S-Reduction
A	27 663.68306 (49)	26 689.76996(20)	A	27 663.68206 (52)	26 689.77054(19)
B	4714.213344 (76)	4558.825014(37)	B	4714.187784 (80)	4558.801153(37)
C	4235.059644 (71)	4086.837093(34)	C	4235.085063 (74)	4086.860712(34)
$\Delta_K/10^3$	548.1249 (29)	529.2239(12)	$\Delta_K/10^3$	547.7770 (29)	528.9146(12)
$\Delta_{JK}/10^3$	−47.65818(37)	−46.03111(16)	$\Delta_{JK}/10^3$	−47.26453(43)	−45.65681(16)
$\Delta_J/10^3$	3.073531 (34)	2.881015(16)	$\Delta_J/10^3$	3.008009 (37)	2.818576(16)
$\delta_J/10^3$	0.6859957 (97)	0.6528276(71)	$d_1/10^3$	−0.685888 (10)	−0.6527335(71)
$\delta_K/10^3$	12.7394 (14)	11.87496(71)	$d_2/10^3$	−0.0327755 (35)	−0.0312208(18)
$\Phi_J/10^6$	0.0103841 (66)	0.0093548(37)	$\Phi_J/10^6$	0.0093563 (74)	0.0084246(36)
$\Phi_{JK}/10^6$	−0.02512 (39)	−0.03070(19)	$\Phi_{JK}/10^6$	−0.11860 (14)	−0.114088(51)
$\Phi_{KJ}/10^6$	−1.9066 (15)	−1.83630(86)	$\Phi_{KJ}/10^6$	−1.58325 (89)	−1.54415(43)
$\Phi_K/10^6$	31.6135 (98)	30.3780(39)	$\Phi_K/10^6$	31.3192 (97)	30.1772(38)
$\phi_J/10^6$	0.0039703 (28)	0.0036282(20)	$h_1/10^6$	0.0039036 (30)	0.0035668(20)
$\phi_{JK}/10^6$	0.10144 (37)	0.08599(19)	$h_2/10^6$	0.00051409(97)	0.00046290(49)
$\phi_K/10^6$	6.501 (26)	5.590(13)	$h_3/10^6$	0.00006318(29)	0.00005988(16)
$L_J/10^{12}$	−0.05217 (55)	−0.04413(34)	$L_J/10^{12}$	−0.04237 (63)	−0.03588(34)
$L_{JJK}/10^{12}$	−0.814 (25)	−0.286(15)	$L_{JJK}/10^{12}$	0.522 (19)	0.5287(61)
$L_{JK}/10^9$	−0.1202 (10)	−0.00859(10)	$L_{JK}/10^9$	−0.00657 (16)	−0.004750(81)
$L_{KKJ}/10^9$	0.3986 (30)	0.09649(59)	$L_{KKJ}/10^9$	0.08327 (65)	0.07915(51)
$L_K/10^9$	−2.383 (14)	−1.9356(41)	$L_K/10^9$	−2.105 (14)	−1.9329(41)
$l_J/10^{12}$	−0.02306 (30)	−0.02003(21)	$l_1/10^{12}$	−0.02135 (32)	−0.01868(21)
$l_{JK}/10^{12}$	−0.683 (24)	−0.274(11)	$l_2/10^{12}$	−0.004351 (62)	−0.003585(29)
$l_{KJ}/10^9$	−0.0441 (17)	−0.0114(10)	$l_3/10^{12}$	−0.001170 (23)	−0.001014(13)
$l_K/10^9$	−4.378 (39)	0	$l_4/10^{12}$	−0.0001380 (86)	−0.0001016(42)
$P_J/10^{18}$	0.264 (19)	0.220(11)	$P_J/10^{18}$	0.207 (20)	0.162(11)
$P_{JJK}/10^{18}$	0	0	$P_{JJK}/10^{18}$	−5.12 (90)	−4.33(27)
$P_{JK}/10^{15}$	0.925 (11)	1.142(37)	$P_{JK}/10^{15}$	0.1483 (79)	0.0672(35)
$P_{KJ}/10^{15}$	0	1.911(44)	$P_{KJ}/10^{15}$	−1.707 (92)	−1.920(42)
$P_{KKJ}/10^{12}$	0	−6.33(30)	$P_{KKJ}/10^{12}$		4.26(24)
$P_K/10^{12}$	0.1424 (70)	0	$P_K/10^{12}$	0.1132 (69)	0.0
$p_J/10^{18}$	0.114 (11)	0.1050(79)	$p_1/10^{18}$	0.083 (11)	0.0809(80)
$p_K/10^{12}$	−0.0883 (37)	0	$p_K/10^{12}$	−0.0883 (37)	0
N_{lines}^b	5798	4001			4001
σ^c (kHz)	79.757	28.911		81.371	28.242
$\sigma_{\text{weighted}}^d$	0.985890	0.699187		1.001450	0.686536

Notes. [a] A-reduced fit from (Brauer et al. 2009), [b] this work, A-Reduction, [c] S-reduced fit from (Brauer et al. 2009), [d] this work, S-Reduction.
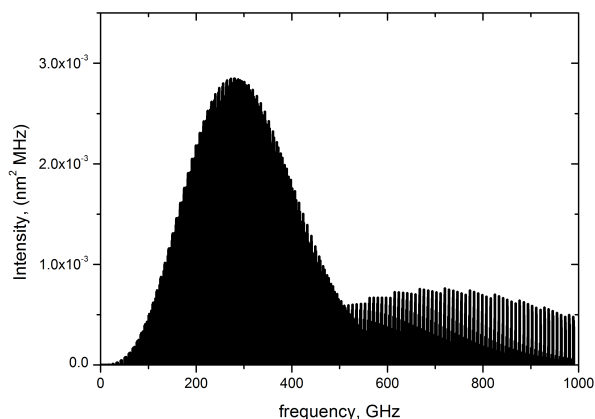
Fig. 2. Simulated spectrum of $^{13}CH_3^{13}CH_2^{13}CN$ at 150 K in the frequency range up to 1 THz.

with the rotational quantum numbers J up to 115 and K_a up to 39. The frequency range covered by direct measurements in this work corresponds to the range where the most intense lines may be observed under the characteristic temperature of 150 K in dense molecular clouds (see Fig. 2). Both A- and S-reduction Hamiltonians allow fitting all the assigned lines within experimental accuracy. The set of determined spectroscopic parameters should provide reliable predictions of the rotational transition frequencies of $^{13}CH_3^{13}CH_2^{13}CN$ up to 1.5 THz and for J and K_a quantum numbers up to 130 and 45 correspondingly.

Using the spectroscopic results of this work we searched for $^{13}CH_3^{13}CH_2^{13}CN$ in the EMoCA survey (Margulès et al. 2016) toward Sgr B2(N). We were not able to identify any isolated rotational transition of $^{13}CH_3^{13}CH_2^{13}CN$ above the detection limit in this survey. The ALMA data from the EMoCA survey suggest a column density ratio of each of the three doubly ^{13}C isotopologs to the triply substituted one of greater than eight (A. Belloche, priv. comm.). Given that we expect a $^{12}C/^{13}C$ ratio of ~25, the current sensitivity is too small for the detection of the triply substituted isotopolog by at least a factor of three. Nevertheless, the present laboratory data permit to search for triply ^{13}C-substituted ethyl cyanide throughout the entire frequency region of ALMA.

References

Alekseev, E. A., Motiyenko, R. A., & Margules, L. 2012, Radio Physics and Radio Astronomy, 3, 75
Altwegg, K., Balsiger, H., & Geiss, J. 1999, Space Sci. Rev., 90, 3
Belloche, A., Garrod, R. T., Müller, H. S. P., et al. 2009, A&A, 499, 215
Belloche, A., Muller, H. S. P., Menten, K. M., Schilke, P., & Comito, C. 2013, A&A, 559, A47
Belloche, A., Garrod, R. T., Müller, H. S. P., & Menten, K. M. 2014, Science, 345, 1584
Belloche, A., Muller, H. S. P., Garrod, R. T., & Menten, K. M. 2016, A&A, 587, A91
Bisschop, S. E., Jørgensen, J. K., van Dishoeck, E. F., & de Wachter, E. B. M. 2007, A&A, 465, 913

Bossa, J.-B., Ordu, M. H., Müller, H. S. P., Lewen, F., & Schlemmer, S. 2014, A&A, 570, A12
Bottinelli, S., Ceccarelli, C., Williams, J. P., & Lefloch, B. 2007, A&A, 463, 601
Bouchez, A., Walters, A., Müller, H. S. P., et al. 2012, J. Quant. Spectr. Rad. Transf., 113, 1148
Brauer, C. S., Pearson, J. C., Drouin, B. J., & Yu, S. 2009, ApJS, 184, 133
Carvajal, M., Margulès, L., Tercero, B., et al. 2009, A&A, 500, 1109
Cazaux, S., Tielens, A. G. G. M., Ceccarelli, C., et al. 2003, ApJ, 593, L51
Cordiner, M. A., Palmer, M. Y., Nixon, C. A., et al. 2015, ApJ, 800, L14
Daly, A. M., Bermúdez, C., López, A., et al. 2013, ApJ, 768, 81
Fortman, S. M., Medvedev, I. R., Neese, C. F., & De Lucia, F. C. 2010a, ApJ, 714, 476
Fortman, S. M., Medvedev, I. R., Neese, C. F., & De Lucia, F. C. 2010b, ApJ, 725, 1682
Friedel, D. N., & Widicus Weaver, S. L. 2012, ApJS, 201, 17
Frisch, M., Trucks, G., Schlegel, H. B., et al. 2009, Gaussian 09, Revision A. 02 (Wallingford Inc., CT)
Fukuyama, Y., Odashima, H., Takagi, K., & Tsunekawa, S. 1996, ApJS, 104, 329
Garrod, R. T., Widicus Weaver, S. L., & Herbst, E. 2008, ApJ, 682, 283
Gibb, E., Nummelin, A., Irvine, W. M., Whittet, D. C. B., & Bergman, P. 2000a, ApJ, 545, 309
Gibb, E., Nummelin, A., Irvine, W. M., Whittet, D. C. B., & Bergman, P. 2000b, ApJ, 545, 309
Heise, H. M., Lutz, H., & Dreizler, H. 1974, Z. Naturforschung A, 29, 1345
Heise, H. M., Winther, F., & Lutz, H. 1981, J. Mol. Spectr., 90, 531
Hollis, J. M., Pedelty, J. A., Boboltz, D. A., et al. 2003, ApJ, 596, L235
Johnson, D. R., Lovas, F. J., Gottlieb, C. A., et al. 1977, ApJ, 218, 370
Kraśnicki, A., & Kisiel, Z. 2011, J. Mol. Spectr., 270, 83
Kuan, Y.-J., Mehringer, D. M., & Snyder, L. E. 1996, ApJ, 459, 619
Laas, J. C., Garrod, R. T., Herbst, E., & Widicus Weaver, S. L. 2011, ApJ, 728, 71
Lovas, F. J. 1982, J. Phys. Chem. Ref. Data, 11, 251
Margulès, L., Motiyenko, R., Demyk, K., et al. 2009, A&A, 493, 565
Margulès, L., Belloche, A., Müller, H. S. P., et al. 2016, A&A, 590, A93
Mehringer, D. M., Pearson, J. C., Keene, J., & Phillips, T. G. 2004, ApJ, 608, 306
Miao, Y., & Snyder, L. E. 1997, ApJ, 480, L67
Miao, Y., Mehringer, D. M., Kuan, Y.-J., & Snyder, L. E. 1995, ApJ, 445, L59
Møllendal, H., Margulès, L., Belloche, A., et al. 2012, A&A, 538, A51
Motiyenko, R. A., Margulès, L., & Guillemin, J.-C. 2013, A&A, 559, A44
Motoki, Y., Tsunoda, Y., Ozeki, H., & Kobayashi, K. 2013, ApJS, 209, 23
Müller, H. S. P., Belloche, A., Menten, K. M., Comito, C., & Schilke, P. 2008, J. Mol. Spectr., 251, 319
Müller, H. S. P., Coutens, A., Walters, A., Grabow, J.-U., & Schlemmer, S. 2011, J. Mol. Spectr., 267, 100
Nummelin, A., Bergman, P., Hjalmarson, Å., et al. 1998, ApJS, 117, 427
Nummelin, A., Bergman, P., Hjalmarson, Å., et al. 2000, ApJS, 128, 213
Ordu, M. H., Müller, H. S. P., Walters, A., et al. 2012, A&A, 541, A121
Pearson, J. C., Sastry, K. V. L. N., Herbst, E., & De Lucia, F. C. 1994, ApJS, 93, 589
Richard, C., Margulès, L., Motiyenko, R. A., & Guillemin, J.-C. 2012, A&A, 543, A135
Schoier, F. L., van der Tak, F. F. S., van Dishoeck, E. F., & Black, J. H. 2005, A&A, 432, 369
Scott, A. P., & Radom, L. 1996, J. Phys. Chem., 100, 16502
Snyder, L. E. 2006, Proc. Natl. Acad. Sci. USA, 103, 12243

Appendix A: Propanenitrile-$^{13}C_3$

^{1}H NMR (CDCl$_3$, 400 MHz) δ 1.29 (dddt, $^1J_{CH}$ = 126.1 Hz, $^3J_{CH}$ = 6.6 Hz, $^2J_{CH}$ = 4.6 Hz, $^3J_{HH}$ = 7.7 Hz, CH$_3$), 2.35 (tdq, 2H, $^1J_{CH}$ = 135.0 Hz, $^2J_{CH}$ = 9.7 Hz, $^3J_{HH}$ = 7.7 Hz, CH$_2$). ^{13}C NMR (CDCl$_3$, 100 MHz) δ 10.5 (ddq, $^1J_{CC}$ = 33.5 Hz, $^2J_{CC}$ = 4.4 Hz, $^1J_{CH}$ = 126.1 Hz, CH$_3$), 11.1 (ddt, $^1J_{CC}$ = 48.7 Hz, $^1J_{CC}$ = 33.5 Hz, $^1J_{CH}$ = 135.0 Hz, CH$_2$); 120.8 (dd, $^1J_{CC}$ = 48.7 Hz, $^2J_{CC}$ = 4.4 Hz, CN).

6.3 Methoxy isocyanate, CH$_3$ONCO

6.3.1 Astrophysical interest and motivation

Several organic isocyanates as methyl isocyanate CH$_3$NCO [136–139], isocyanic acid HNCO [140–144] with its isomers and deuterated species [145, 146] have been already observed in the interstellar medium.

The current study of methoxy isocyanate, CH$_3$ONCO, is motivated by the relatively high abundance of methyl isocyanate, CH$_3$NCO in star-forming regions like OMC-1 and Sgr B2 where it has been observed [147, 148]. Neither identification or laboratory rotational spectra of CH$_3$ONCO has been reported up to now. The set of the spectroscopic constants of CH$_3$ONCO will allow us to attempt the first rigorous search for this species in space. The present investigation also follows the study on acethyl isocyanate [149].

Isocyanates are chemical compounds from the isocyanic acid, having -NCO groups in its structure. The isocyanic group represents a linear structure with double bonds between C = N and C = O on the same axis. A spectroscopic studies on isocyanates mainly have been performed in a microwave domain [150–160] in a laboratory. The organic isocyanate derivatives are poorly studied in the millimeter-wave domain. This lack of data could be the reason of their non detection (aside from those mentioned above) in the ISM up to now. This is mainly due to the difficulties to synthesize this kind of the molecules and their poor kinetic stability, thus making the spectra recording particularly challenging.

From the astronomical point of view, CH$_3$ONCO contains a CH$_3$O- methoxy radical functional group. The methoxy radical CH$_3$O has been detected in the ISM towards the cold core B1-b [161] and may be an important tracer of methanol related chemistry and the methanol in its turn is a key molecule in reactions leading to further complexity.

Beside detecting molecules we also want to understand how they are formed. CH$_3$ONCO is astronomically interesting by its analogy to CH$_3$NCO which could be formed through the grain surface reactions [136, 162]:

$$NCO + CH_3 \rightarrow CH_3NCO \qquad Belloche \quad et \quad al. \quad (2017) \quad [162]$$
$$HNCO + CH_3 \rightarrow CH_3NCO + H \qquad Cernicharo \quad et \quad al. \quad (2016) \quad [136]$$
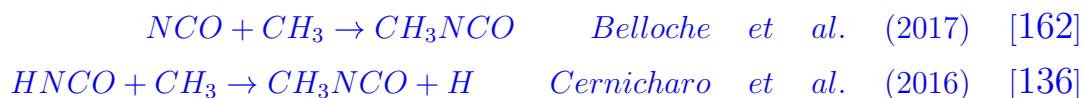
By analogy of reactions leading to formation of CH$_3$NCO in ISM, we can assume the formation path of CH$_3$ONCO is the reaction between isocyanato radical NCO and methoxy radical CH$_3$O:

$$NCO + CH_3O \rightarrow CH_3ONCO$$

Studying structurally related molecules can help to understand the star-formation chemistry in the ISM. Using laboratory data on CH$_3$ONCO astronomers could suggest what other molecules may be present and which processes take place in the ISM for their formation.

6.3.2 Quantum chemical calculations
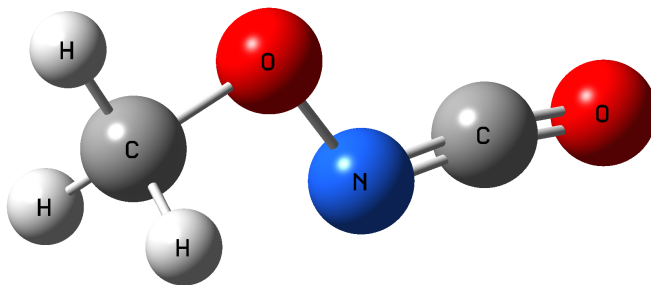
Figure 6.1 – Molecule of methoxy isocyanate, CH$_3$ONCO

In order to provide an initial basis for spectral assignments, the harmonic and anharmonic force field calculations were performed using Gaussian 09 program [163].

Methoxy isocyanate is a near-prolate (Ray's asymmetry parameter, κ=-0.995) symmetric top molecule with C_s point group symmetry, its molecular geometry optimization structure is shown in Fig. 6.1. The spectroscopic parameters (rotational, quartic and sextic centrifugal distortion constants), vibration-rotation interaction constants, have been theoretically evaluated with the DFT method at the B3LYP level of theory employing a 6-311++g(3df,2pd) basis set. The anharmonic frequencies of the vibrational modes were also calculated. The symmetry type of the vibrational modes (A' or A'') of CH$_3$ONCO as well as vibrational energies were also determined. The value of the barrier to internal rotation of the methyl group of CH$_3$ONCO, V_3 is predicted to be about 800 cm^{-1}, it is high compared to that one of CH$_3$NCO, $V_3 = 21$ cm^{-1} [147] and $V_3 = 356$ cm^{-1} of CH$_3$CONCO [149, 150]. In Doppler limited resolution mode as with FSS, no A-E splittings due to the internal rotation of the methyl group of CH$_3$ONCO were observed. The

values of CH_3ONCO dipole moment $\mu_a = 2.32$ D and $\mu_b = 0.24$ D were also determined from the DFT calculations.

Methoxy isocyanate has three low-lying vibrational modes, skeletal torsion ν_{18}, in-plane bending ν_{11} and methyl torsion ν_{17} lying, according to the DFT calculation, at $\approx$ 59 cm^{-1}, $\approx$ 174 cm^{-1} and 235 cm^{-1} above the ground state, respectively. Vibrational modes are illustrated at Fig. **??**. The symmetry types are given according to the C_s point group.
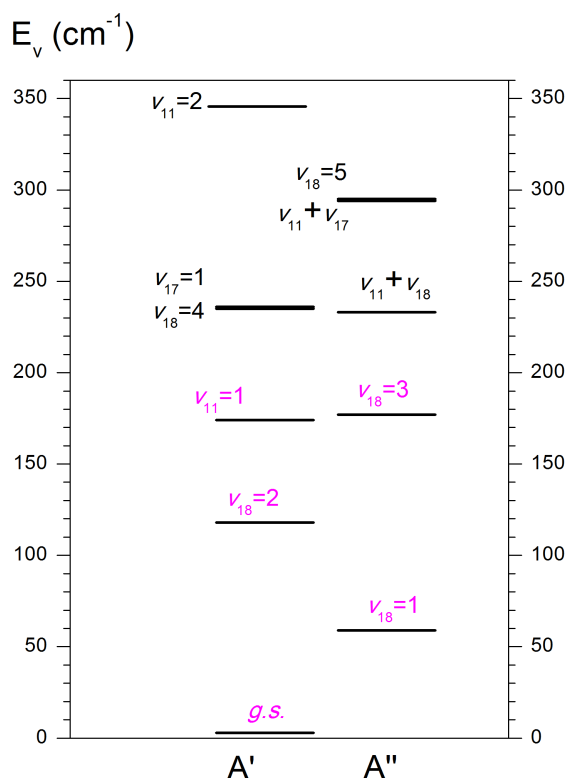
Figure 6.2 – The scheme of the lowest vibrational states in methoxy isocyanate.

In general, the possible interactions between two states depends on the symmetry classification of the states. It is convenient to give the multiplication table of the irreducible representations of the C_s group. Table 6.1 will allow to determine the symmetry of vibrational states of CH_3ONCO.

Table 6.1 – Multiplication table of irreducible representations for C_s point group.

$\Gamma \otimes \Gamma'$	A'	A''
A'	A'	A''
A''	A''	A'

Let us determine the symmetry of the vibrational states for methoxyisocyanate that

belongs to the C_s point group. Molecules belonging to the C_s point group in their ground state (and in-plane vibrations) have A' symmetry, since the direct product of any irreducible representation in C_s group with itself is A', this means that the ground state of methoxyisocyanate ν_{18} will belong to A'. Out-of-plane vibrations like ν_{18} and ν_{17} (both torsion modes) have A'' symmetry. For the ν_{18} mode of species A'', for the 3 lowest vibrational states $\nu_{18}=1$, $\nu_{18}=2$ and $\nu_{18}=3$ we have

$$\Gamma_{(\nu_{18}=1)} = A''$$

$$\Gamma_{(\nu_{18}=2)} = A'' \otimes A'' = A'$$

Similarly

$$\Gamma_{(\nu_{18}=3)} = A'' \otimes A'' \otimes A'' = A''$$

In-plane vibration like ν_{11} (bending) has A' symmetry. The symmetry of all the vibrational states of ν_{11}, $\nu_{11}=1,2,3,..$ of CH₃ONCO will be A'.

The irreducible representation $\Gamma \mid \nu_i \rangle$ to which such a state of mode ν_{18} belongs obtained as

$$\Gamma \mid \nu_i \rangle = \begin{cases} A' & \nu_{18} \quad even \\ A'' & \nu_{18} \quad odd \end{cases}$$

Notes "even" and "odd" indicate the value of the quantum number v.

Vibrational states belonging to different symmetry species may be connected by a- and b-type Coriolis interaction terms, and excited states with the same symmetry species may be coupled through c-type Coriolis and Fermi interactions. Means that states $\nu_{18}=3$ and $\nu_{18}=1$ of CH₃ONCO will be coupled through a- and b-type Coriolis interactions, and states $\nu_{18}=2$ and $\nu_{11}=1$ - through c-type Coriolis and Fermi.

6.3.3 Experiment

1 Synthesis

The scheme of experiment is illustrated in Fig. 6.3. The experimental spectra of CH₃ONCO was recorded in the millimeter-wave range (75-105 GHz and 150-330 GHz) using FSS. Its detailed description was given before in Chapter 2. Methoxy isocyanate sample was synthesized by flash vacuum pyrolysis of N-Methoxy-carbonyl-O-methylhydroxylamine (MeOC(O)NHOMe). Precursor at room temperature (about 300K) was put to the quartz tube in the oven at a temperature of about 800 K, connected directly to the gas cell. The
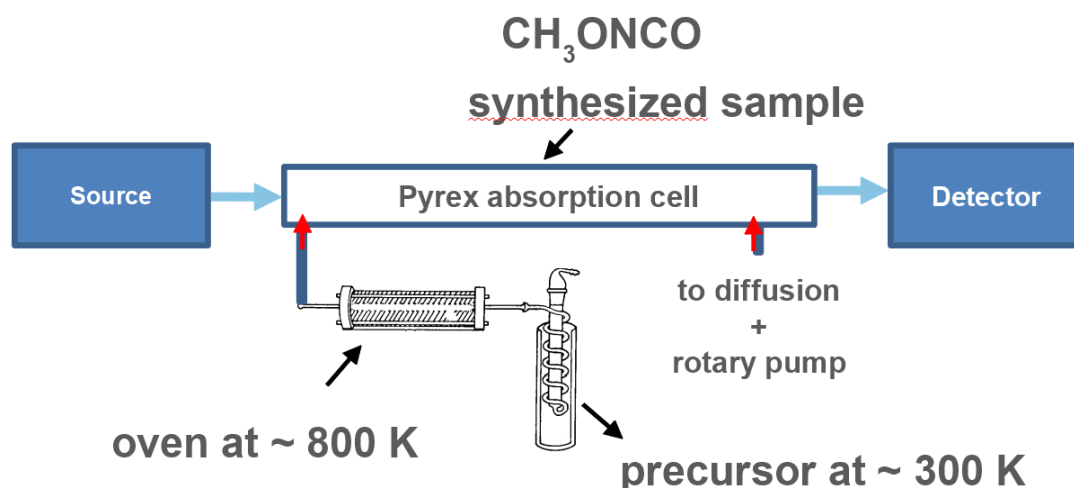
Figure 6.3 – Experimental setup (simplified) for pyrolysis process of methoxyisocyanate. Source and detector are as in the standard configuration of FSS.

CH$_3$ONCO molecule turned out to be unstable at the room temperature thus measurements were made in a flow mode and the experimental spectra were recorded *"in situ"*. Absorption cell from the Pyrex glass of approximately 1.4 m long was used, in order to reduce molecular decomposition. The fast-scan technique was quite important for the studies of the unstable species like methoxyisocyanate, it allowed the optimization of the experimental conditions in a minimum amount of time and rapid data acquisition. The best signal-to-noise ratio was found by adjusting gas pressure in the absorption cell that was between 20 and 40 μbar.

2   Spectra

Fig. 6.4 gives examples of the spectra of CH$_3$ONCO in a frequency range from 150 to 220 GHz. This range of 70 GHz was recorded in 3 hours with a step of 36 kHz. The accuracy of the frequency measurement of the recorded spectra below 400 GHz is estimated to be 30 kHz for isolated lines and can be as poor as 100 kHz for blended or very weak lines. CH$_3$ONCO produces very rich and dense spectra, making the identification complicated. The rotational spectrum of methoxy isocyanate is dominated by a strong series of ^aR-type transitions (i.e. ΔK_a=0 and ΔK_c=1), since the dipole moment component along the a-axis ($\mu_a = 2.32$ D) is much larger than the component along the b-axis ($\mu_b = 0.24$ D). We also found methanol (CH$_3$OH) and isocyanic acid (HNCO) as impurities, which are likely decomposition products from the pyrolysis process.
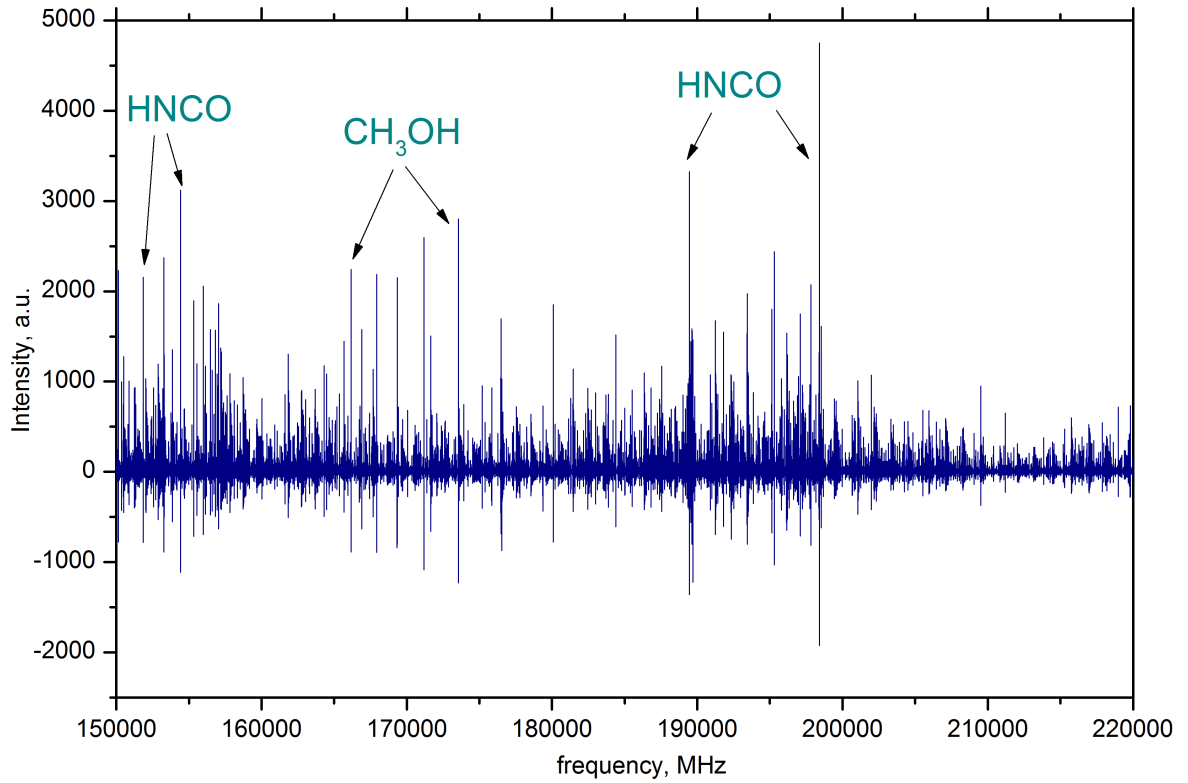
Figure 6.4 – Examples of the spectra of methoxyisocyanate, recorded in a frequency range from 150 to 220 GHz. Step is chosen to 36 kHz, current sample contains ∼280 000 points, so that each 10 GHz is recorded in ∼26 minutes.

6.3.4 Assignment

From an observational perspective, the rotational spectrum of methoxy isocyanate in its ground vibrational state is most important as it demonstrates the most intense lines under conditions prevailing in diffuse interstellar clouds. First, 187 transitions from 75 to 95 and 150 to 190 GHz, belonging to the ground state, with J varying from 15 to 38, and K_a from 0 to 9 were identified, included and correctly fitted with experimental uncertainty. Next, systematically increasing K_a'' we added new identified transitions to the fit. The Figs. 6.6 give spectra example of CH$_3$ONCO spectra recorded around 162 GHz with predictions, based on a single state treatment for the ground state. Observed and predicted transitions of the ground state are labelled with different K_a'' for J= 32 → 31. At K_a=12 and 13 we observed a significant disagreement between measured and predicted transition frequencies (-22 MHz for K_a=12; - 116 MHz for K_a=13 and+ 286 MHz for K_a=14). This disagreement between measurements and predictions was not resolved by adding more high-order parameters. We assumed that a perturbation occurs, shifting all of the transitions and affecting the high-resolution spectra. Analysis of such
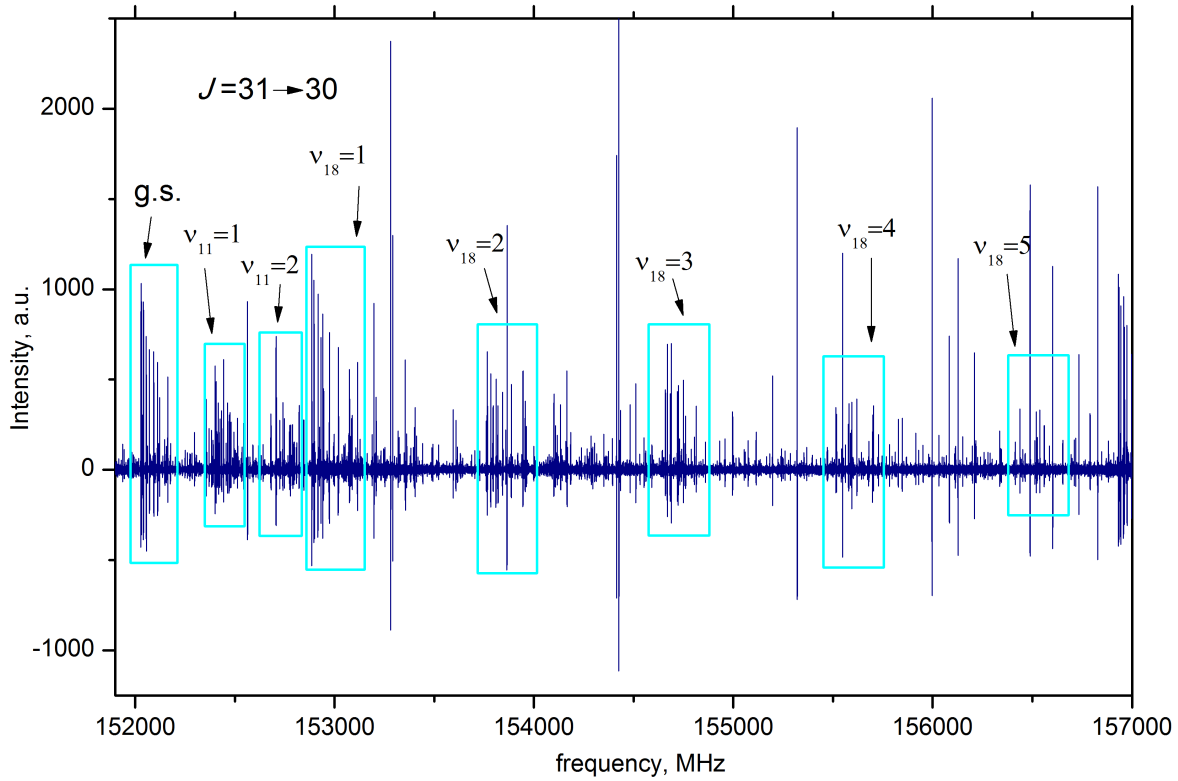
Figure 6.5 – Examples of the spectrum in frequency range from 152 to 157 GHz.

rotational spectrum will be complicated: even the relatively low K_a levels of the ground state are perturbed.

Besides strong lines, associated with the ground state of CH_3ONCO, rotational spectra in 6 excited states corresponding to $\nu_{18}=1$, $\nu_{18}=2$, $\nu_{18}=3$, $\nu_{18}=4$, , $\nu_{18}=5$, $\nu_{11}=1$ and $\nu_{11}=2$ were also observed. These 7 vibrational states below 300 cm^{-1} (Fig. 6.2) are sufficiently populated at a room temperature besides the vibrational ground state and produce a very dense spectrum (Fig. 6.5). Considering Boltzmann distribution, at 300 K, the relative intensities of $\nu_{18}=1$ and $\nu_{18}=2$ are, respectively, 78% and 62%. These vibrational states would represent an interest for astrophysical observations. (In the high-density Sgr B2, level populations are characterized by rotation temperatures around 200 K. At this temperature, the lower vibrationally excited states of a large number of complex molecules are populated.)

CH_3ONCO has a difficult analytical problem since the C_s symmetry of the molecule allows a wide variety of possible perturbations. The vibrationally excited states of CH_3ONCO, studied during this thesis, are coupled through strong $a-$ and $b-$ Coriolis resonances because the energy separation between the resonating states is quite small ($\Delta E \approx 50$ cm^{-1}) and because the values of the first order coupling parameters (ξ^α) involved in the expan-
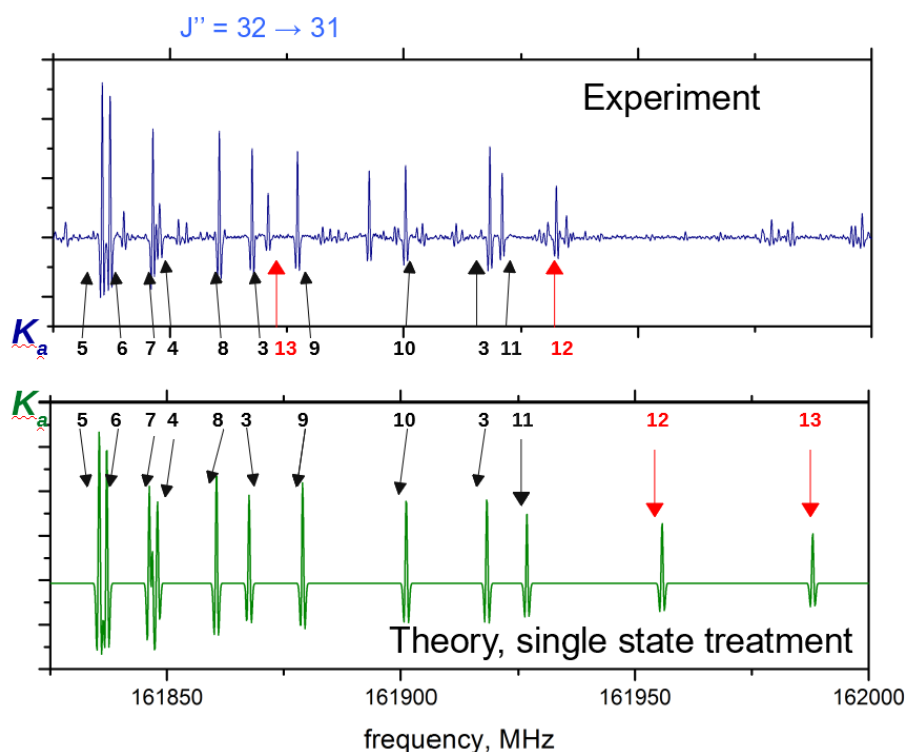
Figure 6.6 – Illustration of disagreement between experimental and predicted transitions due to the perturbations. Predictions are based on the the single state fit treatment up to K_a= 11 for the ground state.

sion of the Coriolis resonances, are large.

The Coriolis interaction arises from the coupling of the total rotation to the in-plane bend under the C_S group leading to c-symmetry Coriolis interactions. The ground state belongs to the A' and the first excited state of the lowest lying mode (ν_{18}=1) to the A'' representation of the C_s symmetry group for the CH_3ONCO molecule, so that Coriolis coupling between the two states is possible about both the a- and the b- axes. In addition, the second excited state of the torsion mode ν_{18}=2 (A') can interact by means of the Coriolis coupling with ν_{18}=1, ν_{18}=3 (a- and the b- type) and ground state (c-type). ν_{18}=3 at the same time, is very close in energy to ν_{11}=1 and so on, leading to ladder resonances. In this way, because of Coriolis coupling, it is necessary to treat ground and lowest excited states of ν_{18}=1, ν_{18}=2 etc. simultaneously.

Due to the interaction between the overall rotation and the vibrational modes ν_{18} and ν_{11} , the rotational spectrum of the CH_3ONCO is strongly perturbed. These perturbations are due to Coriolis interaction between vibrational states that appear in shifting frequency predictions and intensities distortions of the lines. The problem is that perturbations affect rotational transitions with relatively low values of K_a, even for the ground state. To facilitate the analysis of the perturbations occurring in CH_3ONCO spectra because of the

Coriolis interactions, two approaches have been used: Loomis-Wood diagrams technique and energy plots. Plots of energy level are based on .EGY file output from SPFIT/SPCAT program [164]. .EGY file provide output of energy levels (in wavenumbers) for K_a'' level and quantum number J'' for every vibrational state. Fig. 6.7 represents the energy plots for different K_a levels of the ground and 4 vibrational states ($\nu_{18}=1$, $\nu_{18}=2$, $\nu_{18}=3$, $\nu_{11}=1$) of methoxyisocyanate below 400 cm^{-1}. Analyzing the plot, one can carefully find vibrational levels of CH_3ONCO that are close in energy. As seen from Fig. 6.7, rotational levels with $K_a''=9$ of the ground state are close in energy with $K_a''=7$ levels of $\nu_{18}=1$, $K_a''=10$ of the ground state are close with $K_a''=6$ of $\nu_{18}=2$, $K_a''=9$ of $\nu_{18}=1$ with $K_a''=7$ of $\nu_{18}=2$ and so on. With the help of energy plots, the states that are perturbed can be added to a global fit with proper interaction parameters.
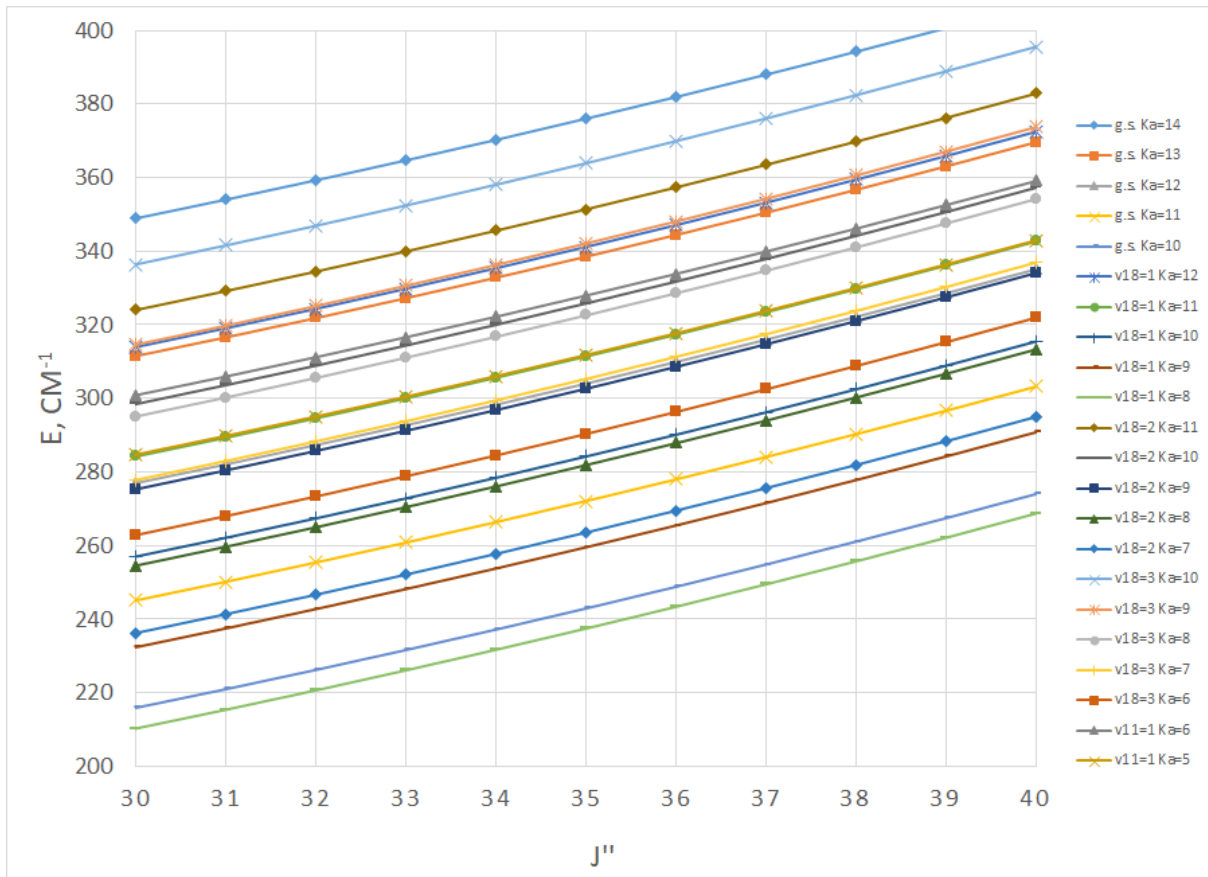
Figure 6.7 – Plots are energies values $E(\text{cm}^{-1})$ as the function of J''

Second technique to recognize perturbations between vibrational levels, was using Loomis-Wood diagrams. Loomis-Wood diagrams is a helpful tool in assignment and analyzing the molecular spectra. Diagram corresponds to series of the transitions in the spectrum such that lines belonging to the same series of transitions are placed on one line. Examples of Loomis-Wood diagrams for $K_a=13$ of ground state and $K_a=12$ of $\nu_{18}=1$ are

given in Fig. 6.8. Similarly for K_a=10 of ν_{18}=2 and K_a=8 of ν_{18}=3 is shown at Fig.6.9. As may been seen, the mirror nature of line positions as a function of J'' reveal the evidence that states are coupled through the Coriolis interaction.
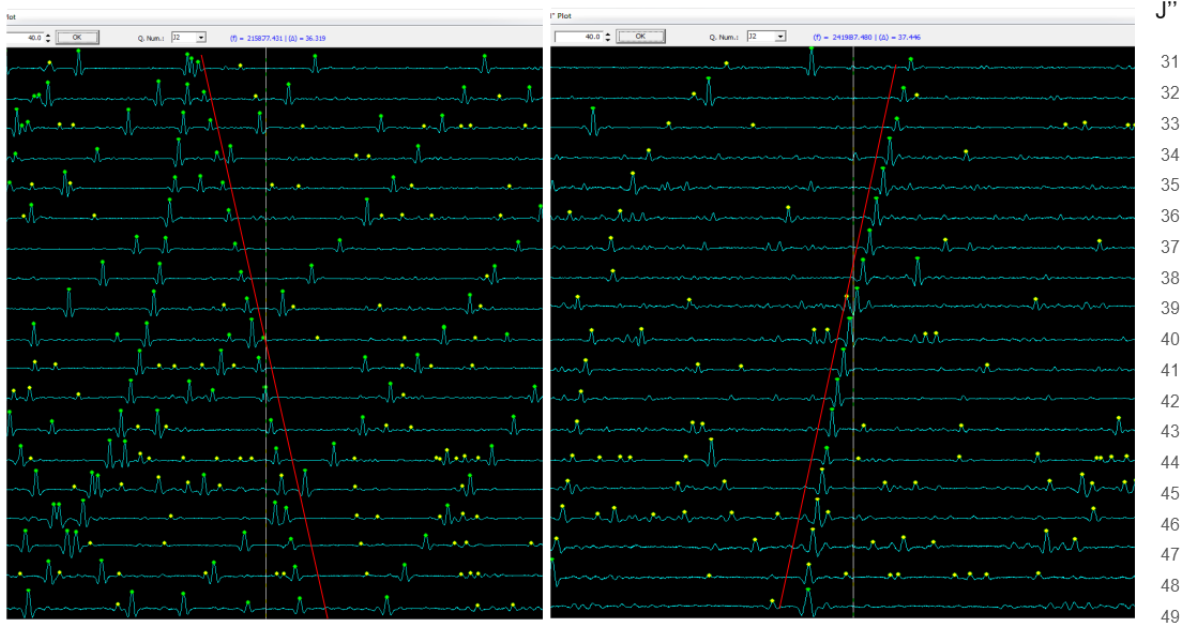
Figure 6.8 – Illustration of the mirror-image dependence of the Coriolis interaction between K_a=13 ^aR-type transitions in ground state (in the left) and K_a=12 ν_{18}=1 (in the right)

6.3.5   Theoretical model of Hamiltonian

The model which we use for the analysis of CH$_3$ONCO spectrum is the effective Hamiltonian in the presence of rotational-vibrational interactions. It is constructed in a standard block matrix form. The diagonal terms $H_v^{(rot)}$, $H_{v'}^{(rot)}$, $H_{v''}^{(rot)}$ etc. consist of the standard Watson's S-reduction Hamiltonian in I^r representation (Watson 1977), augmented by the energy differences $\Delta E_{v,v'}$=$E_{v'}$-E_v, $\Delta E_{v',v''}$=$E_{v''}$-$E_{v'}$, etc. and off- diagonal coupling terms $H_{v,v'}^{Cor}$, $H_{v',v''}^{Cor}$,.. representing second-order Coriolis interactions between vibrational states v, v', v'' and so on. Expressions for terms are given by Eq. 5.9, 5.11 and 5.12.

Hamiltonian for the coupled fit of the five vibrational states, ground state, $\nu_{18} = 1$, $\nu_{18} = 2$, $\nu_{18} = 3$, $\nu_{11} = 1$, analyzed in the current work, can be written as:
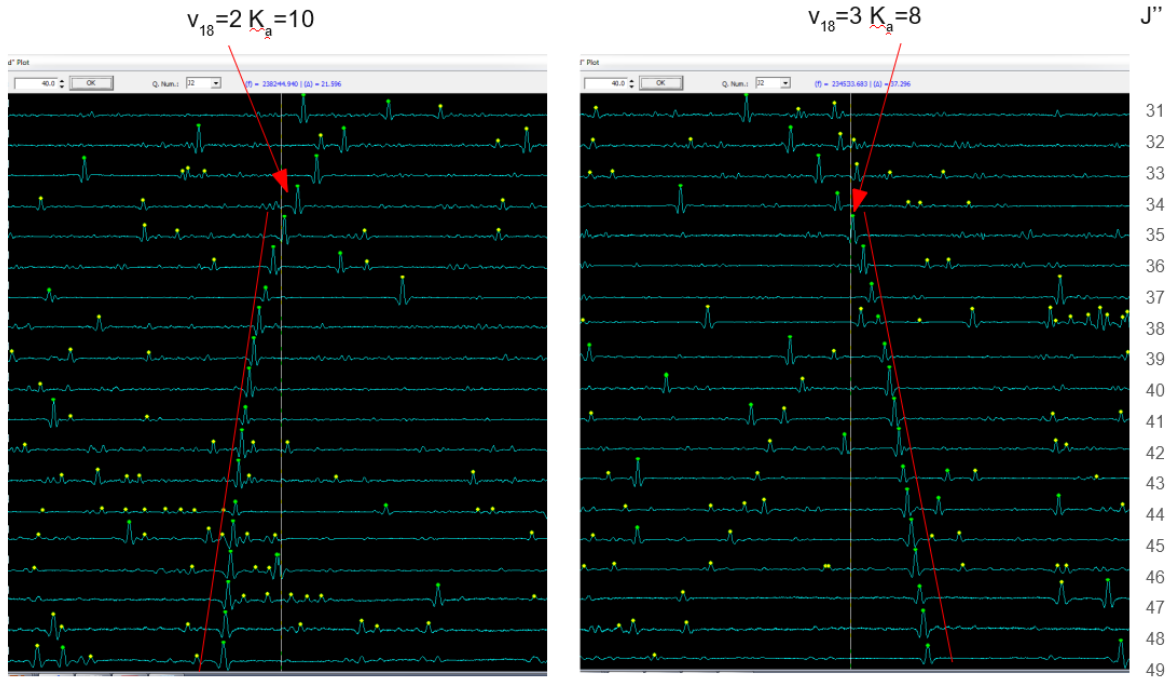
Figure 6.9 – Loomis-Wood diagrams, demonstrating Coriolis coupling between ν_{18}=2 and ν_{18}=3

$$
H = \begin{pmatrix}
H_{g.s}^{(rot)} & H_{v,v'}^{Cor} & 0 & 0 & 0 \\
H_{v,v'}^{Cor} & H_{\nu_{18}=1}^{(rot)} + \Delta E_{v,v'} & H_{v',v''}^{Cor} & 0 & .0 \\
0 & H_{v',v''}^{Cor} & H_{\nu_{18}=2}^{(rot)} + \Delta E_{v',v''} & H_{v'',v'''}^{Cor} & ... \\
0 & 0 & H_{v'',v'''}^{Cor} & H_{\nu_{18}=3}^{(rot)} + \Delta E_{v'',v'''} & H_{v''',v''''}^{Cor} \\
0 & 0 & 0 & H_{v''',v''''}^{Cor} & H_{\nu_{11}=1}^{(rot)} + \Delta E_{v''',v''''} & ...
\end{pmatrix}
$$

The computer SPFIT program [164] used in this work allows fitting symmetric top rotors with vibration-rotation interactions between excited states arising from the presence of Coriolis coupling. Coriolis coupling parameters between different vibrational levels and energy differences between such levels can also be simultaneously fitted and thus spectra can be described reasonably well. Pickett's program also allows to analyse several vibrational states simultaneously by adding a vibrational energy term E to the energy expression and to determine appropriate interaction terms (G_a, G_b etc).

6.3.6   Analysis

The rotational transitions of ν_{18}=1, ν_{18}=2, ν_{18}=3 and ν_{11}=1 were assigned in a manner similar to the ground state, starting from the lines with $K_a'' = 0$ and 1. The assignment

was facilitated by the use of the centrifugal distortion constants of the ground state as a basis for the initial frequency predictions. All of lines with $K_a'' \geqslant 6$ were found to be perturbed. Initially, we performed single fits for the ground and every vibrational state in which we included only transitions, not affected by perturbations. Then we consistently consequentially combined the fits and added perturbed transitions with interaction parameters, that are Coriolis coupling constants and energy differences between the states ΔE. We started from the value of ΔE between vibrational states obtained from DFT calculations and searched for the best fitting solution by manually changing ΔE. In this manner, eventually, we performed global fit.

6.3.7 Results

Transitions of the ground state with K_a'' levels of 12, 13 and 14 have been successfully assigned and added to a 5-state fit. K_a''=15 and 16 were also found, but no possible combination of parameters was found that allowed to fit them correctly. Moreover, if these transitions were included, some higher-order centrifugal distortion constants became undetermined and some lines of lower K_a'' levels that fit previously had become badly predicted. Lines of higher K_a'' were too difficult to be observed either because their intensities were too weak or Coriolis interactions for high K_a levels were too strong to find perturbed transitions in a spectra. The dataset for the ν_{18}=1, ν_{18}=2, ν_{18}=3 and ν_{11}=1 consists, respectively, of 439, 291, 166 and 157 lines with similar J'' coverage as the ground state and with maximum K_a'' values of, respectively, 12, 9, 10 and 5.

The fit for the ground state of CH$_3$ONCO include lines up to K_a''=14. Thus the highest K_a'' for the ground state, included in the final fit, is 14, with a maximum J'' of 70. The final dataset consists of 1720 lines corresponding to xxxx rotational transitions. Table 6.2 gives a complete set of spectroscopic parameters of CH$_3$ONCO in the ground and lowest vibrationally excited states ν_{18}=1, ν_{18}=2, ν_{18}=3 and ν_{11}=1, determined from the global fit, in comparison with the values resulting from the DFT calculations. The weighted standard deviation of 1.20 and a rms of 55.4 kHz indicate that, on average, the data have been fitted within experimental uncertainties.

The spectroscopic parameters for excited states of methoxy iscyanate are reasonably similar to that of the ground state. Precise energies of the vibrations (ΔE), and Coriolis interaction constants (F_{ca}, F_{bc}, F_{ab}, G_a, G_b) between vibrational states were determined from the fit. By inspection of a correlation matrix correlations between G_a, G_b and the related rotational constants A and B corresponding to the rotation about the coupling axis have been revealed.

While all spectroscopic parameters of the CH$_3$ONCO have been firmly determined with small relative uncertainties, some parameters were just barely determined, most

notably d_2. However, the values of this parameter appear to be reasonable in comparison with the corresponding calculated values.

Table 6.2 – Spectroscopic constants for the ground and three lowest vibrationally excited states: $\nu_{18}=1$, $\nu_{18}=2$, $\nu_{18}=3$ and $\nu_{11}=1$ of methoxy isocyanate, CH_3ONCO included in the global 5-state fit.

Parameter , MHz	B3LYP 6-311++g(3df,2pd)	ground state	$\nu_{18}=1$	$\nu_{18}=2$	$\nu_{18}=3$	$\nu_{11}=1$
A	45099.157	44589.81(29)	41665.22(50)	39205.68(57)	37079.4(16)	46493.5(13)
B	2358.3547	2498.23790(27)	2508.13821(42)	2518.37320(60)	2528.9484(74)	2505.7203(74)
C	2273.8254	2405.33930(24)	2423.01749(42)	2441.31340(67)	2460.2418(10)	2409.54361(87)
$\Delta_J/10^3$	0.22364685	0.36011(16)	0.44996(23)	0.54351(14)	0.64851(25)	0.37608(26)
$\Delta_{JK}/10^3$	-43.128583	-20.4377(66)	-31.40(23)	-31.222(45)	-35.90(25)	-23.05(11)
$\Delta_K/10^3$	782.59236	2194.(29)	1970.(36)	[1245.081963]	[1245.081963]	[1245.081963]
$d_1/10^3$		-0.020995(15)	-0.004614(44	0.014735(68)	0.04227(22)	-0.02406(10)
$d_2/10^6$		-0.00241(10)	0.00121(10)	0.003082(24)	0.005395(41)	0.000753(40)
$H_J/10^9$		0.0006816(62)	0.001667(12	-0.4303(25)	-0.7475(56)	0.414(28)
$H_{JK}/10^6$		-0.1695(16)	-0.2552(40)	33.47(34)	53.1(10)	-57.7(21)
$H_{KJ}/10^6$		17.03(11)	43.51(51)	39205.68(57)	37079.4(16)	46493.5(13)
$L_{JK}/10^9$		-0.367(12)	-	-	-	-
$L_{KKJ}/10^9$		30.68(57)	90.1(19)			
E, MHz		-	1510090.(132)	2978512.(475)	4316820.(322)	5150177.(475)
E, cm^{-1}		-	50.37	99.35	143.99	171.79
N_{lines}		667	439	291	166	157
N_{total}		1720				
σ (kHz)		55.465				
$\sigma_{weighted}$		1.20167				

Table 6.3 – Coriolis coupling constants for interacting vibrational states (of methoxyisocyanate, obtained from the global 5-state fit

Constant, MHz	(g.s. $\Leftrightarrow \nu_{18}=1$)	($\nu_{18}=1 \Leftrightarrow \nu_{18}=2$)	($\nu_{18}=2 \Leftrightarrow \nu_{18}=3$)	($\nu_{18}=3 \Leftrightarrow \nu_{11}=1$)	($\nu_{18}=1 \Leftrightarrow \nu_{18}=3$)
G_a				3250.(156)	
G_b				270.(11)	
F_{bc}	3.388(84)	1.7063(80)	29.84(56)		
F_{ca}	38.861(38)	54.60(22)	1.953(18)		
$F_{ca}J$	-0.0005730(26)				
$F_{bc}K$	-0.0256(12)				
$F_{bc}J$	0.0000104(15)				
F_{ab}					-57.5(32)

Fig. 6.10 represents the experimental and theoretical spectra predicted by the SP-CAT program, that based upon the spectroscopic constants of the ground state and 4 vibrational states ($\nu_{18}=1$, $\nu_{18}=2$, $\nu_{18}=3$, $\nu_{11}=1$) of CH_3ONCO. As can be seen, the correspondence in general is good, but there is a number of unidentified lines that could belong to higher vibrational states of CH_3ONCO. By carring out the analysis, they can also be assigned and properly fitted.

The frequency range covered by measurements in this work corresponds to the range where the most intense lines may be observed under the characteristic temperature of 150
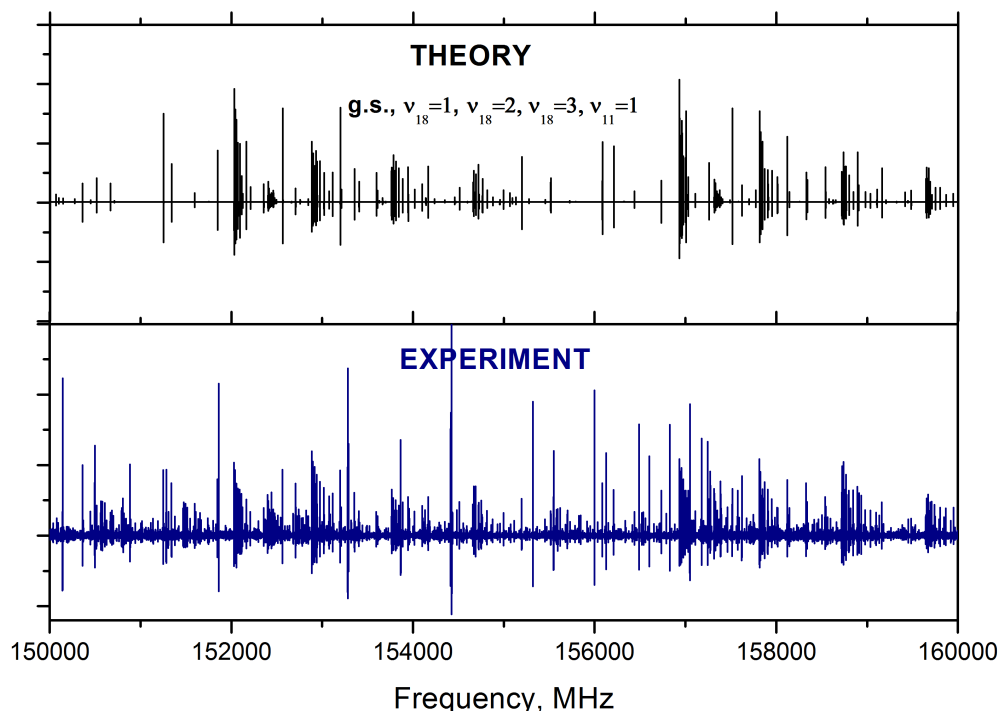
Figure 6.10 – Predicted (in black) and observed (in blue) rotational spectrum of CH₃ONCO between 150 and 160 GHz. A slight inconsistency between predicted and observed spectrum, which may be visible for some strong lines, is due to the methanol lines, source power and detector sensitivity variations.

K in dense molecular clouds (Fig. 6.11).

6.3.8 Conclusion

In the present study, the rotational spectra of methoxy isocyanate, CH₃ONCO, have been recorded in the millimeter-wave range and analyzed in its ground and lowest vibrational excited states. Measurements cover the frequency range from 75 to 330 GHz.

The principal challenge in the analysis of CH₃ONCO spectrum is the strong perturbation between vibrational states, which was found to affect rotational transitions of a ground state with low values of the K_a quantum number. Strong perturbations have significant effect on the high-resolution spectra. The interactions were significant due to the relatively small vibrational energy difference between the states (≈ 50 cm^{-1}). The analysis is based on an effective coupled state rovibrational Hamiltonian which contains Coriolis coupling terms and energies between the excited states. A reliable set of spectroscopic parameters, as well as precise vibrational energies and Coriolis interaction constants have been determined from a global fit analysis.
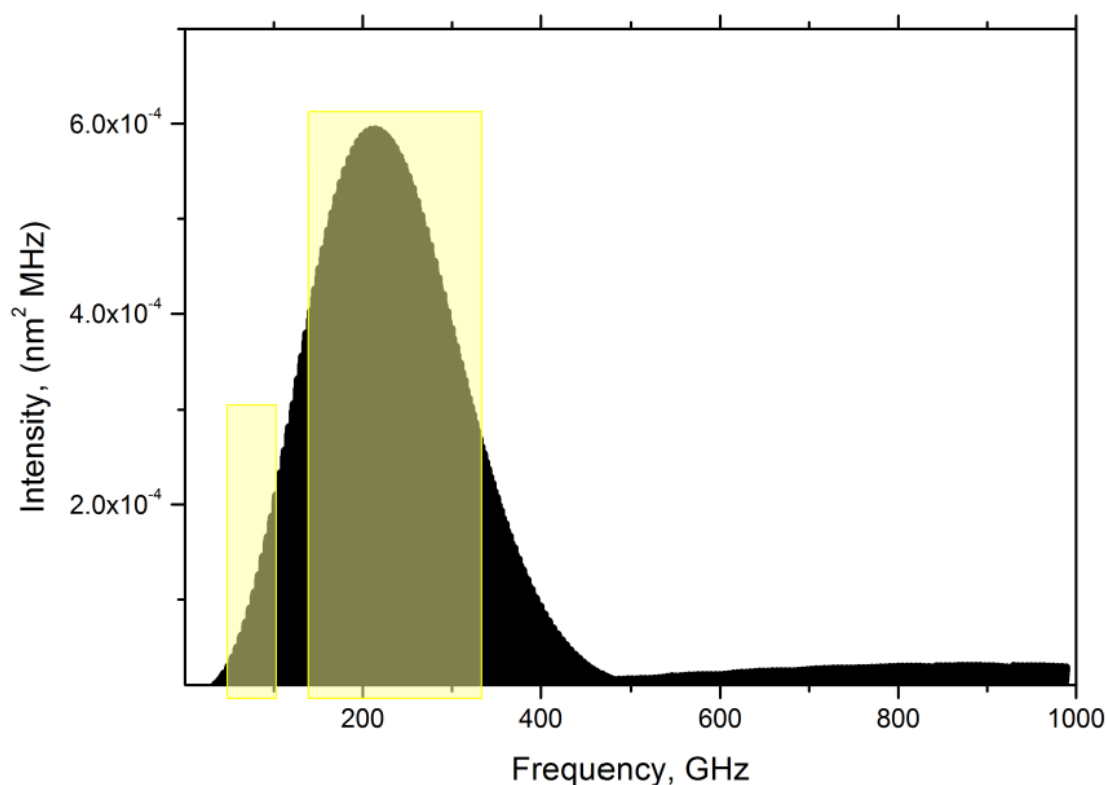
Figure 6.11 – Simulated spectrum of CH_3ONCO in its ground state at 150 K in the frequency range up to 1 THz

The catalog of frequency predictions for both the ground and lowest excited states of methoxy isocyanate will be accessible soon for astronomical observing. CH_3ONCO will be searched in the IRAM 30-m line survey of Orion KL and Sgr B2 (J. Cernicharo, private communication). In case of non detection, its upper limit column density will be derived.

Chapter 7

Conclusions and Future Prospects

During this thesis, both a fundamental research in molecular rotational spectroscopy, the analysis of two complex organic molecules in a laboratory, and instrumental development for THz laboratory spectroscopy, Schottky heterodyne receiver, has been carried out.

Part I

Part I of the thesis is dedicated to the development and testing a prototype of a non-cryogenic solid-state receiver, operating in 600 GHz frequency range, and its integration with FSS. 600 GHz Schottky heterodyne receiver is based on a microwave commercial frequency synthesizer, a sub-harmonic Schottky mixer, pumped by a frequency amplifier multiplier LO chain (AMC). It operates in the 530-590 GHz frequency range and has a DSB noise temperature in the range of 1000 K-1500 K at room temperature. To built a prototype of 600 GHz Schottky heterodyne receiver for Lille, we took existing components to assemble LO chain and Schottky mixer, designed for ESA JUICE.

Test measurements were performed to record the CH_3CH_2CN molecular spectra with the Schottky heterodyne receiver and FSS in the 600 GHz frequency range. Analysis of the obtained spectra showed the Schottky heterodyne receiver's sensitivity and frequency accuracy are comparable to those of 4K QMC HEB. The newly developed receiver has the advantage of being compact and to operate at room temperature. The FSS with Schottky heterodyne receiver provides fast measurements with high resolution, frequency accuracy, and sensitivity.

The integration of the heterodyne receiver with the FSS showed excellent performance during the first tests and has a full potential of becoming the standard measurement set-up, not only in Lille, but potentially in other molecular spectroscopy laboratories.

However there are a few more developments to complete. For the future perspectives,

1. In the near term, we will improve the configuration of the current set-up of a 600 GHz Schottky heterodyne receiver by:

- using a new appropriate LO chain from RPG, specially designed for a receiver, or alternatively to change frequency multipliers to those with better characteristics (fabricated by LERMA for example);

- improve the IF chain: purchase specifically selected for the receiver modern low noise amplifier and narrow band filter from commercial suppliers with superior performances than those we used.

New tests with FSS and a 600 GHz Schottky heterodyne receiver will be performed after replacing some components by a new appropriate equipment.

2. In a second step we intend to expand the frequency coverage. FSS is already equipped with radiation sources from VDI, that operate in 1.1-1.52 THz frequency range. The operating frequency range of a Schottky heterodyne receiver can be extended to 1.0-1.3 THz:

- part of the LO chain for 600 GHz could be used to assemble the new LO chain for a 1.2 THz heterodyne receiver, operating in a 1.2 THz frequency range by adding a frequency doubler (need to be purchased);

- use a Schottky mixer for 1.2 THz that is currently being developed for ESA JUICE;

- use the 1.2 THz components to build, test and qualify 1.0 - 1.3 THz Schottky heterodyne receiver and integrate it with a spectrometer in Lille.

The development of Schottky heterodyne receiver, that operates in 1.2 THz frequency range and its application to the FSS may be the subject for the next research.

Additional work of the Part I included the characterization of materials frequently used in instrumentation for spectroscopy and astronomy in THz frequency range. We designed instrumentation system in the THz frequency range, using a commercial microwave frequency synthesizer, amplifier multiplier chains (AMCs), and a Golay detector. The set-up allows a sample of dielectric to be rotated and its angular transmission properties can be investigated. In contrast to a few other measurements set-up, our set-up is polarization sensitive. We investigated the transmission of variety of materials: High-density Polyethylene (HDPE), high resistivity Silicon, Zitex and Mylar at 600 GHz and 1.4 THz. Experimental studies of the angular dependent transmission of these materials have been performed and very good quality data were obtained. The current study is important for many practical applications.

A numerical method in Matlab has been applied to fit the data to theoretical model and to determine refractive indices of HDPE and the other dielectrics with uncertainties in the forth decimal place.

This method worked very well and a study of angular dependent transmission of various materials will be extended to 2.7 THz. We will might also build a set-up that allows the measurements of materials at cryogenic temperatures and investigation to the changes of material properties with temperature. And, probably, investigation of frequency dependent transmission will be performed in THz frequency range as well.

Part II

Part II of the thesis is dedicated to the gas-phase spectroscopic studies of molecules that are expected to be present in the interstellar media. The new laboratory spectroscopic investigation, presented here, allow us to search for two astronomically interesting species in line surveys for the first time in space. These molecules have not been studied before in a laboratory: methoxyisosocyanate, CH_3ONCO and triple- ^{13}C isotopologue of ethyl cyanide, $^{13}CH_3^{13}CH_2^{13}CN$. We recorded and analyzed the spectra of CH_3ONCO and $^{13}CH_3^{13}CH_2^{13}CN$. Measurements, performed here, cover the frequency range up to 1 THz for $^{13}CH_3^{13}CH_2^{13}CN$ and 330 GHz for CH_3ONCO. The fast-scan technique was essentially extremely important for the studies of the unstable species as CH_3ONCO, thereby allowing the optimization of the experimental conditions in a minimum amount of time.

More than 4000 rotational transitions of $^{13}CH_3^{13}CH_2^{13}CN$ were identified in the laboratory. The quantum numbers reach $J = 115$ and $K_a = 39$. The rotational spectra of the ^{13}C containing species CH_3CH_2CN have been assigned, thus allowing the determination of the rotational and centrifugal distortion constants. Watson's Hamiltonian in the A and S reductions were used to analyze the spectra. The assignments of $^{13}CH_3^{13}CH_2^{13}CN$ were used to search for this molecule the first time in space. IRAM telescope observed Orion, but unfortunately a detection of $^{13}CH_3^{13}CH_2^{13}CN$ has not been obtained.

The analysis of the rotational spectrum of CH_3ONCO in the ground and excited states of two lowest lying vibrational modes ($\nu_{18}=1$, $\nu_{18}=2$, $\nu_{18}=3$ and $\nu_{11}=1$) was also presented. The CH_3ONCO spectrum is dominated by the effects of the large Coriolis interactions which strongly affect the lowest K_a levels. The assigned data, 667 transitions of the ground state with the maximum values of the J and K_a quantum numbers of, respectively, 70 and 14 and more than 1000 lines associated with $\nu_{18}=1$, $\nu_{18}=2$, $\nu_{18}=3$, $\nu_{11}=1$ of the vibrational modes, were simultaneously fitted to an effective rovibrational Watson S-reduced Hamiltonian in the presence of a Coriolis interaction between vibrational

states. An accurate and reliable set of spectroscopic parameters for CH_3ONCO have been obtained thus providing precise predictions for the first possible astronomical detection of this molecule. Furthermore, we were able to determine energies of the vibrations and Coriolis coupling terms so a detailed analysis of perturbations was possible.

Accurate and reliable sets of spectroscopic parameters of $^{13}CH_3^{13}CH_2^{13}CN$ and CH_3ONCO, obtained in the laboratory in this work, will support the astronomical detection of these molecules in space.

Appendix A

Experimental Data, Transmission Properties of Materials at 600 GHz and 1.4 THz

A.1   High-density Polyethylene (HDPE)

A.2   High resistivity Silicon

A.3   Mylar (Polyethylene Terephthalate,PET)

A.4   Zitex
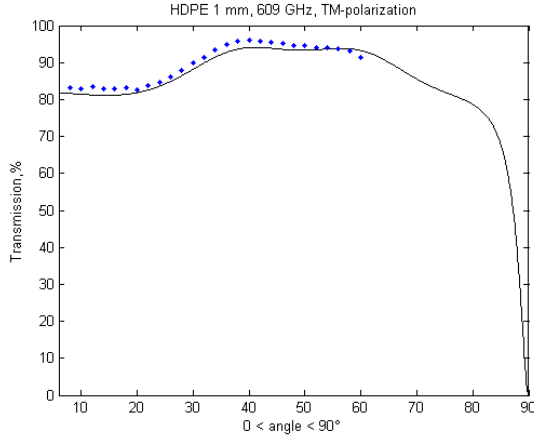
(a) TM-polarization
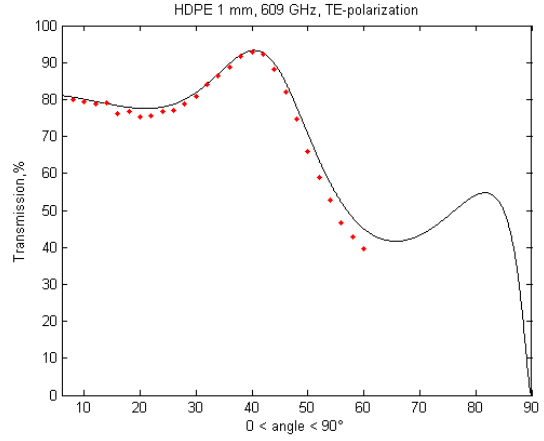
(b) TE-polarization, n=1.531-1.533, α=0.025
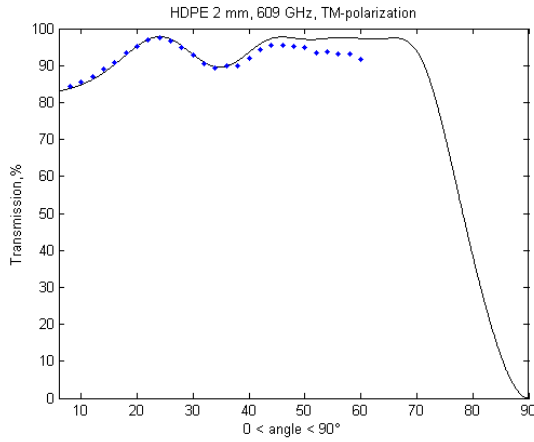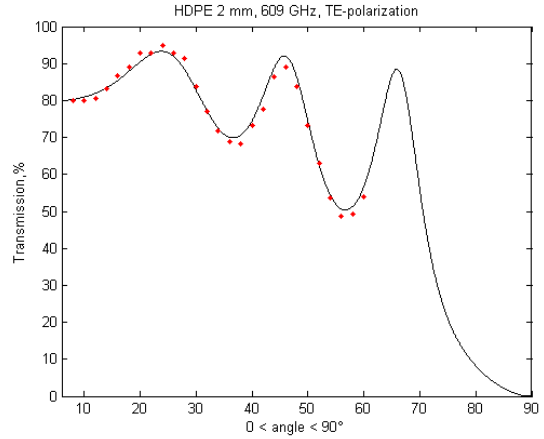
(c) TM-polarization

(d) TE-polarization, n=1.534-1.537, α=0.015-0.005

Figure A.1 – Experimental transmission measurements for HDPE samples with at thickness 1 mm (a, b) and 2 mm (c,d) at 609 GHz (represented by red and blue points) and the fitted theoretical curve (black), determined by Matlab.
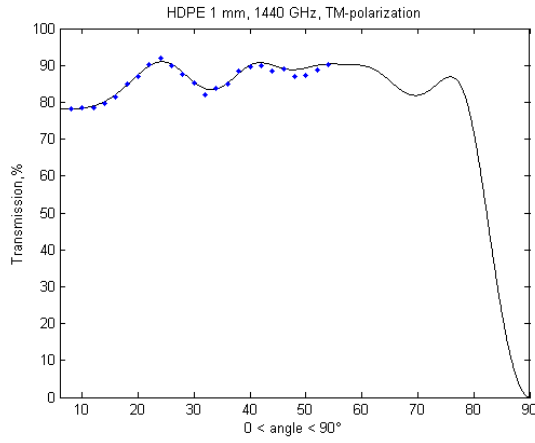
(a) TM-polarization, n=1.534-1.537, α=0.040
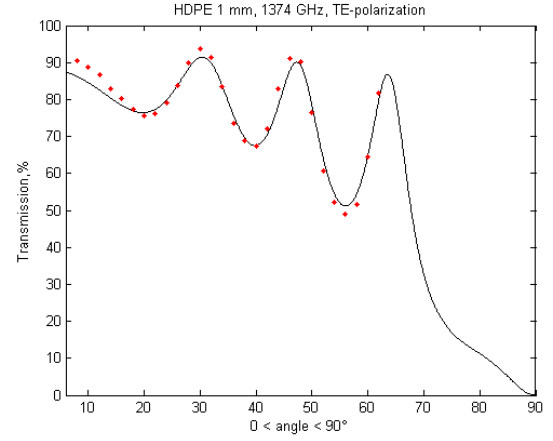
(b) TE-polarization, n=1.521-1.523, α=0.035-0.040
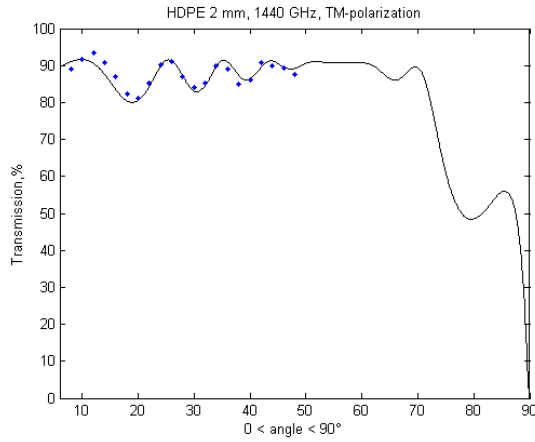
(c) TM-polarization, n=1.521-1.523, α=0.020
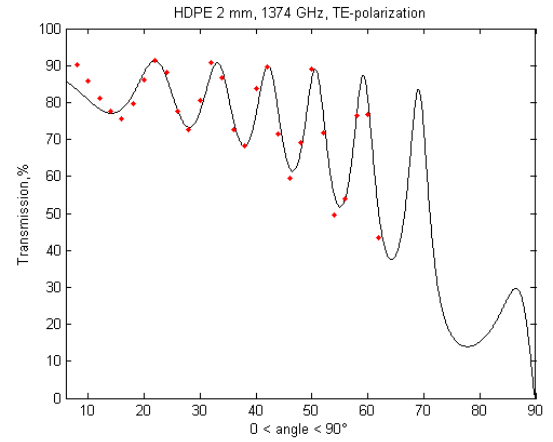
(d) TE-polarization, n=1.523-1.524, α=0.020

Figure A.2 – Experimental transmission measurements for HDPE samples with at thickness 1 mm (a, b) and 2 mm (c,d) at 1440 GHz (represented by red and blue points) and the fitted theoretical curve (black), determined by Matlab.
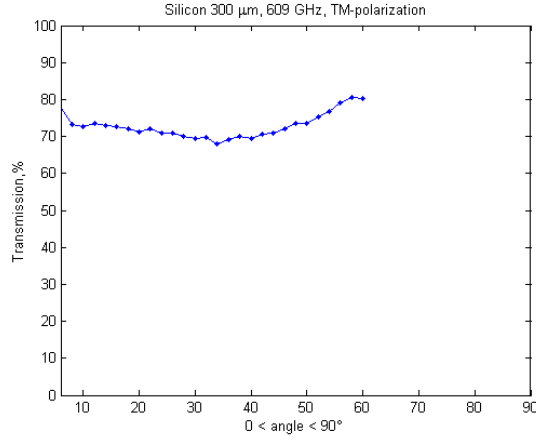
(a) TM-polarization, 609 GHz
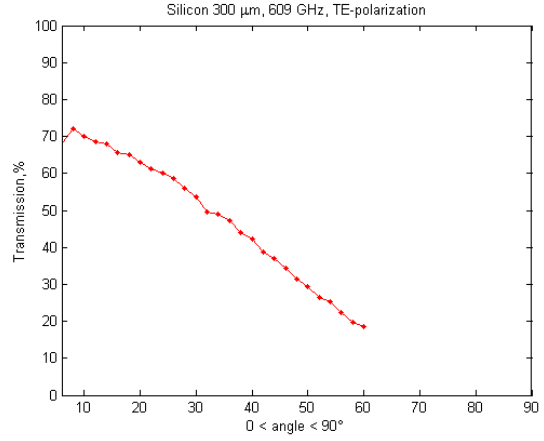
(b) TE-polarization, 609 GHz
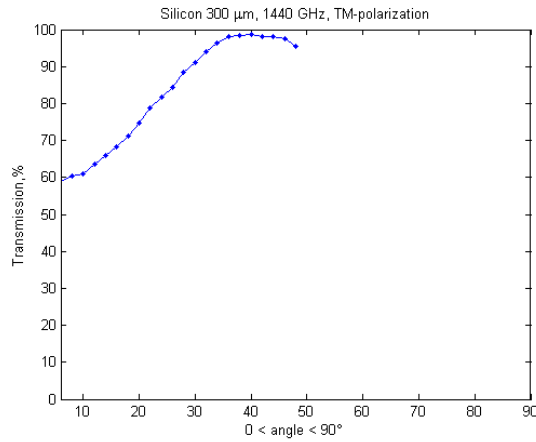
(c) TM-polarization, 1440 GHz
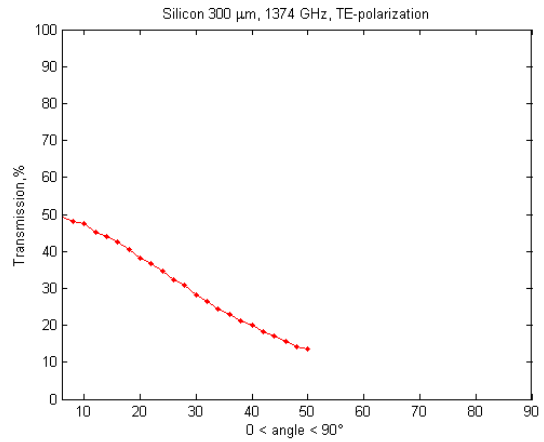
(d) TE-polarization, 1374 GHz

Figure A.3 – Transmission measurements (represented by red and blue lines) for a Silicon of a thickness 300μm at 609 (a,b) and 1400 GHz (c,d).
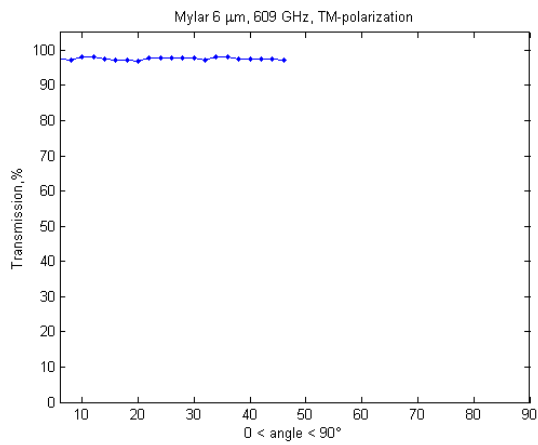
(a) TM-polarization, 609 GHz
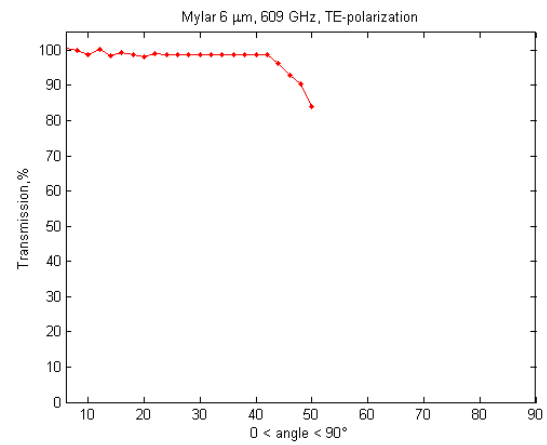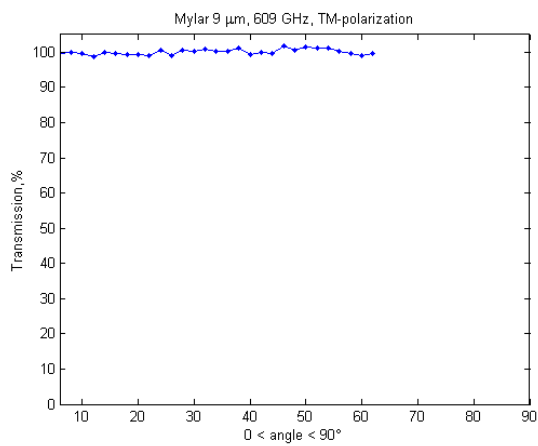
(b) TE-polarization, 609 GHz

(c) TM-polarization, 609 GHz
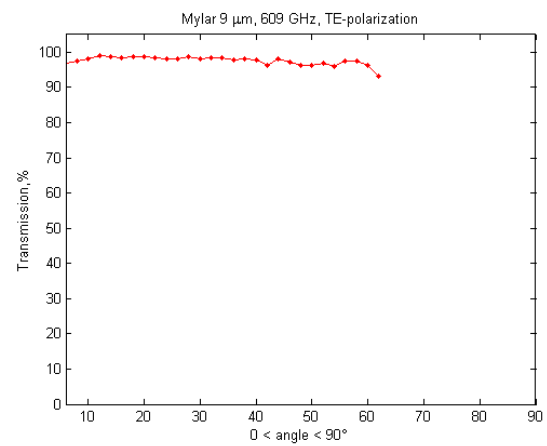
(d) TE-polarization, 609 GHz
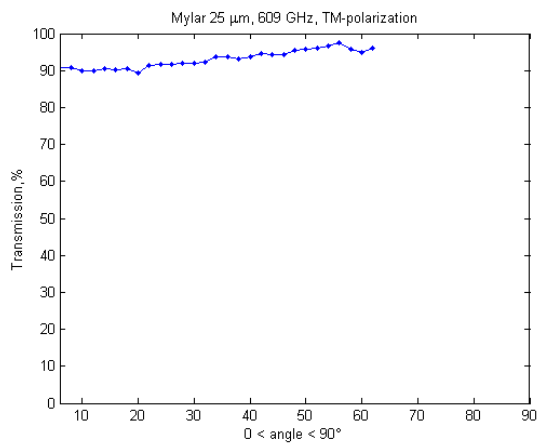
(e) TM-polarization, 609 GHz
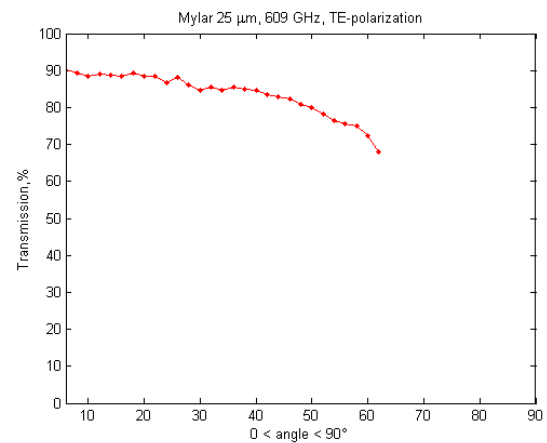
(f) TE-polarization, 609 GHz

Figure A.4 – Transmission measurements (represented by red and blue lines) for a Mylar of a different thickness at 609 GHz.
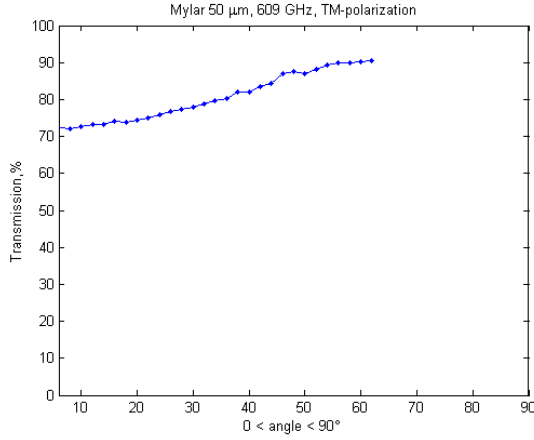
(a) TM-polarization, 609 GHz
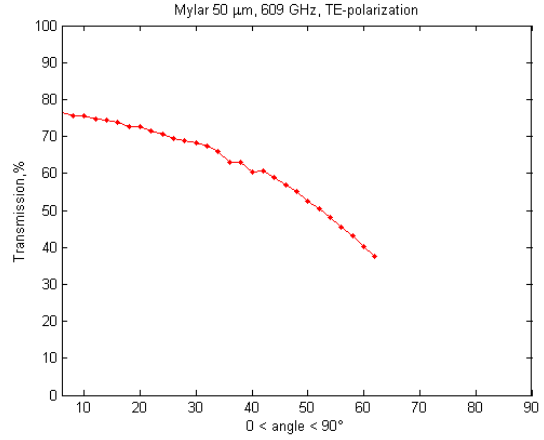
(b) TE-polarization, 609 GHz
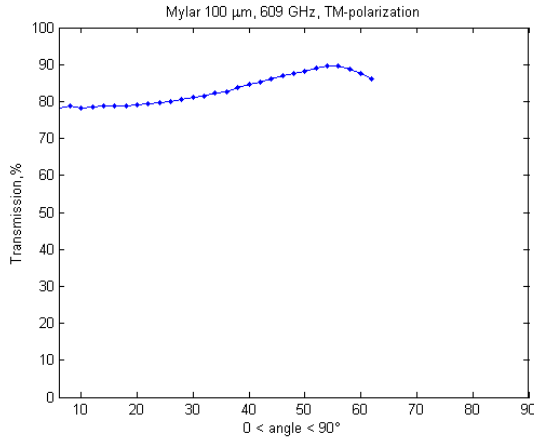
(c) TM-polarization, 609 GHz
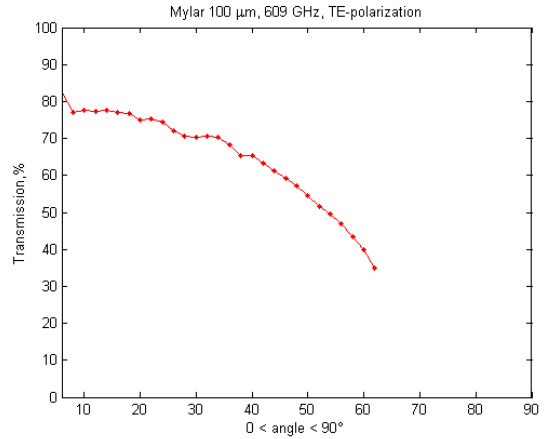
(d) TE-polarization, 609 GHz
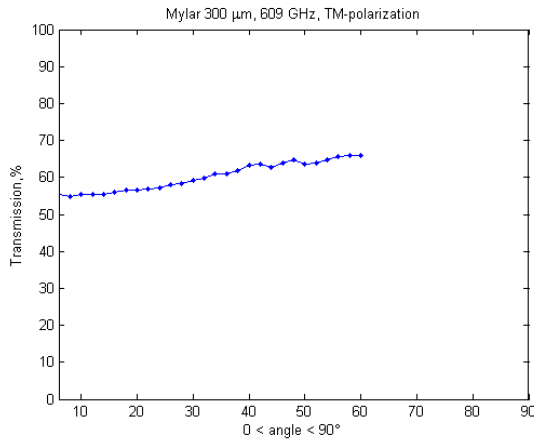
(e) TM-polarization, 609 GHz
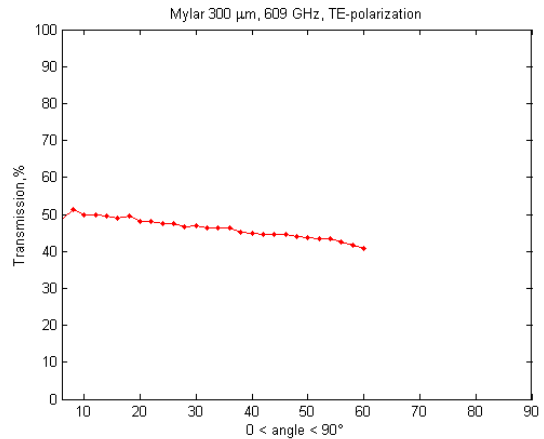
(f) TE-polarization, 609 GHz

Figure A.5 – Transmission measurements (represented by red and blue lines) for a Mylar of a different thickness at 609 GHz.
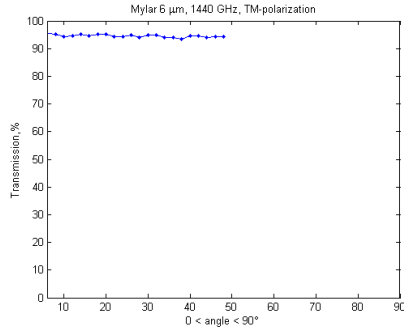
(a) TM-polarization, 1440 GHz
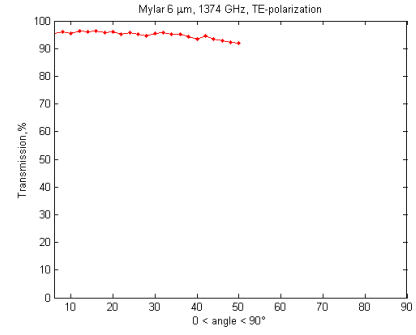
(b) TE-polarization, 1374 GHz
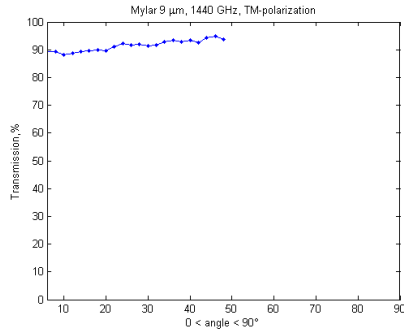
(c) TM-polarization, 1440 GHz
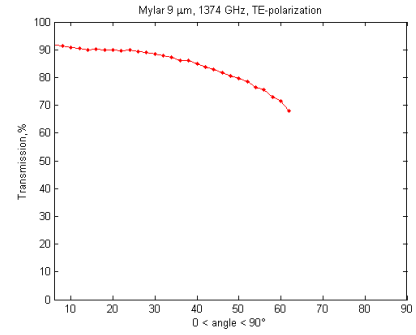
(d) TE-polarization, 1374 GHz
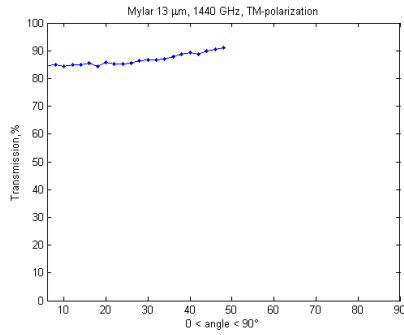
(e) TM-polarization, 1440 GHz
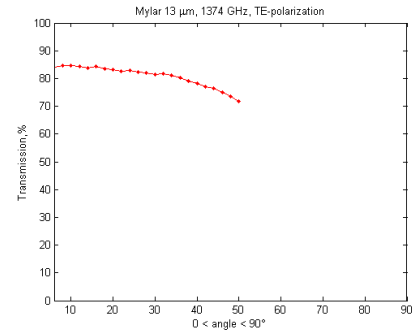
(f) TE-polarization, 1374 GHz

(g) TM-polarization, 1440 GHz

(h) TE-polarization, 1374 GHz

Figure A.6 – Transmission measurements (represented by red and blue lines) for a Mylar of a different thickness at 1400 GHz.
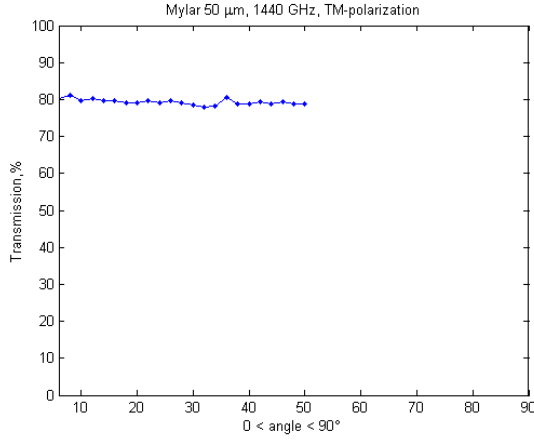
(a) TM-polarization, 1440 GHz
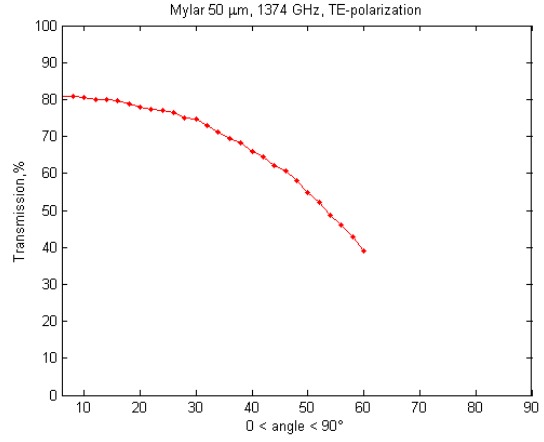
(b) TE-polarization, 1374 GHz
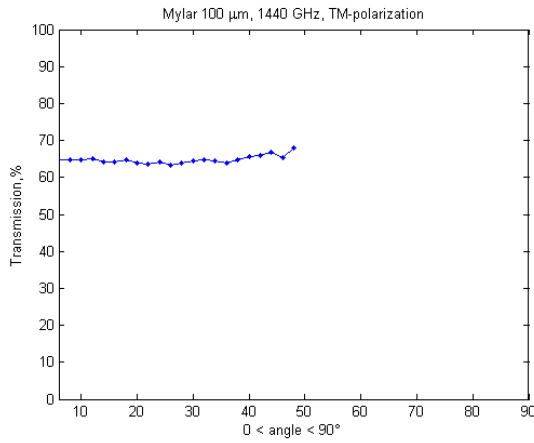
(c) TM-polarization, 1440 GHz
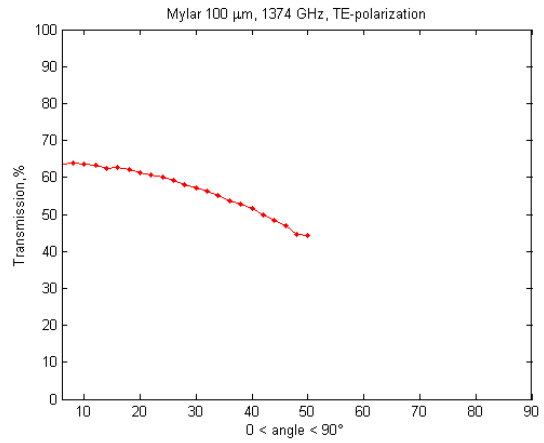
(d) TE-polarization, 1374 GHz
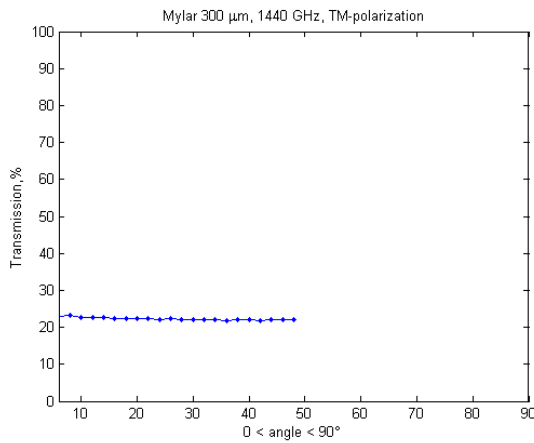
(e) TM-polarization, 1440 GHz
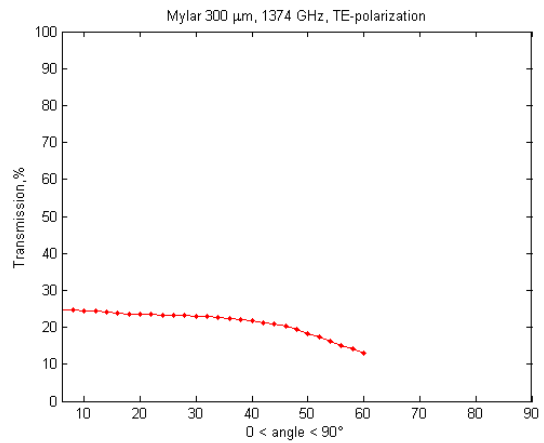
(f) TE-polarization, 1374 GHz

Figure A.7 – Transmission measurements (represented by red and blue lines) for a Mylar of a different thickness at 1400 GHz.
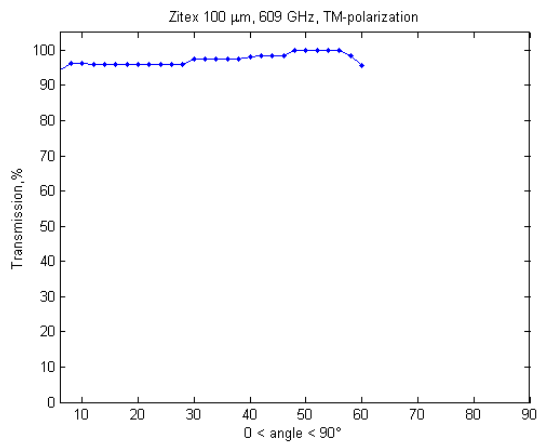
(a) TM-polarization, 609 GHz
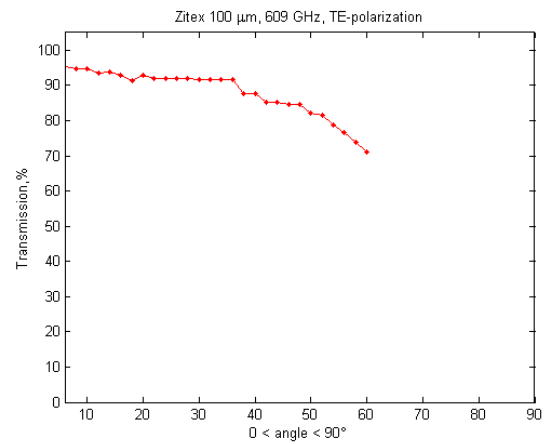
(b) TE-polarization, 609 GHz
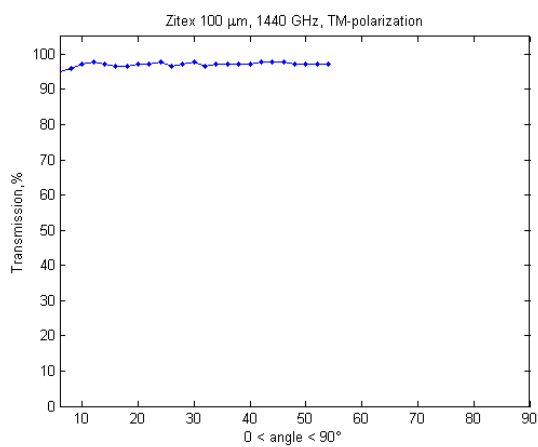
(c) TM-polarization, 1440 GHz

(d) TE-polarization, 1374 GHz

Figure A.8 – Transmission measurements (represented by red and blue lines) for a Zitex of a thickness 100μm at 609 (a,b) and 1400 GHz (c,d).

Appendix B

Data sheets

Radiometer Physics
A Rohde & Schwarz Company

Product Data Sheet

AFM6 60-90 +6
Active Frequency Multiplier 60-90 GHz
Part-No.: 01100017

Product Description

The **AFM6 60-90 +6** is an active frequency multiplier (x6) with a coaxial input and a WR-12 waveguide output.

Product Features:

- Full Band WR12 (60-90 GHz)
- output Power: typ. +6 dBm
- No Mechanical Tuners
- Input Power: +7dBm
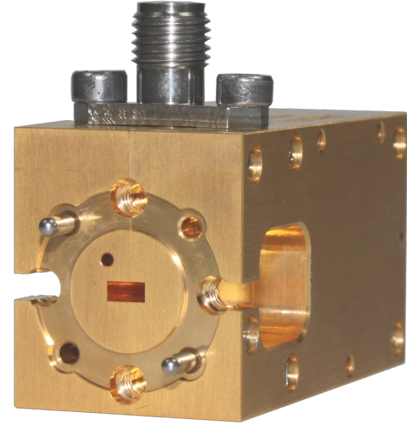
Technical Specifications

Output Frequency [GHz]	60 - 90
RF Port	WR12 (UG387/UM)
Output Power [dBm (typ.)]	+6
Input Frequency [GHz]	10 - 15
Input Connector	2.92 mm female
Input Power [dBm]	+7
DC Voltage [VDC]	+7/ 600mA (typ.)
Max. Input Power [dBm]	+10
Max. DC Voltage [VDC]	+9
Max. Case Temperature	+45 °C

Typical Performance

AFM6 60-90
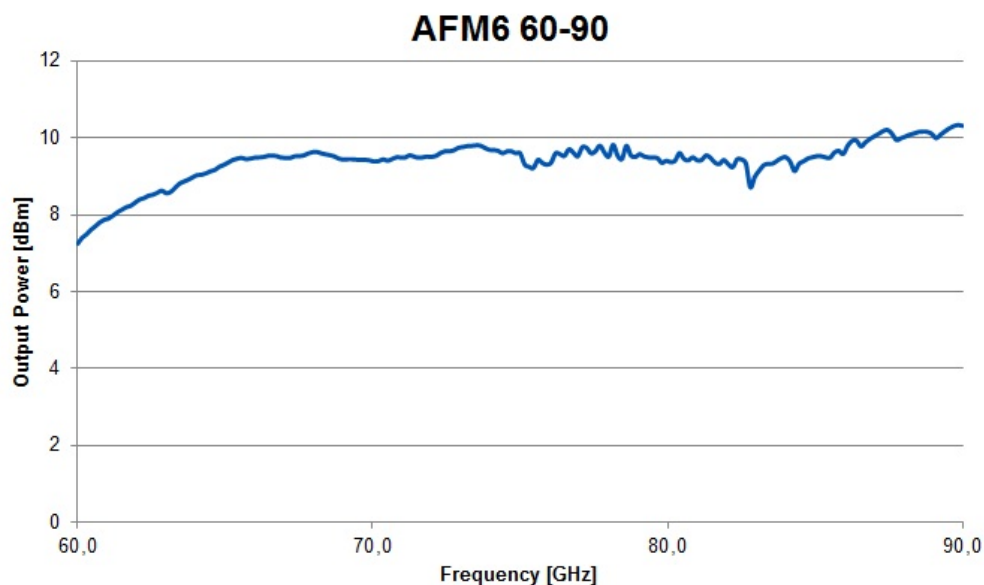
FM2 132-154 HP
High Power Frequency Multiplier 132-154 GHz
Part-No.: 01200011

Technical Specifications	
Output Frequency [GHz]	132 - 154
Output Port	WR6.5 (UG387/UM)
Output Power [dBm typ.]	+17
Input Frequency [GHz]	66 - 77
Input Port	WR12 (UG387/UM)
Input Power [dBm]	+17 to +23
Conversion Efficiency	35-40%
DC Voltage	-5 to-11 V typ.
Max. Input Power [dBm]	+23
Max. Case Temperature	+45 °C

F-MPA 100-130 10 15
Medium Power Amplifier 100-130 GHz
Part-No.: 03100047

Product Description

This **F-MPA 100-130 10 15** operates in the frequency range 100 to 130 GHz.

Technical Specifications

RF Frequency [GHz]	100 - 130
RF Port	WR8 (UG387/UM)
Gain [dB (typ)]	10
Return Loss [dB (typ)]	6
Psat [dB (typ)]	15
DC Voltage	+7 VDC
Max. Input Power	+13 dBm
Max. DC Voltage	+9 VDC
Max. Case Temperature	+45 °C

Typical Performance

F-MPA 100-130 10 15 - Gain and Return Loss Performance

2017/02/22

Radiometer Physics GmbH
Werner-von-Siemens-Str. 4
53340 Meckenheim, Germany

Page 1 of 1
+49 (0) 2225 99981 — 0
www.radiometer-physics.de
info@radiometer-physics.de
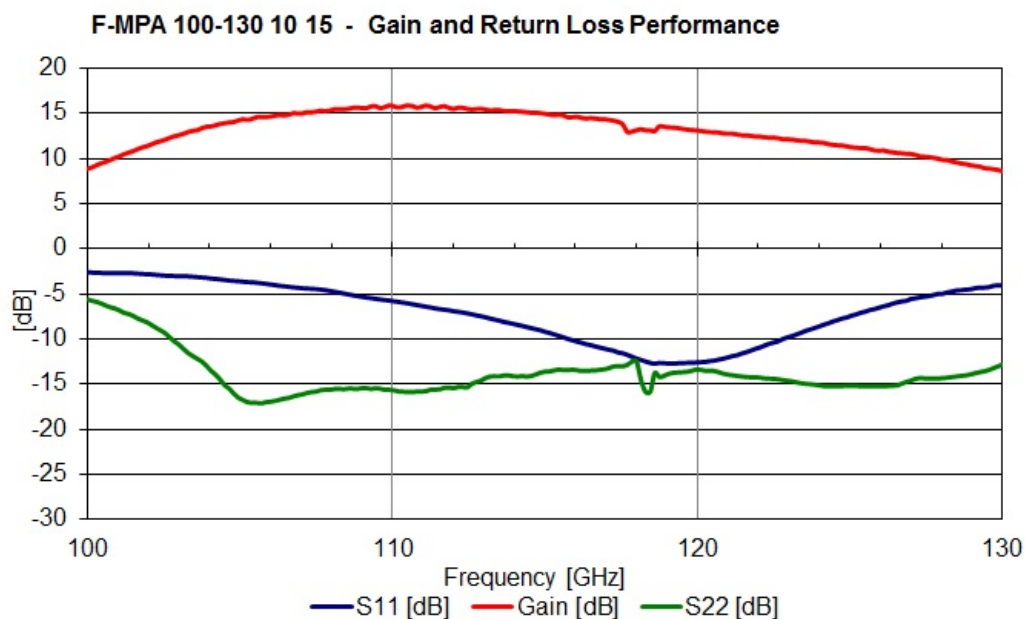
WTA 110-170
Waveguide Tunable Attenuator 110-170 GHz
Part-No.: 04700059

Technical Specifications

Frequency Range [GHz]	110 - 170
RF Port	WR6.5 (UG387/UM)
Attenuation Range [dB]	0 – 40
Max. Input Power [dBm]	+20
Insertion loss [typ. dB]	<1
Tuning	Micrometer

Typical Performance

WTA 90-170

2017/02/20
Radiometer Physics GmbH
Werner-von-Siemens-Str. 4
53340 Meckenheim, Germany

Page 1 of 1
+49 (0) 2225 99981 — 0
www.radiometer-physics.de
info@radiometer-physics.de
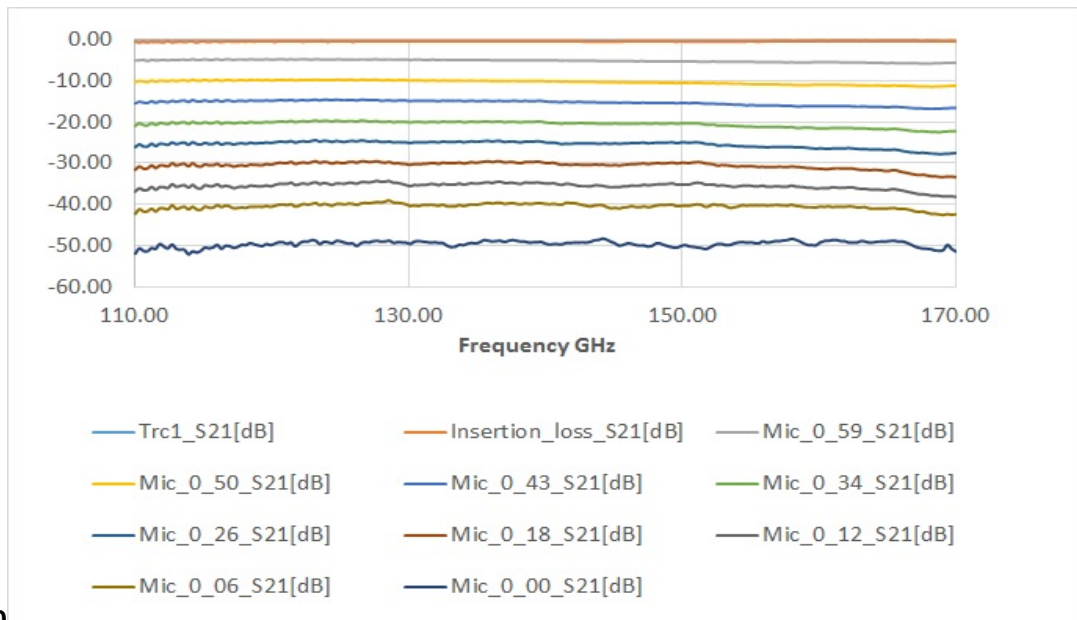
Serial #
1367061

Model #
AFS3-00100600-13-10P-4

Project #
MQ0161836

Customer
IMPULSE TECHNOLOGIES INC.

Customer PO
6386

Stock #
222G W0060034

Voltage (V)
+15v

Current (mA)
133ma

Temp (°C)
23

Tested By
R.Y.

Comments
Noise figure increases below 500MHz

Printed On: 3/14/2008 9:48:57 AM

PASS

WEEE

Input VSWR

100	1.36
500	1.39
1000	1.45
2000	1.48
3000	1.36
4000	1.23
5000	1.15
6000	1.17
MAX	1.49
SPEC:	2.00
ID:107	PASS

3/14/2008 9:10:15 AM ID:107 V2.1.1589

S12

100	-72.29
500	-74.82
1000	-73.33
2000	-65.80
3000	-61.17
4000	-57.32
5000	-53.79
6000	-50.83
ID:108	PASS

3/14/2008 9:10:17 AM ID:108 V2.1.1589

S21

100	33.45
500	33.38
1000	33.18
2000	32.89
3000	33.16
4000	33.54
5000	33.39
6000	32.62
MIN	32.62
SPEC:	28.00
FLAT+/-	0.47
SPEC+/-	1.25
ID:109	PASS

3/14/2008 9:10:18 AM ID:109 V2.1.1589

Output VSWR

100	1.05
500	1.04
1000	1.09
2000	1.12
3000	1.14
4000	1.18
5000	1.20
6000	1.14
MAX	1.20
SPEC:	2.00
ID:110	PASS

3/14/2008 9:10:19 AM ID:110 V2.1.1589

Noise Figure vs Frequency

100	2.06
500	1.20
1000	1.15
2000	0.89
3000	0.98
4000	1.10
5000	1.19
6000	1.27
MAX	1.27
SPEC:	1.30
ID:113	PASS

3/14/2008 9:18:12 AM ID:113 V2.1.1589

Output Power @ 1dB Compression Point

100	15.08
500	14.81
1000	14.80
2000	14.81
3000	14.80
4000	14.67
5000	14.73
6000	14.88
MIN	14.67
SPEC:	10.00
ID:114	PASS

3/14/2008 9:48:29 AM ID:114 V2.1.1589

filter

Window 1
10.00   Tr 1   S11 LogM 10.00dB/   -40.0dB

> 1:	4.800 GHz	-3.86 dB
2:	4.851 GHz	-31.28 dB
3:	4.908 GHz	-3.59 dB

>Ch1: Start 4.00000 GHz   Stop 6.00000 GHz

Channel Settings

Channel	Sweep Type	Points	Start (GHz)	Stop (GHz)	IF BW (kHz)	Sweep Time (s)	Pow 1 (dBm)	Pow 2 (dBm)
1	LinFreq	401	4.000000	6.000000	35.000000	3.990050	-17.000000	-17.000000

Trace Attributes

Window	ID	Trace	Channel	Correction	Options
1	1	S11	1	C 2-Port	

filter

Window 1

Tr 1 S21 LogM 20.00dB/ -40.0dB

> 1:	4.800 GHz	-3.23 dB
2:	4.851 GHz	-0.38 dB
3:	4.908 GHz	-3.44 dB

>Ch1: Start 4.00000 GHz ‾‾‾   Stop 6.00000 GHz

Channel Settings

Channel	Sweep Type	Points	Start (GHz)	Stop (GHz)	IF BW (kHz)	Sweep Time (s)	Pow 1 (dBm)	Pow 2 (dBm)
1	LinFreq	401	4.000000	6.000000	35.000000	3.990050	-17.000000	-17.000000

Trace Attributes

Window	ID	Trace	Channel	Correction	Options
1	1	S21	1	C 2-Port	

27.02.2003

Repair of Local Oscillator

RPG
Radiometer
Physics

Output: 600-642 GHz
S/N: 99137   R/N: 2002 035
Date: February 27, 2003

$637,96\,GHz$ 1— 0,89   2— 0,27   3— 0,78   4— 0,33

$611\,GHz$ 1— 1,105   2— 1,21   3— 0,86   4— 1,30

P_{Gunn}

$F = 0.75$.

$F = 1.09$.

Pennaut

Output		Gunn Osc.		Frequency Doubler		Frequency Tripler	
Frequency	Power	Micrometer		Micrometer		Micrometer	
f_{Out} [GHz]	P_{out} [μW]	F	B	1	2	3	4
598,97	45	0,60	0,00	1,29	0,44	1,17	0,39
605,56	110	0,78	0,11	1,01	1,43	0,92	1,09
609,2	80	0,84	1,80	0,65	1,28	0,34	1,32
617,4	60	0,92	2,09	1,01	1,37	0,88	0,37
624	50	1,02	0,68	0,52	0,31	1,11	0,25
634,86	60	1,19	0,48	0,59	0,30	0,79	0,34
637,96	120	1,20	1,63	0,73	0,28	0,80	0,35
641,7	100	1,25	0,46	0,88	0,18	1,03	0,33

33 mW
36 mW
37 mW
41 mW

$25/07/2011 \Rightarrow 605,56$ $81\mu W$ 1,17   1,37   1,13   1,45

Gunn Oscillator voltage: 10.50 V

DC-Data of multiplier diodes:

	Doubler	Tripler
I [μA]	U [V]	U [V]
-10	-0,75	-0,75
-100	-0,82	-0,82
-1000	-0,89	-0,89
-3000	-0,92	-0,92

The frequency doubler and tripler are operated selfbiased with a 10 kΩ restistor, a 10nF capacitor
and a 4.3 V Zener diode in parallel to the multiplier diode. All components are integrated
in the SMA connector !

Please Note: The Micrometer that is used to adjust the output power of the Frequency Tripler
is Micrometer No. 3
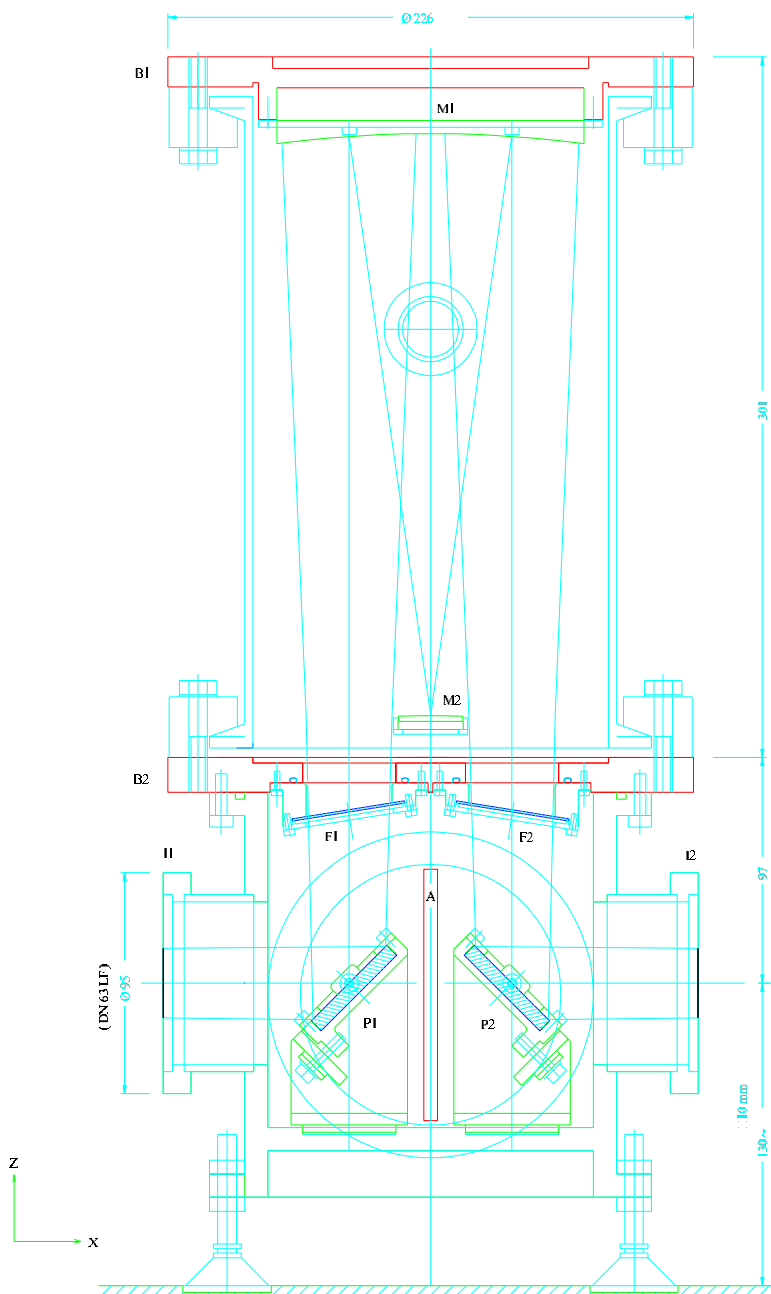
Fig.1: Drawing from the cell as seen laterally. Chief-ray and 4*w* beam envelopes are shown along the entire optical path. Indicated on this figure are the two folding mirrors P1 and P2, as well as the *Offner* relay consisting of spherical mirrors M1 and M2. Also shown are the tilted Mylar windows (F1 and F2).
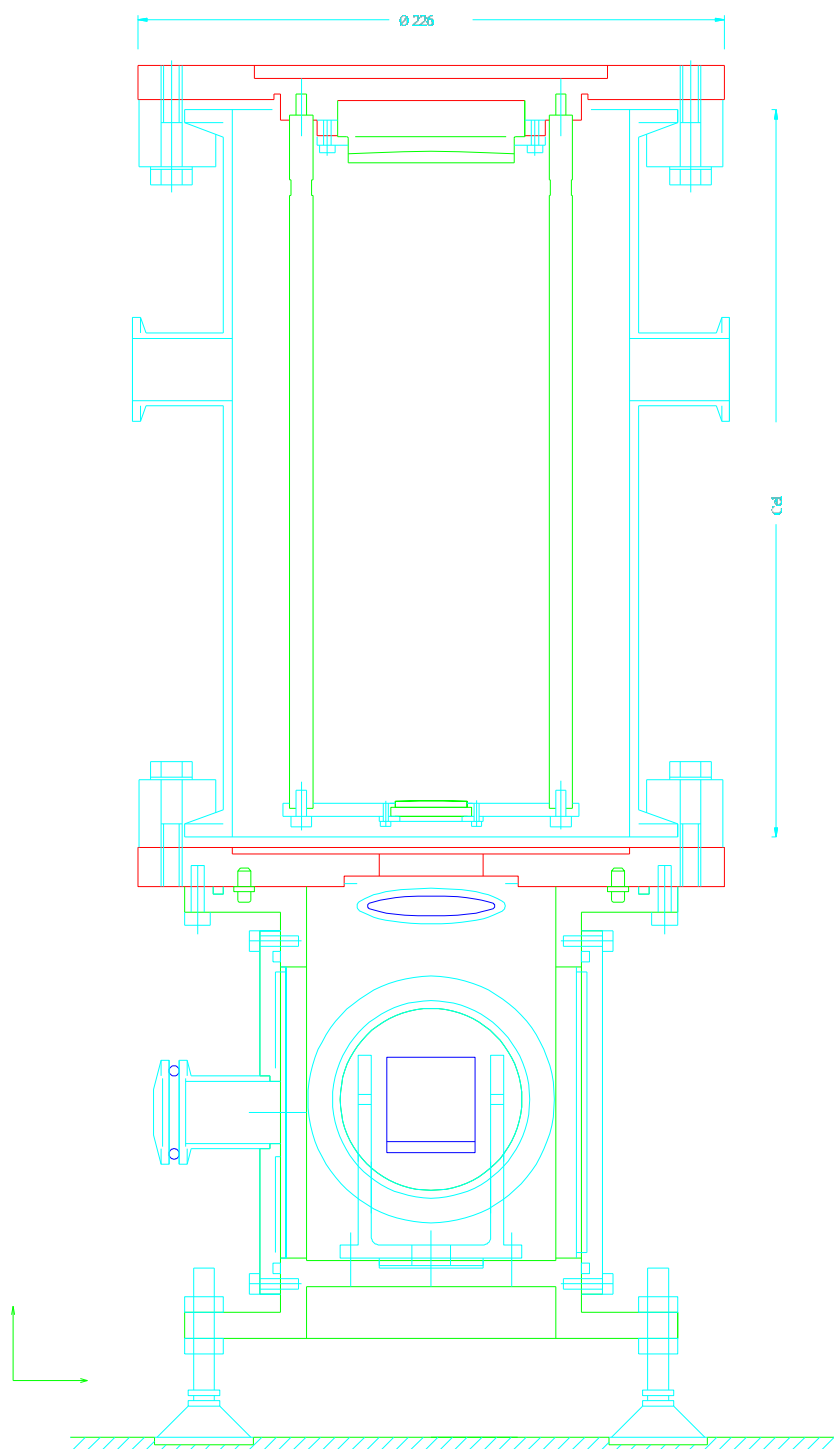
Fig.2: Drawing from the cell as seen from the input (or output) beam. Shown on the cell are two pipes dedicated to the filling and emptying of the gas sample (see next section). Also shown is the pipe at the side of the connection chamber (see text for details).

Parameter	Dimension (mm)
Cell diameter	150 ?
Path length in gas	?
Total path length	?
Total height	528
Total length	230
Waist at entrance ports (4w)	30
Optics surface accuracy	Of order 0.1 microns

5.2 Optics and windows

The gas cell optics are based on an *Offner* relay located inside the cell (mirrors M1 and M2 on Fig.2), offering a total path of more than 1 metre in a very compact (less than 30 cm high) configuration, easing thus operations and integration in a variety of measurement setups. In order to reduce the efforts on the glass cavity, the plate holding the M1 mirror, and located above the cell, is sustained by 4 stainless-steel bars directly screwed onto the connection chamber (see Fig.5 for an overview). This rigid interface also allows for a reproducible alignment even when the glass cell needs to be removed for any reason. In particular, it keeps constant the distance between M1 and M2, as well as their relative positions. The beams at the input and output ports are folded into the gas cell cavity via two flat folding mirrors offering alignment in all degrees of freedom (rotations and translation). The optical chief ray is shown in Fig.3.

The optics are designed to control and keep the beam waists in required ranges at the input and output ports (here 4*w* criterion for the HIFI beams). They offer a 1:1 magnification, allowing the system to be operated with any microwave detection system whose beam properties would fit within the constraints of the gas cell optics. This versatile spectral source can be interfaced to the HIFI detection chain in such a way that measurements can be performed under vacuum conditions, cancelling thus the contribution from the line-of-sight water lines over the whole operating frequency range, and reaching low noise temperatures compared to open-air systems.

All mirrors are made out of glass, with a gold+epoxy coating of surface accuracy of order 0.1 microns (!), allowing use of the gas cell at wavelengths well below those of HIFI. The interface windows isolating the gas sample from the connecting chamber are Mylar windows 50 microns thick.
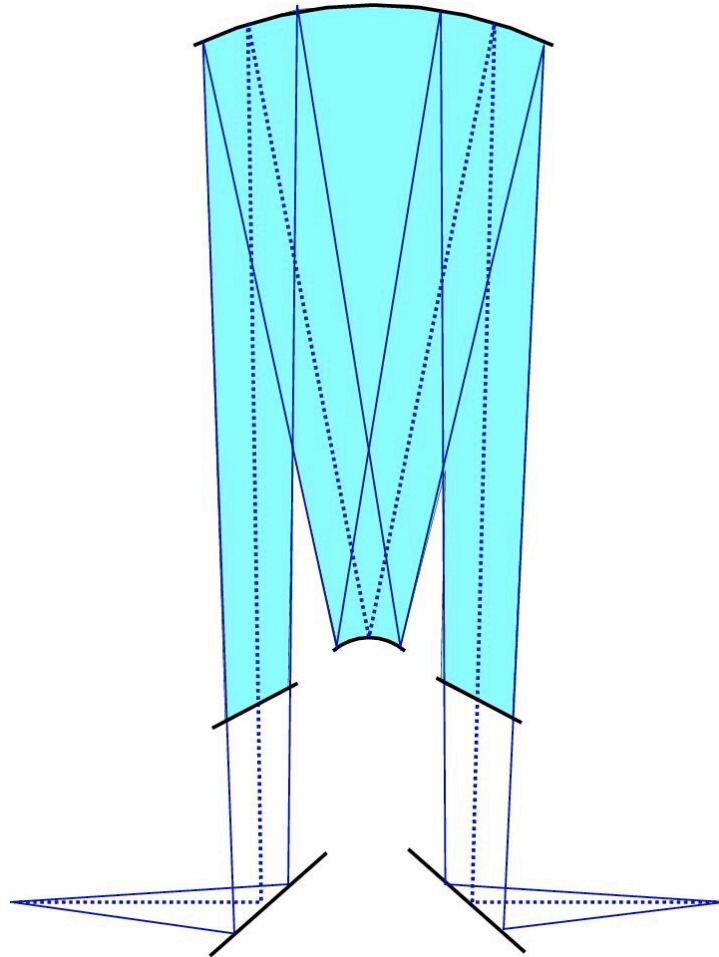
Fig.3: Optical chief ray from input throughout the output port of the gas cell. The shaded-blue parts correspond to the optical path inside the gas cavity.

5.3 Gas cavity

The gas cavity consists of a cylindrical volume made out of Borosilicate glass DURAN (VAT-EVAC). It is sealed to the connecting chamber and the top plate with seals made of Teflon/Viton. It offers two pipes of either sides of the cavity (see Fig. 2). While the first serves to fill in and empty the cavity and connect a pressure sensor for the gas volume, the second one allows connecting a temperature sensor to the cavity. Fig. 4 shows a close-up picture of those areas.

Fig.4: picture of the cell cavity, showing the two pipes for gas injection/removal (front pipe, with gas pressure sensor) and temperature sensor insertion (back pipe). The two golden mirrors of the *Offner* relay can also be seen on this picture.

List of Figures

List of Tables

Bibliography

[1] J. M. Lykke, A. Coutens, J. K. Jørgensen, M. H. D. van der Wiel, R. T. Garrod, H. S. P. Müller, P. Bjerkeli, T. L. Bourke, H. Calcutt, M. N. Drozdovskaya, C. Favre, E. C. Fayolle, S. K. Jacobsen, K. I. Öberg, M. V. Persson, E. F. van Dishoeck, and S. F. Wampfler. The ALMA-PILS survey: First detections of ethylene oxide, acetone and propanal toward the low-mass protostar IRAS 16293-2422. *A&A*, 597:A53, January 2017. (document)

[2] A. Belloche, H. S. P. Muller, K. M. Menten, P. Schilke, and C. Comito. Complex organic molecules in the interstellar medium: IRAM 30 m line survey of Sagittarius B2(N) and (M). *A&A*, 559:A47, November 2013.

[3] A. Belloche, H. S. P. Muller, R. T. Garrod, and K. M. Menten. Exploring molecular complexity with ALMA (EMoCA): Deuterated complex organic molecules in Sagittarius B2(N2). *A&A*, 587:A91, March 2016. (document)

[4] H. S. P. Müller, S. Thorwirth, D. A. Roth, and G. Winnewisser. The Cologne Database for Molecular Spectroscopy, CDMS. *A&A*, 370:L49–L52, April 2001. (document)

[5] H. S. P. Müller, F. Schlöder, J. Stutzki, and G. Winnewisser. The Cologne Database for Molecular Spectroscopy, CDMS: a useful tool for astronomers and spectroscopists. *Journal of Molecular Structure*, 742:215–227, May 2005. (document)

[6] Eric Herbst and Ewine F Van Dishoeck. Complex organic interstellar molecules. *Annual Review of Astronomy and Astrophysics*, 47:427–480, 2009. (document)

[7] Erik Bründermann, Heinz-Wilhelm Hübers, and Maurice FitzGerald Kimmitt. *Terahertz techniques*, volume 151. Springer, 2012. 1.1, 4.4, 4.4.1, B

[8] GP Gallerano, S Biedron, et al. Overview of terahertz radiation sources. In *Proceedings of the 2004 FEL Conference*, number 1, pages 216–221, 2004. 1.4

[9] Xi-Cheng Zhang and Jingzhou Xu. *Introduction to THz wave photonics*, volume 29. Springer, 2010.

[10] Kai-Erik Peiponen, Axel Zeitler, and Makoto Kuwata-Gonokami. *Terahertz spectroscopy and imaging*, volume 171. Springer, 2012. 1.4

[11] Thomas W Crowe, William L Bishop, David W Porterfield, Jeffrey L Hesler, and Robert M Weikle. Opening the terahertz window with integrated diode circuits. *IEEE Journal of Solid-State Circuits*, 40(10):2104–2110, 2005. 1.2, B

[12] A Maestrini. *Bridging the microwave-to-photonics gap with terahertz frequency multipliers*. PhD thesis, Thèse d'habiliation à diriger des recherches (HDR), Univ. Pierre et Marie Curie-Paris 6, Paris, France, 2009. 1.4

[13] Armand Staprans, EarlW McCune, and Jack A Ruetz. High-power linear-beam tubes. *Proceedings of the IEEE*, 61(3):299–330, 1973. 1.4

[14] P Verhoeve, E Zwart, M Versluis, M Drabbels, JJ Ter Meulen, W Leo Meerts, A Dymanus, and DB McLay. A far infrared laser sideband spectrometer in the frequency region 550–2700 ghz. *Review of Scientific Instruments*, 61(6):1612–1625, 1990.

[15] A Khalid, NJ Pilgrim, GM Dunn, MC Holland, CR Stanley, IG Thayne, and DRS Cumming. A planar gunn diode operating above 100 ghz. *IEEE Electron Device Letters*, 28(10):849–851, 2007. 1.4

[16] P Guenard, O Doehler, B Epsztein, and R Warnecke. New uhf tubes with wide electronic tuning. range. *CR Acad. Sci.(Paris)*, 235:235, 1952. 1.4

[17] R Kompfner and NT Williams. Backward-wave tubes. *Proceedings of the IRE*, 41(11):1602–1611, 1953. 1.4

[18] Yun-Shik Lee. *Principles of terahertz science and technology*, volume 170. Springer Science & Business Media, 2009. 1.3, B

[19] KJ Button, M Inguscio, and F Strumia. Book-review-reviews of infrared and millimeter waves-v. 2-optically pumped far infrared lasers. *Science*, 224:1268, 1984. 1.4

[20] Marvin J Weber. *Handbook of laser wavelengths*. CRC press, 1998.

[21] Nigel G Douglas. *Millimetre and submillimetre wavelength lasers: a handbook of cw measurements*, volume 61. Springer, 2013. 1.4

[22] Michel Rochat, Lassaad Ajili, Harald Willenberg, Jerome Faist, Harvey Beere, Giles Davies, Edmund Linfield, and David Ritchie. Low-threshold terahertz quantum-cascade lasers. *Applied Physics Letters*, 81(8):1381–1383, 2002. 1.4

[23] Carlo Sirtori, Sukhdeep Dhillon, Clement Faugeras, A Vasanelli, and Xavier Marcadet. Quantum cascade lasers: The semiconductor solution for lasers in the mid- and far-infrared spectral regions. *physica status solidi (a)*, 203(14):3533–3537, 2006.

[24] Rüdeger Köhler, Alessandro Tredicucci, Fabio Beltram, Harvey E Beere, Edmund H Linfield, A Giles Davies, David A Ritchie, Rita C Iotti, and Fausto Rossi. Terahertz semiconductor-heterostructure laser. *Nature*, 417(6885):156–159, 2002. 1.4

[25] Goutam Chattopadhyay, Erich Schlecht, John S Ward, John J Gill, Hamid HS Javadi, Frank Maiwald, and Imran Mehdi. An all-solid-state broad-band frequency multiplier chain at 1500 ghz. *IEEE Transactions on Microwave Theory and Techniques*, 52(5):1538–1547, 2004. 1.5

[26] Alain Maestrini, John Ward, John Gill, Hamid Javadi, Erich Schlecht, Goutam Chattopadhyay, Frank Maiwald, Neal R Erickson, and Imran Mehdi. A 1.7-1.9 thz local oscillator source. *IEEE Microwave and Wireless Components Letters*, 14(6):253–255, 2004. 1.5

[27] http://aramis.obspm.fr. http://aramis.obspm.fr/~maestrini/Work/Home_files/NTTI-Paris-Multipliers-Jul-2007.pdf. 1.5, B

[28] Alain Maestrini, Bertrand Thomas, Hui Wang, Cécile Jung, Jeanne Treuttel, Yong Jin, Goutam Chattopadhyay, Imran Mehdi, and Gérard Beaudin. Schottky diode-based terahertz frequency multipliers and mixers. *Comptes Rendus Physique*, 11(7-8):480–495, 2010. 1.5

[29] Brian J Drouin, Frank W Maiwald, and John C Pearson. Application of cascaded frequency multiplication to molecular spectroscopy. *Review of Scientific Instruments*, 76(9):093113, 2005. 1.5

[30] Alain Maestrini, John S Ward, John J Gill, Hamid S Javadi, Erich Schlecht, Charlotte Tripon-Canseliet, Goutam Chattopadhyay, and Imran Mehdi. A 540-640-ghz high-efficiency four-anode frequency tripler. *IEEE Transactions on Microwave Theory and Techniques*, 53(9):2835–2843, 2005. 1, 1.9, B

[31] I Mehdi, SC Martin, RJ Dengler, RP Smith, and PH Siegel. Fabrication and performance of planar schottky diodes with t-gate-like anodes in 200-ghz subharmonically

pumped waveguide mixers. *IEEE Microwave and Guided wave letters*, 6(1):49–51, 1996. 2

[32] Imran Mehdi, Steven M Marazita, Dexter A Humphrey, Trong-Huang Lee, Robert J Dengler, John E Oswald, Andrew J Pease, Suzanne C Martin, William L Bishop, Thomas W Crowe, et al. Improved 240-ghz subharmonically pumped planar schottky diode mixers for space-borne applications. *IEEE transactions on microwave theory and techniques*, 46(12):2036–2042, 1998. 2

[33] Suzanne Martin, Barbara Nakamura, Andy Fung, Peter Smith, Jean Bruston, Alain Maestrini, Frank Maiwald, Peter Siegel, Erich Schlecht, and Imran Mehdi. Fabrication of 200 to 2700 ghz multiplier devices using gaas and metal membranes. In *Microwave Symposium Digest, 2001 IEEE MTT-S International*, volume 3, pages 1641–1644. IEEE, 2001. 2

[34] E Schlecht, G Chattopadhyay, A Maestrini, A Fung, S Martin, D Pukala, J Bruston, and I Mehdi. 200, 400 and 800 ghz schottky diode" substrateless" multipliers: design and results. In *Microwave Symposium Digest, 2001 IEEE MTT-S International*, volume 3, pages 1649–1652. IEEE, 2001. 2

[35] Jeffrey L Hesler and Thomas W Crowe. Responsivity and noise measurements of zero-bias schottky diode detectors. *Proc. ISSTT*, pages 89–92, 2007. 1.11, B

[36] David M Pozar. *Microwave engineering.* John Wiley & Sons, 2009. 3

[37] Constantine A Balanis. Antenna theory, ch. 2, 1982. 3

[38] Paul F Goldsmith, Institute of Electrical, Electronics Engineers, Microwave Theory, and Techniques Society. *Quasioptical systems: Gaussian beam quasioptical propagation and applications.* IEEE press New York, 1998. 3

[39] Chris M Mann. Fabrication technologies for terahertz waveguide. In *Terahertz Electronics Proceedings, 1998. THz Ninety Eight. 1998 IEEE Sixth International Conference on*, pages 46–49. IEEE, 1998. 3

[40] JL Hesler, T Crowe, et al. High-power solid-state terahertz sources. *SPIE Newsroom*, 2015. 1.15, B

[41] John S Ward, Goutam Chattopadhyay, John Gill, Hamid Javadi, Choonsup Lee, Robert Lin, Alain Maestrini, Frank Maiwald, Imran Mehdi, Erich Schlecht, et al. Tunable broadband frequency-multiplied terahertz sources. In *Infrared, Millimeter*

and Terahertz Waves, 2008. IRMMW-THz 2008. 33rd International Conference on, pages 1–3. IEEE, 2008. 1.16, B

[42] John David Vincent, John Vampola, Steve Hodges, Greg Pierce, and Mark Stegall. *Fundamentals of Infrared and Visible Detector Operation and Testing*. John Wiley & Sons, 2015. 3

[43] PL Richards. Bolometers for infrared and millimeter waves. *Journal of Applied Physics*, 76(1):1–24, 1994. 1.6

[44] J-X Yang, Farid Agahi, Dong Dai, Charles F Musante, Wes Grammer, Kei May Lau, and K Sigfrid Yngvesson. Wide-bandwidth electron bolometric mixers: A 2deg prototype and potential for low-noise thz receivers. *IEEE transactions on microwave theory and techniques*, 41(4):581–589, 1993. 1.18, B

[45] Frank J Low. Low-temperature germanium bolometer. *JOSA*, 51(11):1300–1304, 1961. 1.6

[46] MA Kinch. Compensated silicon-impurity conduction bolometer. *Journal of Applied Physics*, 42(13):5861–5863, 1971. 1.6

[47] Elliott R Brown, Jocelyn Keene, and TG Phillips. A heterodyne receiver for the submillimeter wavelength region based on cyclotron resonance in insb at low temperatures. *International journal of infrared and millimeter waves*, 6(11):1121–1138, 1985. 1.6

[48] Thomas keating ltd. www.terahertz.co.uk. 1.19, B

[49] William L Bishop, ER Meiburg, RJ Mattauch, Thomas W Crowe, and L Poli. A micron-thickness, planar schottky diode chip for terahertz applications with theoretical minimum parasitic capacitance. In *Microwave Symposium Digest, 1990., IEEE MTT-S International*, pages 1305–1308. IEEE, 1990. 1.6

[50] Virginia diodes, inc. www.virginiadiodes.com. 1.6, 1.20, 2.2.1, B

[51] L Liu, H Xu, Y Duan, AW Lichtenberger, JL Hesler, and RM Weikle. A 200 ghz schottky diode quasi-optical detector based on folded dipole antenna. In *20th International Symposium on Space Terahertz Technology*, 2009. 1.6

[52] Jeffrey L Hesler, Lei Liu, Haiyong Xu, Yiwei Duan, and Robert M Weikle. The development of quasi-optical thz detectors. In *Infrared, Millimeter and Terahertz Waves, 2008. IRMMW-THz 2008. 33rd International Conference on*, pages 1–2. IEEE, 2008. 1.6

[53] Marcel JE Golay. A pneumatic infra-red detector. *Review of Scientific Instruments*, 18(5):357–362, 1947. 1.6

[54] J Cooper. A fast-response pyroelectric thermal detector. *Journal of Scientific Instruments*, 39(9):467, 1962. 1.6

[55] Rolando R Buted. Zero bias detector diodes for the rf/id market. *Hewlett Packard Journal*, 46:94–94, 1995. 1.6

[56] Raymond W Waugh. Designing detectors for rf/id tags. In *RF EXPO WEST*, pages 212–223, 1995. 1.6

[57] RA Motiyenko, B Tercero, J Cernicharo, and L Margulès. Rotational spectrum of formamide up to 1 thz and first ism detection of its ν12 vibrational state. *Astronomy & Astrophysics*, 548:A71, 2012. 2.1

[58] RA Motiyenko, VV Ilyushin, BJ Drouin, S Yu, and L Margulès. Rotational spectroscopy of methylamine up to 2.6 thz. *Astronomy & Astrophysics*, 563:A137, 2014. 2.1

[59] SB Bteich, B Tercero, J Cernicharo, RA Motiyenko, L Margulès, and J-C Guillemin. Millimeter wave spectra of carbonyl cyanide. *Astronomy & Astrophysics*, 592:A43, 2016. 2.1

[60] E. A. Alekseev, R. A. Motiyenko, and L. Margules. Millimeter- and submillimeter-wave spectrometers on the basis of direct digital frequency synthesizers. *Radio Physics and Radio Astronomy*, 3(1):75–88, 2012. 2.2.1

[61] Olena Zakharenko, Roman A Motiyenko, Laurent Margulès, and Thérèse R Huet. Terahertz spectroscopy of deuterated formaldehyde using a frequency multiplication chain. *Journal of Molecular Spectroscopy*, 317:41–46, 2015. 2.2.1

[62] E8257d psg analog signal generator. http://www.keysight.com/en/pdx-x202237-pn-E8257D/psg-analog-signal-generator-100-khz-to-67-ghz?pm=spc&nid=-32488.1150403&cc=FR&lc=fre. 2.2.1

[63] Cmos 180 mhz dds/dac synthesizer ad9851. http://www.analog.com/media/en/technical-documentation/data-sheets/AD9915.pdf. 2.2.1

[64] http://www.ameteksi.com. http://www.ameteksi.com/products/lock-in-amplifiers/7270-general-purpose-dsp-lock-in-amplifier. 2.2.1

[65] Elijah Kannatey-Asibu Jr. *Principles of laser materials processing*, volume 4. John Wiley & Sons, 2009. 2.6, B

[66] JR Birch. The far infrared optical constants of polyethylene. *Infrared Physics*, 30(2):195–197, 1990. 3.4

[67] GW Chantry, JW Fleming, Patricia M Smith, M Cudby, and HA Willis. Far infrared and millimetre-wave absorption spectra of some low-loss polymers. *Chemical Physics Letters*, 10(4):473–477, 1971.

[68] William R Folks, Sidhartha K Pandey, and Glenn Boreman. Refractive index at thz frequencies of various plastics. In *Optical Terahertz Science and Technology*, page MD10. Optical Society of America, 2007.

[69] Yun-Sik Jin, Geun-Ju Kim, and Seok-Gy Jeon. Terahertz dielectric properties of polymers. *Journal of the Korean Physical Society*, 49(2):513–517, 2006. 3.4

[70] Zoltan Seres, Aaron Galonsky, Kazuo Ieki, Jon J Kruse, and Philip D Zecher. Optical transmission of mylar and teflon films. *Opt. Eng*, 33(9):3031, 1994. 3.4

[71] Donald R Smith and Ernest V Loewenstein. Optical constants of far infrared materials. 3: plastics. *Applied optics*, 14(6):1335–1341, 1975. 3.4

[72] Dominic J Benford, Michael C Gaidis, and Jacob W Kooi. Transmission properties of zitex in the infrared to submillimeter. 2001. 3.4

[73] Dominic J Benford, Michael C Gaidis, and Jacob W Kooi. Optical properties of zitex in the infrared to submillimeter. *Applied Optics*, 42(25):5118–5122, 2003. 3.4

[74] Akram KS Aqili and Asghari Maqsood. Determination of thickness, refractive index, and thickness irregularity for semiconductor thin films from transmission spectra. *applied Optics*, 41(1):218–224, 2002. 3.4

[75] Martin Van Exter and D Grischkowsky. Optical and electronic properties of doped silicon from 0.1 to 2 thz. *Applied Physics Letters*, 56(17):1694–1696, 1990. 3.4

[76] Hee Joo Choi, Hwan Hong Lim, Han Seb Moon, Tae Bong Eom, Jung Jin Ju, and Myoungsik Cha. Measurement of refractive index and thickness of transparent plate by dual-wavelength interference. *Optics express*, 18(9):9429–9434, 2010. 3.4, 3.11

[77] R Swanepoel. Determination of the thickness and optical constants of amorphous silicon. *Journal of Physics E: Scientific Instruments*, 16(12):1214, 1983. 3.4

[78] James W Lamb. Miscellaneous data on materials for millimetre and submillimetre optics. *International Journal of Infrared and Millimeter Waves*, 17(12):1997–2034, 1996. 3.4

[79] Jianming Dai, Jiangquan Zhang, Weili Zhang, and Daniel Grischkowsky. Terahertz time-domain spectroscopy characterization of the far-infrared absorption and index of refraction of high-resistivity, float-zone silicon. *JOSA B*, 21(7):1379–1386, 2004. 3.4

[80] David Crouse and Pavan Keshavareddy. Polarization independent enhanced optical transmission in one-dimensional gratings and device applications. *Optics Express*, 15(4):1415–1427, 2007. 3.4

[81] Max Born and Emil Wolf. *Principles of optics: electromagnetic theory of propagation, interference and diffraction of light.* Elsevier, 1980. 3.5.1, 3.5.1, 3.5.1, 3.5.1

[82] Fabian DJ Brunner, Arno Schneider, and Peter Günter. A terahertz time-domain spectrometer for simultaneous transmission and reflection measurements at normal incidence. *Optics express*, 17(23):20684–20693, 2009. 3.5.2

[83] O. Grasset, M. K. Dougherty, A. Coustenis, E. J. Bunce, C. Erd, D. Titov, M. Blanc, A. Coates, P. Drossart, L. N. Fletcher, H. Hussmann, R. Jaumann, N. Krupp, J.-P. Lebreton, O. Prieto-Ballesteros, P. Tortora, F. Tosi, and T. Van Hoolst. JUpiter ICy moons Explorer (JUICE): An ESA mission to orbit Ganymede and to characterise the Jupiter system. *Planetary and Space Science*, 78:1–21, April 2013. 4.1, 4.4.2

[84] J. Treuttel, L. Gatilova, A. Maestrini, D. Moro-Melgar, F.and Tamazouzt F. Yang, T. Vacelet, Y. Jin, A. Cavanna, J. Matéos, A. Féret, and C. Chaumont, C.and Goldstein. A 520–620 ghz schottky receiver front-end for planetary science and remote sensing with 1070 k 1500 k dsb noise temperature at room temperature. *IEEE Transactions on Terahertz Science and Technology*, 6(1):148–155, January 2016. 4.1, 4.4.2, 4.5, 4.13, B

[85] Olivier Grasset, MK Dougherty, A Coustenis, EJ Bunce, C Erd, D Titov, M Blanc, A Coates, P Drossart, LN Fletcher, et al. Jupiter icy moons explorer (juice): An esa mission to orbit ganymede and to characterise the jupiter system. *Planetary and Space Science*, 78:1–21, 2013. 4.2

[86] J Burie, D Boucher, J Demaison, and A Dubrulle. Spectre de rotation millimétrique du malononitrile. *Journal de Physique*, 43(9):1319–1325, 1982. 4.2

[87] Florin Lucian Constantin. Phase-coherent heterodyne detection in the terahertz regime with a photomixer. *IEEE Journal of Quantum Electronics*, 47(11):1458–1462, 2011. 4.2

[88] Fabrice Willaert. *Spectroscopie millimétrique et submillimétrique de molécules d'intérêts atmosphérique et/ou astrophysique: développement du spectromètre térahertz de Lille.* PhD thesis, Lille 1, 2005. 4.2

[89] Ling Jiang, Wei Miao, Wen Zhang, Ning Li, Zhen Hui Lin, Qi Jun Yao, Sheng-Cai Shi, S. I. Svechnikov, Y. B. Vakhtomin, S. V. Antipov, B. M. Voronov, N. S. Kaurova, and G. N. Gol'tsman. Characterization of a quasi-optical nbn superconducting heb mixer. *IEEE Transactions on Microwave Theory and Techniques*, 54(7):2944–2948, July 2006. 2, 4.3b

[90] Alexandre Karpov, David Miller, Frank R Rice, Jeffrey A Stern, Bruce Bumble, Henry G LeDuc, and Jonas Zmuidzinas. Low-noise sis mixer for far-infrared radio astronomy. In *Proceedings of SPIE*, volume 5498, pages 616–621, 2004. 2, 4.3c

[91] JW Kooi, JA Stern, G Chattopadhyay, HG LeDuc, B Bumble, and J Zmuidzinas. Low-loss nbtin films for thz sis mixer tuning circuits. *International journal of infrared and millimeter waves*, 19(3):373–383, 1998. 2

[92] F. Boussaha, J. Kawamura, J. Stern, and C. Jung-Kubiak. 2.7 thz balanced waveguide heb mixer. *IEEE Transactions on Terahertz Science and Technology*, 4(5):545–551, Sept 2014. 2

[93] M. Kroug, S. Cherednichenko, H. Merkel, E. Kollberg, B. Voronov, G. Gol'tsman, H. W. Huebers, and H. Richter. Nbn hot electron bolometric mixers for terahertz receivers. *IEEE Transactions on Applied Superconductivity*, 11(1):962–965, Mar 2001.

[94] B. S. Karasik, M. C. Gaidis, W. R. McGrath, B. Bumble, and H. G. LeDuc. A low-noise 2.5 thz superconductive nb hot-electron mixer. *IEEE Transactions on Applied Superconductivity*, 7(2):3580–3583, June 1997.

[95] Y Delorme, R Lefèvre, W Miao, A Féret, W Zhang, T Vacelet, F Dauplay, L Pelay, J Spatazza, M Ba Trung, et al. A quasi-optical nbn heb mixer with 800k dsb noise temperature at 2.5 thz. *Proc. 22nd ISSTT*, pages 135–138, 2011. 2

[96] Bertrand Thomas, Alain Maestrini, John Gill, Choonsup Lee, Robert Lin, Imran Mehdi, and Peter de Maagt. A broadband 835–900-ghz fundamental balanced mixer

based on monolithic gaas membrane schottky diodes. *IEEE Transactions on Microwave Theory and Techniques*, 58(7):1917–1924, 2010. 2

[97] Erich T Schlecht, John J Gill, Robert H Lin, Robert J Dengler, and Imran Mehdi. A 520–590 ghz crossbar balanced fundamental schottky mixer. *IEEE Microwave and Wireless Components Letters*, 20(7):387–389, 2010.

[98] B Thomas, A Maestrini, J Gill, C Lee, R Lin, I Mehdi, and P De Maagt. An 874 ghz fundamental balanced mixer based on mmic membrane planar schottky diodes. In *21st International Symposium on Space Terahertz Technology*, pages 155–58, 2010. 2

[99] E. Schlecht, J. V. Siles, C. Lee, R. Lin, B. Thomas, G. Chattopadhyay, and I. Mehdi. Schottky diode based 1.2 thz receivers operating at room-temperature and below for planetary atmospheric sounding. *IEEE Transactions on Terahertz Science and Technology*, 4(6):661–669, Nov 2014. 4.4.2

[100] Peter H Siegel. Thz instruments for space. *IEEE Transactions on Antennas and Propagation*, 55(11):2957–2965, 2007. 4.4.2

[101] Stefan Heyminck, UU Graf, R Güsten, Jürgen Stutzki, HW Hübers, and P Hartogh. Great: the sofia high-frequency heterodyne instrument. *Astronomy & Astrophysics*, 542:L1, 2012. 4.4.2

[102] ET Young, EE Becklin, PM Marcum, TL Roellig, JM De Buizer, Terry L Herter, R Güsten, EW Dunham, P Temi, B-G Andersson, et al. Early science with sofia, the stratospheric observatory for infrared astronomy. *The Astrophysical Journal Letters*, 749(2):L17, 2012. 4.4.2

[103] Gary J Melnick, John R Stauffer, Matthew LN Ashby, Edwin A Bergin, Gordon Chin, Neal R Erickson, Paul F Goldsmith, Martin Harwit, John E Howe, Steven C Kleiner, et al. The submillimeter wave astronomy satellite: Science objectives and instrument description. *The Astrophysical Journal Letters*, 539(2):L77, 2000. 4.4.2

[104] Gary J Melnick. The submillimeter wave astronomy satellite. In *From Gas to Stars to Dust*, volume 73, 1995. 4.4.2

[105] U Frisk, Magne Hagström, J Ala-Laurinaho, S Andersson, J-C Berges, J-P Chabaud, Magnus Dahlgren, A Emrich, H-G Florén, G Florin, et al. The odin satellite-i. radiometer design and test. *Astronomy & Astrophysics*, 402(3):L27–L34, 2003. 4.4.2

[106] JUICE Jupiter Icy Moons Explorer SWI. Submillimetre wave instrument (swi), science concept document. Technical report, JUI-MPS-SWI-PL-002, 13/05, 2013. 4.4.2

[107] A Maestrini, L Gatilova, J Treuttel, F Yang, Y Jin, A Cavanna, D Moro Melgar, F Tamazouzt, T Vacelet, A Féret, et al. 1200ghz and 600ghz schottky receivers for juice-swi. In *27th International Symposium on Space Terahertz Technology*, 2016. 4.4.2

[108] Peter Sobis, Vladimir Drakinskiy, Niklas Wadefalk, Yogesh Karandikhar, Arvid Hammar, Anders Emrich, Huan Zhao, Tomas Bryllert, Aik-Yean Tang, PA Nilsson, et al. Low noise gaas schottky tmic and inp hemt mmic based receivers for the ismar and swi instruments. In *Proc. Micro-and Millimetre Wave Technology and Techniques Workshop*, pages 25–27, 2014. 4.4.2

[109] J Treuttel, L Gatilova, A Maestrini, D Moro-Melgar, F Yang, F Tamazouzt, T Vacelet, Y Jin, A Cavanna, J Matéos, et al. A 520–620-ghz schottky receiver front-end for planetary science and remote sensing with 1070 k–1500 k dsb noise temperature at room temperature. *IEEE Transactions on Terahertz Science and Technology*, 6(1):148–155, 2016. 4.5

[110] J. Treuttel, L. Gatilova, F. Yang, A. Maestrini, Y. Jin, A. Cavanna, T. Vacelet, F. Tamazouzt, J. M. Krieg, and C. Goldstein. A 330 ghz frequency doubler using european mmic schottky process based on e-beam lithography. In *2014 XXXIth URSI General Assembly and Scientific Symposium (URSI GASS)*, pages 1–4, Aug 2014. 4.7, 1, B

[111] D. Teyssier, E. Dartois, and D. Deboffle. Herschel astronomers' website, 2006. http://herschel.esac.esa.int/twiki/pub/Public/HifiDocsEditableTable/Gascell_manual_v0.2.pdf. 4.6.1

[112] H. M. Pickett, R. L. Poynter, E. A. Cohen, M. L. Delitsky, J. C. Pearson, and H. S. P. Müller. Submillimeter, millimeter and microwave spectral line catalog. *Journal of Quantitative Spectroscopy & Radiative Transfer*, 60:883–890, November 1998. 4.6.1

[113] J. C. Pearson, B. J. Drouin, and H. M. Pickett. Molecular Spectroscopy and Line Catalogs at JPL. In *IAU Symposium*, volume 235 of *IAU Symposium*, page 270, 2005. 4.6.1

[114] L.-H. Xu, J. Fisher, R. M. Lees, H. Y. Shi, J. T. Hougen, J. C. Pearson, B. J. Drouin, G. A. Blake, and R. Braakman. Torsion rotation global analysis of the first three torsional states ($\nu_t = 0$, 1, 2) and terahertz database for methanol. *Journal of Molecular Spectroscopy*, 251:305–313, September 2008. 4.6.1

[115] Carolyn S Brauer, John C Pearson, Brian J Drouin, and Shanshan Yu. New ground-state measurements of ethyl cyanide. *The Astrophysical Journal Supplement Series*, 184(1):133, 2009. 4.8

[116] John C Pearson, Ken Cooper, and Brian J Drouin. Spectroscopic detection, fundamental limits and system considerations. In *Infrared, Millimeter and Terahertz Waves, 2008. IRMMW-THz 2008. 33rd International Conference on*, pages 1–2. IEEE, 2008. 4.9.1

[117] CH Townes and S Geschwind. Limiting sensitivity of a microwave spectrometer. *Journal of Applied Physics*, 19(8):795–796, 1948. 4.9.1

[118] Nadav Levanon. Radar principles. *New York, Wiley-Interscience, 1988, 320 p.*, 1988. 4.9.1

[119] Robert Hildreth Kingston. *Detection of optical and infrared radiation*, volume 10. Springer, 2013. 4.9.2

[120] Raymond Blundell et al. Submillimeter receivers for radio astronomy. *Proceedings of the IEEE*, 80(11):1702–1720, 1992. 4.9.2

[121] Christopher K Walker. *Terahertz astronomy*. Crc Press, 2015. 4.9.2

[122] HM Pickett, RL Poynter, EA Cohen, ML Delitsky, JC Pearson, and HSP Müller. Submillimeter, millimeter, and microwave spectral line catalog. *Journal of Quantitative Spectroscopy and Radiative Transfer*, 60(5):883–890, 1998. 4.9.3

[123] Walter Gordy and Robert L Cook. *Microwave molecular spectra*. Wiley,, 1984. 5.1, 3

[124] D. Papousek and M. R. Aliev. *Molecular vibrational-rotational spectra*. Elsevier, Amsterdam New York, 1982. 5.1, 1, 2

[125] Charles H Townes and Arthur L Schawlow. *Microwave spectroscopy*. Courier Corporation, 2013. 5.1

[126] Harold W Kroto. *Molecular rotation spectra*. Dover, 1992. 5.1

[127] James KG Watson. Simplification of the molecular vibration-rotation hamiltonian. *Molecular Physics*, 15(5):479–490, 1968. 5.4.2, 5.4.2

[128] MR Aliev and James KG Watson. Calculated sextic centrifugal distortion constants of polyatomic molecules. *Journal of Molecular Spectroscopy*, 61(1):29–52, 1976. 5.4.2

[129] Gilbert Amat, Harald Herborg Nielsen, Ginette Tarrago, et al. Rotation-vibration of polyatomic molecules. 1971. 5.4.2

[130] MR Aliev, JKG Watson, and K Narahari Rao. Molecular spectroscopy: Modern research, vol. iii. *Academic, New York*, pages 1–67, 1985. 5.4.2

[131] MR Aliev JKG Watson. Higher-order effects in the vibration-rotation spectra of semirigid molecules. *Molecular spectroscopy: modern research*, 3:1, 1985. 5.4.3

[132] HA Jahn. Note on coriolis coupling terms in polyatomic molecules. *Physical Review*, 56(7):680, 1939. 1

[133] Zbigniew Kisiel, Lech Pszczółkowski, Brian J Drouin, Carolyn S Brauer, Shanshan Yu, and John C Pearson. The rotational spectrum of acrylonitrile up to 1.67 thz. *Journal of Molecular Spectroscopy*, 258(1):26–34, 2009. 2

[134] Herbert M Pickett. The fitting and prediction of vibration-rotation spectra with spin interactions. *Journal of Molecular Spectroscopy*, 148(2):371–377, 1991. 5.5.5

[135] L Margulès, A Belloche, HSP Müller, RA Motiyenko, J-C Guillemin, RT Garrod, and KM Menten. Spectroscopic study and astronomical detection of doubly 13c-substituted ethyl cyanide. *Astronomy & Astrophysics*, 590:A93, 2016. 6.2.1

[136] J Cernicharo, Z Kisiel, B Tercero, L Kolesniková, IR Medvedev, A López, S Fortman, M Winnewisser, FC de Lucia, JL Alonso, et al. A rigorous detection of interstellar ch3nco: an important missing species in astrochemical networks. *Astronomy & Astrophysics*, 587:L4, 2016. 6.3.1

[137] DT Halfen, Vadim V Ilyushin, and Lucy M Ziurys. Interstellar detection of methyl isocyanate ch3nco in sgr b2 (n): a link from molecular clouds to comets. *The Astrophysical Journal Letters*, 812(1):L5, 2015.

[138] NFW Ligterink, A Coutens, V Kofman, HSP Müller, RT Garrod, H Calcutt, SF Wampfler, JK Jørgensen, H Linnartz, and EF van Dishoeck. The alma-pils survey: detection of ch3nco towards the low-mass protostar iras 16293- 2422 and laboratory constraints on its formation. *Monthly Notices of the Royal Astronomical Society*, 469(2):2219–2229, 2017.

[139] Fred Goesmann, Helmut Rosenbauer, Jan Hendrik Bredehöft, Michel Cabane, Pascale Ehrenfreund, Thomas Gautier, Chaitanya Giri, Harald Krüger, Léna Le Roy, Alexandra J MacDermott, et al. Organic compounds on comet 67p/churyumov-gerasimenko revealed by cosac mass spectrometry. *Science*, 349(6247):aab0689, 2015. 6.3.1

[140] Lewis E Snyder and David Buhl. Interstellar isocyanic acid. *The Astrophysical Journal*, 177:619, 1972. 6.3.1

[141] L. E. Snyder and D. Buhl. Interstellar Isocyanic Acid. *ApJ*, 177:619, November 1972.

[142] L. E. Snyder and D. Buhl. Interstellar Methylacetylene and Isocyanic Acid. *Nature Physical Science*, 243:45–46, May 1973.

[143] M. A. Frerking, R. A. Linke, and P. Thaddeus. Interstellar isothiocyanic acid. *Astrophysical Journal Letters*, 234:L143–L145, December 1979.

[144] D. Buhl, L. E. Snyder, and J. Edrich. An Interstellar Emission Line from Isocyanic Acid at 1.4 Centimeters. *ApJ*, 177:625, November 1972. 6.3.1

[145] A Coutens, Jes Kristian Jørgensen, Matthijs Hendrik Daniël Van der Wiel, HSP Müller, Julie Maria Lykke, Per Bjerkeli, TL Bourke, Hannah Calcutt, MN Drozdovskaya, C Favre, et al. The alma-pils survey: First detections of deuterated formamide and deuterated isocyanic acid in the interstellar medium. *Astronomy & Astrophysics*, 590:L6, 2016. 6.3.1

[146] A. Coutens, J. K. Jørgensen, M. H. D. van der Wiel, H. S. P. Müller, J. M. Lykke, P. Bjerkeli, T. L. Bourke, H. Calcutt, M. N. Drozdovskaya, C. Favre, E. C. Fayolle, R. T. Garrod, S. K. Jacobsen, N. F. W. Ligterink, K. I. Öberg, M. V. Persson, E. F. van Dishoeck, and S. F. Wampfler. The ALMA-PILS survey: First detections of deuterated formamide and deuterated isocyanic acid in the interstellar medium. *A&A*, 590:L6, May 2016. 6.3.1

[147] J. Cernicharo, Z. Kisiel, B. Tercero, L. Kolesniková, I. R. Medvedev, A. López, S. Fortman, M. Winnewisser, F. C. de Lucia, J. L. Alonso, and J.-C. Guillemin. A rigorous detection of interstellar CH_3NCO: An important missing species in astrochemical networks. *A&A*, 587:L4, February 2016. 6.3.1, 6.3.2

[148] D. T. Halfen, V. V. Ilyushin, and L. M. Ziurys. Interstellar Detection of Methyl Isocyanate CH_3NCO in Sgr B2(N): A Link from Molecular Clouds to Comets. *Astrophysical Journal Letters*, 812:L5, October 2015. 6.3.1

[149] L. Margulès, R. A. Motiyenko, J.-C. Guillemin, J. Cernicharo, B. Tercero, V. V. Ilyushin, and I. Kleiner. SUBMILLIMETER WAVE SPECTROSCOPY OF ACETYL ISOCYANATE : CH3C(O)NCO. In *69th International Symposium on Molecular Spectroscopy*, June 2014. 6.3.1, 6.3.2

[150] Barry M. Landsberg and Khalid Iqbal. Microwave spectrum of acetyl isocyanate. *J. Chem. Soc., Faraday Trans. 2*, 76:1208–1213, 1980. 6.3.1, 6.3.2

[151] C. V. Stephenson, W. C. Coburn, and W. S. Wilcox. The vibrational spectra and assignments of nitrobenzene, phenyl isocyanate, phenyl isothiocyanate, thionylaniline and anisole. *Spectrochimica Acta*, 17:933–946, 1961.

[152] M. C. L. Gerry, J. C. Thompson, and T. M. Sugden. Microwave Spectrum of Silyl Isocyanate. *Nature*, 211:846–847, August 1966.

[153] J. Koput. The microwave spectrum of methyl isocyanate. *Journal of Molecular Spectroscopy*, 115:131–146, January 1986.

[154] J. A. Duckett, A. G. Robiette, and M. C. L. Gerry. The microwave spectrum of silyl isocyanate, SiH $_3$NCO: Spectra of isotopically substituted species and correction of the r$_s$ structure. *Journal of Molecular Spectroscopy*, 90:374–393, December 1981.

[155] R. F. Curl, Jr., V. M. Rao, K. V. L. N. Sastry, and J. A. Hodgeson. Microwave Spectrum of Methyl Isocyanate. *The Journal of Chemical Physics*, 39:3335–3340, December 1963.

[156] W. H. Hocking and M. C. L. Gerry. The microwave spectrum and structure of chlorine isocyanate. *Journal of Molecular Spectroscopy*, 42:547–566, June 1972.

[157] H. M. Jemson, W. Lewis-Bevan, N. P. C. Westwood, and M. C. L. Gerry. The microwave spectrum and structure of the unstable molecule bromine isocyanate, BrNCO. *Journal of Molecular Spectroscopy*, 118:481–499, August 1986.

[158] W. H. Hocking, M. L. Williams, and M. C. L. Gerry. Further study of the microwave spectrum of chlorine lsocyanate: The substitution structure and nuclear quadrupole coupling. *Journal of Molecular Spectroscopy*, 58:250–260, November 1975.

[159] R. P. Hirschmann, R. N. Kniseley, and V. A. Fassel. The infrared spectra of alkyl isocyanates. *Spectrochimica Acta*, 21:2125–2133, December 1965.

[160] J. F. Sullivan, S. K. Nandy, M. J. Lee, and J. R. Durig. Raman and infrared spectra, conformational stability andab initio calculations for chlorocarbonyl isocyanate. *Journal of Raman Spectroscopy*, 23:51–60, January 1992. 6.3.1

[161] J Cernicharo, N Marcelino, E Roueff, M Gerin, A Jiménez-Escobar, and GM Muñoz Caro. Discovery of the methoxy radical, ch3o, toward b1: dust grain and gas-phase chemistry in cold dark clouds. *The Astrophysical Journal Letters*, 759(2):L43, 2012. 6.3.1

[162] A Belloche, AA Meshcheryakov, RT Garrod, VV Ilyushin, EA Alekseev, RA Motiyenko, L Margulès, HSP Müller, and KM Menten. Rotational spectroscopy, tentative interstellar detection, and chemical modeling of n-methylformamide. *Astronomy & Astrophysics*, 601:A49, 2017. 6.3.1

[163] MJEA Frisch, GW Trucks, Hs B Schlegel, GE Scuseria, MA Robb, JR Cheeseman, G Scalmani, V Barone, B Mennucci, GAea Petersson, et al. Gaussian 09. *Gaussian 09, Revision A. 02, Wallingford Inc., CT*, 2009. 6.3.2

[164] Herbert M. Pickett. The fitting and prediction of vibration-rotation spectra with spin interactions. *J. Mol. Spectrosc.*, 148(2):371 – 377, 1991. 6.3.4, 6.3.5